



UNIVERSITAT AUTÒNOMA DE BARCELONA

# Observations of $\gamma$ -rays from the Galactic Center with the MAGIC Telescope

Indirect searches of supersymmetric dark matter

Ph.D. Dissertation

Josep Flix Molina

Universitat Autònoma de Barcelona

Departament de Física

08193 Bellaterra (Barcelona)

Spain

<jflix@ifae.es>

April 2006

*supervised by:*

Enrique Fernández

*and co-supervised by:*

Manel Martínez

IFAE

Edifici Cn, UAB

08193 Bellaterra (Barcelona)



# Agraïments

Aquesta tesi és la culminació d'una tasca que vaig iniciar ara ja fa uns anys a l'IFAE. Durant aquest temps he tingut l'oportunitat de treballar i conèixer gent molt agradable, fent bons amics aquí a Barcelona i a fora, amb els quals he passat els moments més agradables d'aquesta època, i també, tot s'ha de dir, els 'menys bons'... encara que aquests, amb la perspectiva, han quedat eclipsats pels millors. Sense cap dubte.

Primer de tot vull agrair a l'Enrique Fernández, ja que va ser ell qui em va donar l'oportunitat d'entrar a formar part d'aquest grup de recerca, i cap al final d'aquesta etapa m'ha donat tot el suport necessari com a director per poder finalitzar la tesi en unes condicions més que acceptables. A Manel Martínez per captar la meua atenció cap a l'astrofísica i donar-me la possibilitat de formar part de la col·laboració MAGIC. Manel sempre és una font inesgotable d'idees inspiradores i tasques a fer, que han estat molt útils per a aquesta tesi. Aquí vull afegir al Juan Cortina, que hem va ajudar molt amb la part tècnica d'aquesta tesi i amb d'altres converses, aquí i a La Palma.

Tinc molt bon record del meu pas per l'IFAE i per la col·laboració MAGIC. Encara recordo quan vaig entrar a formar-ne part. Vaig anar a la illa de La Palma, a Canàries, i al lloc on havia d'anar el telescopi no hi havia més que herba... Just en aquell moment començaria la construcció del telescopi, procés que vaig viure molt intensament, participant en la construcció de la càmera i la seva instal·lació. Això em va permetre viure en primera persona què és realment la posada en marxa d'un experiment d'aquestes característiques, treballant-hi amb unes persones amb gran grau d'humanitat i companyerisme. Tot això va portar a que finalment hagi tingut la sort de participar en un dels primers anàlisis 'seriosos' del telescopi i les primeres publicacions científiques de MAGIC, que a dia d'avui, estan essent considerades molt valuoses per la comunitat científica. Així que m'emporto molts bons moments de tota aquesta època i amb tota la gent de MAGIC amb qui he treballat aquí a l'IFAE, allà a La Palma, i amb d'altres persones d'altres institucions amb qui he coincidit regularment aquí i allà.

Començaré dedicant unes línies als d'aquí, a l'IFAE, que són amb qui he treballat de més aprop: l'Eva, les nits interminables passades a La Palma i la nostra super-parametrització del DISP; l'Oscar, super-company de despatx i d'aventures de tirar cables a La Palma (passa'm el 'Cutter')!... i amb qui vaig practicar la 'morositat compulsiva'; el Markus i les caòtiques sessions d'instal·lació de la caixa de cal·libracció i recerca incansable d'spikes!; el Javi, amb qui he compartit moltes nits de feina, moltes més de diversió, i moltes converses sobre tot el què ens envolta. De tots ells n'he après moltíssim. Després estan els qui van arribar més tard, com la Núria, que ara ja s'ha convertit en tota una experta de La Guagua (ho sento!), el Roger (on tens aquell plot?, no el trobo), l'Àlex (més conegut al meu barri com el 'xiquet' de Fraga), l'Emma (Oxe, chiquillo!), el Javi Rico (merci por todo!), l'Ester (companya de despatx i de desesperacions), la Laia (encara no sé com es fa un esquemàtic amb l'auto-router!), el Manel (encara no he tripat del tot, no...), i els nous fixatges, el Diego (Ciao, bambino) i l'Abelardo (l'home simulació)... I la gent de fora de l'IFAE, amb els qui he compartit estades a l'estranger, converses, esquíades, sortides de nit, etc.: el Diego, Wolfgang, Florian, Pratik, Nadia, Adrian, Sabrina, Sebastian, Ciro, Mose, Villi, Toni, Andreu, Raquel, Arnau, Fabrizio, Daniela, Thomas, entre d'altres...

Tornant a l'IFAE, donat que és un institut amb cert tamany, també he compartit molts moments amb d'altres persones. La llista és llarga, així que quedeu tots convocats per ser agraïts... ;)

Ara toca el torn a tots aquells que han sofert aquest període de tesi i que no tenen res a veure amb la física... Ejem... alguns si que també cauen en aquest bloc... El Super-Combo inestable de Jazz (deu ser l'únic sextet de Jazz format per físics, exclusivament, a tota Catalunya!), que han patit tota mena de síncope i contratemps de baix (i moltes absències!, tot s'ha de dir) mentre escrivia la tesi: l'Àlvar (cuida't la 'melena', eh?), el Jordi Round (i les seves re-harmonitzacions... això és eòlic, no?), el Jordi 'Virtu' (de virtu... virtu... virtuòs?), l'Octavi (toquem en clau de Soul?), el Gon ('tú...tú... tú si que eres bueno!'); i els del nou grup de Jazz: l'Àlex (algun dia et faré algun bolo, t'ho prometo!), l'Stefan (sí, crec que això que ve ara és un Swing!), i el Jordi (quan quedem per gravar?). Després els músics de lluny, amb els que visc les sessions musicals més salvatges: els *4versions*; el Robert, quants Kms compartits amb els que he après moltíssim de música. Ets el millor, i algun dia t'ho reconeixeràn; el Jordi, a veure quan troba la configuració de pedals 'guitarrrerus' estables; el Ferran, que m'ha ensenyat que s'ha de ser musicalment perseverant i també que es pot fer un super-bombo amb un goliat; la Noèlia i les seves aparicions musicals estelars; el William i els seus Xupitos de Whiskys!... A la gent del grup alemany *Public Address*, que van haver d'aguantar la meua veu una estona: Safa, Toni, Uli i Luca. Al Dam, al que li prometo que llegiré (millor, entendre!) totes les teves lletres i a veure quan acabem el disc! Als 'funkerus': Pau, Jordi, Cristian, etc... I també a Charlie Moreno, per ser el millor professor de baix que es pot tenir!... i als meus alumnes musicals, que no se si pensaràn això de mi... ;) Gràcies a tots per donar-me un hobby tant excitant i apassionant! ;)

I els compis, que també han sofert una mica el què els hi tocava i que ara sofriràn més, perquè torno a ser més actiu socialment: a la Digna, el Jordi i el Miquel, per tots els nostres moments de vici compartits; el Victor i l'Andrea, us juro que no tornarem a anar una setmana en vaixell!; la Rebeck (capital de Canadà) i el Dam, per tots els moments que compartim i pel nostre viatge d'estiu!; el Lluís i la Narda, que m'han de comprar una guitarra nova!; el Juan Luís, tu sí que t'ho montes bé!; el Carles i la Laia, i les excursions de muntanya; l'Isaac i la Mònica (i el Pol, que ho ha sofert parcialment!), a veure si us anem a visitar algun dia a Cambridge!; Bonache, però no anaves a l'empresa?; l'Encarna-maligna i les seves mega-escultures; el Gabi, i els matins musicals de botigues; el Martin, no anirem en vaixell mai més, t'ho juro...

I per acabar, els que queden molt més aprop i que m'han donat tot el recolzament possible i per haver-hi... No es pot demanar més, ja que clarament he tingut molt més del què és imaginable.

La meua germana i els meus pares, que sempre estan disposats a ajudar-me en tot el què ha calgut, i que a dia d'avui encara s'esforçen bastant en entendre una mica el que he fet o faig a la ciència... Gràcies per haver-me cuidat tant, pel vostre esforç i per tota la confiança depositada... Ara si que finalment la tesi ja està acabada. Podeu estar ben orgullosos.

I la Neus: una ràfaga d'aire fresc que em va eclipsar enmig d'aquest embolic tan gran de tesi i bogeria. Gràcies companya per cuidar-me tant, per aguantar-me, per les absències, per estimar-me, i per donar-me molts dels millors moments de la meua vida i els que han de venir, de ben segur. Putunets molt grans, Japen!

I a tots i totes a qui no he anomenat, però que sempre han estat a prop. Gràcies.

I ara, prometeu-me que passareu l'índex i que llegireu la tesi, que ha costat molt d'esforç... Salut!

# Contents

<b>1</b>	<b>Introduction</b>	<b>2</b>
1.1	Motivations and distribution of the Thesis contents . . . . .	3
<b>I</b>	<b>Supersymmetric dark matter and indirect searches with the MAGIC Cherenkov Telescope</b>	<b>5</b>
<b>2</b>	<b>The dark matter paradigm</b>	<b>6</b>
2.1	Historical highlights . . . . .	7
2.2	The dark matter evidence . . . . .	8
2.2.1	Local fact: dark matter in galactic halos . . . . .	8
2.2.2	Non-local fact: dark matter in galaxy clusters . . . . .	9
2.2.3	Cosmological fact . . . . .	10
2.3	The Standard Cosmological Model . . . . .	11
2.3.1	Mathematical description of the SCM model . . . . .	12
2.4	The most relevant cosmological data . . . . .	14
2.4.1	Large Scale Structure (LSS) . . . . .	15
2.4.2	Cosmic Microwave Background (CMB) . . . . .	16
2.4.3	Type Ia supernovae . . . . .	18
2.5	Precise determination of cosmological parameters . . . . .	18
2.5.1	Best-mean values of cosmological parameters . . . . .	19
2.5.2	Direct estimates of the Hubble constant . . . . .	20
2.5.3	The temperature $T_0$ . . . . .	21
2.6	Computational cosmology: N-body simulations . . . . .	22
2.7	Limitations of the SCM . . . . .	24
2.7.1	Improvements from the observational side . . . . .	26
2.7.2	Conceptual problems of the SCM . . . . .	27
2.7.3	Any alternative to dark matter? . . . . .	28
2.8	Dark matter: what can it be? . . . . .	28
2.8.1	Non-baryonic candidates . . . . .	29
2.8.2	The neutralino as the preferred dark matter particle . . . . .	31
<b>3</b>	<b>Supersymmetric dark matter</b>	<b>33</b>
3.1	Introduction . . . . .	33
3.2	The Standard Model (SM): its successes, failures, and its limitations . . . . .	33
3.3	Minimal SUSY extension of the SM: the MSSM . . . . .	35
3.3.1	The minimal supergravity (mSUGRA) . . . . .	36
3.4	Neutralino as the dark matter SUSY candidate . . . . .	37
3.5	Evaluating the relic density of neutralinos . . . . .	37

3.5.1	Most relevant annihilation channels . . . . .	38
3.6	Experimental research of SUSY dark matter . . . . .	39
3.6.1	Direct detection . . . . .	39
3.6.2	Indirect detection . . . . .	40
3.7	$\gamma$ -rays from Dark Matter halos . . . . .	42
3.7.1	Dark matter halo $\gamma$ -ray emissivity . . . . .	43
3.7.2	$\gamma$ -ray flux from dark matter halo arriving to earth . . . . .	43
3.8	SUSY flux component: expected $f_{SUSY}$ . . . . .	44
3.8.1	Phenomenological constrains . . . . .	45
3.8.2	Scanning the mSUGRA parameter space . . . . .	45
3.8.3	Evaluation of $f_{SUSY}$ in mSUGRA . . . . .	47
3.8.4	Evaluation of $f_{SUSY}$ in non-constrained MSSM . . . . .	49
<b>4</b>	<b>Indirect dark matter detection in <math>\gamma</math>-ray astronomy: MAGIC search strategies</b>	<b>53</b>
4.1	Introduction . . . . .	53
4.2	Modeling a DM halo . . . . .	54
4.2.1	Estimating the $\alpha$ parameter: N-body simulations . . . . .	54
4.2.2	Experimental constrains on the $\alpha$ parameter . . . . .	54
4.3	The center of the Milky Way galaxy . . . . .	55
4.3.1	Milky Way mass models with adiabatic compression . . . . .	56
4.4	Evaluation of $J(\Psi)$ for the GC $\rho_{dm}$ models . . . . .	58
4.5	The Draco dwarf spheroidal galaxy . . . . .	59
4.5.1	Evaluation of $J(\Psi)$ for the considered Draco DM density profiles . . . . .	61
4.6	The nearest galaxy: M31 (Andromeda) . . . . .	61
4.6.1	Evaluation of $J(\Psi)$ for the considered M31 DM density profiles . . . . .	62
4.7	$\gamma$ -ray flux predictions for the selected candidates: MAGIC search strategies . . . . .	64
4.8	Observation proposals . . . . .	66
<b>II The MAGIC telescope for <math>\gamma</math>-ray astronomy: description and technical work</b>		<b>69</b>
<b>5</b>	<b><math>\gamma</math>-ray astronomy and the MAGIC Telescope</b>	<b>70</b>
5.1	Introduction . . . . .	70
5.2	The Universe at GeV energies . . . . .	71
5.3	The Universe at TeV energies . . . . .	72
5.4	The physics of Extended Air Showers . . . . .	74
5.4.1	Electromagnetic EAS . . . . .	75
5.4.2	Hadronic EAS . . . . .	77
5.5	The Imaging Atmospheric Čerenkov Technique . . . . .	78
5.5.1	Čerenkov radiation in an EAS . . . . .	78
5.6	Imaging Air Čerenkov Telescopes: detection technique . . . . .	82
5.7	The MAGIC telescope . . . . .	86
5.7.1	The frame and the large mirror surface . . . . .	87
5.7.2	The camera . . . . .	91
5.7.3	The trigger system . . . . .	99
5.7.4	The data acquisition system . . . . .	101
5.7.5	The calibration system . . . . .	103
5.8	Status and first results of MAGIC telescope . . . . .	105

<b>6</b>	<b>Camera and Calibration remote control system, and software design</b>	<b>107</b>
6.1	Camera slow control electronics . . . . .	107
6.2	Calibration slow control electronics . . . . .	116
6.2.1	Calibration pulser box . . . . .	116
6.2.2	Calibration trigger . . . . .	120
6.3	Outline of the MAGIC control system . . . . .	121
6.4	Camera and Calibration software control system . . . . .	124
6.4.1	Subsystem drivers: Control-subsystem interaction . . . . .	124
6.4.2	State-machine decision manager . . . . .	126
6.4.3	Sentinel routine as security manager . . . . .	128
6.5	Control operations in observation mode . . . . .	129
 <b>III The detection of <math>\gamma</math>-rays from the Galactic Center with the MAGIC telescope</b>		<b>133</b>
<b>7</b>	<b>MAGIC data analysis techniques</b>	<b>134</b>
7.1	Main background sources . . . . .	134
7.2	Monte Carlo simulation of MAGIC response to EAS . . . . .	135
7.3	Selection of the data sample . . . . .	136
7.3.1	Types of data runs . . . . .	137
7.3.2	Run selection . . . . .	137
7.4	Signal extraction . . . . .	138
7.4.1	Signal extraction method . . . . .	138
7.4.2	Pedestal evaluation . . . . .	140
7.4.3	Calibration of the data . . . . .	140
7.5	Image cleaning . . . . .	141
7.6	EAS shower image characterization: the Hillas parameters . . . . .	142
7.6.1	Hillas parameters: implications for $\gamma$ -hadron separation. . . . .	144
7.7	Data quality checks and filter cuts . . . . .	147
7.8	$\gamma$ /hadron separation . . . . .	148
7.9	Energy estimation of primary $\gamma$ -candidate showers . . . . .	150
7.10	Source position reconstruction: The DISP method . . . . .	150
7.11	Cuts optimization . . . . .	154
7.12	Evaluation of the detected signal . . . . .	155
7.13	Effective area and flux evaluation . . . . .	157
<b>8</b>	<b>Analysis of the GC data taken with MAGIC</b>	<b>161</b>
8.1	The center of the Milky Way . . . . .	161
8.1.1	The GC in the X-ray band . . . . .	162
8.1.2	The GC in the HE-band . . . . .	163
8.1.3	The GC in the VHE-band . . . . .	164
8.2	Motivations for GC observations with MAGIC . . . . .	164
8.3	GC observational constrains with MAGIC . . . . .	165
8.4	The Data Samples . . . . .	166
8.5	Dedicated MC simulations at large ZA . . . . .	168
8.6	Preprocessing of the data: Online Analysis . . . . .	168
8.7	Calibration of the GC data . . . . .	169
8.8	Image cleaning and Hillas parameters calculation . . . . .	171

8.9	GC Data Quality . . . . .	171
8.9.1	ON and OFF event rate after image cleaning . . . . .	172
8.9.2	Subtraction of spark events . . . . .	172
8.9.3	Curing camera inhomogeneities: modifying the signal extractor . . . . .	174
8.9.4	Mispointing corrections with the Starguider . . . . .	175
8.10	Random Forest for $\gamma$ -hadron separation . . . . .	180
8.11	Random Forest for energy reconstruction . . . . .	181
8.12	Cuts applied to the data . . . . .	184
8.13	ALPHA analysis: differential energy spectra determination . . . . .	186
8.14	Flux stability: light-curve . . . . .	190
8.15	DISP Analysis: location and possible extension of the GC emission . . . . .	190
<b>IV</b>	<b>The nature of the observed Galactic Center emission</b>	<b>195</b>
<b>9</b>	<b>Discussion</b>	<b>196</b>
9.1	Galactic Center VHE emission: observational results . . . . .	196
9.2	Interpretations of the results in a DM paradigm . . . . .	199
9.2.1	Other proposed (and most probable) production mechanisms for the VHE emission . . . . .	202
9.3	Outlook for dark matter searches . . . . .	203
<b>10</b>	<b>Concluding Remarks</b>	<b>205</b>
<b>V</b>	<b>Appendix</b>	<b>207</b>
<b>A</b>	<b>Analysis of the data: Technical details</b>	<b>208</b>
<b>B</b>	<b>Analysis of the data: Differential Energy Spectrum <math>\alpha</math>-plots</b>	<b>211</b>
<b>C</b>	<b>The Camera and Calibration Control: Technical details</b>	<b>213</b>
<b>D</b>	<b>The analysis techniques applied to the Crab Nebula</b>	<b>217</b>
D.1	The Crab Nebula . . . . .	217
D.2	Data Analysis . . . . .	217
<b>E</b>	<b>The Hillas formalism</b>	<b>221</b>
	References . . . . .	223

# List of Figures

2.1	Rotation curve decomposition for NGC 6503. The dots are the observed values and the upper solid line is the fit to these for disc mass and rotation implied by stellar velocity dispersions (Figure taken from [16]). . . . .	9
2.2	Chandra X-ray Image and DSS Optical Image of the galaxy cluster Abell 2029. Credit: X-ray: NASA/CXC/UCI/A.Lewis et al. Optical: Pal.Obs. . . . .	10
2.3	Abell galaxy cluster 2218 is the most spectacular example of cluster lensing. Image taken by the Hubble Space Telescope with the Wide Field/Planetary Camera-2. Credit: Andrew Fruchter (STScI) et al., WFPC2, HST, NASA. . . . .	10
2.4	Final 2dFGRS power spectrum $\mathcal{P}(k, \tau)$ in the cases of a SCM basic-five (solid line) and basic-six (dashed line) parameter models (figure extracted from [41]). . . . .	15
2.5	A comparison of all sky image of temperature fluctuations in the early Universe with COBE (upper image) and the WMAP (lower image). Figures taken from [43]. . . . .	16
2.6	The WMAP angular power spectrum (top) and temperature-polarization (TE) cross-power spectrum, consistent with the ACBAR and CBI measurements. Best fit running index $\Lambda$ CDM model is shown. The grey band represents the cosmic variance expected for that model. (figure extracted from [31]). . . . .	17
2.7	Strong evidence for the existence of a cosmological vacuum energy density. Plotted are the 68% (dark) and 95% (light) confidence regions for supernovae, cluster measurements, and CMB data. . . . .	20
2.8	N-Body simulations of structure formation for CDM (top), WDM (middle) and HDM (bottom) dominated Universes. Figure taken from Been Moore's group website [67].	23
2.9	Rotation curve (circular rotation velocity as a function of radius) for the low surface brightness galaxy NGC 6822. The points show data obtained from the 21cm emission of atomic hydrogen, while the line gives the best-fit model assuming that the galaxy's mass is dominated by a centrally-cusped dark matter halo. (Figure from [71]). . . . .	24
2.10	High resolution N-body simulation of a galaxy. At the final time, at redshift zero, subhalo identification algorithms are able to identify almost 5000 gravitationally bound subhalos in this object. From Volker Springer Website: <a href="http://www.mpa-garching.mpg.de/~volker/">http://www.mpa-garching.mpg.de/~volker/</a> . . . . .	25
3.1	Unification of the sparticle mass at the GUT scale. Universal scalar mass $m_0$ and gaugino mass $m_{1/2}$ are part of the GUT inputs of mSUGRA. . . . .	36
3.2	Dominant neutralino annihilation diagrams. Relevant parts of the amplitudes are shown explicitly. V and Z are chargino and neutralino mixing matrices. . . . .	39
3.3	Experimental residual rate for <i>single-hit events</i> in different keV energy intervals as a function of the time over 7 DAMA annual cycles (total exposure 107731 kg x day); The superimposed curves represent the cosine function behaviors expected for a WIMP signal with a period equal to 1 year and phase exactly at 2nd June. . . . .	41

3.4	90 % C.L. spin independent WIMP-nucleon cross section limits obtained by different WIMP Direct Detection experiments. Closed contour shows the allowed region at 3 C.L. from the DAMA 1-4 annual modulation data. . . . .	42
3.5	The gamma-ray spectrum (per annihilation) generated through dark matter annihilations for a variety of channels. A 500 GeV dark matter mass has been used. Figure taken from [140] . . . . .	48
3.6	Integral $\gamma$ -ray yield $N_\gamma(E>E_0)$ per $\chi$ -annihilation for several neutralinos produced in the mSUGRA model. In particular, they corresponds to different SUSY benchmark points defined in [141]. The solid line is the result obtained with DarkSUSY, while the dashed line corresponds to the parameterization given in Equation 3.19. . . . .	49
3.7	Allowed $\tilde{\chi}_1^0$ masses, cross sections, and $f_{SUSY}$ parameter for the mSUGRA scan. See text for details. . . . .	50
3.8	Allowed $\tilde{\chi}_1^0$ masses, cross sections, and $f_{SUSY}$ parameter for the MSSM scan. See text for details. . . . .	50
4.1	<i>Left:</i> the top curve is the density of baryons. The dashed and full curves 'DM' are for the compressed Moore et al. and NFW models. The long-dashed curve corresponds to the uncompressed NFW profile. <i>Right:</i> The solid and dashed curves are the total mass in compressed NFW and Moore et al. models. DM mass in the NFW model is the thick curve. Symbols displays observational constraints as taken from Klypin et al [152]. . . . .	57
4.2	The averaged l.o.s integral $\langle J(\Psi) \rangle_{\Delta\Omega}$ for all DM profiles considered for the GC modeling. $\Psi$ is the pointing angle from the GC. . . . .	59
4.3	Different DM density profiles considered for Draco, as a function of estimated distance to the dynamical center (in <i>arcmin</i> , for a Draco distance of 82 kpc). . . . .	61
4.4	The averaged l.o.s integral $\langle J(\Psi) \rangle_{\Delta\Omega}$ for all DM profiles considered for the Draco modeling. $\Psi$ is the pointing angle from the dynamical center of the system. . . . .	62
4.5	The averaged l.o.s integral $\langle J(\Psi) \rangle_{\Delta\Omega}$ for all DM profiles considered for the M31 galaxy. $\Psi$ is the pointing angle from the dynamical center of the galaxy. . . . .	63
4.6	Variations of the $\langle J(\Psi) \rangle_{\Delta\Omega}$ as we vary the heliocentric distance: as farther we are located from a galaxy, we are less affected by the central spiky structure, as the sum more contributions from the halo. . . . .	63
4.7	Exclusion limits ( $5\sigma$ ) in the SUSY parameter space that can be derived with MAGIC for 30h observation time for each considered source. The curves are obtained for the different DM models considered. The Galactic Center is expected to give the largest flux (lowest exclusion limits) amongst all the sources. . . . .	65
5.1	The EGRET point-like sources $\gamma$ -ray sky. About 170 significant signals are still unidentified sources. . . . .	71
5.2	Simulated predictions of the one-year all-sky survey of the LAT experiment ( $E>1$ GeV). . . . .	72
5.3	Significance map of the H.E.S.S. 2004 Galactic plane scan. 14 sources with $\sigma >4$ have been detected [184]. . . . .	74
5.4	The Very High Energy $\gamma$ -ray sky in 2005. Not shown are 8 more sources discovered by HESS in a survey of the galactic plane. Red symbols indicate the most recent detections, brought during 2004 and 2005 by the last generation of IACTs: HESS and MAGIC. Figure from [186]. . . . .	75
5.5	Sketch of the structure and the interactions present in an EAS, induced by a cosmic $\gamma$ -ray (left) and by a charged cosmic nucleus (right). . . . .	76

5.6	Simulation of an electromagnetic (left panels) and hadronic (right panels) Extended Air Showers. The top panels show the development of the shower in the atmosphere and the bottom ones the angular distribution of the Čerenkov photons at ground levels. Evident morphological differences can be seen which are crucial for imaging-based background subtraction methods. . . . .	78
5.7	Polarization of the medium induced by a charged particle with low velocity (a) and with high velocity (b). Huygens construction of Čerenkov waves that only finds coherence for the Čerenkov angle $\theta_c$ with respect to the charged particle trajectory (c). . . . .	79
5.8	Scheme of the Čerenkov light ring produced by an ultra-relativistic charged particle at the observation level. The first two beams on panel (a) hit the ground at roughly the same radial distance even if they are produced at different heights. Panel (b) shows the simulation of the Čerenkov light pool produced by $\gamma$ -ray and proton showers. The $\gamma$ -induced Čerenkov light profile is practically constant until a radius of a hundred meters, where the hump occurs, and then decay rapidly for higher radius. Taken from [193]. . . . .	81
5.9	Differential Čerenkov photon spectrum in arbitrary units in the ultraviolet and visible wavelength ranges, emitted at 10 km above sea level (dotted line) and detected at 2 km (solid line) after suffering absorption in the Ozone layer and Rayleigh and Mie scattering. Graphic taken from [194]. . . . .	82
5.10	Sketch of the principle of the Čerenkov technique, through the formation of the image of an EAS in an IACT pixelized camera. The numbers in the Figure correspond to a typical 1 TeV $\gamma$ -ray induced shower. . . . .	84
5.11	Čerenkov photon density at 2km height above sea level for different type of incident primary particles and as a function of their energy. Figure taken from [196]. . . . .	85
5.12	Photograph of the MAGIC telescope with main elements labeled. . . . .	87
5.13	MAGIC telescope pointing upwards. In this position, the carbon fiber frame can be photographed easily. Mirrors were partially installed. . . . .	88
5.14	Left: mirror panels ready to be shipped from MPI to La Palma. Right: a single mirror element. . . . .	89
5.15	Mirror panel lasers switched on during re-alignment procedure. Not all mirror panels were installed at the time of the photograph. . . . .	90
5.16	Schematic of the MAGIC camera. Inner region (colored orange) is equipped with 397 0.1° Ø PMTs; outer region (colored red) is equipped with 180 0.2° Ø PMTs. . . . .	92
5.17	The MAGIC camera ready to be shipped from IFAE to La Palma with the light collectors matrix already installed. . . . .	93
5.18	Photograph of the MAGIC camera installed in the Telescope frame. . . . .	94
5.19	Left: the two pixel sizes in the MAGIC Telescope's camera (without coating). Right: QE of the ET9116A PMT before and after coating with a scattering layer and a wavelength shifter. . . . .	95
5.20	Scheme of the HV distribution system in the PMT. The six dynodes are labeled as D1, D2, etc... $HV_{C-1}$ is the cathode to first dynode voltage, $HV_{1-2}$ the first to second cathode, etc, and $HV_{6-A}$ is the sixth dynode to anode voltage. . . . .	97
5.21	Rear part of the PMT camera. Shown are the coaxial cables that connect the pixel base and the Transmitter Boards (black cables in the central part), the VCSELs (inside the metal boxes the blue connectors are attached to) and the optical fibers (green cables). . . . .	98

5.22	Photograph of two transmitter boards installed in the MAGIC telescope camera (left) and a receiver board used to convert the light pulses to electrical ones at the control house (right). . . . .	98
5.23	Schematic of the data stream in the MAGIC telescope. . . . .	100
5.24	The trigger region in the MAGIC camera. . . . .	101
5.25	The DAQ system of the MAGIC camera. . . . .	102
6.1	Top: an image of the complete electronic base is shown. Bottom: a scheme of the 8-pin connector at the bottom of the base, with a description of the functions of the pins (see text for more details). . . . .	108
6.2	Layout of the camera sectors. The two halves of the camera are powered by independent low and high voltage power supplies, as well as two separate slow control communication lines. . . . .	109
6.3	The back side of an outer mother board. A short text identifies the functions of the connectors. The PMT bases are plugged into the front part. . . . .	110
6.4	High Voltage power supplies of the MAGIC camera. Left: the two High Voltage power supplies embedded in a rack. Right: The Active Load power supplies (350V) and independent power supplies for the 6th PMT dynodes (175V) and their V/I output lines which goes to the monitor ADC board. . . . .	110
6.5	Upper view of one of the 48 HV Masters inside the camera, with its corresponding 12 HV regulators. . . . .	111
6.6	Pixel HV stability (for 65 pixels, averaged) when the voltage is directly provided by the HV power supplies and when voltage is controlled by the HV regulators, in which more stable values are obtained. . . . .	112
6.7	Multiplexer card for the monitoring of the DC or the HV. The main elements are pointed out. . . . .	113
6.8	Special test to evaluate the optimized delay time for digitalization purposes. . . . .	115
6.9	Maximum rate for the anode DC currents monitor (up to 6 Hz). When another CANbus system is read through the same bus, the rate drops to lower values. The access to the HV power supply is quite slow (because RS232 to CANbus converter) and nearly blocks the bus when is accessed. . . . .	115
6.10	Evaluation of calibration factors (ADC counts to Voltage/Current) for HV/DC multiplexed monitor cards. . . . .	116
6.11	Calibration pulser box installed in the middle of the telescope mirror dish. . . . .	117
6.12	Scheme of the calibration LEDs slots available in the pulser box. . . . .	117
6.13	Left: One of the three blinded pixels installed in the camera. Right: Pin-diode box installed in front of the pulser box. . . . .	119
6.14	Schematic of main calibration system elements installed in the telescope: pulser box, LV box, PIN-diode and Blinded Pixels. . . . .	119
6.15	Front panel of the calibration trigger board with the test lines an indicator LEDs. . . . .	120
6.16	Schematic of the calibration system (mainly trigger) elements installed in the control house. . . . .	121
6.17	First MAGIC pulsed light observations of pulses coming from a first version of the calibration pulser box. . . . .	121
6.18	Outline of the MAGIC telescope control and DAQ system. . . . .	123
6.19	GUI of the Camera and Calibration Control (La Guagua). . . . .	125
6.20	Camera and Calibration slow control. . . . .	126
6.21	Schematic view of La Guagua software architecture. . . . .	128
6.22	Subsystem states and Guagua camera and calibration global states. . . . .	129

6.23	2 calibration sequences defined in the previous script example. . . . .	130
6.24	Instrumented lids. . . . .	132
7.1	FADC sampling of a small and a large signal from one pixel of the MAGIC telescope. Left: high gain signal. If signal reaches the maximum of 250 FADC digital counts (bottom), the same signal is recorded after a certain delay and with a reduced amplification. Note that the high gain signal is amplified by a factor 10 with respect to the low-gain signal. If no saturation occurs, the low gain branch is not activated (top). . . . .	139
7.2	Example of image cleaning procedure: an event recorded by the MAGIC telescope after calibration (left) is cleaned with the absolute cleaning method (10,5) (right). . . . .	142
7.3	Definition of the Hillas parameters. $(x, y)$ are the coordinates in the original camera system and $(x_0, y_0)$ are the coordinates of a reference point, like the source position or the camera center position. . . . .	144
7.4	Distribution of ALPHA, WIDTH, LENGTH, DIST, CONC and NUMISLANDS parameters for simulated $\gamma$ -induced showers (blue filled histograms) and proton-induced showers (red filled histograms), after trigger and image cleaning procedure. All distributions are normalized to unit area for a better comparison (a cut in SIZE > 100 <i>phes</i> is applied to both samples). . . . .	145
7.5	Same caption as Figure 7.4, but a cut in SIZE < 100 <i>phes</i> is applied to both MC samples. . . . .	146
7.6	Percentage of events with $ \alpha  < 45^\circ$ for both $\gamma$ and proton MC described in the text. For $\gamma$ s, the ALPHA peakness starts to lose its power at about 100 <i>phes</i> , which corresponds to a $\gamma$ energy of about 90 GeV. Note that <i>hadrons</i> are quite flat distributed in ALPHA, as expected for isotropic showers in the field of view. . . . .	147
7.7	(left) Results of 2-dimensional Gaussian fits to the distribution of reconstructed arrival directions, both for MC and Crab Nebula, for the different SIZE bins considered. The PSF obtained for SIZE > 180 phe is displayed in lower-right text. (right) Smoothed sky-map for Crab Observations using the DISP analysis method. . . . .	153
7.8	Crab Nebula $\alpha$ -plot and $\theta^2$ -plot for SIZE>180 phe. Two cuts applied: the one which maximize significance and the one which retain 99% of the excess signal. Results for ON-OFF <sub>fit</sub> are displayed in brackets. . . . .	153
8.1	The GC region seen by the VLA at 90 cm. . . . .	162
8.2	The 20-40 keV INTEGRAL/IBIS image of the GC region showing the central source IGRJ17456-2901, labeled as Sgr A*. . . . .	164
8.3	The VHE gamma flux from the Galactic Center as observed by Whipple, Cangaroo, HESS and by the EGRET experiment (figure from [239]). . . . .	165
8.4	Favored observation time windows for the GC observation schedule, as a function of the ZA, and for periods 30 and 31. . . . .	166
8.5	Star field around the GC region. Stars up to a magnitude of 14 are plotted. The 2 big circles correspond to distances of $1^\circ$ and $1.75^\circ$ from the pointing directions (GC and GC-Off), respectively. The grid spacing in the declination is 20 arc-minutes. The Galactic Plane is given by the line. . . . .	167
8.6	Results from the calibration <i>callisto</i> program. From left to right: average pedestal RMS, mean interpolated signal in <i>phes</i> , mean signal pulse arrival time, and mean calibration signal pulse arrival time. . . . .	170

8.7	Hillas parameters distributions for ON (blue points) and OFF (black dashed) data samples, obtained well after image cleaning. Nor $\gamma/h$ separation cut, or any quality cut, is applied. . . . .	171
8.8	Event rates after image cleaning for both GC ON and OFF samples (see text for details). . . . .	173
8.9	Center of Gravity (CoG) for the shower images plotted in the camera reference system. These special runs taken with the camera closed shows the camera pixels that most likely generate the light sparks. . . . .	174
8.10	Events in a SIZE vs CONC plot. (left) These are events from special camera closed runs, i.e, only the spark events trigger the DAQ; (center) $\gamma$ s from the MC sample; (right) the whole GC ON data sample. The 'spark cut' is displayed with a red line. . . . .	174
8.11	CoG of image showers after image cleaning. (left) GC data from the <i>Online Analysis</i> , (middle) GC data processed with modified extractor parameters, (right) $\gamma$ -MC. . . . .	175
8.12	$\phi$ distribution of CoG of shower images for GC data from the <i>Online Analysis</i> (red), GC data processed with modified extractor parameters (green), and $\gamma$ -MC (black). . . . .	176
8.13	Plotted are the tracking $ZA$ and $Az$ values, and deviations in $ZA$ and $Az$ provided by the Starguider system, for night of 11/06/2005 and GC ON data-taking period. The mispointing when source passes trough culmination is clearly seen in upper-left panel. The calibration $ZA$ and $Az$ offsets for the Starguider data are shown with the red dashed lines. . . . .	177
8.14	GC positions in the camera reference system evaluated with the DC currents (left) and the Starguider (right) methods. These positions are evaluated in a run-to-run basis. The different colors correspond to different GC ON nights. . . . .	178
8.15	DISP-sky-maps in a camera reference system for GC data before (left), after (right), and during the culmination culmination jump (middle). The data is not corrected by the mispointing effects, and GC is detected off-axis while the culmination problem is present. . . . .	179
8.16	Global DISP-skymaps in a camera reference system for GC data with mispointing not corrected (left) and corrected(right). . . . .	179
8.17	Mean decrease in Gini index for the training variables used in the RFStd and RFDisp RF training methods. . . . .	181
8.18	For different SIZE bins [phe], the HADRONNESS distributions (top), $Q$ -factors (middle), and $\gamma$ -acceptance (bottom) for $\gamma$ s (solid lines) and hadrons (dashed lines). The RFStd (RFDisp) training method applied to the test sample is displayed in black (red). . . . .	182
8.19	Correlation of the image shower SIZE parameter to the energy of the primary $\gamma$ -ray, from the large ZA MC- $\gamma$ test sample. . . . .	183
8.20	Mean $\Delta E$ and RMS of $\Delta E$ for different energy bins: (left) against true energy, and (right) against reconstructed energy. From the large ZA MC- $\gamma$ test sample, with HADRONNESS<0.125 (RFStd method used). . . . .	184
8.21	Comparison of the reconstructed energy $E_{rec}$ with the simulated shower energy $E_{mc}$ for the large ZA MC- $\gamma$ test sample, with HADRONNESS<0.125 (RFStd method used). (left) Applying the RF Energy estimation algorithm and (b) applying the SIZE dependence shown in Figure 8.19. . . . .	184
8.22	Cuts used on the analysis, obtained from the MC test sample. The behavior of OFF data (background) is also shown (see text for details). . . . .	186
8.23	Effective ON and OFF times. . . . .	187
8.24	ALPHA-plot for SIZE>275 phe (corresponding to an energy threshold of 1 TeV, approximately). See text for details. . . . .	187

8.25	Reconstructed VHE $\gamma$ -ray spectrum of the GC (statistical errors only). The full line shows the result of a power-law fit to the data points. Dashed line shows the energy spectrum of the Crab Nebula as measured with MAGIC. The grey shaded-region shows the spread from several realizations changing the analysis cuts (see text for details). . . . .	189
8.26	Light-curve: Reconstructed integral VHE gamma-ray flux above 1 TeV as a function of time. Within errors ( $1\sigma$ ) the data are consistent with a steady emission. . . . .	191
8.27	Smoothed skymap of $\gamma$ -ray candidates (background subtracted) in the direction of the GC for SIZE>300 phe (corresponding to an energy threshold of about 1 TeV), and Az<180 degrees. Overlaid are shown the best fit values for source location: the maximum excess (red), and the location from correlated and uncorrelated Gaussian fits (green and blue, respectively). . . . .	192
8.28	Smoothed skymaps of $\gamma$ -ray candidates (background subtracted) in the direction of the GC for SIZE>300 phe (corresponding to an energy threshold of about 1 TeV), and Az<180 degrees. (left) RFDisp RF method applied. (right) RFStd RF method applied. Overlaid are shown the best fit values for source location: the maximum excess (red), and the location from correlated and uncorrelated Gaussian fits (green and blue, respectively). . . . .	193
9.1	(left) Excess map as published by Whipple: marginal detection of the GC VHE emission. (right) Latest HESS excess maps on the GC direction: (a) $\gamma$ -ray count map; (b) the same map after subtraction of the two dominant point sources, showing an extended assymmetric band of $\gamma$ -ray emission. The 95% confidence region for the positions of the two unidentified EGRET sources in the region are shown as dashed green ellipses. . . . .	198
9.2	Observed VHE $\gamma$ -ray differential energy spectra derived from different GC observations by IACTs: HESS results as presented in the ICRC 2005 conference, CANGAROO results published in [242], and MAGIC results obtained in this Thesis. . . . .	199
9.3	The minimal $\chi^2$ resulting from fits to the 2003+2004 HESS data set (right panel) on the $\gamma$ -rays flux from the Galactic Center, as a function of the annihilating Dark Matter particle mass, for different final state channels (Figure extracted from [247], check therein for details). The two horizontal lines in each panel indicate the 90% and 95% C.L. exclusion limits corresponding to the set of data under consideration. . . . .	200
9.4	Exclusion limits from HESS and MAGIC measurements of the GC VHE emission for the two cuspy profiles discussed in the Thesis ( $3\sigma$ HESS and $1\sigma$ MAGIC). . . . .	201
B.1	(left) Excess and background events in the signal region for the different energy bins considered to evaluate the GC differential energy spectrum. (right) Significance per energy bin. . . . .	211
B.2	ALPHA-plots for the different energy bins considered to evaluate the GC differential energy spectrum. . . . .	212
D.1	ALPHA distribution for 64 minutes of Crab Nebula data. . . . .	218
D.2	Integral flux of the Crab Nebula for all days considered in the analysis. A fit assuming a constant flux gave a $\chi^2/\text{ndof} = 1.06$ . . . . .	219
D.3	Observed differential crab spectra for the 2004 and 2005 datasets. A power-law fit to the combined data is shown (from 300 GeV to 4 TeV), as well as the fit to the HEGRA data and the parameterization of WHIPPLE data. . . . .	219

# List of Tables

2.1	Parameters of the Standard Cosmological Model (SCM).	14
2.2	Recommended values of SCM parameters, according to [60].	21
3.1	Fermions have bosonic superpartners, and bosons have fermionic superpartners. The simplest (or minimal MSSM) theory poses a single pair of Higgsinos.	35
3.2	Mass limits from particle accelerator searches.	46
4.1	Models and constraints for the Milky Way Galaxy	57
4.2	Properties of the Draco dSph [80].	60
4.3	Parameters of the DM halo models considered for the Draco dwarf.	60
4.4	Parameters of the DM halo models considered for the M31 galaxy.	62
4.5	Relevant parameters to evaluate the expected fluxes for all objects and DM halo models considered in this study (ext. = extended emission; VHE = possible $\gamma$ -ray emitters in the FOV; no VHE = probably, no $\gamma$ -ray emitters in the FOV).	64
6.1	Main subsystem reported values through <code>subsys_report</code> pipe.	127
6.2	Calibration shell script example: 2 different calibration sequences are defined in the script, which is further processed by 'Guagua'.	130
7.1	Results for the DISP-analysis to Crab Nebula compared to ALPHA-analysis (numbers in brackets)	154
8.1	Data set per observation period of the GC. The column 'time' states the effective observation time, the column 'events' states the events after image cleaning. Colored is the data analyzed in this Thesis.	167
8.2	Most important parameters of the simulations used in this analysis. (*) For flux calculations, the energy spectra is weighted to properly derive the results, i.e. the MC is generated following $E^{-\delta}$ , and $\delta$ is changed recursively. (**) NSB level for $0.1 \times 0.1 \text{ deg}^2$ , i.e. inner pixel size.	168
8.3	Distance of the GC signal to the camera center, resulting from a bi-dimensional Gaussian fit to the signal excess in the DISP-skymaps, before and after source correction.	180
8.4	Set of variables used in the RF training procedures for the two separate analysis chains: ALPHA-analysis and DISP-analysis.	180
8.5	Parameters involved in the differential energy spectra calculation: $E_{lw}$ , mean Energy for the bin (according to [229]); $N_{exc}$ , excess events in signal region; $\langle N_{off} \rangle$ , normalized background events in signal region; $S$ , significance; $\Gamma$ , normalization factor; $\epsilon_\gamma$ , $\gamma$ -efficiency; $A_{eff}^{after\ cuts}$ , effective area after cuts; $\kappa$ , spill-over correction factors; $dF/dE$ , differential energy spectrum value. Only statistical errors shown.	188
8.6	Light-curve analysis relevant values.	192

---

A.1	Runs which are excluded from the analysis. The individual runs correspond to corrupted runs. Two nights excluded from the analysis are due to bad atmospheric conditions. . . . .	208
A.2	Estimated offsets for $\Delta ZA$ and $\Delta Az$ , corresponding to the different GC observation nights. . . . .	208
A.3	Excluded pixels for the 32 sequences of ON and OFF GC data analyzed. In <b>red</b> are marked the most frequent excluded pixels. The categories are <b>dead:</b> already known dead pixels; <b>~dead:</b> Pedestal RMS is 4.5 smaller than the average pedestal RMS; <b>Fluctuating gains:</b> fluctuating charge response; <b>Fluctuating arr. times:</b> RMS of arrival times is bigger than 1.7 FADC counts. <b>Very low signal:</b> mean reconstructed charge is smaller than half the mean charge average of the camera; <b>No signal:</b> mean reconstructed signal of the calibration light pulses is smaller than 3.5 pedestal RMS. . . . .	209
A.4	List of runs corresponding to GC ON data used on this analysis. <b>Pedestal runs</b> and <b>Calibration runs</b> used, as well as the observation time, and zenith angle window, are also indicated. . . . .	209
A.5	List of runs corresponding to GC OFF data used on this analysis. <b>Pedestal runs</b> and <b>Calibration runs</b> used, as well as the observation time, and zenith angle window, are also indicated. . . . .	210
C.1	Description of commands sent by the CeCo to “Guagua”. . . . .	213
C.2	Description of commands sent by the “Guagua” to each subsystem (Part I). . . . .	214
C.3	Description of commands sent by the “Guagua” to each subsystem (Part II). . . . .	215
C.4	Main ‘Guagua’ directories and files. . . . .	215

# Chapter 1

## Introduction

This Thesis deals with one of the most fundamental questions in modern science: *unveil the nature of the dark matter*.

Modern cosmology has progressed very rapidly during the last decades and, with the help of new instruments and telescopes, the universe history has been traced up to its very early stages, even before galaxies were formed. These exciting and challenging measurements indicate that at the present date we are quite sure that everything we can observe in the Universe makes up only a small fraction of its content and the rest is in the form of an invisible 'substance' called dark energy and 'unknown' dark matter.

There is no doubt that cosmology is going to be cataloged as a new scientific revolution for the 21<sup>st</sup> century. Related to the topic which is discussed in this Thesis, at present, the nature of the dominant dark matter component is still unknown. None of the known particles satisfy all requirements to account for it, and a number of viable Weakly Interacting Massive Particle (WIMP) candidates have been proposed in several theoretical frameworks, mainly motivated by extensions of the Standard Model of particle physics, (e.g. supersymmetry, SUSY). Among this variety of particles, the most plausible dark matter candidate is the neutralino: the neutral and lightest (hence stable) weakly interacting SUSY particle.

Any WIMP candidate (SUSY or not) may be detected directly through its elastic scattering while impinging on nuclei targets on Earth. Currently, there are several experiments already working exploiting this signature (direct detection technique), but their results do not claim any strong WIMP detection up to now. Complementary, neutralinos might be indirectly detected by their self-annihilation products in high-density dark matter environments (indirect detection technique). In particular, channels that produce  $\gamma$ -rays are interesting, as  $\gamma$ -rays are not deflected by galactic or inter-galactic magnetic fields (charged products are interpreted as excess signals). The  $\gamma$ -rays would preserve the information of the original annihilation region, and they would act as tracers of the dark matter density distribution in which the emission is produced. This high energetic radiation can be indirectly observed in the Earth with dedicated ground-based  $\gamma$ -ray telescopes or with the use of satellite detectors.

A major development of  $\gamma$ -ray astronomy has been accomplished by the second generation of Atmospheric Imaging Čerenkov Telescopes (IACTs), namely MAGIC and HESS. To date, MAGIC (acronym of Major Atmospheric Imaging Čerenkov telescope) is the biggest world-wide IACT, with 17m diameter reflector. This Thesis makes use of this installation for specific observations carried out for indirect dark matter searches purposes.

## 1.1 Motivations and distribution of the Thesis contents

It is the aim of this Thesis to focus on one of the multiple astrophysical targets of  $\gamma$ -ray astronomy: the hypothetical  $\gamma$ -ray production from neutralino annihilations in high dense dark matter regions. Dark matter is considered one of the most exciting and fundamental unresolved questions in astrophysics, and in general in modern science. In this Thesis, many detailed dark matter distribution models for some selected astrophysical objects are studied, as well as the repercussions for neutralino self-annihilation  $\gamma$ -ray detectability with the MAGIC telescope. In light of these phenomenological studies, in which Astrophysics and Particle Physics inputs are needed, we conclude that the center of the Milky Way should be the most brilliant object in  $\gamma$ -rays from neutralino annihilations.

In the Thesis, an analysis of 17 hours of data taken with MAGIC in the Galactic Center direction is presented. The positive detection of  $\gamma$ -ray radiation is reported, as well as its interpretation in a dark matter inspired framework. Other  $\gamma$ -ray production scenarios in the GC region are as well indicated.

The work herein presented is divided in four parts:

- A **theoretical and phenomenological approach** to identify which are the favorite places for indirect dark matter searches with the MAGIC telescope. Chapter 2 gives an overview of the current cosmological scenario, the need of dark matter, and which are the proposed candidate particles. Chapter 3 deals with the modeling of the neutralino properties in given supersymmetric scenarios, consistent with the cosmological context and current accelerator bounds, and their implications for  $\gamma$ -ray emissivity from their self-annihilations. Chapter 4 presents a detailed modeling of each of the considered candidate regions to search for this very high energy emission, proposing as the best candidate the center of the Milky Way. Here we discuss an important effect which was previously ignored: the adiabatic compression of the dark matter from baryonic matter infall during Milky Way galaxy formation.
- The second part of the Thesis introduces **the MAGIC telescope and technical tasks** in which the Thesis Author has actively participated during the telescope construction and commissioning phase. This starts in Chapter 5, summarizing the fundamentals of the Čerenkov technique for  $\gamma$ -ray astronomy, an overview of present  $\gamma$ -ray field status, the main characteristics of the MAGIC Telescope, and its first results. This part ends with a description of the telescope's camera and fundamentals of the remote camera control software and camera performance tests (Chapter 6).
- The third part of the Thesis explains **the Galactic Center analysis**. The techniques applied for the reduction of MAGIC data are given in Chapter 7, focusing in a developed analysis technique to study extended emissions, as the expected emissions from neutralino annihilations are not likely to behave like a point source (e.g. distant Active Galactic Nuclei). Chapter 8 provides the results of the analysis of the first MAGIC observations of the Galactic Center.
- Finally, Chapter 9 gives a **discussion** about the detected emission and how it fits into the exposed dark matter context. Chapter 10 gives some final concluding remarks.

This Thesis represents the Author's effort to understand a little more about high energy astrophysics and dark matter searches in  $\gamma$ -ray energy domain. This effort was threefold. On one hand, **technical**: participating in the tasks and developments to bring a new Imaging Air Čerenkov Telescope (MAGIC) to work. On the other, **theoretical and phenomenological**: in order to

study what  $\gamma$ -ray output is expected from these dark matter regions based on the most detailed possible theoretical models, with inputs from Particle Physics and Astrophysics, in a field close to a fundamental piece of scientific knowledge. And finally, **observational**: in order to begin the long and yet unfinished path to thoroughly solve which is the origin and the nature of dark matter. It is here hoped that some of these lines of research will inspire new developments.

## Part I

# Supersymmetric dark matter and indirect searches with the MAGIC Cherenkov Telescope

## Chapter 2

# The dark matter paradigm

In light of current known and established physics, it seems that a huge fraction of the Universe is constituted by an 'invisible' form of matter. There are clear evidences about its existence. For example, the mass of a galaxy estimated from its dynamics is systematically greater than that inferred from its luminous content ( $M_{dyn}/M_{visible} \geq 10$ ). Other evidences, from local to large distances, posits a conceptual problem into the current cosmological knowledge.

This Chapter is intended to give a brief, but comprehensive, overview of the concept of dark matter, a fundamental piece of the current cosmology paradigm. The evidence for dark matter, as well as the so-called Standard Cosmological Model (SCM), which has gained wide acceptance during the last decade, are explained. The most relevant cosmological measurements, and in particular the current precise determination of the parameters of the SCM, including how much dark matter is present in the Universe, are also given. Limitations and alternatives to this scenario are then reviewed.

In addition, an overview is given of the present observations of inferred dark matter distribution on isolated galaxies and galaxy clusters. How the dark matter is distributed can also be determined by powerful computer-based simulations of structure formation. A comparison between both approaches is given, as well as some apparent contradictory results for the dark matter distribution at the center of the dark matter halos.

What can dark matter be made of? This question is raised at the end of the Chapter, in which some dark matter candidate particles are presented. The *Neutralino*, the lightest stable particle in the supersymmetric extension of the Standard Model of Particle Physics, is described as the most popular candidate. This particle could be detected through its annihilating  $\gamma$ -ray products in high dark matter density regions. The resulting fluxes are considered as detectable by Imaging Air Čerenkov Telescopes (IACTs). Suitable signals are expected for the new generation of IACTs, and in particular for MAGIC (see Lorenz et al 2004 [1], the biggest gamma-ray telescope up to the present date, which is possibly the best instrument to carry out dedicated dark matter observations.

The explanations here are intended to put the reader into context. All *Neutralino* phenomenological studies, dark matter distribution for suitable objects and expected fluxes and/or capabilities to carry out such dedicated observations with MAGIC are given in a separate Chapter, as well as the bulk analysis of the data. Good reviews about dark matter, as well as about dark matter particle candidates, and detection techniques can be found elsewhere (see e.g. [2–4], respectively, and references therein).

## 2.1 Historical highlights

The first known modern study of the possible presence of dark matter elsewhere in the Universe might be attributed to Ernst Öpik, early in 1922 [5]. Some years before, in 1918, F. G. Pease had studied the nearby galaxy M31 and obtained the first rotation curve of a galaxy ever produced [6]. Öpik used this result and concluded that M31 had up to 3 times as much mass for its light compared to the Milky Way. However, rather than concluding that some fraction of mass was in some form of invisible mass, he proposed revising the estimated M31 distance, suggesting it was twice as far away as estimations available at the time.

A similar problem was found some years after by Oort (1932) when determining the dynamical density of matter present in the solar neighborhood. His results claimed that the mass density was exceeding slightly the density of visible stars nearby the solar system, in particular by a factor 2 [7]. The first hypothesis for this low and local dark matter, close to the plane of our Galaxy, pointed to some kind of invisible matter in the form of brown dwarfs, Jupiters or similar compact baryonic objects. At the time, both the dynamical measurement and the star inventory were difficult tasks, and this result has been a topic of significant debate, continually re-examined and, almost always confirmed<sup>1</sup> [9].

The concept of global dark matter, i.e. for distances farther than the *Local Group*, was firstly adopted by Zwicky in 1933 [10], when dealing with the large measured velocities of individual galaxies in the Coma cluster. With such velocities, these galaxies would have dispersed on short time-scales, unless there was a large fraction of invisible material present, increasing the strength of the gravitational potential of the system. Zwicky called it 'missing mass', matter with practically zero luminosity, detected only by its gravitational effects. Zwicky found that the system was roughly a factor 1000 more massive than the mass inferred by the luminous matter<sup>2</sup>. This was more revealing than the factor of 2 found by Oort one year before.

From here, the story of dark matter spans many decades, in which, for some reason, these early studies did not awake the attention of the astronomical community. However, the awareness of the presence of a controversy with the masses of galaxies and of galaxy systems slowly increased. It was not until the 1970s that it became generally accepted that galaxies contain a substantial component of unknown form of dark mass. This was influenced by independent studies of prestigious astronomers, which suggested that all giant galaxies are surrounded by massive halos (coronas), and that dark matter is dynamically dominant in the Universe [12].

The most accepted theoretical foundation of a dark matter dominated Universe was established by Blumenthal et al. (1984) with the non-baryonic cold dark matter (CDM) hypothesis [13]. The need for non-baryonic and cold dark matter was clarified, otherwise the main constituents of the Universe - galaxies, clusters and filamentary superclusters - could not had been able to form.

Consequently, experimenters devoted themselves to find new evidences in favor of (or against) this new paradigm. The most recent years have been devoted to a detailed elaboration of the concept of the CDM dominated Universe. The central issue has been to determine how much dark matter exists in the Universe, how it is distributed in galaxies and clusters, and to attempt to constrain its nature, both from the experimental and theoretical sides. In parallel, the need to include a cosmological constant ( $\Lambda$ ) into the CDM paradigm has been established, as it has been discovered that as much as 95% of the Universe is dark in its nature<sup>3</sup> and we do not know still what it is.

---

<sup>1</sup>Recently, it has been pointed out that there are some errors on these estimations and thus the presence of an unexplained local mass might be doubted. Nevertheless, these new results agree with previous ones within errors (which were underestimated) [8].

<sup>2</sup>The distance to the Coma cluster was over-estimated by a factor ten, but Coma is still at the foundation of the case for dark matter, with the less extreme value of  $M/L \sim 100$  [11].

<sup>3</sup>We do live in a Universe dominated by *dark matter* and the so-called *dark energy*!

As often in a paradigm shift, there is still no single discovery and the dark matter concept is growing slowly. Of course, the story of dark matter is not over yet. Dark matter, as well as dark energy, has become one of the most important, recent and hot topic in astrophysics and cosmology, whose history might be cataloged in a near future as a typical scientific revolution [14].

## 2.2 The dark matter evidence

The recent progress on the experimental side has provide valuable results, from the internal structure of galaxies up to their large-scale clustering properties. Theoretical models and interpretations of the data have improved in parallel, putting more light into the knowledge about what we call 'dark matter'.

Our understanding is still only partial, but it gives an initial prescription for a robust theory, in which new physics might be indisputably necessary. The next sections are devoted to briefly describe the most important evidences for the need of a dark component of matter.

### 2.2.1 Local fact: dark matter in galactic halos

The most convincing and direct evidence for dark matter associated to individual galaxies comes from the rotational curves, i.e, the circular velocity of stars and gas as a function of the distance to their galactic center. Most galaxies are like our Milky Way, spiral galaxies in which the stars and gas move on circular orbits confined to a thin disc-like plane. Normally, the rotation curves can be obtained by combining observations of neutral Hydrogen 21cm-line with optical surface photometry. This gives a direct estimate of the internal galaxy mass [see [15] and references therein for details].

Rotation curves reveal that the contribution of inferred baryonic component is insufficient to account for the observations, thus the need of a dark component of matter, if one accepts the standard gravitational law to be valid. In particular, rotation curves show an unexpected flat behavior beyond the edge of visible stars, indicating that the halo of dark matter extends farther than the visible component. In other words, the dark matter associated with spiral galaxies appears to be independent of its luminosity: *dark matter does not trace light* (see Figure 2.1).

Observations on many galaxies show that the distribution of dark matter needed to explain these rotational curves has a unique structure, with a density profile that can be characterized by a universal law, inferred from balance studies of kinetic and potential energies using the virial theorem. There is ample consensus for the shape of the dark matter distribution at large radii varying with a mass density  $\rho_{dm} \sim r^{-2}$ , but it is still unclear whether galaxies present cuspy or shallow profiles in their innermost regions (i.e,  $\rho_{dm} \sim r^{-\alpha}$ , with  $\alpha=0-1.5$ ). In some cases, numerical simulations on galaxy formation and some observational data are in conflict in such near distances to the center of the galaxy<sup>4</sup>. These differences are of vital importance for the topic which is discussed in this Thesis, thus these effects will be discussed separately.

A common way to determine the quantity of dark matter in a galaxy is trough the mass-to-light ratio, M/L, normally expressed in solar units,  $M_{\odot}/L_{\odot}$ . This ratio depends on the distance to the galaxy center  $r$ , with typical values for spirals galaxies of about  $M/L \sim 10$  at  $r \sim 10$  kpc, and up to 30 at  $r \sim 100$  kpc.

The most dark matter dominated objects are the *Low Surface Brightness* (LSB) galaxies [17]. These galaxies show very low luminosity (i.e. low stars content), while their dynamics indicate a huge presence of dark matter. These are considered to be the best places to make tests of the models. Other objects in which the dark matter is the dominant component are the *Dwarf Spheroidal Galaxies*, frequent satellites of bigger hosts galaxies. These objects have the bigger

---

<sup>4</sup>For very low distances, it is quite difficult to measure the rotation curves (lack of stars, and low velocities), and numerical simulations encounter a limitation, due to their resolution and computational limits.

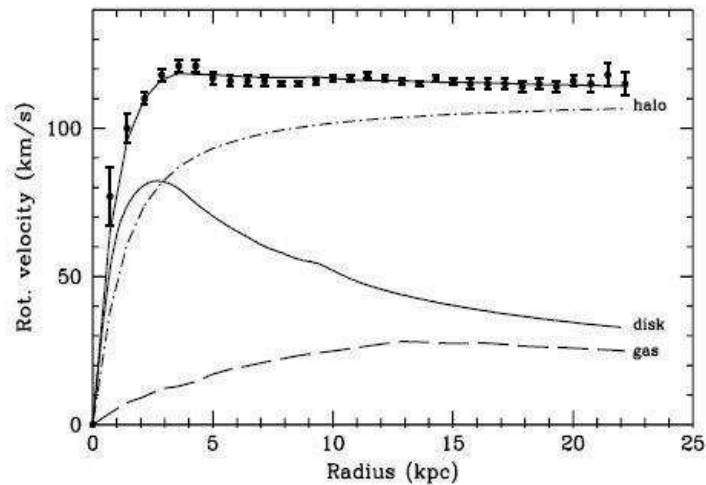


Figure 2.1: Rotation curve decomposition for NGC 6503. The dots are the observed values and the upper solid line is the fit to these for disc mass and rotation implied by stellar velocity dispersions (Figure taken from [16]).

mass-to-light ratios known. For example, the Draco dwarf spheroidal has  $M/L \geq 200$  [18], which makes this Milky Way satellite a good place for dark matter studies<sup>5</sup>.

Although rotation curves of disk galaxies provide strong evidence for the existence of a dark matter component, some galaxies show this evidence via strong gravitational lensing [19]. In addition, X-ray observations reveal the presence of extended atmospheres of hot gas that almost fill the dark halos of isolated galaxies, and whose hydrostatic support provides evidence of dark matter [20].

### 2.2.2 Non-local fact: dark matter in galaxy clusters

The first evidence of dark matter in these kind of systems was already pointed by Zwicky when studying the Coma cluster [10]. Clusters of galaxies are the most massive structures known to exist. These large systems did not have time to collapse since the Big Bang and they have reached a gravitational equilibrium. Most of the mass of the galaxy clusters resides in a relatively smooth dark matter component, stripped from the individual halos of the galaxies.

The mass of the cluster can be determined via several independent methods, all them pointing to a large fraction of dark matter in clusters ( $M/L \sim 100 - 400$  [11]):

- Application of the *virial theorem* ( $2T + U = 0$ , for objects in dynamical equilibrium) to the observed distribution of radial velocities (i.e, the use of galaxies as tracers of the whole gravitational potential).
- *Hydrodynamics of X-ray emitting gas*, which normally is spread over the whole cluster in a smooth way (see Figure 2.2).
- *Weak gravitational lensing*, i.e, the distortion of images of background objects due to the gravitational potential of the cluster, from which the mass of the cluster can be inferred (see Figure 2.3).

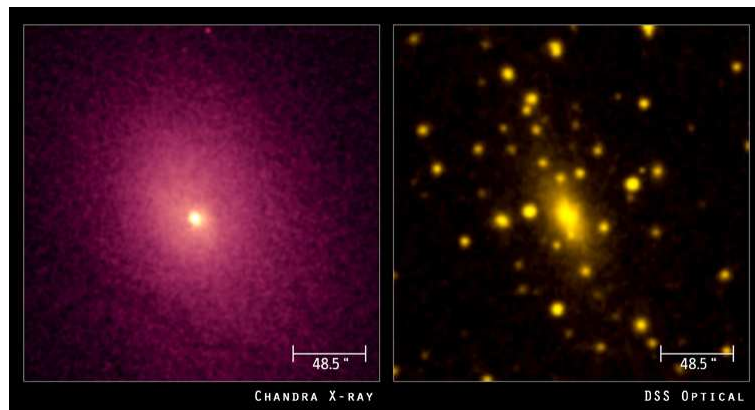


Figure 2.2: Chandra X-ray Image and DSS Optical Image of the galaxy cluster Abell 2029. Credit: X-ray: NASA/CXC/UCI/A.Lewis et al. Optical: Pal.Obs.

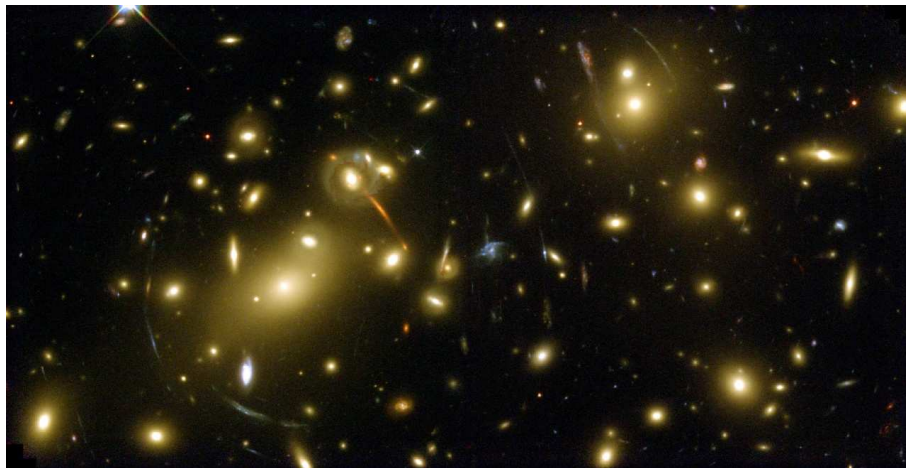


Figure 2.3: Abell galaxy cluster 2218 is the most spectacular example of cluster lensing. Image taken by the Hubble Space Telescope with the Wide Field/Planetary Camera-2. Credit: Andrew Fruchter (STScI) et al., WFPC2, HST, NASA.

Like for an isolated galaxy, in clusters there is a good agreement between the dark matter density profile at large radii and numerical simulations, whether it is unclear the comparison on the cores of the clusters. Gravitational lensing appears to be in conflict with cuspy profiles [21] (i.e.,  $\rho_{dm} \sim r^{-\alpha}$ , with  $\alpha \geq 1$ ), although recent Chandra observations of X-ray emission from Abell 2029 suggest a full compatibility of dark matter distributions with cuspy profiles [22]. This evidences the controversies coming from different results, although gravitational lensing results are under debate (see for example [23]).

### 2.2.3 Cosmological fact

The detection of the Cosmic Microwave Background (CMB) radiation, relic from the early Universe, has firmly established the hot Big Bang model in which the need for a huge dark component of matter in the Universe is supported. In this scenario, the Universe evolves from a dense and

---

<sup>5</sup>This dwarf will be extensively modeled in Chapter 4.

extremely smooth 'hot fireball', into the complex distribution of stars and galaxies that we observe today. The tiny fluctuations which are seen in the CMB reflect real initial matter fluctuations from which we can extract relevant cosmological information, in particular combinations of the mean mass density, cosmological constant, baryonic density and the Hubble constant.

Due to the importance of the CMB measurements, and combinations to other measures, like type Ia supernovae or large scale structure measurements, the results are explained in a separate section, well after the current cosmological model is exposed. It is important to remark that due to the amount of dark matter component in the Universe (5/6 of total matter content), it governs the way in which structures form in the expanding Universe, i.e, it has a huge cosmological impact.

## 2.3 The Standard Cosmological Model

Cosmology is probably the most ancient body of knowledge. Our understanding of the Universe has grown significantly during the last decades. Nowadays, a coherent theoretical framework has been set and is widely accepted by the scientific community: the so-called *standard cosmological model* (SCM). The experiments have provided precise measurements on a wide range of the current model parameters and there are projects to measure some of these observables with a few percent accuracy. We are perhaps living in the golden age of cosmology.

The SCM is based on the successful hot Big Bang framework and the inflationary model paradigm, in which the Universe evolution can be traced since the first fraction of a second up to our present age, around 14 billion years later. The theory is built on four strong pillars:

- **Theoretical framework:** based on general relativity, set by A. Einstein [24] and A. Friedmann [25], in the 1920s.
- **Observational fact 1:** the expansion of the Universe, as a recession of galaxies with a speed proportional to their distance from us, discovered by E. P. Hubble [26], in the 1930s.
- **Observational fact 2:** relative abundance of light elements, mainly that of helium, deuterium and lithium, created from nuclear reactions that took place at around a second to a few minutes after the Big Bang, explained by G. Gamow, in the 1940s [27].
- **Observational fact 3:** the CMB, the afterglow of the Big Bang. Discovered accidentally in 1965 by A. Penzias and R. Wilson [28] as a very isotropic blackbody radiation at a temperature of about 3 degrees Kelvin, emitted when the Universe was cold enough to form neutral atoms, so that the photons decoupled from matter<sup>6</sup>.

Recent CMB experiments have been decisive to set the preferred cosmological model. In particular, the COBE satellite detection of large-scale (degree-scale) CMB anisotropies in 1992 [29], which pointed to the ' $\Lambda$ CDM' variant of the CDM model, i.e, the addition of the cosmological constant  $\Lambda$  term [30], giving better fits to the obtained data. The need for a cosmological constant became accepted as a basic ingredient of the model by late 1990s, supported as well by results from distant type Ia supernovae observations. Soon the concept of  $\Lambda$  was generalized to that of dark energy, as the CMB anisotropies were measured with an unprecedented precision by the WMAP satellite [31].

Nowadays, several parameters from the model have been measured with great accuracy and first constrains to the inflation model have been imposed. The model is based on the original ideas developed during the last 100 years, but crystallized only a decade ago. Although difficult to

---

<sup>6</sup>Approximately 500,000 years after the Big Bang.

assign, it seems that the first articles containing all the ingredients of the SCM were published in 1995 [32] [33].

This section contains a mathematical description of the model, an explanation of the recent estimates of the cosmological parameters, the problems that the model may have, and a brief outlook of what is expected in the near future.

### 2.3.1 Mathematical description of the SCM model

The standard cosmological model is based on the relationship between the geometry of the Universe and its matter/energy content (Einstein equations), the introduced symmetries (metric) and on the *equation of state*, that specifies the physical properties of the matter and energy content.

Dynamics are governed by Einstein's equations, resulting in the field equation<sup>7</sup>,

$$G_{\mu\nu} \equiv R_{\mu\nu} - \frac{1}{2}g_{\mu\nu}R = -8\pi GT_{\mu\nu} + \Lambda g_{\mu\nu} \quad (2.1)$$

where  $R_{\mu\nu}$  is the Ricci tensor ( $R \equiv R^\nu_\nu$ ),  $g_{\mu\nu}$  is the space-time metric tensor,  $G$  the universal gravitational constant,  $T_{\mu\nu}$  the energy-momentum tensor, and  $\Lambda$  the so-called cosmological constant<sup>8</sup>.

The addition of the constant term was initially adopted by Einstein to get an stationary solution for the Universe. This term represents a *vacuum energy* associated with the space-time itself, rather than its matter content. It is a source of gravitational field, even in absence of matter. This term was abandoned when the expansion of the Universe was discovered, but it has been again included in light of the recent cosmological measurements, in which this term contributes significantly to the total energy content of the Universe.

These non-linear equations are too difficult to solve without a characterization of the symmetry of the Universe. It is normally assumed that the Universe is statistically *homogeneous* and *isotropic* (the cosmological principle). These properties are confirmed by experimental results (mainly from CMB measurements), which show remarkable isotropy, while certain homogeneity is confirmed by galaxy surveys [34] [35] [36] (for galaxy distributions at scales in excess of 100 Mpc).

The most general metric which satisfies homogeneity and isotropy is the *Friedman-Robertson-Walker* (FRW) metric, which can be expressed in terms of the invariant geodesic distance  $ds^2 = g_{\mu\nu}dx^\mu dx^\nu$ ,

$$ds^2 = dt^2 - a^2(t) \left[ \frac{dr^2}{1 - kr^2} + r^2 d\Omega^2 \right] \quad (2.2)$$

characterized by two factors, the so-called *scale factor*  $a(t)$ , which determines the physical size of the Universe, and the constant  $k$ , describing the 3-dimensional *spatial curvature*,

$$R = \frac{6k}{a^2(t)} \quad (2.3)$$

where  $k$  takes values of  $k = -1$  (open Universe),  $k = 0$  (flat Universe), and  $k = +1$  (closed Universe).

Light geodesics on these Universes behave differently, and thus could in principle be distinguished observationally. Depending on the dynamics (and thus on the matter/energy content) of the Universe, we will have different outcomes for its evolution. The Universe may expand forever, recollapse in the future or approach an asymptotic state in between.

<sup>7</sup>unless specified,  $\hbar = c = 1$  everywhere. All model parameters depend on time (i.e, the Universe scale parameter  $a$  must be read as  $a(t)$ ). Present parameter values are indicated as  $a_0$ .

<sup>8</sup>By construction, these equations tend to Newton's law in the limit of weak fields.

With respect to the matter and energy of the Universe, the most general matter fluid consistent with the assumption of homogeneity and isotropy is a *perfect fluid*, in which an observer comoving with the fluid would see the Universe around it as isotropic. The energy momentum tensor associated with such fluid can be written as [37]

$$T_{\mu\nu} = p g_{\mu\nu} + (p + \rho)U_\mu U_\nu \quad (2.4)$$

where  $p$  and  $\rho$  are the pressure and energy density of the fluid at a given time of the expansion, and  $U_\nu$  is the comoving four-velocity<sup>9</sup>.

According to the Einstein equations, the equations of motion of such a fluid in an expanding Universe can be derived, assuming the FRW metric and the perfect fluid tensor. The  $\mu=\nu=0$  component of the Einstein equations constitutes the Friedmann equation

$$H^2 \equiv \left(\frac{\dot{a}}{a}\right)^2 = \frac{8\pi G}{3}\rho + \frac{\Lambda}{3} - \frac{k}{a^2} \quad (2.5)$$

where the cosmological constant  $\Lambda$  can be treated separately<sup>10</sup> from matter (described as the density  $\rho$ ).  $H$  is the Hubble parameter, normally expressed in units of  $100 \text{ km s}^{-1} \text{ Mpc}^{-1}$  (i.e, parameter  $h$ ), as

$$H = 100h \text{ km s}^{-1} \text{ Mpc}^{-1} \quad (2.6)$$

The conservation of energy (i.e,  $T_{;\nu}^{\nu\mu} = 0$ ) can be written in terms of the FRW metric and the perfect fluid tensor as

$$\frac{d}{dt}(\rho a^3) + p \frac{d}{dt}(a^3) = 0 \quad (2.7)$$

The Friedman equation and the energy-conservation equation gives the evolution equation for the scale factor

$$\frac{\ddot{a}}{a} = -\frac{4\pi G}{3}(\rho + 3p) + \frac{\Lambda}{3} \quad (2.8)$$

A critical density,  $\rho_c$ , can be defined as that in absence of a cosmological constant would result in a flat Universe

$$\rho_c \equiv \frac{3H_0^2}{8\pi G} \quad (2.9)$$

The abundance of a substance in the Universe (matter, radiation or vacuum energy) is normally expressed in units of  $\rho_c$ . It is common to use the quantities  $\Omega_i$  of a substance  $i$  with density  $\rho_i$  expressed as  $\Omega_i \equiv \frac{\rho_i}{\rho_c}$ , for matter, radiation, cosmological constant and even curvature, at the present epoch

$$\Omega_m = \frac{8\pi G \rho_m}{3H_0^2} \quad \Omega_r = \frac{8\pi G \rho_r}{3H_0^2} \quad (2.10)$$

$$\Omega_\Lambda = \frac{\Lambda}{3H_0^2} \quad \Omega_k = -\frac{k}{a_0^2 H_0^2} \quad (2.11)$$

Another useful quantity is  $\Omega_{total}$ , defined as  $\Omega_{total} = \sum \Omega_i$ . With all these redefinitions, the Friedmann equation today ( $a \equiv a_0$ ) can be re-written as the *cosmic sum rule*<sup>11</sup>

<sup>9</sup>With  $U^\mu U_\mu = -1$ .

<sup>10</sup>This is normally done, as  $\Lambda$  is associated to the vacuum energy of quantum field theory.

<sup>11</sup>It is normally neglected the  $\Omega_r$  today value, due to it smaller contribution ( $\mathcal{O}(10^{-5})$ ).

$$1 = \Omega_m + \Omega_\Lambda + \Omega_k \quad (2.12)$$

The  $\Omega_i$  components are mainly dominated by particles as baryons, dark matter or massive neutrinos ( $\Omega_m = \Omega_{baryons} + \Omega_{cdm} + \Omega_\nu$ ) or by a cosmological constant. Present experimental results constrains  $\Omega_k$  to negligible values, so the *cosmic sum rule* is normally expressed as  $\Omega_m + \Omega_\Lambda = 1$ .

Another relationship which becomes useful is that of the cosmological deceleration parameter today,  $q_0$ , in terms of matter and cosmological components of the Universe (independent of spatial curvature)

$$q_0 \equiv - \left. \frac{\ddot{a}}{aH^2} \right|_{t=t_0} = \frac{1}{2}\Omega_m - \Omega_\Lambda \quad (2.13)$$

Uniform expansion corresponds to  $q_0 = 0$  (thus requires precise cancellation  $\Omega_m = 2\Omega_\Lambda$ ), and accelerated expansion corresponds to  $q_0 < 0$ .

Originally, cosmological models were entirely baryonic and involved simple *ad hoc* initial conditions. In many ways, this picture has not changed drastically since then, as the SCM is based in nearly scale-invariant and adiabatic initial conditions, in an almost isotropic and homogeneous Friedmann-Robertson-Walker solution to the Einstein equations.

Normally some deviations from homogeneity are introduced in the early Universe, in a statistical way, as perturbations which normally obey Gaussian statistics. The simplest viable mechanism for generating the observed perturbations<sup>12</sup> is the *inflationary cosmology*, which posits a period of accelerated expansion in the Universe's early stages [38] [39]. Tiny quantum fluctuations before inflation grow to real fluctuations in the mass distribution at very early epochs, after inflation, which are the seeds of galaxy formation later on in the evolution of the Universe.

1 Temperature	$T_0$				
1 timescale	$H_0$				
5 densities	$\Omega_\Lambda$	$\Omega_{cdm}$	$\Omega_{baryons}$	$\Omega_\nu$	$\Omega_k$
1 pressure	$w \equiv p/\rho$				
4 fluctuation descriptors	$A$	$n$	$n' \equiv dn/d \ln k$	$r \equiv T/S$	

Table 2.1: Parameters of the Standard Cosmological Model (SCM).

The number of parameters required to describe the SCM model varies depending on the taste of individual cosmologists, but a typical count is listed in Table 2.1. Maybe this is not a complete set of parameters, but nowadays there is no evidence that we need any more. Maybe, the final understanding of the cosmological model may actually give fewer parameters.

## 2.4 The most relevant cosmological data

Very recent observational techniques have moved Cosmology into an unprecedented era of precise cosmological parameter determination (values determined with <10% error), far from the expectations from two decades ago. This boost has been accomplished due to precise measurements of the CMB, large scale structure (LSS) of galaxies, and distant type Ia supernovae. With all these ingredients the so-called SCM has been emerged.

In this scenario, the geometry is flat ( $k = 0$ ), so  $\Omega_{total} \sim 1$ , the total energy density is made up of matter ( $\Omega_m \sim 0.3$ , with  $\Omega_{baryons} \sim 0.05$  and  $\Omega_{cdm} \sim 0.25$ ), and dark energy ( $\Omega_\Lambda \sim 0.7$ ).  $\Omega_r$  is

<sup>12</sup>Which are seen in the CMB, as we will describe later, the so-called anisotropies.

negligible at the present epoch, but it played an important role in the primordial Universe, when it was the dominant factor. With only a few free parameters, the SCM provides an excellent fit to all observational data. Although, it should be reminded, that cosmology is almost entirely driven by the experiments and that its underlying pillars involve physics in which our understanding is still very limited.

### 2.4.1 Large Scale Structure (LSS)

The matter distribution in the Universe can be used to constrain the cosmological parameters. The growth of structures is thought to be governed by the dark matter. The entire history of the cosmos in all its complexity, as governed by a handful of cosmological parameters, imprints its influence into the large scale structure, from which we can derive their values.

Two recent huge galaxy surveys of comparable size have taken place: the Sloan Digital Sky Survey (SDSS) and the 2-degree Field Galaxy Survey (2dFGRS) (see [40] for details about the different existing redshift catalogs). Once SDSS will be completed, it will contain an accurate galaxy count of one quarter of the entire sky (up to 1 million galaxies), maybe the most ambitious astronomical survey ever undertaken.

Both surveys measure angular positions and distances of galaxies, yielding a 3-dimensional map of the visible Universe. Various statistical properties related to large scale matter distribution can be inferred from these measurements. A key quantity defining gravitational clustering is the *power spectrum* of density perturbations (see Figure 2.4). The power spectrum can be decomposed into a primordial part which is generated by some mechanism in the early Universe (presumably inflation) and a transfer function, which contains the imprints of the Universe evolution.

The power spectrum reflects the distribution of matter at different epochs, and this depends on the cosmological parameters. In particular, by using the current value of the Hubble parameter ( $h_0$ ), the data itself suggest the need of the  $\Lambda$  term within the CDM paradigm<sup>13</sup>.

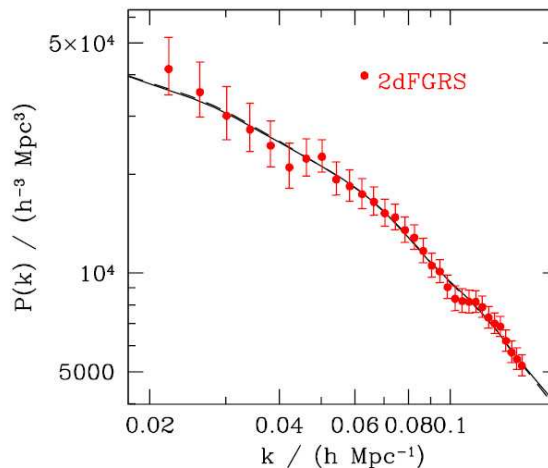


Figure 2.4: Final 2dFGRS power spectrum  $\mathcal{P}(k, \tau)$  in the cases of a SCM basic-five (solid line) and basic-six (dashed line) parameter models (figure extracted from [41]).

<sup>13</sup>Otherwise, the predicted 'shape parameter'  $\Gamma$  is much larger than the observed, and the shape of the power spectrum could not be adjusted by the model.

### 2.4.2 Cosmic Microwave Background (CMB)

The measurements of the cosmic microwave background (CMB) can be considered as the most accurate results added to the cosmological puzzle, and their analysis has been the main focus for cosmologists during the last decade. Some experiments have provided useful data, but here we will focus on the precise results obtained by the WMAP satellite [31]. A good review on other CMB measurements and the CMB analysis can be found in [42].

In the early Universe stage, before electrons and protons combined into neutral atoms (a process called *recombination*), the baryons and photons were tightly coupled. After decoupling from matter, these photons started their free travel through the Universe. Their properties carry a record of the conditions at the time of decoupling and, in addition, of some properties of the Universe itself, as these photons have traversed the Universe structure, which depends on the cosmological parameters.

The CMB is extremely isotropic ( $\Delta T/T \sim 10^{-5}$  level) and follows with extraordinary precision the spectrum of a black body corresponding to a temperature  $T \sim 2.73K$ . The CMB contains minute anisotropies, first detected by COBE and confirmed by several experiments, in particular WMAP (see Figure 2.5).

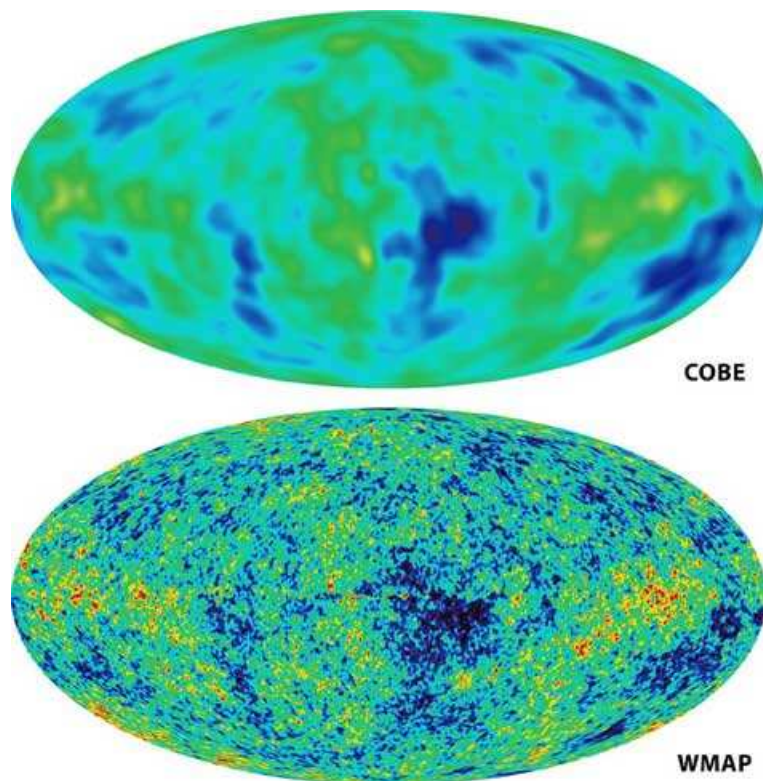


Figure 2.5: A comparison of all sky image of temperature fluctuations in the early Universe with COBE (upper image) and the WMAP (lower image). Figures taken from [43].

The power spectrum of these anisotropies is a fundamental quantity, in which all relevant cosmological parameters play an important role. The observed temperature anisotropies can be expanded as

$$\frac{\delta T}{T}(\theta, \phi) = \sum_{\ell=2}^{+\infty} \sum_{m=-\ell}^{+\ell} a_{\ell m} Y_{\ell m}(\theta, \phi) \quad (2.14)$$

where  $Y_{\ell m}(\theta, \phi)$  are spherical harmonics. The variance  $C_\ell$  of amplitudes  $a_{\ell m}$  is given by

$$C_\ell \equiv \langle |a_{\ell m}|^2 \rangle \equiv \frac{1}{2\ell + 1} \sum_{m=-\ell}^{\ell} |a_{\ell m}|^2 \quad (2.15)$$

If the temperature perturbations are Gaussian, the power spectrum describes all of the statistical information (non-Gaussianities are weak in all inflationary-type models). The anisotropy power spectrum is often plotted as  $\ell(\ell + 1)C_\ell$ , as can be seen in Figure 2.6.

Four different regions can be identified in the power spectrum, each of which takes up about one decade in  $\ell$ . The peaks (oscillatory features) on the power spectrum arise from acoustic vibration modes in the coupled photon-baryon fluid (i.e, amplitudes of standing waves at the last scattering epoch), with the first and most prominent peak at around one degree ( $\ell = 200$ , primary anisotropy), damped at higher  $\ell$ s because of incomplete coupling. At larger angular scales (small  $\ell$ s) we have the effect due to the photons having encountered changes in gravitational potentials during their travel since the early Universe (the integrated Sachs-Wolfe effect or secondary anisotropies).

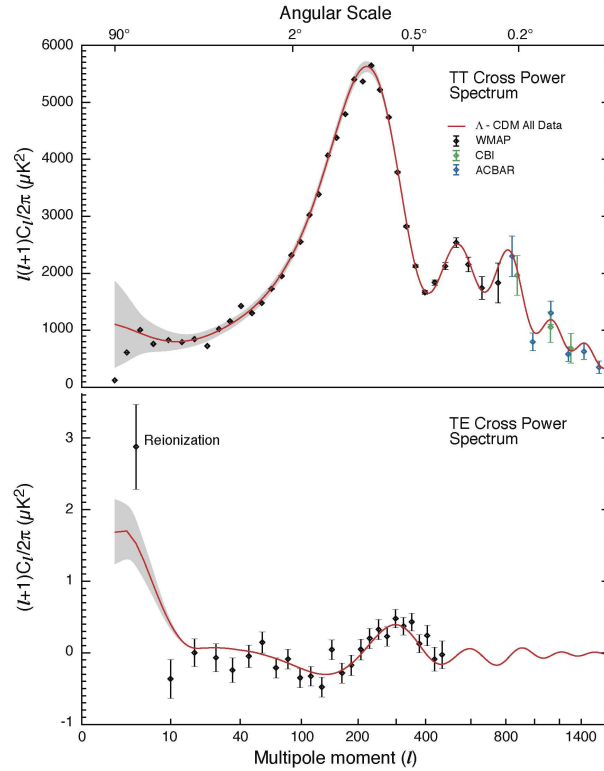


Figure 2.6: The WMAP angular power spectrum (top) and temperature-polarization (TE) cross-power spectrum, consistent with the ACBAR and CBI measurements. Best fit running index  $\Lambda$ CDM model is shown. The grey band represents the cosmic variance expected for that model. (figure extracted from [31]).

The physics which generates the anisotropies is quite well understood, requiring just linear perturbation theory for gravity-driven oscillations, together with simple *Thompson scattering* of the photons off free electrons. Some of these features are closely related to specific cosmological parameters: the location of the first peak probes the spatial geometry, while the relative heights of the peaks probes the baryon density. Other parameters combine to determine the global shape

of the oscillatory feature. Moreover, as polarization is expected from Thompson scattering, its measurement provides additional information.

The WMAP experiment has provided the spectrum of the CMB fluctuations, with the determination of the power spectrum up to  $\ell=900$ , see Figure 2.6. The first three acoustic peaks are now convincingly detected. These results are consistent with the SCM and an overall fit in the multi-parameter space has provided accurate determinations on many of the involved SCM parameters. In particular, the general paradigm, of a hot early Universe, containing roughly scale invariant and adiabatic initial perturbations, is clearly supported.

A 6 parameter cosmological model is very tightly constrained by the current CMB data. The precise measured position of the location of the first peak, which directly probes the spatial geometry, yields a total density  $\Omega_{total} = \sum \Omega_i + \Omega_\Lambda$  ( $i = baryons, dm, \nu$ ) of [44]

$$\Omega_{total} = 1.02 \pm 0.02 \quad (2.16)$$

The derived baryon density is consistent with that coming from Big Bang nucleosynthesis [45] and affirms the need for both dark matter and dark energy, with no evidence for the dynamics of dark energy (i.e, consistent with a pure cosmological constant). From the WMAP analysis, the best-fit parameters for the abundance of baryons and matter is

$$\Omega_{baryons} h^2 = 0.024 \pm 0.001 \quad \Omega_m h^2 = 0.14 \pm 0.02 \quad (2.17)$$

From these  $\Omega_m$  and  $\Omega_{total}$  values, it is derived that the Universe is almost dominated by dark energy (i.e,  $\Omega_\Lambda$ ). The radiation density today has a negligible value of  $\Omega_r h^2 \sim 2.5 \cdot 10^{-5}$ .

An extended set of parameters can be constrained using other astrophysical measurements (in particular, their precision is improved). Several degeneracies in fitting the parameters are easily broken when including other data, e.g, from supernovas, galaxy clustering or direct estimates of  $\Omega_m$  and  $h_0$ <sup>14</sup>.

### 2.4.3 Type Ia supernovae

The relation between observed flux and the intrinsic luminosity of an object depends on the luminosity distance, which particularly depends on the cosmological parameters. Empirically, the peak luminosity of supernovae of type Ia can be used as an efficient distance indicator. Although they are not considered to be perfect *standard candles*, it has been demonstrated that by using the light curve shape and the luminosity at the maximum brightness, the dispersion on the measured luminosity is greatly reduced [46].

Regular observations of distant supernovae have been carried out on a large scale for about a decade. The major outcome of the *Supernova Cosmology Project* and the *High-z Supernova Search Team* was the evidence that the Universe is accelerating [47] [48] ( $q_0 < 0$ ), interpreted as due to a cosmological constant or a more general 'dark energy' component.

Supernova Ia data alone can only constrain a combination of  $\Omega_m$  and  $\Omega_\Lambda$  (see Figure 2.7), although later it can be recombined with the CMB data, resulting in best fit-values  $\Omega_m \sim 0.3$  and  $\Omega_\Lambda \sim 0.7$ . More details are given in the next section.

## 2.5 Precise determination of cosmological parameters

The goal of the observational cosmologist is to utilize astronomical objects to derive the cosmological parameters. The transformation from the observables to the key parameters usually involves many

---

<sup>14</sup>Note that when constraining the cosmological parameters, some priors and restrictions in the parameter space are used, previously to the multi-parameter fit.

assumptions about the nature of the objects, as well as about the nature of the dark matter and dark energy.

Traditionally, this has included estimating distances of very distant objects, estimating masses of large amounts of matter, measuring clustering of galaxies, and determining the primordial abundances. All these measurements are quite hard to be done, require precise distance and mass determination, and all might be largely affected by systematic effects. Fortunately, the Universe has offered an opportunity to learn about its large-scale properties through the anisotropies in the CMB, providing essentially a projection of the 3-dimensional structure at early times, when densities were still very much in the linear regime.

### 2.5.1 Best-mean values of cosmological parameters

Based on the present cosmological data many different groups have performed likelihood analysis based on the  $\Lambda$ CDM. The  $\Lambda$ CDM is almost universally accepted by cosmologists as the best description of present data, despite the fact that both dark matter and dark energy have not been verified in laboratory experiments. A good fit is obtained for a flat and expanding Universe, in which 30% of the energy density is in the form of non-relativistic matter and 70% in the form of a new, unknown dark energy component with strong negative pressure. Spatial geometry is very close to flat, and the initial perturbations Gaussian, adiabatic, and nearly scale-invariant [44]<sup>15</sup>.

Normally, combined datasets have to be used in order to constrain better the cosmological parameters. Since July 2004, five large analysis have been carried out [49] [50] [51] [41] [52], based on partly overlapping data. These papers quote slightly different, but consistent, values for the species densities, as they depend on priors used or the number of cosmological parameters to be constrained in the multi-parameter fit<sup>16</sup>.

All these studies mainly use combinations of different relevant results, like the CMB power spectra on large angular scales from the first year of WMAP observations, normally combined with other CMB measures on small scales from CBI [53], VSA [54], ACBAR [55], and data from BOOMERANG [51], DASI [56], and MAXIMA [57]. The results from SDSS galaxy clustering analysis [58], including the 2dF-GRS [59], and the SNIa constrains [49] are also included.

The most general parameter space explored in all these five articles is 14-dimensional:

$$\mathcal{P} = \{\omega_{baryons}, \omega_m, \Omega_k, \sum m_\nu, \tau, h, \sigma_8, b, w, w_1, n_s, A_s, \alpha_s, r\} \quad (2.18)$$

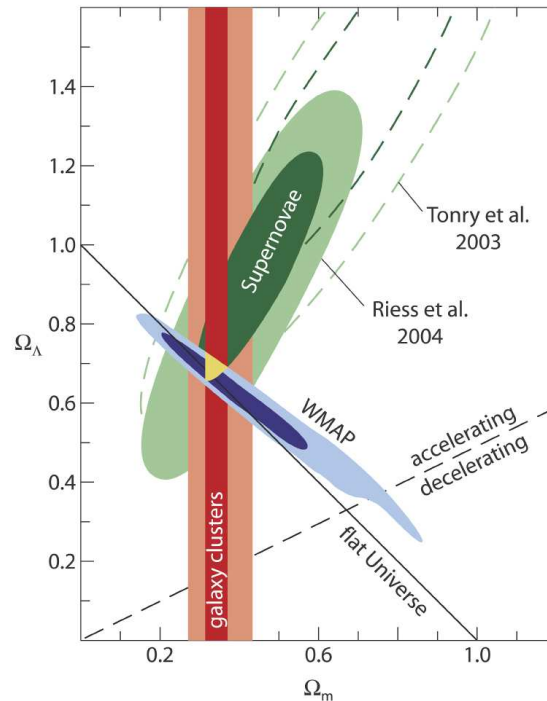
where  $\Omega_i$  is given by  $\Omega_i = \omega_i/h^2$ . The value  $\Omega_m = \Omega_{baryons} + \Omega_{cdm} + \Omega_\nu$ . The ratio of pressure to energy density for dark energy is  $w = w_0 + w_1(1 - a)$ , where  $a$  is the parameter scale of the Universe.  $\sigma_8$  is the *rms* linear mass perturbation in  $8h^{-1}$  Mpc spheres. The parameters  $\tau$ ,  $n_s$ ,  $A_s$ ,  $\alpha_s$ ,  $r$ ,  $b$  describe fluctuation properties, which are not discussed in this Thesis.

Since the data sets from all these analysis are to a large extent overlapping, they are not independent. Moreover, parts of the errors reported are systematic, so the different data sets cannot be summarized using standard statistical methods. A recent study from M. Roos [60] takes all these major results, i.e. all these different independent studies, and the best median values for cosmological parameters are given. Shown in Table 2.2 are the recommended values to be used, extracted from this study.

This study finds that no significant values can be obtained at present for  $r$ ,  $\alpha_s$ ,  $w$ ,  $w_0$ ,  $w_1$ , and that the values for  $\Omega_k$  and  $n_s$  are only marginally significant, consistent with flat space. An upper limit for  $\sum m_\nu$  is also quoted.

<sup>15</sup>The only experiment that supports all these main tenets is the WMAP, considered the most successful detector, from cosmological point of view.

<sup>16</sup>As more parameters are included into the multi-parameter fit, bigger is the quoted errors for individual parameters. Normally, these errors are expressed as  $1\sigma$  errors.



Constraining the Cosmological Parameters

ESO PR Photo 18d/04 (3 June 2004)

© European Southern Observatory



Figure 2.7: Strong evidence for the existence of a cosmological vacuum energy density. Plotted are the 68% (dark) and 95% (light) confidence regions for supernovae, cluster measurements, and CMB data.

Concerning inflation, data supports all the main predictions of the simplest inflation models: spatial flatness and adiabatic, Gaussian, nearly scale-invariant density perturbations.

### 2.5.2 Direct estimates of the Hubble constant

The slope of the relation between the distance and recession velocity is defined to be the Hubble constant. Locally, it provides the calibration of the Hubble expansion law,  $v = Hr$  ( $H$  is usually given in units of  $\text{km s}^{-1} \text{Mpc}^{-1}$ , and sometimes defined as  $h = H/100$ ).

For many decades, the determination of  $H$  have suffered from large systematic uncertainties and the derived values were spread over a wide range of values. One of the most reliable and recent results on the Hubble constant from a single detector comes from the *Hubble Space Telescope Key Project* [61] (HST).

Type Ia supernovae (SNe Ia) are the most precise indicators known for measuring the expansion rate of the Universe. Their extreme and relatively uniform luminosities provide the key to precise distance determinations across a significant fraction of the visible Universe. The first evidence for an accelerating Universe came from these measurements.

The distance determination uses mainly a relationship between the light-curve and luminosity, yielding distances with relative precision approaching 7%, using modern photometry. Moreover, precise calibration of the peak luminosity is needed in order to fix the distance scale to determine the Hubble constant. This is done with independent measurements of the distance to a few SN Ia hosts from Cepheids or other means [62].

Parameter	Best-fit value ( $1\sigma$ error)
$\Omega_{baryons}$	$0.048^{+0.005}_{-0.004}$
$\Omega_m$	$0.286^{+0.030}_{-0.028}$
$\Omega_{dm}$	$0.238^{+0.030}_{-0.028}$
$\Omega_\Lambda$	$0.714^{+0.028}_{-0.030}$
$\Omega_k$	$-0.023^{+0.017}_{-0.050}$
$\tau$	$0.147^{+0.068}_{-0.064}$
$n_s$	$0.962^{+0.030}_{-0.027}$
$\ln(10^{10} A_s)$	$3.12^{+0.14}_{-0.12}$
$\sigma_8$	$0.81^{+0.09}_{-0.14}$
$r$	$< 0.4$
$\alpha_s$	$-0.011 \pm 0.012$
$w$	$-0.93^{+0.13}_{-0.10}$
$h$	$0.687^{+0.034}_{-0.047}$
$\sum m_\nu$	$< 1.1eV$

Table 2.2: Recommended values of SCM parameters, according to [60].

One of the most recent supernovae Ia Hubble constant estimation is [62]

$$h_0 = 0.73 \pm 0.04(stat) \pm 0.05(syst) = 0.730 \pm 0.064(total) \quad (2.19)$$

which is in quite good agreement with the best mean value quoted in Table 2.2.

Since the Hubble constant is a rate, the reciprocal defines a timescale. In particular, for the current cosmological parameters, the age of the Universe is  $t_0 = 1/H_0$  within 10%. This derived quantity is in the range 13–14 Gyr [63]. The WMAP-alone, assuming flatness, results in  $13.4 \pm 0.3$  Gyr. This is consistent with the age of the oldest globular clusters and radioactive dating.

### 2.5.3 The temperature $T_0$

The CMB was discovered by Penzias and Wilson in 1965 [28] and its temperature distribution was found to follow very accurately a blackbody spectrum, with deviations severely constrained over 3 decades in wavelength. The CMB temperature is measured to be [64]:

$$T_0 = 2.728 \pm 0.004K(1\sigma) \quad (2.20)$$

This represents the strongest evidence for the hot Big Bang picture. It is extremely difficult to produce such thermal spectrum through some local process, and easy to achieve it in a hot early period of the Universe, since the thermal equilibrium timescale is naturally very much shorter than the expansion rate.

The value of the temperature changes with cosmological epoch, so  $T_\gamma(z) = T_0(1+z)$ . There is some evidence that this temperature value was higher in the past, consistent with cooling through expansion. The need for extraordinary precision to detect changes on  $T_0$  over the human lifetime, makes viable to consider  $T_0$  as a fundamental constant, which fixes the energy density of radiation today to be small and negligible.

This temperature corresponds to a photon number density of  $n_\gamma = 411 \text{ cm}^{-3}$  and an energy density of  $0.26 \text{ eV cm}^{-3}$  for the thermal spectrum. The current contribution to the total Universe content is negligible ( $\Omega_r h^2 \sim 10^{-5}$ ).

## 2.6 Computational cosmology: N-body simulations

Our understanding of the large scale structure is deep but still limited. The description of the structures from seed inhomogeneities, i.e. primordial density fluctuations, is complicated as it accounts for many physical processes, like gas dynamics, radiative cooling, photo-ionization, recombination and radiative transfer. These are the ingredients for any theoretical comparison with the observed luminous Universe, regions in which all these dissipative effects are of vital importance.

The most widely adopted approach to the problem of large-scale structure formation involves the use of *N-body simulations* (see [65] for a review). Numerical simulations have played a key role in the interpretation of observational data since computers first become available for research. Nowadays, high resolution simulations make full use of tremendous parallel computational power.

Structure formation is often approximated with non-linear gravitational clustering from specific initial conditions of dark matter particles. This approach can be refined by including effects of gas dynamics, chemistry, radiative transfer and other astrophysical processes. Reliability of the simulation is measured by its mass and length resolution. The *mass resolution* is characterized by the mass of the smallest (elementary) particle considered, being the scale below which fluctuations become negligible. The *length resolution* is limited by the so-called softening scale, introduced to avoid infinities in the gravitational force when particles collide<sup>17</sup>.

Two opposite scenarios were normally taken into account prior the results from N-body simulations and cosmological results. The dark matter at the time of decoupling could be relativistic or non-relativistic. Normally, authors talked about *Hot Dark Matter* (HDM) or *Cold Dark Matter* (CDM), respectively. An intermediate stage was indeed taken into account: *Warm Dark Matter* (WDM).

The result from the same primordial fluctuation spectra seen from the CMB would be very different for CDM, HDM and WDM, as the structure formation process would have behave differently from what we observe from Large Scale Structure measurements. Figure 2.6 shows a simulation of the hierarchical evolution of a galaxy cluster in a Universe dominated by CDM, HDM and WDM particles (snapshots at different redshifts for a simulation of the Local Group). These N-Body simulations take months to be produced on dedicated parallel computing systems. In general, only the CDM simulations reproduce the observables at a large-scale, while at local scales there are some failures. For example, they predict more expected substructure orbiting within galactic haloes [66] (see Figure 2.10).

N-body simulations suggest the existence of a Universal dark matter density profile, with the same shape for all galaxy masses, epochs and input power. The usual parameterization for the dark matter halo density profile is

$$\rho(r) = \frac{\rho_0}{(r/r_s)^\gamma [1 + (r/r_s)^\alpha]^{(\beta-\gamma)/\alpha}} \quad (2.21)$$

Various groups have obtained different results for the spectral shape in the innermost regions of galaxies and galaxy clusters. These regions are the hardest regions to be simulated because of the short dynamical time-scales and strong gravitational forces, normally dominated by the resolution of the simulation, i.e. the computational power. Initially, Navarro, Frenk and White [68] found that the value of the power-law index in the innermost region of the galaxy haloes was  $\alpha = 1$  ( $\rho \sim r^{-1}$ ),

<sup>17</sup>This reduces considerably the computational time.

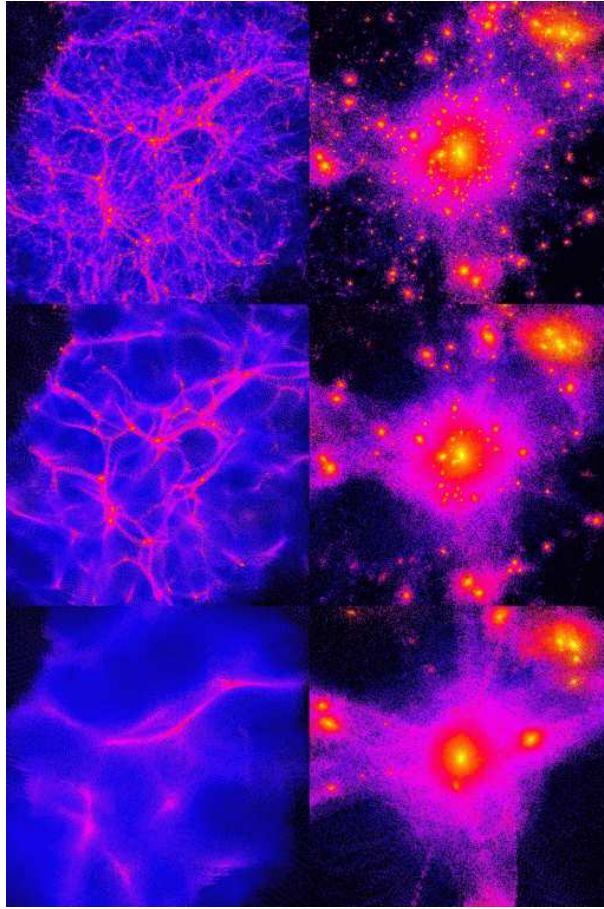


Figure 2.8: N-Body simulations of structure formation for CDM (top), WDM (middle) and HDM (bottom) dominated Universes. Figure taken from Been Moore’s group website [67].

while later simulations have given different results, like Moore et al [69] with  $\alpha = 1.5$ <sup>18</sup>. Normally, these results are based only on one simulation, each made by separate groups (i.e, different length scales, numerical resolutions or numerical codes), so some deviations are to be expected.

### The central cusp issue

The result of the density profile slope in the innermost region of a halo is of vital importance for the subject which is discussed in this Thesis and it will be revisited later. Particularly interesting are some disagreements when comparing the central cusps predicted by simulations and some observations on Low Surface Brightness Galaxies (LSBs). These galaxies contain a very low density of luminous material, even in the innermost parts, so that the observed dynamics should be dominated by the gravitational potential of the dark matter halo, at small and large radii. Moreover, the interaction of baryons and dark matter is at minimum level, so if a central cusp exists, it should be still there.

Using high-resolution rotation velocity data of 21cm emission of atomic hydrogen for 13 LSB galaxies, de Block et al. [17] showed that the distribution of these inner slopes suggests the presence of a shallow, or even flat, cores. These results suggest that these galaxies are not dominated

<sup>18</sup> $\alpha=1.5$  has been widely used, although the most recent value quoted by Diemand, Moore et al is  $\alpha=1.16$  [70].

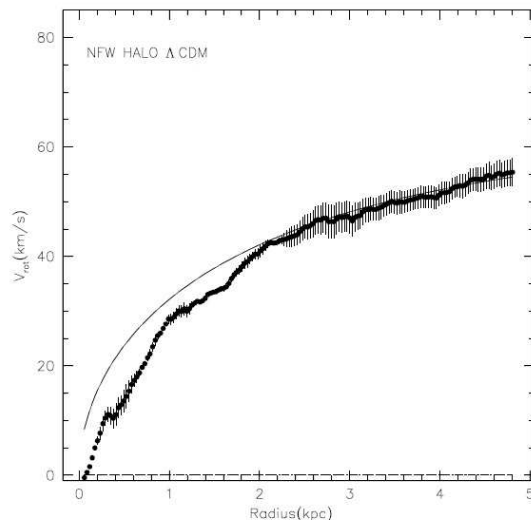


Figure 2.9: Rotation curve (circular rotation velocity as a function of radius) for the low surface brightness galaxy NGC 6822. The points show data obtained from the 21cm emission of atomic hydrogen, while the line gives the best-fit model assuming that the galaxy’s mass is dominated by a centrally-cusped dark matter halo. (Figure from [71]).

by a centrally-cusped dark matter halo. Recent simulations [72] [73] [74] seem to add a new paradigm: the density profiles tend to flatten at the center of the haloes. But, this result is under debate, as these conclusions come from extrapolations: no real high resolution actually has shown a core [75] [70] [76].

We argue in this Thesis that the effects of the adiabatic baryonic compression of the dark matter near the center of haloes (in particular our study focuses on the Galactic Center) enhances the dark matter density by an order of magnitude [77]. This can be considered as one of the first attempts to make a realistic halo model including the baryons. Indeed, since the total mass of the inner galaxy is dominated by baryons, the dark matter distribution is likely to have been influenced by the baryonic potential. Of course, the effect of the central Black Hole might be important. See [78] and [79] for a discussion.

## 2.7 Limitations of the SCM

There are several assumptions in the SCM. It is assumed that physics is the same everywhere in the observable Universe, and that General Relativity fully describes gravity on large-scales. Moreover, the model relies on the hot Big Bang picture being correct, and that something akin to inflation created the density perturbations. Most of these assumptions are testable (or at least falsifiable) in light of modern cosmology.

Although this model can be extended, there are not still evidences in favor of doing that, as to trace the effects of the extensions is at a level below present observational capability. These extensions might include a more general perturbation approach, inclusion of dark matter properties (i.e, dark matter self-interactions), the further possibilities under dark energy (i.e, Quintessence), include the full ionization history of the Universe as a function of redshift, etc...

Presently, maybe there is little room for dramatic changes. But, despite the very good agreement of the  $\Lambda$ CDM with large-scale observations, some concerns are present when dealing with small-

scale observations, which can be summarized as:

- The **substructure problem**: in that  $\Lambda$ CDM model (with or without cosmological constant) an excessive number of dark matter subhalos (or substructure) within a larger halo are predicted. If everyone of these subhalos is associated with a gravitationally bound baryonic object, then the predicted satellites within the Local Group exceeds by more than an order of magnitude the observed ones [80]. N-Body simulations and semi-analytical approaches predict around 1000 dark matter satellites in our Local Group, while we have observed around 40 dwarf satellites at present. This dark matter satellites might be still undetectable if they do not contain any baryonic fraction.



Figure 2.10: High resolution N-body simulation of a galaxy. At the final time, at redshift zero, subhalo identification algorithms are able to identify almost 5000 gravitationally bound subhalos in this object. From Volker Springer Website: <http://www.mpa-garching.mpg.de/~volker/>.

Several possible explanations for this discrepancy include identification of some satellites with the High Velocity Clouds observed in the Local Group [66] [81], and the existence of dark matter satellites that failed to accrete gas and form stars due either to the expulsion of gas in the supernovae-driven winds or to gas heating by the intergalactic ionizing background.

- The **cusp problem**: in the CDM scenario, the dark matter present in a halo follows a *universal density profile*, which applies both to galaxy clusters as well as to individual galaxies, including dwarfs and LSB's.

From computational cosmology, all these density profiles are cusped at small radii ( $\rho \propto r^{-1}$  or  $\rho \propto r^{-1.5}$ ). The *cuspy core problem* refers to an apparent contradiction between N-body simulations and observations, which appear to favor significantly shallower density cores in galaxy clusters as well as individual dwarf and LSB galaxies, although these effects are still under debate.

It might be premature to condemn the SCM model because of these disagreements, as it has had a considerable success when explaining the clustering large-scale observations. These difficulties might be due to an over-simplification of the physical processes involved in galaxy formation and the

baryonic physics on small scales, including hydro-dynamical effects of star formation and supernovae feedbacks.

For instance, related to the missing dark matter subhalos, there exist a viable hypothesis for an explanation. Both dwarfs and LSB's have a very shallow gravitational potential wells and a strong burst of star formation and supernovae activity may empty the dark matter subhalos from their baryonic component, providing a possible solution to the 'satellite problem'. These subhalos may act as gravitational lenses, therefore detectable through careful observations.

Other issues, involving beam smearing, influence of bars and the interaction of baryons and dark matter at the central regions of galaxies and clusters, are important and intimately related to the central cusp issue [77]. These effects have to be better understood, in order to test the SCM hypothesis on small scales.

### 2.7.1 Improvements from the observational side

Although the SCM has given an scenario in which almost all observational data seems to fit nicely, it seems clear that there must be a bigger picture which still remains to be uncovered. In particular, near future detectors might evidence the need for new parameters, which is very interesting, offering the route to new physics with cosmological implications to be understood.

Ongoing, and planned, surveys and detectors will improve the precision on the determination of the SCM parameters. Deviations from the SCM might soon become available.

A highlight of what is expected in a near future, in different areas, includes:

- **Cosmic Microwave Background:** The *Planck* satellite [82], to be launched in 2007, will measure the CMB spectrum up to  $\ell \sim 2500$ . High accuracy all-sky maps of temperature and polarization will be decisive to understand the inflation mechanism. The *Atacama Cosmology Telescope* [83] will carry out small scale CMB measurements, fundamental to understand non-linear effects or secondary anisotropies, like the Sunyaev-Zeldovich effect and weak gravitational lensing.

A new frontier is the deep study of polarization patterns. Dedicated ground-based polarization experiments, such MAXIPOL [84] or CBI [53], may be able to separate between different modes of polarization.

- **Deep galaxy surveys:** At the time of writing this Thesis, SDSS is finishing its survey. Large samples of galaxy positions at high redshift ( $z \sim 1$ ) will begin to be obtained by the DEEP2 survey [85] and VIRMOS survey [86]. Moreover, the *6dF* [87] is planned to take about 170.000 redshifts.
- **Type Ia supernovae:** Several programs are dedicated to measure high redshifted supernovas. *Supernova Legacy Survey* [88] is currently in progress. ESSENCE [89] will improve the measurement of the parameter  $w$ . The future *Dark Energy Survey* [90] and *Supernova Acceleration Probe* [91] satellite mission (SNAP) will find several thousands supernovas out to  $z \sim 2$ . These results will be a powerful probe of the dark energy.
- **Weak lensing on large-scales:** Perhaps the most interesting probe for cosmological measurements. These measurements will be a direct probe of the large-scale distribution of the gravitational potential (see [92] for a review). Surveys will start on 2006 with the Pan-STARRS project [93]. In a more distant future, the *Large Synoptic Survey Telescope* [94] will be available.

It is expected that these results (as well as results coming from the *Large Hadron Collider* [95] (LHC) will put light into some of the major features which are still currently missing in the current cosmological scenario:

- What is the dark matter made of?
- What is the dark energy? Is  $w = -1$  at high confidence? Does  $\Lambda = \Lambda(t)$ ?
- How did Baryogenesis work?
- Did inflation really happened?
- Which are the physics beyond the *Standard Model of Particle Physics*?
- Where did everything come from?

Although the SMC answers some questions, it raises more than it resolves, and new results will help, hopefully, to understand some of them.

### 2.7.2 Conceptual problems of the SCM

Some authors have some arguments against the SCM model. In particular, they point to conceptual problems which affect the pillars of the cosmological model. A review of all arguments can be found in [96]. Let us just point to some of their suggestions.

- **95% of  $\Omega_{total}$  is based on unknown physics!** The first unpleasant argument is that the SCM is widely accepted by the scientific community, while most of the total matter density is based on unknown physics. Both dark matter and dark energy are two hypothetical entities not at all tested in laboratory.
- **Rely on General Relativity?** The SCM model is based on General Relativity, which was successfully tested in the weak gravity condition of the Solar System and binary neutron stars. From there, it is assumed that General Relativity is a prescription that can be applied to the Universe as a whole. In addition, all fundamental forces in physics (strong, weak, electromagnetic) have quantum nature, while General Relativity is (still) a non-quantum theory.
- **Believing in the Cosmological Principle?** Another of the pillars of the SCM is the cosmological principle, i.e, the Universe is homogeneous and isotropic on 'large scales'. Certainly, the Universe is inhomogeneous at scales of galaxies and cluster of galaxies.
- **Hubble-deVaucouleurs paradox:** According to the SCM, the linear Hubble law is a consequence of the homogeneity of matter distribution. Galaxy surveys show that indeed in the range of scales from 1 to 100 Mpc, the galaxy distribution is strongly inhomogeneous.

On the other hand, modern measurements from Cepheid distances to local galaxies demonstrates that the linear Hubble law is well established within the Local Volume ( $r < 10$  Mpc), starting at distances as small as 1 Mpc. The puzzling conclusion is that the linear law is found inside an inhomogeneous distribution of matter. This empirical fact demonstrates that the Hubble law is not a consequence of the homogeneity of visible matter.

Also, it is pointed out that the SCM is not the only possible model of the Universe. There are several models based on other fundamental hypothesis which give different interpretation of observable phenomena (see [96] and references therein). Crucial tests or even newer data might be decisive to elucidate between several cosmological models which are proposed, as well as the development of quantum gravitational theory needed to understand the *real cosmological physics*<sup>19</sup>.

---

<sup>19</sup>According to these authors.

### 2.7.3 Any alternative to dark matter?

Many other authors consider the *Modified Newtonian Dynamics* [97] (MOND) as an alternative to the dark matter hypothesis. MOND suggest a modification of Newtonian physics to explain the flat rotational curves of galaxies, without the need of any dark component of matter.

Briefly, MOND assumes that the Newton's law of inertia ( $F = ma$ ) is modified at sufficiently low accelerations ( $a < a_0$ ) to

$$\mathbf{F} = m\mathbf{a}\mu(a/a_0) \quad (2.22)$$

where  $\mu(x) = x$  when  $x \ll 1$  and  $\mu(x) = 1$  when  $x \gg 1$ . With this modification, for sufficiently low values of the acceleration, the rotation curve of a galaxy does not depend of the radial distance in which the velocity is measured.

Indeed there are some issues which may posit some problems for MOND, like:

- **Individual halo associated to a galaxy is infinite in extent.** Of course, this is a problem, since recent galaxy-galaxy lensing results [98] suggest that galaxy halos may have a maximum extent of about 0.5 Mpc.
- MOND seems to give good results when applied to local galaxies, but there might be some **problems when applied to clusters**, as gravitational lensing indicates a larger mass concentration at cluster centers than that accounted by MOND [99].
- It is **difficult to embed this new paradigm within general relativity** and, in addition, it is not clear which implications it may have for gravitational lensing and other curved space-time effects.

## 2.8 Dark matter: what can it be?

Once we do accept that the dark matter is a necessary Universe ingredient, the key question is, *what is the dark matter made of?*. Before the recent results, which now point to cold dark matter with non-baryonic origin, there were some hypothesis considering that baryonic particles were responsible for the 'missing mass'.

Cosmology has given part of the answer. The primordial nucleosynthesis is the door to know about the baryon content of the Universe. Based on the fraction of observed light elements (H, D, and He), one can infer the baryon density of the Universe. With high uncertainty, though, the value obtained is  $\Omega_{baryons}h^2 \sim 0.02$ . Such value is not high enough to explain the large scale structure formation.

Authors started thinking on baryonic dark matter, i.e. ordinary matter difficult to be observed with current instruments. For example:

- **MAssive Compact Halo Objects (MACHOs):** baryonic candidates like faint stars (red dwarfs, white dwarfs, neutron stars), failed stars (brown dwarfs and Jupiters) and massive remnants from an early epoch generation of stars (so called Population III stars). The research has used the gravitational microlensing technique.
- **Cold H2 gas:** difficult to be observed.

After 30 years, the MACHO era seems to be over with the advent of the new available data [100]. Microlensing signals from MACHO and EROS experiments evidence that the dark matter in the halo of the Milky Way is not in the form of massive, compact halo objects. All signal can be

attributed to the known and expected population of stars. The new POINT-AGAPE experiment will add more microlensing results, in the direction of M31, but it is expected that this scenario is not going to change.

This is consistent with what it is inferred from CMB-combined cosmological measurements: dark matter is present in the Universe, and it should be of non-baryonic type. So, what we know about its nature? A priori, we do need to make use of physics beyond the Standard Model of Particles, as none of known particle satisfy the requirements to fit within the  $\Lambda$ CDM model.

What do we know then? We know that the non-baryonic particle (or particles) related to dark matter should be long-lived enough for being present in the Universe since their decoupling at the early Big Bang epoch (period in which we assume they were created). It should be weakly interacting to ordinary matter and electrically neutral (charged particles interact readily with light, and would not be dark). Moreover, it should be massive enough to account significantly for the energy density of the Universe. These particles are the so-called *Weakly Interacting Massive Particles* or WIMPs.

Some WIMP candidates have been exhaustively discussed in the literature. A good review is presented in [101] and references therein. We will discuss briefly some of these candidates, most of them which have appeared recently in the literature. All these candidates (except the neutrino) are *purely theoretically motivated particles*, in which normally new physics are involved (super-symmetry, extra-dimensions, etc...), with no evidence still for their existence.

Probably, the most studied candidate is the *neutralino*, a super-symmetric [102] (SUSY) particle which appears to be a suitable candidate in the super-symmetric extension of the Standard Model of Particle Physics (SMPP). There is not still any strong evidence for the need of super-symmetry from the recent experimental results, mainly from particle accelerators. It is certainly encouraging that SUSY might be definitely verified or falsified in light of upcoming accelerators like the LHC. If SUSY particles are expected, the neutralino may be the best candidate to account for the Universe dark matter, and dedicated searches can be addressed.

This Thesis is focused on the neutralino particle, so we will describe its basic properties and its detection techniques in a separate section and we leave the bulk description to the next Chapter, in which we discuss some SUSY models and the detection prospects. The next section puts the reader into context.

### 2.8.1 Non-baryonic candidates

Since almost two decades ago, several candidates have been proposed for being hot, warm or cold dark matter particles. Here we summarize the most relevant candidates, consistent with the current  $\Lambda$ CDM picture, as well as a short description.

- *Standard Model Neutrinos.*

The only *known-to-exist* dark matter candidates. They have been considered as excellent candidates, until very recently. We do know from solar and atmospheric neutrino data that *neutrinos* have a small mass [103]. The best laboratory *neutrino* mass limits comes from tritium  $\beta$ -decay experiments [104], which give an upper limit of  $m_\nu < 2$  eV.

We have seen that a more stringent constrain comes from combined-WMAP cosmological measurements, suggesting that  $\sum m_\nu < 1.1eV$ . This, combined with the oscillation measurements (which indicate that  $\sum m_\nu \geq 50$  meV), corresponds to approximately  $0.0005 < \Omega_\nu h^2 < 0.0076$ , which means that *neutrinos* are not a dominant component of dark matter in the Universe.

Furthermore, *neutrinos* are relativistic collision-less particles, cataloged as hot dark matter (HDM). We do know that a Universe dominated by relativistic particles would have provide a

Universe evolution different from what we infer from Universe structure measurements [105]. This argument favors the fact that they cannot be dominant.

- *Axions.*

Theoretically motivated to explain the absence of CP violation in strong interactions. Laboratory searches, stellar cooling and dynamics of supernovae 1987A, constrain the *axions* to be very light ( $\leq 0.01$  eV).

They are expected to be weakly interacting with ordinary particles, which implies that they were not in thermal equilibrium in the early Universe. So, their abundance depends on some assumptions on their production mechanism (i.e, the relic density depends on it). It is possible to find an acceptable range were *axions* satisfy all present-day constrains and represent a possible viable dark matter candidate [106].

- *SUSY candidates*

*Neutralinos*

*Neutralinos* are by far the most studied dark matter candidate particle. In SUSY models, in which R-parity is conserved, the *neutralino* is the lightest SUSY particle, hence stable, and neutral. This Thesis focuses on this particular candidate. An extensive description of SUSY, the *neutralino* and its properties under certain SUSY models will be given in the next Chapter.

*Gravitinos*

They are the SUSY partners of the standard model (undetected) graviton. In some SUSY scenarios, like the Gauge Mediated Supersymmetry Breaking (GMSB) models, the *gravitino* is the lightest particle and is stable. With only gravitational interactions, gravitinos are very difficult to observe [107].

However, it has been extensively shown that long lived *gravitinos* pose some cosmological difficulties. In some scenarios, their presence can destroy the abundances of primordial light elements [108], however these problems can be circumvented in some others (for example, [109]).

*Axinos*

The superpartner of the *Axion*. For quite low reheating temperatures, cold *axino* dark matter might be a viable particle, with relic densities within the measured values [110].

- *Light scalar dark matter*

Considering fermionic particles with standard Fermi interactions, Lee and Weinberg concluded (from relic density arguments) that such a WIMP should have a lower mass limit of a few GeV. If dark matter is made of another type of particles, this limit can be evaded. In such case, a 1 – 100 MeV scalar candidate can be proposed [111].

Recently, this particle has become experimentally suggested as the origin of the 511 keV gamma-ray emission observed by the INTEGRAL satellite from the galactic bulge [112]. It is argued that it could be the product of *light scalar dark matter* particles annihilating into positrons, those later annihilating as well producing this monochromatic gamma-ray line. This hypothesis still needs more tests and more arguments, as there are other dark matter candidates that can explain the observed line, like *axinos* with R-parity violation or *sterile neutrinos*. Moreover, the same effect should be visible in the center of dwarf spheroidal galaxies, still debated.

- *Dark matter from Little Higgs models*

The so-called *little Higgs model* [113] was suggested as an alternative mechanism (to SUSY) to stabilize the weak scale. In these models, the Standard Model Higgs is a pseudo-Goldstone boson, in which the weak scale is stabilized in an effective field theory, up to  $\sim 10$  TeV.

Two of these models contain a suitable dark matter candidate. One is the ‘*theory space*’ *little Higgs models*, which provides a nearly stable scalar particle with appropriate relic density [114]. The detection prospects do not differ from those related to SUSY WIMPs.

- *Kaluza-Klein States*

Another proposed candidate is related to Kaluza-Klein excitations of Standard Model fields, in models of universal extra-dimensions [115]. The lightest Kaluza-Klein particle (LKP) is stable and provides an alternative convincing suitable dark matter candidate. The LKP will be revisited when discussing the viability of the results presented in this Thesis within a dark matter scenario.

- *Super-heavy dark matter*

These particles are sometimes called *wimpzillas* [116]. They present an interesting phenomenology, including a possible solution to the problem of cosmic rays observed above the GZK cutoff. These are really massive particles ( $m_{DM} \sim 10^{10}$  GeV!), extensively believed to be created by gravitational effects at the end of inflation epoch. Even, more massive candidates are proposed, the so-called *simpzillas* [117].

## 2.8.2 The neutralino as the preferred dark matter particle

In this Chapter we have exposed that the nature of dark matter is still unknown, and none of the known particles satisfy all requirements to account for it. A number of viable WIMP candidates have been proposed within several theoretical frameworks, mainly motivated by extensions of the standard model of particle physics, e.g. supersymmetry (SUSY). Among this variety of particles, the most plausible (or the most popular) candidate is the *neutralino* ( $\chi$ ) [102].

Any WIMP candidate (SUSY or not) can be detected directly via elastic scattering with targets in the Earth. There are several experiments already exploiting this detection technique, but they do not claim any strong and solid detection up to now (see review [118] and section 3.6.1).

Complementary, neutralinos might be indirectly detected by their self annihilation products in high density dark matter environments (i.e. center of galaxies, dwarfs, dark matter subhalos, and galaxy clusters). In particular, channels that produce  $\gamma$ -rays are interesting because  $\gamma$ -rays are not deflected by magnetic fields and preserve the information of the original annihilation region, i.e. they act as tracers of the dark matter density distribution, which is not completely constrained but approximated by the observations and simulations.

This annihilation into  $\gamma$ -rays provides two distinct spectral lines from the processes  $\chi\chi \rightarrow \gamma\gamma$  and  $\chi\chi \rightarrow \gamma Z$ , although in almost all SUSY scenarios the expected fluxes are quite far from observational capabilities [119]. A distinct process is  $\chi\chi \rightarrow q\bar{q}$ , generates a continuum of  $\gamma$ -rays mainly by the decay of  $\pi_0$ -mesons produced within these jets. This continuum  $\gamma$ -ray spectra (almost stable in time) can be indirectly observed by means of Atmospheric Imaging Čerenkov telescopes (IACTs) or  $\gamma$ -ray satellites, like the past EGRET or coming GLAST detector.

This Thesis focuses on the neutralino as the most suitable dark matter candidate. The predicted continuum  $\gamma$ -ray flux from high dense dark matter regions depends on the SUSY model adopted and on the spatial distribution of the dark matter in the selected object. In Chapter 4 we explain in detail the procedure done in order to choose the best astrophysical object to carry out dedicated indirect dark matter observations [120] with the largest world-wide IACT, MAGIC [121], located

on the European Northern Observatory (ENO), in the Canary Islands. In particular, several SUSY models will be discussed as well as the expected  $\gamma$ -ray fluxes for the Galactic Center, Draco dwarf-spheroidal, Milky Way dark matter subhalos, and the nearby galaxy M31.

We advance that the outcome of this phenomenological study is that the most promising places considered to provide the best observational conditions for indirect dark matter searches with MAGIC are the *Galactic Center* and the *Draco* dwarf spheroidal. Of about 17 hours of data has been taken during summer 2005 (ON/OFF mode) in the direction of the Galactic Center. The analysis of the data and their implications for the dark matter paradigm are explained in separate Chapters.

## Chapter 3

# Supersymmetric dark matter

*In this Chapter we briefly expose the basis for the minimal SUSY extension of the Standard Model of Particle Physics (SM). The supersymmetry (SUSY) provides the leading dark matter candidate: the neutralino, considered the most plausible weakly interacting massive dark particle (WIMP). We focus on the neutralino properties in supergravity inspired model (mSUGRA) and we discuss the implications for its indirect detection through  $\gamma$ -rays, as the  $\gamma$ -ray production in their self-annihilations may give detectable signals in current IACTs. Other SUSY scenarios are also considered.*

*This Chapter is partially based on the papers F. Prada, A. Klypin, J. Flix et al (2004) [77] and J. Flix (2005) [120].*

### 3.1 Introduction

We have already discussed that dark matter seems to constitute a non-negligible part of the Universe content. As 'matter', it has to fit within a theoretical framework based on a given Particle Physics model. The Standard Model (SM) scenario by itself cannot provide the necessary dark matter candidate. As a starting point, we can think of a theoretical extension of this model. Suitable is the one that appears when introducing a symmetry between bosons and fermions. The so-called minimal supersymmetric (SUSY) extension of the Standard Model (MSSM) provides a suitable CDM particle: the neutralino.

Exhaustive reviews of the SM, SUSY and SUSY CDM can be found elsewhere [122–129]. We review in this chapter some of the most important features concerning them and the implications for dark matter searches with IACTs.

### 3.2 The Standard Model (SM): its successes, failures, and its limitations

The Standard Model (SM) of fundamental interactions consist on an explicit description of the strong, weak and electromagnetic interactions that governs the dynamics of the elementary particles. This theory is based on the Gauge principle, in which all forces are driven by Gauge fields of the local symmetry group  $SU(3)_{color} \otimes SU(2)_{gauge} \otimes U(1)_{hypercharge}$ . Since the 1970s, extensive experimental tests of the theory have been carried out, mainly in particle accelerators. Most of the theory has been successfully tested and it has shown a high level of predictability. Besides some still open questions and problems about the model, that we list afterwards, the SM constitutes without any doubt the most spectacular and exciting theory framework of modern physics.

In the SM, the field contents can be described by 3 sectors: the *bosonic sector* (interactions with spin 1), the *fermionic sector* (spin 1/2), and the *Higgs boson sector* (spin 0). The last is imposed in the theory *ad hoc* and it is necessary to allow the spontaneous electroweak symmetry breaking (EWSB) and allows the elementary particles to poses a physical mass.

In the *Lagrangian* of the SM there exist 19 free parameters, which experimentally can be determined<sup>1</sup>: 3 coupling constants ( $g$ ,  $g'$ , and  $g_s$ ), 6 quark and 3 lepton masses (if all neutrinos are massless), 1 Higgs coupling constant ( $\lambda$ ) and a mass value ( $\mu^2$ ), 3 mixing angles and a phase to model the CP violation (CKM matrix), and the angle  $\theta_{QCD}$  for the strong CP violation.

Besides being extremely predictive and successful, there are a few arguments that points that the SM is in fact (or it should be treated as) an effective theory at small energy scale. In other words, it seems to be the iceberg top of a big and more extense theory driven at a higher energy scale, in which even the gravitational force might be included (this is the only force that is not included in the SM framework).

There are theoretical, or conceptual, problems in the SM that cannot be solved without adding new physics into the current paradigm:

- In the SM, the electroweak (EW) symmetry has to be broken in order to generate the masses of the weak gauge bosons. The Higgs sector is introduced to mediate the EWSB. The associated particle, the *Higgs boson*, has not still been discovered, although it is predicted to be mass-light from indirect measurements. Considered as one of the most important pillars of the SM theory, **the Higgs mechanism is not experimentally established yet.**
- The SM cannot easily be included in a grand unified theory (GUT). GUT is based on the idea that at extremely high energies, all symmetries have the same gauge coupling strength, which is consistent with the speculation that at the EW scale all of them are different manifestations of a single overarching gauge symmetry. For example, the 3 gauge coupling constants measured with excellent precision by LEP or the Tevatron would converge into an unique value at the GUT scale<sup>2</sup> ( $\Lambda_{GUT} \sim 10^{16}$  GeV).
- Due to quadratically divergent contributions to the Higgs boson mass, the huge gap between the EW and the GUT scale requires the introduction of a fine-tuned mass counter term in order to establish an intermediate Higgs mass. This problem is known as the hierarchy problem.
- The SM does not merge gravity with the other three gauge symmetries. As the later in fact are merged, there is the hope that there should be something more extense that the SM<sup>3</sup>.
- The SM does not provide a suitable particle candidate for CDM.

In addition, there are some experimental measurements that even open new questions. The recent discovery of neutrino oscillations and that they poses a non-null mass is not still well understood within the SM. Other measurements indicate deviations from the expected SM values, for example the ones measured for the magnetic moment of the muon.

In order to address these questions, some alternatives or complements to the SM have been proposed. SUSY is one of the best motivated candidate theory for physics beyond the SM. It

<sup>1</sup>In fact, there exist an extended 26 parameter version of the SM to include the observed neutralino oscillations and their masses (the Maki-Nakagawa-Sakata matrix).

<sup>2</sup>The gauge coupling strengths of QCD, the weak interaction and hypercharge seem to meet at a common length scale called the GUT scale and equal approximately to  $10^{16}$  GeV, which is slightly suggestive observation.

<sup>3</sup>A *theory of everything* (at least everything we think we know).

cannot solve all the problems of the SM, but it does most of those listed above<sup>4</sup>. In SUSY, new particles appear at the TeV scale, modifying the  $\beta$ -functions of the three gauge couplings, such that they meet at about  $\Lambda_{GUT}$ . SUSY-GUT theories provide the EW symmetry breaking dynamically, if the top mass ranges between about 100 and 200 GeV. This is assured from the measured top mass. SUSY pairs bosons with fermions, and this connection solves the hierarchy problem. The quadratic divergences are canceled systematically order by order, if the corresponding couplings between SM and SUSY particles are identical. Fine tuning of the counter terms is not required, if the masses of the SUSY particles are not too large, i.e. of the  $\mathcal{O}(\text{TeV})$ . The neutral lightest supersymmetric particle (LSP), if stable, provides a good candidate for CDM.

### 3.3 Minimal SUSY extension of the SM: the MSSM

The minimal SUSY extension of the SM, the so-called MSSM, is obtained when a minimum SUSY generators are considered. The MSSM requires a doubling of the SM degrees of freedom including two complex Higgs doublets:  $H_d = (H_d^0, H_d^-)$  and  $H_u = (H_u^+, H_u^0)$ . A single Higgs doublet would lead to a gauge anomaly and would cause the theory to be inconsistent. As SUSY pairs bosons with fermions, every SM particle has a superpartner (at the TeV scale) that has yet to be discovered, in fact. As superparticles (sparticles) are expected to be very massive they can only be tested at powerful particle accelerators, like the *Tevatron* or the *Large Hadron Collider* (LHC). There are expectations that some of these spartners, if exist, will be definitely discovered at the LHC. These measurements could provide evidence for grand unification and might even provide hints on how a string theory could describe nature.

Out of the particle content of the MSSM (see Table 3.1), there are five classes of physical particles that superpartners of the SM fall into: *squarks*, *gluinos*, *charginos*, *neutralinos*, and *sleptons*. Particularly, the resulting four neutralinos ( $\tilde{\chi}_{1\dots 4}^0$ ) are linear combinations of the SUSY partners of the neutral gauge bosons,  $\tilde{W}^0$  and  $\tilde{B}^0$ , and the neutral Higgsinos  $\tilde{H}_{u,d}^0$ , the spartners of the neutral components of the two Higgs doublets. All these sparticles have their interactions and subsequent decays described by the MSSM, and each particle has characteristic signatures.

SM Particle type	Particle	Symbol	Spin	R-Parity	Superpartner	Symbol	Spin	R-parity
<i>Fermions</i>	Quark	$q$	1/2	+1	Squark	$\tilde{q}$	0	-1
	Lepton	$\ell$	1/2	+1	Slepton	$\tilde{\ell}$	0	-1
<i>Bosons</i>	W	$W$	1	+1	Wino	$\tilde{W}$	1/2	-1
	B	$B$	1	+1	Bino	$\tilde{B}$	1/2	-1
	Gluon	$g$	1	+1	Gluino	$\tilde{g}$	1/2	-1
<i>Higgs bosons</i>	Higgs	$H_1, H_2$	0	+1	Higgsinos	$\tilde{H}_1^0, \tilde{H}_2^0$	1/2	-1

Table 3.1: Fermions have bosonic superpartners, and bosons have fermionic superpartners. The simplest (or minimal MSSM) theory poses a single pair of Higgsinos.

The MSSM introduces R-parity, a new discrete symmetry which distinguishes SM particles (R=1) and their SUSY partners (R=-1). If R-parity is conserved, the proton is stable, and renders the lightest supersymmetric particle (LSP) stable as well; provided the LSP is neutral and sufficiently weak interacting, the MSSM yields an ideal candidate for dark matter.

The MSSM adds supersymmetry breaking by introducing explicit soft supersymmetry breaking operators into the *Lagrangian*, that is communicated to it by some unknown (and unspecified)

<sup>4</sup>Several problems of the SM remain unexplained in SUSY extensions of the SM as e.g. the masses of the fermions or the origin of the three generations.

dynamics. Unfortunately, the outcome is that this general *Lagrangian* contains about **120 new parameters**, which makes any phenomenological study based on a blind approach to the MSSM parameter space very problematic. The usual way of studying SUSY effects is to assume *specific frameworks*, for example that all parameters at the EW depend on a few inputs given at a certain high energy scale. These are the so-called *constrained MSSM scenarios*.

### 3.3.1 The minimal supergravity (mSUGRA)

Since no SUSY particle with the same mass as its SM partner has been discovered, SUSY has to be broken. Different scenarios for SUSY breaking mechanisms have been proposed. It is typically assumed, that the breaking takes place at a high energy scale (the GUT scale). There are several models with different messenger particles (gravitons, gauge bosons,...) mediating the SUSY breaking effects from the GUT down to the EW scale.

Among the variety of specific SUSY frameworks, the supergravity (SUGRA) models, in which the gravity is included as a new field, have received particular attention. In these models, the EW and the higher energy scale are communicated by pure gravitational effects and the EWSB is characterized by the appearance of the *graviton* boson (spin 2) and its superpartner the *gravitino* (spin 3/2). A limit from renormalization is imposed and the limit GUT energy scale is characterized by  $\Lambda_{SUGRA}^{max} \sim M_{Pl} (\sim 10^{19} \text{ GeV})$ .

The most popular SUGRA model is the minimal supergravity (mSUGRA), where the important feature is the universality hypothesis imposed at  $\Lambda_{GUT}$ : all scalar masses  $m_i$  converge to  $m_0$ , all gauginos feature the same soft mass  $m_{1/2}$ , and all of the trilinear scalar couplings are also taken to be flavor independent and universal at the GUT scale, in addition to gauge coupling unification.

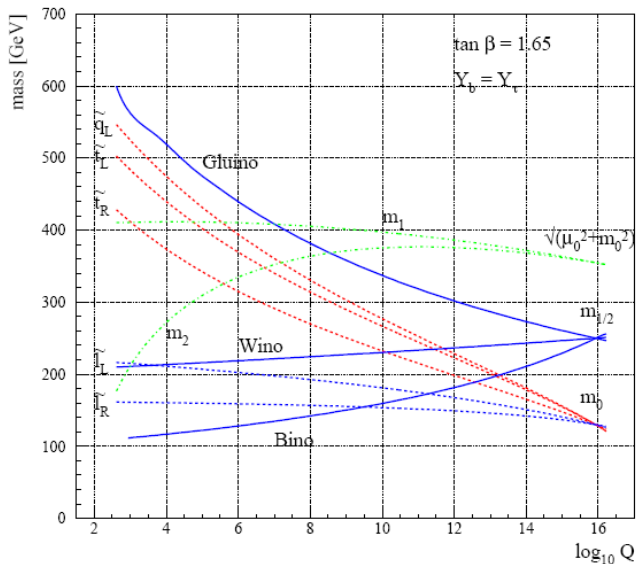


Figure 3.1: Unification of the sparticle mass at the GUT scale. Universal scalar mass  $m_0$  and gaugino mass  $m_{1/2}$  are part of the GUT inputs of mSUGRA.

As a consequence, the whole mSUGRA scenario can be described by only five additional parameters to the SM ones defined at the GUT scale (instead of more than 100 parameters as in the general MSSM). These parameters are: the soft scalar mass  $m_0$ , the soft gaugino mass  $m_{1/2}$ , the ratio of the Higgs vacuum expectation values  $\tan \beta = \langle H_2^0 \rangle / \langle H_1^0 \rangle$ , the soft trilinear coupling

$A_0$  and the sign of the Higgsino mass parameter  $\mu$ . The useful aspect of this parameterization of supersymmetry breaking is that it results in phenomenologically acceptable model involving a few parameters. All parameters of the MSSM can be derived by renormalization group equations (RGE) from the values of these five input parameters (which define a specific mSUGRA model) at the GUT scale, as illustrated in Figure 3.1.

In R-parity conserved mSUGRA models the LSP is the neutralino in large regions of the parameter space, if cosmological bounds are included. As the  $\tilde{\chi}^0$  is electrically neutral, it does not directly couple to photons, an essential condition for any dark matter candidate. The universality principle has important consequences in the parameters at the EWS and, in particular, important for the characterization of the neutralinos.

There exist other scenarios of supersymmetry breaking, namely *Gauge Mediated SUSY breaking* (GMSB) models (in which the *gravitino* is the LSP) or the *Anomaly Mediated SUSY* (AMSB) (in which often the Wino-type neutralino is the LSP).

### 3.4 Neutralino as the dark matter SUSY candidate

Four neutralinos,  $\tilde{\chi}_i^0$ , results from the physical superpositions of the fermionic partners of the neutral electroweak gauge bosons, called Bino ( $\tilde{B}$ ) and Wino ( $\tilde{W}$ ), and of the fermionic partners of the neutral Higgs bosons, called Higgsinos ( $\tilde{H}_1^0$  and  $\tilde{H}_2^0$ ). Thus one can express the lightest neutralino as

$$\tilde{\chi}_1^0 = Z_{11}\tilde{B} + Z_{12}\tilde{W} + Z_{13}\tilde{H}_1^0 + Z_{14}\tilde{H}_2^0 \quad (3.1)$$

The coefficients  $Z_{ij}$  are obtained by diagonalizing the neutralino mass matrix, and are mainly function of the Bino and Wino masses ( $M_1$  and  $M_2$ ) and of the parameter  $\mu$ . It is commonly defined that the lightest neutralino,  $\tilde{\chi}_1^0$ , is mostly gaugino-like if  $P \equiv |Z_{11}|^2 + |Z_{12}|^2 > 0.9$ , Higgsino-like if  $P < 0.1$ , and mixed otherwise.

From the assumption of gaugino mass unification at the GUT scale, it follows that the hierarchy between  $M_1$  and  $M_2$  at the weak scale is fixed to about  $M_1 \simeq 0.5M_2$ , and hence that the wino component of the LSP is always very small. In mSUGRA, the neutralino LSP is very often bino-like and in rare occasions it poses a considerable Higgsino fraction.

The typical mass of the lightest neutralino is of about 10 GeV to (conservative)  $\sim 1 \text{ TeV}^5$ . Although experimentally undetected, some lower limits have been imposed to this and other sparticles.

### 3.5 Evaluating the relic density of neutralinos

As mentioned, the neutralino is considered a very interesting candidate for CDM particle. The direct consequence, if SUSY is right, is that there must exist a relic population of neutralinos from the early primordial Universe. They were in thermal equilibrium with the SM particles in the early Universe, and decoupled when they were non-relativistic. A brief view of the thermal decoupling is given in this section.

In general, any particle specie  $\Upsilon$  decouples from the primordial plasma at a temperature  $T_{\Upsilon,dec}$  when the expansion rate of the Universe is of the same order of the interaction rate of the considered specie. Within an effective cross section  $\sigma$ , to account for all interactions of the  $\Upsilon$  particle, at the decoupling time it is satisfied:

$$\Gamma_{\Upsilon,dec} = \langle \sigma v \rangle n_{\Upsilon} \cdot T_{\Upsilon,dec} \simeq H \cdot T_{\Upsilon,dec} \quad (3.2)$$

---

<sup>5</sup>This upper limit depends on the taste of the theorist and the scenario considered.

where  $n_\Upsilon$  is the specie density,  $v$  the relative 2-body interaction velocity, and  $H$  the expansion rate.

In a CDM scenario, the considered dark matter particle (the Weakly Interacting Massive Particle, WIMP) is non-relativistic [ $v/c \rightarrow 0$ ] at the decoupling time. In such a case, the Universe temperature drops below the mass of the WIMP and:

$$n_\Upsilon \propto \exp(-m_\Upsilon/T_{\Upsilon,dec}) \quad (3.3)$$

Due to the small annihilation cross-sections, the thermal history of the  $\Upsilon$  particle should not modify the primordial nucleo-synthesis. Then, the decoupling (or freeze-out) should take place at higher times, hence lower temperatures (of about  $m_\Upsilon/20$ ). Once the particle decouples, the covolume density frozen, and the quantity  $n_\Upsilon/s$  ( $s$  is the entropy per unit volume) gets a constant value (i.e.  $(n_\Upsilon/s)_{dec} = (n_\Upsilon/s)_0$ , where 0 is the actual epoch) and the relic density of the  $\Upsilon$  particles can be derived:

$$\Omega_\Upsilon h^2 = \frac{n_{\Upsilon,0} m_\Upsilon}{\rho_c} h^2 \sim \frac{3 \cdot 10^{-27} \text{ cm}^3 \text{ s}^{-1}}{\langle \sigma v \rangle} \quad (3.4)$$

Given a particle  $\Upsilon$  with rather low cross section, and massive, typically one can obtain a relic density of the specie consistent to the dark matter abundance measured today value. This is a general approach, in which the WIMPs are left over from the Big Bang in the right amount to account for the observed dark matter density.

This procedure is applicable to any particle, and in particular to the SUSY neutralino, that fulfills all requirements. Of course, when focusing on the neutralino, this formulation need of corrections to make a much more accurate estimation of the relic density. This implies to numerically solve the Boltzmann equation taking into account that the SUSY particle spectra does not only contain the neutralino(s), so the thermal history must include the interaction of the neutralinos to other sparticles (in particular the next-to-lightest SUSY particle (NLSP), that decouples almost at the same temperature, with important LSP-NLSP coannihilations), the neutralino self-annihilations, and even the neutralino non-thermal production from disintegrations<sup>6</sup>. All these effects defines a total effective cross section, which is normally denoted as  $\langle \sigma_{eff} v \rangle$ .

The relic density of neutralinos in the MSSM has been calculated by several authors during the last years with various degrees of precision. Numerical tools to make a complete and precise calculation including relativistic Boltzmann averaging, subthreshold and resonant annihilations, and coannihilation processes are available.

### 3.5.1 Most relevant annihilation channels

At present, relic neutralinos from the early Universe still may interact with each other. There are numerous final states in which the neutralino can annihilate. The most important of these are the two body final states which occur at tree level. Specially they are the production of two fermions  $f\tilde{f}$  in the final state through the exchange of boson  $Z^0$  or the pseudo-scalar Higgs  $A$ , in the s-channel, or through the exchange of sfermions  $\tilde{f}$ , in the t-channel. These are the dominant neutralino annihilation diagrams (see Figure 3.2).

In mSUGRA, the lightest neutralino  $\tilde{\chi}_1^0$  is mainly bino (only  $Z_{11}$  is large), and then the contributions of these diagrams will be typically small, except for the  $\tilde{f}$  t-channel, that is highly suppressed by the high  $\tilde{f}$  masses. Only the s-channels are favored for the (unprovable in mSUGRA) Higgsino-like neutralinos. There exist other less favorable channels, like the  $W^+W^-$  production via exchange of chargino in t-channel, and many others, but less important.

---

<sup>6</sup>This is an special case: for example neutralinos can be produced by the disintegration of Q-balls, increasing the relic density as measured today.

As a consequence, the neutralino self-annihilation cross-section can be considered small, with typical values of about  $10^{-26} \text{ cm}^3\text{s}^{-1}$ . However, this value can be enhanced through the A-exchange with reduced Higgs mass, or models that increase the Higgsino component of the neutralino, via exchange of  $Z^-$ , or charginos exchange channels. These effects are produced when non-universality of Higgs and gaugino masses are considered at the GUT scale.

Figure 3.2: Dominant neutralino annihilation diagrams. Relevant parts of the amplitudes are shown explicitly. V and Z are chargino and neutralino mixing matrices.

## 3.6 Experimental research of SUSY dark matter

Searches for non-baryonic, cold dark matter exist in a large variety of techniques. One can classify them in three different blocks:

- **Direct production** in laboratory experiments (typically at accelerators). At present being tested by Tevatron and in a near future by LHC. Some lower bounds already imposed to some sparticles, mainly from LEP2 analysis.
- **Direct detection** of dark matter particles trough their elastic scattering on target nuclei, via measuring nuclear recoils.
- **Indirect detection** of self-annihilation products of these particles in high density dark matter regions.

These techniques presume that this exotic form of matter consists of unknown or known particles, which are not 'dark' in the strict sense but shine in 'some' detectable form. Let us briefly review the last two techniques.

### 3.6.1 Direct detection

The earth moves within the dark matter halo of our galaxy. There exist a non-null probability that the dark matter particles elastically interact with the ordinary matter. The predicted energy depositions are very small, ranging from a few keV to a few tens of keV. With current detector sensitivities, the number of detected interactions (rates) are expected to be very small. This imposes a serious difficulty for this searching technique as it is an experimental challenge to discriminate these rare events from the much larger background from natural radioactivity (normally, these detectors are placed in low background radiation environments). Different searching techniques have been developed: the use of cryogenic detectors with nuclear recoil identification capabilities (via heat detection), measuring the ionization yield in a semiconductor crystal, and measuring light yield in a scintillating crystal.

The direct detection techniques are many and it would take more than a few lines to describe them. A recent review is given in [118]. Maybe the most important signature of WIMP interactions would be an annual modulation of these rare selected events, as the Earth moves in a dark matter halo. The DAMA collaboration, operating almost 100 kg of low background NaI scintillator detectors in the Gran Sasso laboratory in Italy has published evidence for the detection of such a modulation at  $6.3 \sigma$  CL [130] (see Figure 3.3), consistent with the WIMP hypothesis. Taking into account the uncertainties on the halo model, it is claimed that the preferred range of the WIMP-nucleon cross-section is  $\sigma \sim 10^{-6} - 10^{-5}$  pb for a small WIMP mass of about 30 – 100 GeV. Besides this spectacular result, other collaborations such as CDMS and EDELWEISS, claim to have excluded important regions of the DAMA parameter space (see Figure 3.4). In particular the CDMS Soudan collaboration totally excludes the DAMA results, and moreover has started proving the allowed WIMP-nucleon cross-section allowed in the MSSM [131]. The DAMA data, however, if it is due to the coherent process, is not consistent with other recent experiments, see e.g. EDELWEISS and CDMS. Nevertheless, it could still be interpreted as due to the spin cross section, but with a new interpretation of the extracted nucleon cross section.

While the present direct WIMP-search experiments, with target masses of a few kgs, already provide interesting constraints on the hypothetical WIMP particle properties (and thus constraints on models of SUSY, given the local DM density uncertainties), there is a strong demand to perform more sensitive direct WIMP searches with larger detector mass. Other experiments are bound to confirm or exclude the existing controversies. That compelling development happens at the moment and new results are expected very soon by experiments like GEDEON, EDELWEISS II, and GENIUS. The later will be able to test a WIMP-nucleon cross section as low as  $\sigma \sim 10^{-9}$  pb [132].

### 3.6.2 Indirect detection

For the neutralino case, indirect methods search for products of self-annihilation processes, such as energetic leptons, hadrons, neutrinos or high energetic photons ( $\gamma$ -rays) emerging in the follow up hadronization and fragmentation processes involved in the self-annihilation processes. A complete review is given in [123].

High energetic neutrinos are produced either in quark jets ( $b\bar{b}$  interactions) or in the decay of  $\tau$  leptons and gauge bosons. Neutrinos produced in the former process are less energetic than those produced in the latter. The neutralinos can be decelerated by scattering off nuclei and then accumulating at the center of the Earth and/or at the center of the Sun (or inside any other gravitational potential well, like the Galactic Center as well), thus increasing their annihilation rate. Searches for neutrinos resulting from the above processes in the center of the Earth have been performed by different experiments as Super-Kamiokande, AMANDA, and others. So far, these experiments have only managed to set upper limits on neutrino fluxes coming from the center of the Earth or from the Sun. However, many uncertainties still exist in estimates of the capture rate of WIMPs by the Earth.

Besides high energy neutrinos, antiprotons and positrons are produced in the annihilation processes too. Antiprotons are the consequence of the hadronization of quarks and gluons where as positrons are mainly the result of the decay of charged gauge bosons. Antiprotons (and positrons) are also expected to be generated by interactions of cosmic rays with interstellar matter. However, the energy spectrum of secondary antiprotons falls steeply for energies less than a few GeV, which could favor the distinction between production by cosmic ray interactions and neutralino annihilation. Antiprotons with energies in the range 0.18-1.4 GeV were detected by the balloon borne experiment BESS. Uncertainties on the parameters characterizing the Milky Way diffusive halo difficult the interpretation of such data. In spite of these unresolved problems, the present data seem

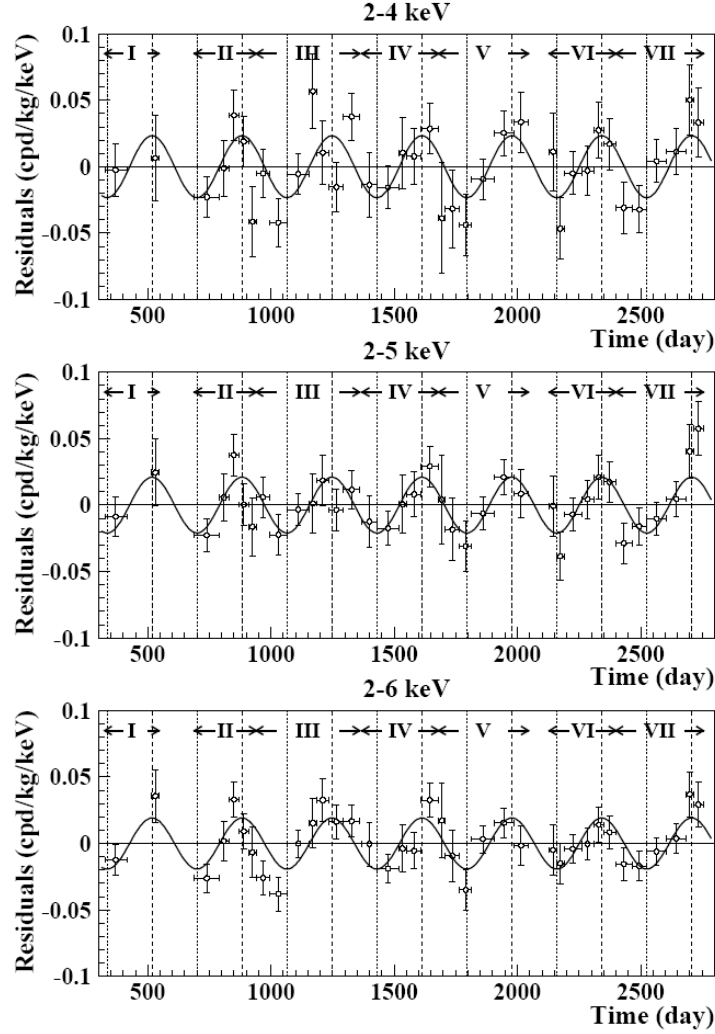


Figure 3.3: Experimental residual rate for *single-hit events* in different keV energy intervals as a function of the time over 7 DAMA annual cycles (total exposure 107731 kg x day); The superimposed curves represent the cosinus function behaviors expected for a WIMP signal with a period equal to 1 year and phase exactly at 2nd June.

to exclude neutralino masses higher than 100 GeV. Concerning cosmic positrons, data obtained by the High-Energy Antimatter Telescope (HEAT) suggest a slight flux excess above 5 GeV. It was shown that such an excess cannot be explained by annihilation of dark matter particles, unless a substantial number of substructures are present in the galactic halo at a rather unlikely amount. So far, none of these results yields consistent conclusions.

It is also speculated that decaying or annihilating Light Dark Matter (LDM) particles could explain the flux and extension of the 511 keV line extended emission detected by INTEGRAL in the galactic center direction (see [133] for a recent discussion). Enough statistical evidence puts tight constraints on the shape of the dark matter halo of our galaxy, if the galactic positrons originate from dark matter. For annihilating candidates, the best fit to the observed 511 keV emission is provided by a radial density profile with inner logarithmic slope  $\gamma=1.03\pm 0.04$ .

Energetic  $\gamma$ -rays are also produced during the neutralino annihilation processes. Since this is

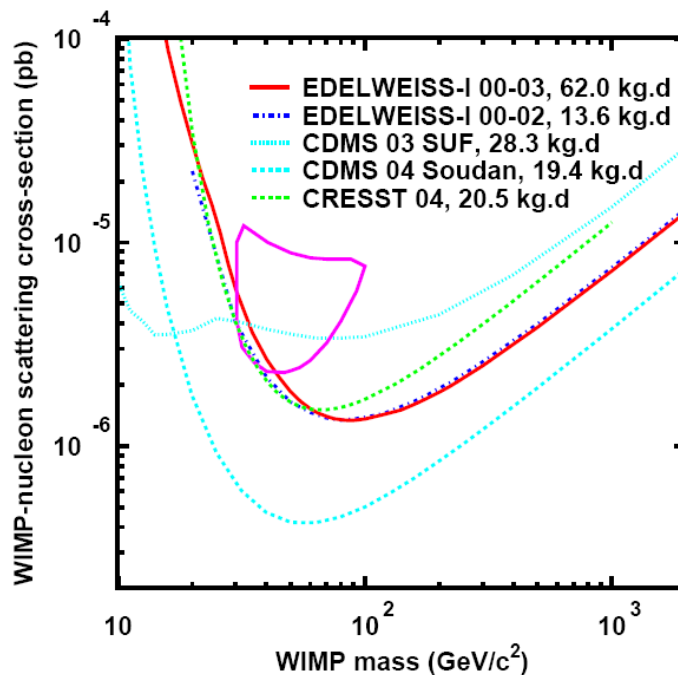


Figure 3.4: 90 % C.L. spin independent WIMP-nucleon cross section limits obtained by different WIMP Direct Detection experiments. Closed contour shows the allowed region at 3 C.L. from the DAMA 1-4 annual modulation data.

one of the most interesting possibilities for indirect detection of supersymmetric matter, we will describe this aspect in some more detail in the next section.

### 3.7 $\gamma$ -rays from Dark Matter halos

The  $\gamma$ -ray research from neutralino annihilations in the heart of galaxies (where the concentration of dark matter is higher) is considered to be very promising. From one side, it allows to check for emission created even outside our galaxy, as the  $\gamma$ -rays are not deflected by magnetic fields. As  $\gamma$ -rays point to the DM dominated regions, they should act as tracers of the dark matter density (neutrinos do as well). For very distant sources, the  $\gamma$ -rays should contribute to the measured diffuse galactic and extragalactic background  $\gamma$ -ray emission. The formidable development of the techniques involved in  $\gamma$ -ray astronomy favor the indirect detection in the  $\gamma$ -ray channel.

There are two possible types of gamma rays that can be produced in the annihilation. First, gamma-ray lines can be generated from processes like  $\chi\chi \rightarrow \gamma\gamma$ , where the photon energy is  $\sim m_\chi$ , and  $\chi\chi \rightarrow Z^0\gamma$ , where the photon energy satisfies  $E_\gamma = (4m_\chi^2 - M_Z^2)/4m_\chi$ . This signal would be very clear since the photons are basically mono-energetic (the so-called *smoking gun* signature). Unfortunately, the neutralino does not couple directly to the photon, and these Feynmann diagrams are loop suppressed, and therefore the expected flux is be small<sup>7</sup>. On the other hand,  $\gamma$ -rays produced by the decay of neutral pions ( $\pi^0$ s) formed in the hadronization processes yields a larger flux of continuum  $\gamma$ -rays. We focus this study on the dominant continuum contribution.

<sup>7</sup>In addition, the expected energy resolution of the  $\gamma$ -ray detector should be good enough to resolve these mono-energetic lines.

### 3.7.1 Dark matter halo $\gamma$ -ray emissivity

To evaluate the  $\gamma$ -ray emissivity of a dark matter region, both the properties of the DM halo and of the neutralino have to be taken into account. If we consider a spherical dark matter halo, the distribution function of neutralinos in the halo can be determined by the form  $f(r, \vec{v})$ , where  $r$  is the distance to the center of the halo, and  $\vec{v}$  the velocity of the particle. Under the hypothesis that the velocity distribution is homogeneous and isotropic, one can decouple the velocity distribution from the spatial distribution. Hence, the spatial distribution of the neutralino can be written as  $\rho_\chi(r)/m_\chi$  (i.e. as a function of the dark matter density profile), and the expression of emitted  $\gamma$ -ray flux for the considered halo per solid angle  $d\Omega$  can be derived:

$$\frac{dN_\gamma}{dS dt d\Omega}(E > E_0) = \frac{1}{4\pi} \frac{\sum_i N_\gamma^i \cdot BR_i \langle \sigma v \rangle_{ann}}{2m_\chi^2} \cdot \int_{\text{los}} \rho_\chi^2[r(s)] ds \quad (3.5)$$

The  $\gamma$ -ray flux is generated by the contribution of all final states  $i$  that produce  $N_i$  photons with energy above  $E_0$ . The term  $\langle \sigma v \rangle_{ann}$  indicates the thermally averaged annihilation cross-section (proper branching ratios  $BR_i$  per channel are considered),  $m_\chi$  the neutralino mass, and  $\rho_\chi(r)$  the dark matter density profile of the considered halo<sup>8</sup>.

Basically, the prediction of continuum  $\gamma$ -ray fluxes require *two independent inputs*: that coming from **particle physics** for issues such as the interaction cross section and the number of photons per neutralino annihilation (what we call  $f_{SUSY}$ ), and the input from **astrophysics** for problems such as the spatial distribution of dark matter in potential sources (the l.o.s integral, so-called  $J$ ).

Equation 3.5 may incorrectly suggest that the bigger the cross section the higher the expected  $\gamma$ -ray flux. This is correct if we think on a dark matter halo populated by such neutralinos. But, one has to take into account the cosmological history of these neutralinos. As the mass density  $\rho_\chi \sim 1/\langle \sigma v \rangle_{ann}$  (equation 3.4), the flux goes as:

$$\frac{dN_\gamma}{dS dt d\Omega} \propto \frac{1}{\langle \sigma v \rangle_{ann}} \quad (3.6)$$

hence, there exist a balance between the flux and the relic density of neutralinos: bigger annihilation cross sections results in small universe dark matter densities (and low fluxes), while small cross sections results on higher fluxes but in an overestimation of the relic density.

### 3.7.2 $\gamma$ -ray flux from dark matter halo arriving to earth

The expected annihilation  $\gamma$ -ray flux, as measured by an instrument (an IACT or a satellite), above an energy  $E_0$  arriving to the Earth from a given dark matter halo is:

$$\int d\Omega \int \frac{dN_\gamma}{dS dt d\Omega} dE \equiv \Phi_\gamma(\Psi, E > E_0) = f_{SUSY} \cdot J(\Psi, \theta) \quad (3.7)$$

where,

$$f_{SUSY} = \frac{1}{4\pi} \frac{\sum_i N_\gamma^i \cdot BR_i \langle \sigma v \rangle_{ann}}{2m_\chi^2} \quad (3.8)$$

and the number of gammas is integrated above  $E_0$ , and

$$J(\Psi, \theta) = \int_{\Delta\Omega} B(\Omega) d\Omega \int_{\text{los}} \rho_\chi^2[r(s)] ds \quad (3.9)$$

---

<sup>8</sup>If take into account the halo substructures, the l.o.s integral is evaluated with the halo density profile and multiplied by an enhancement factor. This accounts for the annihilations that occurs in dark matter clumps located within the l.o.s.

The line-of-sight integral is evaluated given an instrument angular solid angle  $\Delta\Omega(\Psi, \theta)$ , for an observation pointing in the direction  $\Psi$  for an angular resolution of the detector  $\theta$ . This integral is usually called  $J(\Psi, \theta)$ , and is normally averaged with the instrument angular resolution  $\Delta\Omega$  and expressed as:

$$\langle J \rangle_{\Delta\Omega} \equiv \langle J(\Psi, \theta) \rangle_{\Delta\Omega} = \frac{1}{\Delta\Omega} J(\Psi, \theta) \quad (3.10)$$

The term  $B(\Omega)d\Omega$  accounts for the Gaussian beam of the telescope:

$$B(\Omega)d\Omega = \exp\left[-\frac{\theta^2}{2\sigma_t^2}\right] \sin\theta d\theta d\varphi \quad (3.11)$$

The angles  $\theta$  and  $\varphi$  are related with the direction of observation  $\Psi_0$  and the line-of-sight angle  $\Psi$  by  $\cos\Psi = \cos\Psi_0 \cos\theta + \sin\Psi_0 \sin\theta \cos\varphi$ , and  $\sigma_t$  is the PSF of the detector.

Equation 3.7 is used to evaluate the emission from our galaxy, and in general for any external galaxy or dark matter subhalo. The general expression to evaluate l.o.s. integral is given by<sup>9</sup>:

$$J(\Psi, \theta) = \int_{\Delta\Omega(\Psi, \theta)} B(\Omega')d\Omega' \int_{\text{l.o.s.}} \rho_\chi^2[r(\lambda, \Psi')]d\lambda(r, \Psi') \quad (3.12)$$

where  $r$  is the galactocentric distance, related to the distance  $\lambda$  to the Earth by:

$$r = \sqrt{\lambda^2 + R^2 - 2\lambda R \cos\Psi} \quad (3.13)$$

To evaluate the integral for the Milky Way halo  $R=R_\odot$  (distance of the sun from the galactic center). For a distant galaxy or DM subhalo,  $R=D$  (distance from the Earth to the center of the galaxy or DM subhalo).

### 3.8 SUSY flux component: expected $f_{SUSY}$

In this analysis, the expected  $f_{SUSY}$  parameter is evaluated in the mSUGRA context. This scenario has to be taken as a 'representative' scenario. Many other scenarios are found in literature, leading to different evaluations of  $f_{SUSY}$ , but the essence of the results does not change significantly.

The mSUGRA framework considered assumes universality at the grand unification (GUT) scale, both in the gaugino and the scalar sector of the theory. The mSUGRA scenario is then fully defined, by only four parameters and one sign. The appropriate set of renormalization group equations (RGEs) allows to relate univocally the GUT scale structure to the low energy (weak scale) spectrum of the theory. Here, soft breaking parameters, gauge and Yukawa couplings are evolved down to the weak scale with the ISASUGRA RGE code as given in version 7.67 of the ISAJET software package [134], interfaced within the DarkSUSY package [135].

The mSUGRA setup is probably the most popular framework for studying supersymmetric (SUSY) extensions of the Standard Model, and its rather constrained low energy structure has been extensively discussed. Here we review the results for a deep scan on the mSUGRA scenario and focus on those features which will be relevant in our discussion of the detection prospects for SUSY dark matter.

---

<sup>9</sup>This integral on the l.o.s has been often approximated in literature for distant dark matter objects located at a distance  $D$ . These approximations gives wrong results (overestimation of the flux) when applied to nearby dark matter subhalos (<50kpc, even 1 order of magnitude), but it is a good approximation for very distant halos.

### 3.8.1 Phenomenological constraints

The mSUGRA models which are considered here confront current accelerator and cosmological constraints, that give rise to important constraints on the SUSY parameter space.

The following phenomenological constraints are applied (see [135] and references therein):

- **Unphysical models:** The presence of non-zero trilinear couplings could give rise to tachyonic sfermions. We exclude all such unphysical models.
- **Neutralino LSP:** The DM candidate is the neutralino (LSP) of the sparticle spectra: electrically neutral, stable, and not strongly interacting. In particular corners of the mSUGRA parameter space, other sparticles turn to be the LSP (in particular the stau,  $\tilde{\tau}_1$ ), but they are not suitable dark matter candidates. These models (or mSUGRA regions) are excluded.
- $b \rightarrow s\gamma$ : In SUSY models with minimal flavor violation the decay  $b \rightarrow s\gamma$  proceeds through the  $\tilde{t}\tilde{W}$  and  $tH^+$  loops, in addition to the SM contribution from the  $tW$  loop. The branching fraction  $BF(b \rightarrow s\gamma)$  has been measured by the BELLE, ALEPH, and CLEO collaborations. A weighted averaging of these measurements of  $B \rightarrow X_s\gamma$  decays at CLEO and BELLE lead to bounds on the branching ratio of  $b \rightarrow s\gamma$ . The allowed range of branching ratios is  $2.0 \cdot 10^{-4} \leq \text{BR}[b \rightarrow s\gamma] \leq 4.6 \cdot 10^{-4}$ .

In DarkSUSY, the calculation of  $\text{BR}(b \rightarrow s\gamma)$  includes the complete next-to-leading order (NLO) correction for the SM contribution and the dominant NLO corrections for the SUSY term.

- $g_\mu - 2$ : The anomalous magnetic moment of the muon  $a_\mu = (g_\mu - 2)/2$ , is sensitive to new physics, such as SUSY. The experimental measurement has improved greatly in recent years, and there is a hint of a discrepancy with the Standard Model, though the theoretical calculations of the Standard Model hadronic contribution are somewhat in doubt. Based on the analysis in, the discrepancy is of about  $-5 \cdot 10^{-10} < a_{exp} - a_{SM} < 47 \cdot 10^{-10}$  [2 $\sigma$ ]. The SM prediction depends on experimentally measured quantities that can be obtained from  $\tau$  decay or  $e + e^-$  annihilation data. As these two methods give different results, to be conservative, the most lower and upper limit derived have to be considered. With this broad range of allowed values, it turns out that the  $(g_\mu - 2)$  does not place any tight constraints for  $\mu > 0$ , while almost rules out the  $\mu < 0$ . Of astrophysical interest, only neutralinos for models with  $\mu > 0$  will be considered.
- **Direct accelerator searches:** We also take into account the limits derived from the unsuccessful searches for sparticles and the Higgs boson, at the LEP2 collider and others. In Table 3.2 we detail the lower mass limits imposed on some particles<sup>10</sup>.
- **Relic density:** Finally, we require that the neutralino relic density lies below the cosmological estimated upper bound:  $\Omega_{dm}h^2 \leq 0.13$ . The allowed lower bound ( $\Omega_{dm}h^2 \geq 0.09$ ) is not imposed since it may well be that neutralinos are only a subdominant dark matter component.

### 3.8.2 Scanning the mSUGRA parameter space

To scan the mSUGRA parameter space for models that yields suitable LSP consistent with all bounds we use DarkSUSY [135], a publicly-available advanced numerical package for neutralino dark

<sup>10</sup>DarkSUSY version 4.1 we used the values from the PDG2002. We updated these values to the ones quoted in PDG2004 (<http://pdg.lbl.gov/>).

Particle	Mass Limit [GeV/c <sup>2</sup> ]	Particle	Mass Limit [GeV/c <sup>2</sup> ]
Charginos	103.5	sneutrinos	43.7
charged sleptons	81.9 – 95.0	sbottoms	95.7
stops	89.0	other squarks	99.5
gluino	195.0	Higgs boson	114.1
Pseudoscalar Higgs boson	78.6	LSP Neutralino	37.0

Table 3.2: Mass limits from particle accelerator searches.

matter calculations. The evaluation of the neutralino relic density includes all possible sfermions, neutralino and chargino coannihilations and applies the state of the art technique to trace the freeze-out of a species in the early Universe. The density evolution equation (which determines the evolution of the number density of neutralinos) is solved numerically, including all possible resonance and threshold effects, and avoiding approximations in the thermally averaged cross sections. This tool computes the neutralino relic abundances with an estimated precision of 1% or better. Masses and mixings of supersymmetric particles are computed with the help of external programs such as FeynHiggs and ISASUGRA<sup>11</sup>.

In order to scan the mSUGRA parameter space, about  $10^6$  random models were produced in the GUT parameter intervals:

$$0 < m_{1/2} < 5 \text{ TeV} \quad (3.14)$$

$$0 < m_0 < 10 \text{ TeV} \quad (3.15)$$

$$3 < \tan \beta < 52 \quad (3.16)$$

$$-10 < A_0 < 10 \text{ TeV} \quad (3.17)$$

$$\mu > 0 \quad (3.18)$$

Out of the  $10^6$  input models, about 18% are declared unphysical (i.e. the charged stau is the LSP or tachyonic sfermions are obtained), 6% of models are excluded by the accelerator constrains (mainly Higgs mass bounds for  $\tan \beta < 5$  and  $\text{BR}(b \rightarrow s\gamma)$  for  $\tan \beta > 50$ ),  $\sim 1.8\%$  of models have values of  $\Omega_{dm} h^2 < 0.13$  (we will refer to them as *Viable models*), and only 0.25% of models are consistent to the cosmological  $\Omega_{dm} h^2$  bounds (we will refer to them as *WMAP models*).

It is worth to mention the most relevant regions of the mSUGRA scan that renders interesting phenomenological regions. These are<sup>12</sup>:

- **Bulk region:** For small values of  $m_0$  and  $m_{1/2}$  the relic density of pure bino-like neutralinos is set by their annihilation strength into fermions mediated by sfermion. This region is almost excluded by accelerator bounds. In Figure 3.7, this corresponds to models located at the lowest  $m_\chi$  with  $\langle \sigma v \rangle$  from  $10^{-28}$  to  $10^{-26} \text{ cm}^3 \text{ s}^{-1}$ .
- **Coannihilations effects:** neutralino typically produces a relic abundance much larger than the WMAP bounds<sup>13</sup>, but peculiar mechanisms suppress the relic density: coannihilation

<sup>11</sup>In addition, we developed a link between DarkSUSY and other programs like SUSPECT [136] and SOFTSUSY [137] to crosscheck the obtained results with different Monte Carlo tools. As the results do not change quantitatively (only for large  $\tan \beta$ ), we show only the results of the scans made with ISASUGRA. We kindly provided these link programs (interfaces), scripts, and the necessary help to the authors of the work which was published in [138].

<sup>12</sup>Extense details can be found elsewhere, e.g. [139].

<sup>13</sup>This depends on the LSP nature: for example, bino-like neutralinos annihilation cross sections are by far smaller compared to wino or higgsino neutralinos.

processes when the next-to-LSP particles are close in mass to the LSP. In such a case, the evolution of particles are tightly correlated and the interactions of the LSP with the NLSPs reduces the  $\chi^0$  number density.

- *Coannihilations with sleptons:* For  $m_0 < m_{1/2}$  and moderate values of  $m_{1/2}$ , the relic density suppression is dominated by coannihilations with  $\tilde{\tau}_1$ , as well with lightest  $\tilde{e}_1$  and  $\tilde{\mu}_1$  (this happens nearby the mSUGRA region in which the lightest stau,  $\tilde{\tau}_1$ , is the LSP). In Figure 3.7, this corresponds to models located at  $m_\chi > 100$  GeV with  $\langle\sigma v\rangle$  spanning from  $10^{-29}$  to  $3 \cdot 10^{-26}$   $\text{cm}^3\text{s}^{-1}$ .
- *Coannihilations with chargino and NLSP-neutralino:* In the regime  $m_0 \gg m_{1/2}$ , a high Higgsino fraction give raise to chargino and NLSP-neutralino coannihilation processes (this is nearby the excluded region due to no radiative electro-weak symmetry breaking). In Figure 3.7, this roughly yields models located at  $m_\chi > 100$  GeV<sup>14</sup> with the highest  $\langle\sigma v\rangle$ , from  $3 \cdot 10^{-26}$  up to  $3 \cdot 10^{-25}$   $\text{cm}^3\text{s}^{-1}$ .
- *Coannihilations with stop:* For large scalar trilinear coupling, it might be that the NLSP is the stop. This happens at intermediate values of  $m_0$  and  $m_{1/2}$ , yielding intermediate massive neutralinos with  $\langle\sigma v\rangle \sim 10^{-27}$  to  $10^{-28}$   $\text{cm}^3\text{s}^{-1}$ .
- **A-exchange resonance:** also called the *funnel region*. For large  $\tan\beta$ , one hits the region where neutralino mass is close to the half of the CP-odd  $A$  and/or CP-even  $H$  Higgs bosons masses. Then, the pair annihilation of neutralinos proceeds via the s-channel resonance through  $A$  and/or  $H$ . This reduces the relic abundance calculation very efficiently.
- *Varying  $A_0$ :* Historically, the trilinear couplings were set to 0. This is not justified by any theoretical argument, but simplicity. Varying  $A_0$ , the sfermion masses do change, and the annihilation cross-section varies as well. This affects the relic abundance calculation [138].

### 3.8.3 Evaluation of $f_{SUSY}$ in mSUGRA

Here we illustrate the expected variations of  $f_{SUSY}$  for the surviving models in this mSUGRA scan. Figure 3.7(left) shows the result of the scan in a  $\langle\sigma v\rangle$  vs.  $m_\chi$  plane, which covers the relevant regimes in mSUGRA parameter space. All models within WMAP allowed relic densities leads to  $\tilde{\chi}_1^0$  masses from 70 GeV up to 1400 GeV, approximately. The  $\langle\sigma v\rangle$  lies in the range  $1 \cdot 10^{-29}$  to  $3 \cdot 10^{-26}$   $\text{cm}^3\text{s}^{-1}$ . Note that for the *Viable models* the neutralino mass can extend up to 2 TeV, while the  $\langle\sigma v\rangle$  can increase by one order of magnitude, in the region  $100 < m_\chi < 200$  GeV/ $c^2$ .

In order to compute the expected  $f_{SUSY}$  we do need to evaluate the integral photon yield above a certain energy  $E_0$ . The parameterization for the continuum  $\gamma$ -ray spectrum depends on the nature of the SUSY particle and cannot be given in general: it can vary depending on the annihilation mode considered. In Figure 3.5, we show the photon yield for various annihilation channels. In most cases ( $b\bar{b}$ ,  $t\bar{t}$ ,  $W^+W^-$ , etc.), the spectrum produced does not vary much. The exception to this is the somewhat harder spectrum generated through annihilations to  $\tau^+\tau^-$ . Particle physics models very rarely predict a dark matter candidate that annihilates mostly to  $\tau^+\tau^-$ , however. Neutralinos, for example, generally annihilate through this channel only a few percent of the time or less, although carefully selected model parameters can allow for this to be exceeded. We will assume throughout our study that the continuum  $\gamma$ -ray emission from dark matter annihilation resembles the spectrum shown in Figure 3.5 for heavy quarks or gauge bosons, etc., rather than  $\tau^+\tau^-$ .

<sup>14</sup>These higgsino-like neutralinos are very massive, if consistent to WMAP bounds ( $m \sim 1$  TeV).

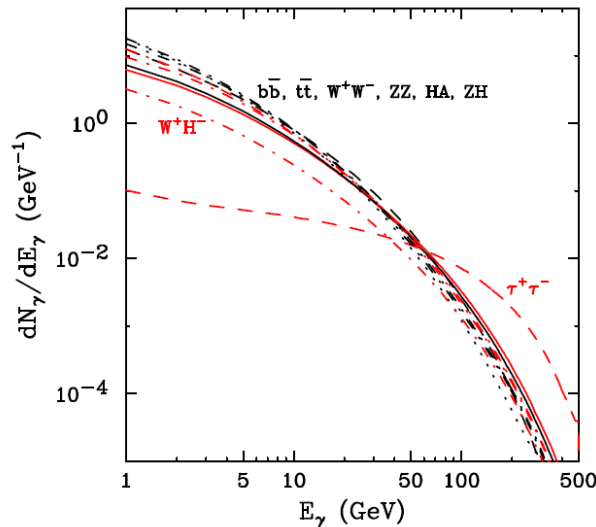


Figure 3.5: The gamma-ray spectrum (per annihilation) generated through dark matter annihilations for a variety of channels. A 500 GeV dark matter mass has been used. Figure taken from [140]

In this case, the differential photon yield per neutralino annihilation can be reasonably parameterized as:

$$\frac{dN_\gamma}{dx} = \frac{0.73}{m_\chi} \cdot \frac{e^{-7.76x}}{x^{1.5}} \quad (3.19)$$

where  $x = E_0/m_\chi$ , and  $m_\chi$  is the neutralino mass. This expression is quite accurate for neutralinos in which the dominant annihilation channels are  $W^+W^-$ ,  $Z^0Z^0$  and  $q\bar{q}$ . The use of more exact PYTHIA fragmentation Monte Carlo yields more accurate results, but variations of a few decens percent level do not change the outcome of the results on  $f_{SUSY}$  parameter substantially. Figure 3.19 shows the integral photon yield per neutralino annihilation calculated with the PYTHIA Monte Carlo and with the use of Equation 3.6, for several mSUGRA models. Differences of about 10–20% are visible.

On the other hand, to be strict, in SUSY extensions of the SM the hierarchy problem is stabilized only when the scale of superpartner masses is roughly of the order of the EW scale. The derived sparticle masses should in principle not violate the naturalness of the SUSY theory if they are not very massive. In particular, the choice of the GUT parameters has important consequences on the naturalness of the SUSY framework. Although this depends on the taste of the theorist, we display all models in Figure 3.7(left), but differentiating those with  $m_{1/2} > 2$  TeV, in which large fine-tuning starts to be present, according to [142]<sup>15</sup>. These models have to be considered as the extreme or non-natural models.

We also compute the  $f_{SUSY}/10^{-32}$  dependence with the  $E_{thr}$  of the detector. For a given  $E_{thr}$ , the shadow region of Figure 3.7(right) displays the results of the scan of all the  $m_\chi$ ,  $\langle\sigma v\rangle$  and  $N_\gamma$  intervals accessible beyond the  $E_{thr}$ , for the WMAP and Viable mSUGRA models (it does not display any statistical region, only the allowed). This curve reflects the allowed  $f_{SUSY}$  region for

<sup>15</sup>If multi-TeV parameters are set in the scan, neutralino with masses of about 15 TeV can arise, for values of  $m_0$  and  $m_{1/2} \sim 50$  TeV. The neutralino is the LSP, meaning that the rest of sparticles would have masses  $>15$  TeV. This result is not natural in the SUSY scheme.

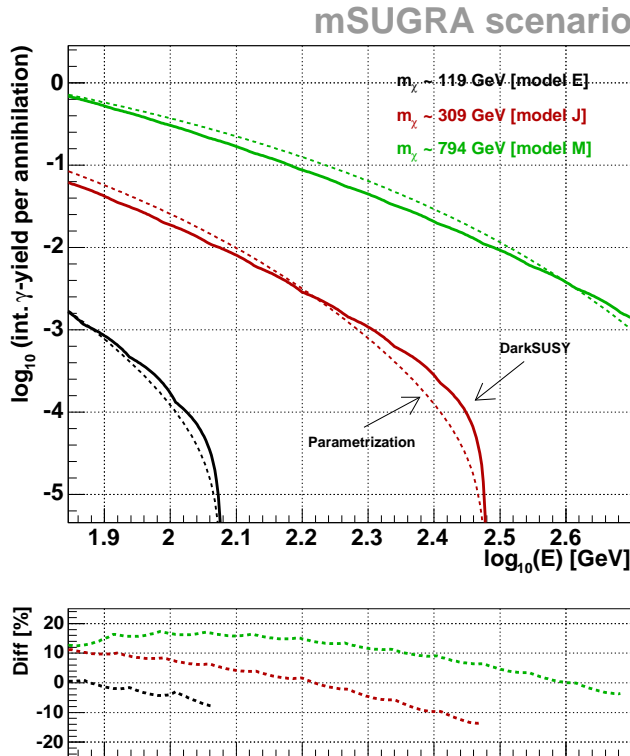


Figure 3.6: Integral  $\gamma$ -ray yield  $N_{\gamma}(E>E_0)$  per  $\chi$ -annihilation for several neutralinos produced in the mSUGRA model. In particular, they correspond to different SUSY benchmark points defined in [141]. The solid line is the result obtained with DarkSUSY, while the dashed line corresponds to the parameterization given in Equation 3.19.

a neutralino to be detected with an IACT<sup>16</sup>. The expectation for a detection spans 4–6 orders of magnitude: this directly affects the expected  $\gamma$ -ray flux from neutralino annihilations, for all survival models. Note that for high  $m_{\chi}$ , the spread in the  $f_{SUSY}$  is reduced, as we enter into a narrow band of allowed models in  $\langle\sigma v\rangle$  (the so-called *Focus point region*).

### 3.8.4 Evaluation of $f_{SUSY}$ in non-constrained MSSM

A complete analysis of all different SUSY scenarios is well above the scope of this phenomenological exercise. The results can be left as a function of the factor  $f_{SUSY}$ , as other SUSY scenarios may give different results on the factor  $f_{SUSY}$  and upper  $\tilde{\chi}^0$  mass limits.

Here we consider quite interesting the statistical study made in [143], in which SUSY dark matter is studied in the general flavor diagonal MSSM by means of an extensive random scan of its parameter space, but at the EW scale. In contrast with the standard mSUGRA lore, the large majority of viable models features either a higgsino or a wino-like lightest neutralino, and yields a relic abundance well below the WMAP bound. Among the models with neutralino relic density within the WMAP range, higgsino-like neutralinos are still dominant, though a sizeable fraction of bins is also present.

<sup>16</sup>To be exact, for a given  $E_{\text{thr}}$  we consider the  $m_{\chi} \geq E_{\text{thr}} + 50 \text{ GeV}$ , i.e., for a given threshold we should have a minimum quantity of signal (flux) to be detected (the spectra should extend at least 50 GeV from the threshold, to allow for signal reconstruction).

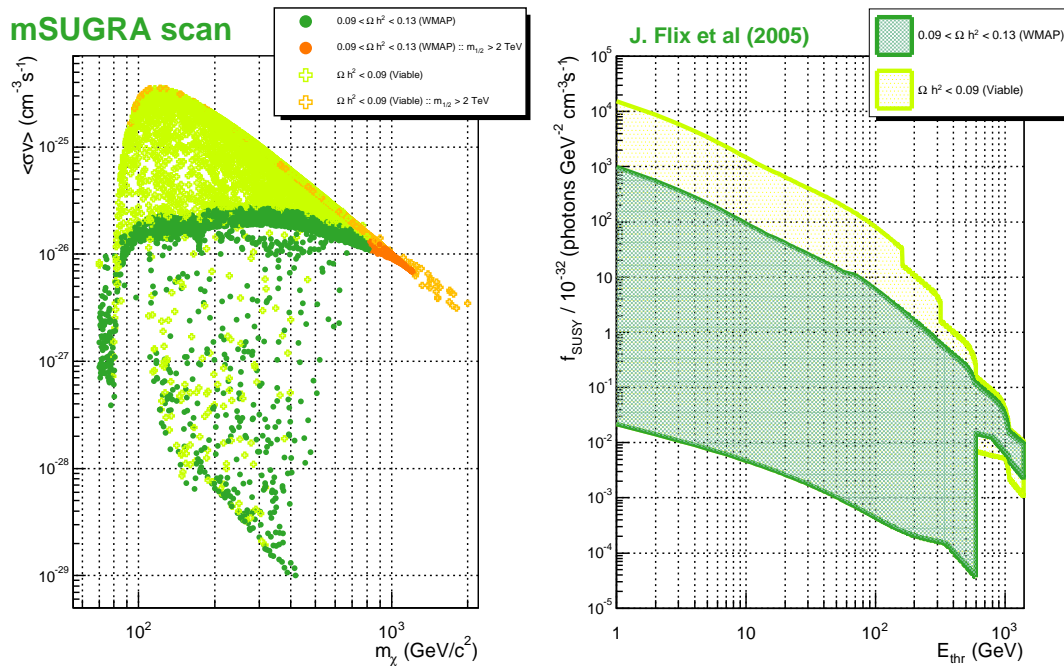


Figure 3.7: Allowed  $\tilde{\chi}_1^0$  masses, cross sections, and  $f_{\text{SUSY}}$  parameter for the mSUGRA scan. See text for details.

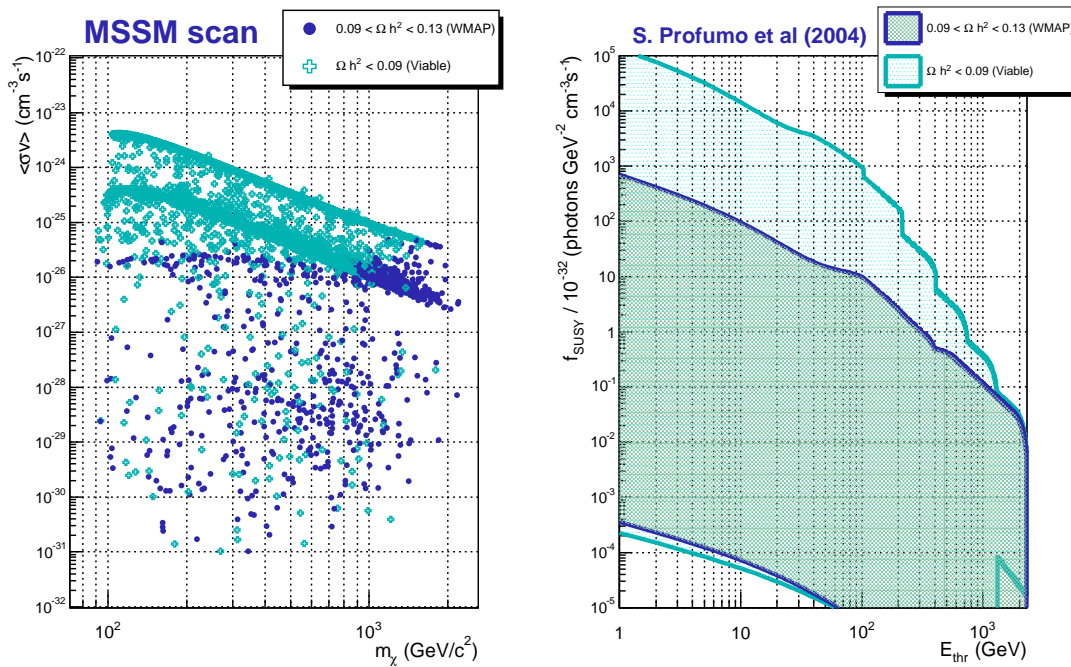


Figure 3.8: Allowed  $\tilde{\chi}_1^0$  masses, cross sections, and  $f_{\text{SUSY}}$  parameter for the MSSM scan. See text for details.

The result of the 20-dimensional parameter space scan at the EW scale using a uniform probability distribution is shown in Figure 3.8<sup>17</sup>. Here,  $\tan\beta$  takes values between 2 and 50, whereas all mass parameters are generated in the interval (50 GeV, 5 TeV). The authors claim that this scan covers what can be considered a natural MSSM parameter space range, and that it is largely free of theoretical prejudices. From this set of low energy parameters, the mass spectra and mixing matrices of the superparticles are evaluated.

In this non-constrained scenario, the  $f_{SUSY}$  variations are bigger: about 6–8 orders of magnitude. This is driven almost by the presence of bino-like neutralinos. The explanation is simple: in mSUGRA one has gaugino mass unification,  $M_2 \simeq 2 \cdot M_1$ , and all wino-like phenomenology (that happens for models with  $M_2 < M_1$ ) is lost. Since Wino-like neutralinos efficiently annihilate into gauge bosons, and since they have a larger coupling than higgsinos, they also represent (as well as the higgsino-like  $\tilde{\chi}^0$ ) the neutralino-type which gives the larger  $\langle\sigma v\rangle$  values, up to  $3 \cdot 10^{-24} \text{ cm}^3\text{s}^{-1}$ , and higher  $\gamma$ -ray fluxes<sup>18</sup>. These models can be easily indentified in Figure 3.8(left).

This MSSM scan is a nice example of how dealing with mSUGRA cuts out a lot of phenomenologically interesting MSSM parameter space. Wino-like  $\tilde{\chi}$  are found in other ordinary and well-motivated SUSY-breaking scenarios, like the minimal anomaly mediated SUSY breaking.

---

<sup>17</sup>The authors kindly provided us the values to produce this Figure, which is not shown in their article.

<sup>18</sup>S. Profumo, priv. communication.



## Chapter 4

# Indirect dark matter detection in $\gamma$ -ray astronomy: MAGIC search strategies

*This section describes halo models and the expected high energy  $\gamma$ -ray fluxes from  $\chi$  annihilations in the densest and nearby dark matter (DM) regions. In particular, we focus on the study of the center of the Milky Way (accounting for an important DM enhancement effect, previously neglected), Draco (the most DM dominated dwarf spheroidal), and the nearby M31 galaxy. We make use of several models of the DM distribution to derive the expected fluxes, and the strategy for indirect DM searches with the use of the MAGIC telescope.*

*This Chapter is partially based on the papers F. Prada, A. Klypin, J. Flix et al (2004) [77] and J. Flix (2005) [120].*

### 4.1 Introduction

In the previous Chapter we have indicated that the foremost candidate for the CDM composing dark matter halos is considered to be the neutralino LSP, and we have studied in detail their self-annihilation properties. The neutralino pair annihilation may lead to important observable consequences, in particular the emission of high energy  $\gamma$ -radiation in dense DM regions. It is of clear importance to identify and model the DM distribution in such places, as it constitutes the input to compute the expected annihilation signal.

Regardless of the neutralino particle properties, we have argued that the annihilation rate is proportional to the square of its density. The annihilation signal is expected to be enhanced in the densest DM regions, like the center of galaxies, center of galaxy clusters, the center of DM substructures predicted within a galaxy halo, or the center of DM dominated observed galaxy satellites, like dwarf spheroidal galaxy companions. The possibility that such  $\gamma$ -rays may be detected by IACTs, like MAGIC, HESS, or VERITAS, or by satellite-borne detectors, like GLAST, has generated considerable interest.

We are interested in performing detailed studies for the MAGIC telescope. MAGIC is located in the northern hemisphere and the best targets that we have considered are: the center of the Milky Way, the most DM dominated dwarf spheroidal galaxy, Draco<sup>1</sup>, and the nearby M31 galaxy.

---

<sup>1</sup>Canis Major dwarf and Sagittarius dwarf are not considered in this study, as they are believed to be highly affected by tidal effects. This introduces large uncertainties when modeling the DM distribution present in these dwarfs.

The central regions of DM halos are far from being well determined. This leads to uncertainties in the calculation of the expected fluxes, which may span several orders of magnitude. We consider a wide variety of models in order to estimate, in a realistic way, which are the present uncertainties that affect these objects and which are the observational consequences. The expected fluxes are derived, focusing in the capabilities of the MAGIC telescope to search for DM annihilation  $\gamma$ -rays.

## 4.2 Modeling a DM halo

The modeling of the DM density profile in the innermost region of a DM halo is still an open question. The modeling can be addressed through N-body simulations, up to a certain radius scale resolution. The innermost region of the profile is just extrapolated. As expected, several simulations yield different results in the central halo regions: a cuspy DM halo  $\rho_{dm}(r) \propto r^{-\alpha}$  is normally predicted with  $\alpha = 1-1.5$ . In addition, recent numerical models indicate that the central slope might be shallower than  $\alpha = 1$ , but no real high resolution simulation actually has shown any core [70, 75, 76].

Some theoretical arguments seem to favor cusps [144, 145] but make only vague predictions about the inner slopes. A recent model combines simulation results and analytical arguments to predict an inner slope of -1.27 [146].

On the other hand,  $\alpha$  can be indirectly determined from observations. Different techniques yield different results: the halos are estimated to be cored-type ( $\alpha \rightarrow 0$ ) or cusped ( $\alpha \geq 1$ ).

A recent review for the cusp topic can be found in [79].

### 4.2.1 Estimating the $\alpha$ parameter: N-body simulations

The different  $\alpha$  values estimated from N-body simulations prefer cuspy DM halos ( $\alpha \geq 1$ ):

- Historically, two values of  $\alpha$  have been widely considered:  $\alpha=1$  (NFW model [68]) and  $\alpha=1.5$  (Moore et al. model [69]). Moore et al. DM density profile is now considered as an unrealistic upper limit, in light of recent high-resolution simulations, that point to  $\alpha \rightarrow 1.16$  [70]. In addition, extrapolations that result on cored profiles are also discussed in the literature, although no high-simulation has ever shown a core. All these results are obtained from simulations in which baryons are not taken into account: the DM halos are populated exclusively with DM non-interacting particles.
- If the innermost region of a galaxy is dominated by baryons, due to baryonic infall during galaxy formation, **adiabatic compression of DM** is expected. This results in an enhancement of DM at the center of the halo, resulting in a cuspy DM density profile  $\alpha=1.45$ . This effect was usually ignored. We made use of detailed Milky Way mass models to derive, for the first time, an adiabatic DM contracted profile [77], with a prescription tested in one of the first high-resolution numerical simulations that include the effect of baryons during the DM halo formation [147]. We explain the model in section 4.3.1.

### 4.2.2 Experimental constraints on the $\alpha$ parameter

Observations which should constrain the  $\alpha$  parameter do not give clear and definitive answers on its value. As a result, cuspy dark matter density profiles have been contested by some authors as being overly optimistic, due to some astrophysical evidences that the halo of the Milky Way and other galaxies is not cusped at all, but a number of works give in fact non-unique values for the inner  $\alpha$  slope (see [148] and references therein):

- Spatially resolved spectra of the diffuse hot (X-rays) gas of galaxies and clusters measured with the *Chandra* satellite were used to infer the radial mass distribution of the considered systems. An analysis done on 2 clusters reveal  $\alpha=1.25, 1.35$ . A value of  $\alpha < 1$  is found when disturbed X-ray surface brightness clusters are considered. Yet the X-ray method uses the double assumption of a single phase gas in hydrostatic equilibrium, which for instance is questionable in the central regions where rapid cooling occurs.
- Other studies of radial mass profiles inferred by the radial profile of the intracluster medium density and temperature measured with *Chandra* on 5 clusters gives  $1 < \alpha < 2$ .
- Using Low Surface Brightness (LSB) Galaxies rotation curves fits, a mean value  $\alpha=0.2$  is obtained, although tails in the distribution extend further, up to  $\alpha=2$ .
- Combination of strong-lensing data and spectroscopic measurements of stellar dynamics of the brightest cluster galaxies can be used to derive values of  $\alpha$ . The results on three clusters, containing both radial and tangential arcs, gives  $\alpha=0.52 \pm 0.3$ .
- Another study of high resolution  $H\alpha$  rotation curves for dwarf and LSB galaxies has been recently carried out. In that work it is shown that rotation curves data are insufficient to rule out halos with  $\alpha=1$ , although none of the galaxies require an inner cuspy profile instead of a core density feature. Results on  $\alpha$  range from 0 to 1.2, although the quality of the fit is good only up to  $\alpha=1$ . Other analysis on large sets of data of high-resolution rotation curves also show consistency with cored mass distributions.
- An indirect estimate of  $\alpha$  can be inferred through the weak gravitational lensing measurements of X-ray luminous clusters: one finds  $0.9 < \alpha < 1.6$ . From the high microlensing optical depth towards the Galactic Center (GC) a lower limit on the contribution from baryons to the rotation curve in the inner region ( $r < 8$  kpc) is derived. Assuming a spherically symmetric profile normalized to our position in the Milky Way,  $\alpha=0.4$ . A value of  $\alpha=1$  can be reached by considering a flattened halo with a ratio of polar to equatorial axis of 0.7.
- At the GC, the accretion flow onto the SMBH sustains strong magnetic fields that can induce synchrotron emission by  $e^\pm$  generated in  $\chi\chi$  annihilations. The measured radio emission is inconsistent with DM profile more spike than a NFW, although this value relies on the assumed magnetic field values.
- For the Milky Way, depending on the history of the central black hole, the DM density profile can be either cuspy or cored at the center of the galaxy. The Black Hole in the GC center was probably triggered by a major merger, in which the quasi-stationary conditions critical for the formation of a central spike may not have existed.

The predictions of CDM theories concerning halo structure seem to disagree in some cases with the observations and in other cases they seem to give coherent results. There is no direct evidence either for or against central cusps in the dark matter distribution in halos, and all these prescriptions should be taken with caution. It seems very prudent to use both cored and cusped halo models to estimate the range of the expected  $\gamma$ -ray annihilation signal for the considered objects.

### 4.3 The center of the Milky Way galaxy

During the past decade dissipationless cosmological simulations have shown that the density distribution within virialized halos of different masses can be approximately described by universal profiles: NFW-type ( $\alpha = 1$ ) and Moore-type ( $\alpha=1.5$ , recent estimations  $\alpha=1.16$ ).

Although non-baryonic dark matter exceeds baryonic matter by a factor of  $\Omega_{dm}/\Omega_b \sim 6$  on the average, the gravitational field in the central regions of galaxies is dominated by stars. In the hierarchical galaxy formation model the stars are formed in the condensations of cooling baryons in the halo center. As the baryons condense in the center, they pull the dark matter particles inward thereby increasing their density in the central region. The response of dark matter to baryonic infall has traditionally been ignored when computing the expected  $\gamma$ -rays from neutralino annihilations in the Galactic Center (GC). Here we present a modified adiabatic prescription and its application to the Milky Way galaxy [77].

### 4.3.1 Milky Way mass models with adiabatic compression

When normal gas ('baryons') loses its energy through radiative processes, it falls to the central region of the forming galaxy. As the result of this mass redistribution, the gravitational potential in the center changes substantially. The DM must react to this deeper potential by moving closer to the center and increasing its density. This increase in the DM density is often treated using adiabatic invariants. This is justified because there is a limit to the time-scale of changes in the mass distribution: changes of the potential at a given radius cannot happen faster than the dynamical time-scale defined by the mass inside the radius.

Adiabatic contraction of dark matter in a collapsing protogalaxy was used already in 1962 [149]. In 1980, Zeldovich et al. [150] used it to set constraints on properties of elementary particles (annihilating massive neutrinos). The present form of analytical approximation (circular orbits) was introduced in [13]. If  $M_{in}(r_{in})$  is the initial distribution of mass (the one predicted by cosmological simulations), then the final (after compression and formation of the galaxy) mass distribution is given by  $M_{fin}(r)r = M_{in}(r_{in})r_{in}$ , where  $M_{fin} = M_{DM} + M_{bar}$ . This approximation was tested in numerical simulations [147,151]. The approximation assumes that orbits are circular and, thus  $M(r)$  is the mass inside the orbit. This is not true for elongated orbits: the mass  $M(r)$  is smaller than the real mass, which a particle 'feels' when it travels along on elongated trajectory. This difference in masses requires a relatively small correction: the mass  $M$  should be replaced by the mass inside the time-averaged radius of trajectories passing through given radius  $r$ :  $M_{fin}(\langle r \rangle)r = M_{in}(\langle r_{in} \rangle)r_{in}$ .

We find the correction using Monte Carlo realizations of trajectories in the NFW equilibrium halo and finding the time-averaged radii  $\langle x \rangle \approx 1.72x^{0.82}/(1+5x)^{0.085}$ ,  $x \equiv r/r_s$ . This approximation predicts a factor of 2 smaller contraction in the central regions, where individual trajectories are very elongated. It gives better fits when compared with realistic cosmological simulations [147].

To make realistic predictions for annihilation rates occurring in the GC, we construct two detailed models of the MW Galaxy by redoing the full analysis of numerous observational data collected in [152]: a NFW and Moore et al. DM density profiles<sup>2</sup>. Both models are compatible with the available observational data for the MW and their main parameters are given in Table 4.1.

Models assume that without cooling the density of baryons is proportional to that of the DM and the final baryon distribution is constrained by the observational data. Figure 4.1 presents the distribution of mass and density in the models. While all observations were included, some of them are more important than others. The solar neighborhood is relatively well studied and, thus, provides important observational constraints. In Table 4.1 we present two local parameters: the total density of matter inside 1.1 kpc ( $\Sigma_{total}$ , obtained from kinematics of stars) and the surface density of gas and stellar components ( $\Sigma_{baryon}$ ). The circular velocity,  $V_{circ}$ , at 3 kpc distance from the center provides another crucial constraint on models as emphasized in [153]. It is difficult to estimate errors of this parameter because of the uncertain contribution of the galactic bar. We use  $\pm 5$ km/s error, which is realistic, but it can be even twice as large.

---

<sup>2</sup>Although, the Moore et al. profile is considered as unrealistic upper limit. Moore et al. private communication. At the time of our study, the newest Moore et al. results were not still published.

	Model A	Model B	Constr.
	NFW	Moore et al.	
Virial mass, $10^{12} M_{\odot}$	1.07	1.14	–
Virial radius, kpc	264	270	–
Halo concentration C	11	12	10.3-21.5 ( $1.5\sigma$ )
Disk mass, $10^{10} M_{\odot}$	3.7	4.0	–
Disk scale length, kpc	3.2	3.5	2.5-3.5
Bulge mass, $10^9 M_{\odot}$	8.0	8.0	–
Black Hole mass, $10^6 M_{\odot}$	2.6	2.6	2.6
$M(< 100\text{kpc})$ , $10^{11} M_{\odot}$	6.25	5.8	$7.5 \pm 2.5$
$\Sigma_{\text{total}}$ , $ z  < 1.1$ kpc at $R_{\odot}$ , $M_{\odot}\text{pc}^{-2}$	65	70	$71 \pm 6$
$\Sigma_{\text{baryon}}$ at $R_{\odot}$ , $M_{\odot}\text{pc}^{-2}$	47	53	$48 \pm 8$
$V_{\text{circ}}$ at 3 kpc, km/s	203	205	$200 \pm 5$

Table 4.1: Models and constraints for the Milky Way Galaxy

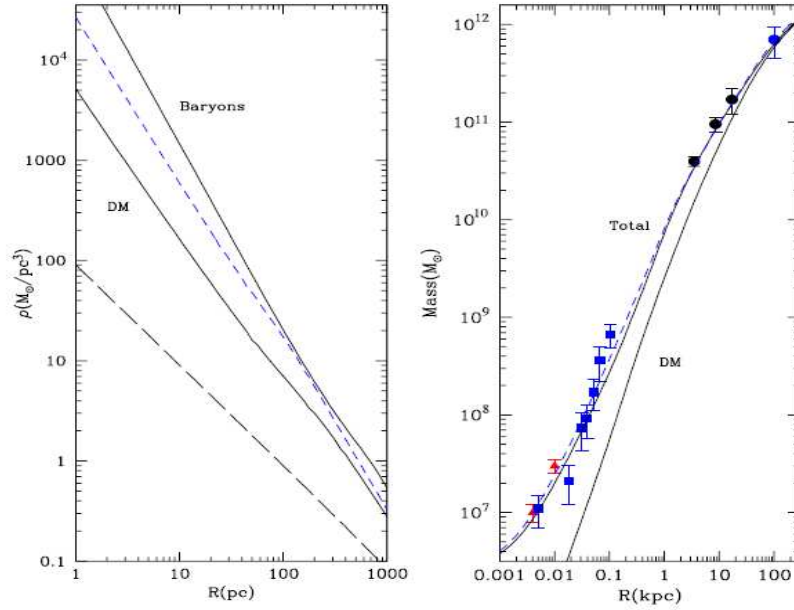


Figure 4.1: *Left*: the top curve is the density of baryons. The dashed and full curves 'DM' are for the compressed Moore et al. and NFW models. The long-dashed curve corresponds to the uncompressed NFW profile. *Right*: The solid and dashed curves are the total mass in compressed NFW and Moore et al. models. DM mass in the NFW model is the thick curve. Symbols displays observational constraints as taken from Klypin et al [152].

Probably the most debated constraint is coming from counts of microlensing events in the direction of the galactic bulge. Our models are expected to have the optical depth of microlensing events  $\tau = 1.2 - 1.6 \times 10^{-6}$  and, thus, they are compatible with the values of  $\tau$  determined recently from the observations  $\tau = 1 - 1.5 \times 10^{-6}$  [154, 155], but are excluded if  $\tau > 2 \times 10^{-6}$  (see [152] for a detailed discussion on the bulge optical depth in our models).

### Parametrisation of the compressed NFW dark matter density profile

In [156] the compressed NFW dark matter density profile has been adjusted with the parametrization:

$$\rho_{\text{NFW}_c} = \frac{\rho_0 [1 + (R_0/a)^\alpha]^{(\beta-\gamma)/\alpha}}{(r/R_0)^\gamma [1 + (r/a)^\alpha]^{(\beta-\gamma)/\alpha}} \quad (4.1)$$

where  $\rho_0$  is the local (solar neighborhood) halo density (fixed to  $0.3 \text{ GeV/cm}^3$ ),  $R_0$  is the solar galactocentric distance,  $a$  is the characteristic length ( $a=20 \text{ kpc}$ ),  $\alpha=0.8$ ,  $\beta=2.7$ , and  $\gamma=1.45$ . As one can see, at small  $r$  the dark matter density profile following the adiabatic cooling of the baryonic fraction is a steep power law with slope  $-1.45$ .

## 4.4 Evaluation of $J(\Psi)$ for the GC $\rho_{dm}$ models

In the literature, there are a finite number of suitable DM density profiles proposed for the GC. We consider three models as representative of model uncertainties at present: the adiabatic contracted NFW profile derived in the last section, an uncompressed NFW profile, plus a cored profile, so-called N03, with  $\alpha=0.17$ , that has been discussed in [72]:

$$\rho_{\text{NFW}} = \frac{\rho_s}{(r/r_s)(1 + r/r_s)^2} \quad (4.2)$$

$$\rho_{\text{N03}} = \rho_c \exp \left[ -\frac{2}{\alpha} \left[ \left( \frac{r}{r_c} \right)^\alpha - 1 \right] \right] \quad (4.3)$$

For the uncompressed NFW and cored profiles we considered the following parameters: scale radii  $r_s=21.746 \text{ kpc}$  ( $r_c=r_s$ ) and scale density  $\rho_s=5.376 \cdot 10^6 \text{ M}_\odot \text{ kpc}^{-3}$  ( $\rho_c=\rho_s/4$ ).

Integrating the squared density along the line of sight introduces divergences when cuspy profiles are considered. The radius in which the self-annihilation rate  $t_l \sim (\langle \sigma_{ann} v \rangle n_{dm}(r_{cut}))^{-1}$  equals to the dynamical time of the halo  $t_{dyn} \sim (G\bar{\rho})^{-1/2}$ , where  $\bar{\rho}$  is the mean halo density and  $n_{dm}$  is the neutralino number density, is normally taken as a reference to enforce a cut-off radius  $r_{cut}$  to the density profile, with a constant density core therein [148]. When this procedure is applied to the density profiles, the evaluated  $r_{cut}$  are of the order of  $10^{-8}$ – $10^{-9} \text{ kpc}$  for the compressed NFW profile (or very cuspy profiles) and  $10^{-13}$ – $10^{-14} \text{ kpc}$  for the uncompressed NFW profile. A constant density central region of radius  $r_{cut} = 10^{-8} \text{ kpc}$  is used in our computations<sup>3</sup>. Since the chosen value of  $r_{cut}$  somehow represents a lower bound on the acceptable values of this parameter, the values of the  $J(\Psi)$  integral can be taken as upper bounds. Clearly the non-cuspy profiles are not affected by the choice of  $r_{cut}$ .

Figure 4.2 shows the angular resolution averaged l.o.s  $J(\Psi)$  integral ( $\langle J(\Psi) \rangle_{\Delta\Omega}$ ) as a function of the  $\Psi$  pointing direction ( $\Psi=0$  corresponds to the GC direct pointing). The heliocentric distance to the GC is set to  $8.5 \text{ kpc}$  and the point spread function (PSF) of the MAGIC telescope is taken (of about  $0.1^\circ$  [157]), that corresponds to an angular resolution  $\Delta\Omega=10^{-5} \text{ sr}$ .

The integral  $\langle J(\Psi) \rangle_{\Delta\Omega}$  evidences the big disagreements in the DM distribution for the considered models in the innermost regions of the galaxy (these differences enter into the computation squared). This results in variations on the observable  $\gamma$ -ray flux from neutralino annihilations that span several orders of magnitude. In particular, the flux varies by 3 orders of magnitude if considering a compressed or uncompressed NFW DM density profile. Note that as more cuspy the profile, more point-like the detected emission should be. The spatial distribution of the expected radiation

<sup>3</sup>We fix this  $r_{cut}$  value for all computations of  $\langle J(\Psi) \rangle_{\Delta\Omega}$  in this Chapter.

varies from an extended emission to a point-like source emission, depending on the nature of the DM density profile.

With the use of the adiabatic contraction prescription, the GC is expected to yield the largest DM flux amongst the favored candidates, due to its proximity and high DM content estimated at the center. The GC is then considered as prime candidate for MAGIC observations, except for being too close to the horizon, as the telescope is located in the northern hemisphere.

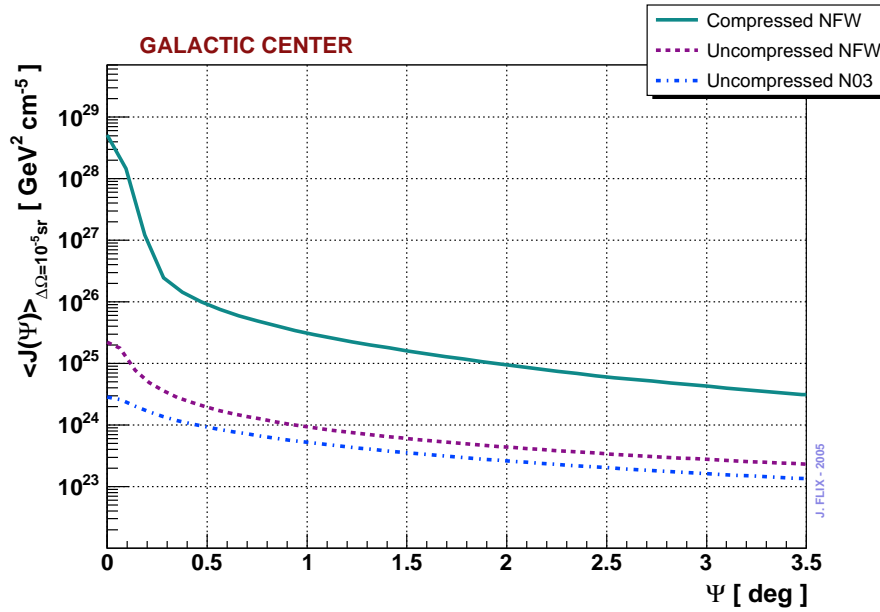


Figure 4.2: The averaged l.o.s integral  $\langle J(\Psi) \rangle_{\Delta\Omega}$  for all DM profiles considered for the GC modeling.  $\Psi$  is the pointing angle from the GC.

## 4.5 The Draco dwarf spheroidal galaxy

Dwarf spheroidals (dSphs) warrant attention because they are amongst the most extreme dark matter dominated environments. For example, the mass-to-light ratio of Draco is  $\sim 300$  in Solar units, while that of the Sagittarius is  $\sim 100$ . The recently discovered possible Canis Major dSph seems similar to the Sagittarius in structural properties and dark matter content. Both Sagittarius and Canis Major dwarfs are highly affected by tidal effects, so they are not considered in this study, as their dark matter density profiles might be highly affected <sup>4</sup>.

The Draco dwarf satellite ( $17^h 20^m 19^s, 57^{\circ} 54' .8$ ) is an excellent candidate to seek for gamma-rays from neutralino annihilations as it poses a high mass to light ratio (recent estimates  $\mathcal{O}(300) M_{\odot}/L_{\odot}$ ). It is the largest of all Milky Way satellites and is relatively near us, about 82 kpc away. The data about Draco are summarized in Table 4.2. Contrary to the rest of dwarfs, most of the stars forming Draco have been identified and the dark matter distribution has been modeled with rather good accuracy [159,160]. Draco is close to dynamical equilibrium, and there is little evidence for stars beyond the tidal radius, so no strong tidal effects are present [161].

In Draco, the parameters of the star distribution are determined by fitting the parameters of the various theoretical models to the measured star counts per solid angle. For example, the Plummer profile [162] is used to model the star density  $\nu(r)$  as well as the Sersic profile [163] to

<sup>4</sup>See [158], in which these objects are considered for SUSY dark matter indirect detection.

heliocentric distance	$82 \pm 6$ kpc (1 arcmin = 24 pc)
heliocentric velocity (optical)	$-290.6 \pm 0.8$ km/s
integrated apparent V-band magnitude	$10.9 \pm 0.3$ mag
integrated V-band absolute	-8.8 mag
tidal radius (King model)	$(40.1 \pm 0.9)$ mag
luminous core radius (King model)	$(7.7 \pm 0.1)$ arcmin
ellipticity	$e = 1 - a_{\text{minor}}/a_{\text{major}} = 0.30 \pm 0.2$
line-of-sight velocity dispersion	$\approx 10$ km/s
i-band luminosity	$L_i = (2.4 \pm 0.5)10^5 L_{\odot i}$
total stellar mass	$M_{\text{stars}} = 6.6 \cdot 10^5 M_{\odot}$
total mass (stars + DM) in $r < 30'$	$M_{\text{tot}} = (6.3 \dots 18) \cdot 10^7 M_{\odot}$
mass-to-light ratio	$\geq 300(M_{\odot}/L_{\odot})_i$

Table 4.2: Properties of the Draco dSph [80].

model the source brightness  $\Sigma(R)$ . For pressure supported relaxed systems the Jeans equations have to be fulfilled. A dark matter distribution function is assumed and their properties are derived from star velocity moments data and parameters adjusted to reproduce the measured line-of-sight velocity dispersion, under the condition that the Jeans equations are satisfied. The DM halo profiles which are commonly suggested are compatible with numerical simulations of cold dark matter halo simulations, see [68,164]. Other profiles may be considered which are compatible with the measured velocity profiles of low surface brightness galaxies [165].

We consider a representative set of 4 DM halo models for the Draco dwarf spheroidal derived from velocity available data reported in [166] (2002 data) and [159] (2004 data). The profiles were derived by [158] and [18]. From 2002 velocity data, we consider the following profiles: a cusped NFW DM profile (inner slope  $\alpha=1$ ) and intermediate cusped NFW DM profile ( $\alpha=0.5$ ):

$$\rho_{NFW}(r) = \frac{A}{r^{\alpha}(r + r_s)^{3-\alpha}} \quad (4.4)$$

and a cored DM profile ( $\alpha=0$ ), given by:

$$\rho_{cored}(r) = \frac{v_a^2}{4\pi G} \frac{3r_c^2 + r^2}{(r^2 + r_c^2)^2} \quad (4.5)$$

Very recent and more accurate data has been analyzed (2004 data), in which the outermost region from the Draco dynamical center suggest a tiny tidal effect on the dwarf. The DM distribution in this case has been modeled as a cusped profile ( $\alpha = 1$ ), with an exponential cut-off to reproduce accordingly the newest velocity measurements:

$$\rho_{Lokas2004}(r) = \frac{C}{r} \exp\left(-\frac{r}{r_b}\right) \quad (4.6)$$

The parameters regarding the 4 DM density profile models considered are shown in Table 4.3. Figure 4.3 shows the DM density profiles for all models as a function of the radius from the estimated Draco dynamical center.

DM profile	Parameters	
NFW ( $\alpha=0.5$ )	$A=2.3 \cdot 10^4 M_{\odot}$	$r_s=0.32$ kpc
NFW ( $\alpha=1$ )	$A=3.3 \cdot 10^7 M_{\odot}$	$r_s=0.23$ kpc
Cored ( $\alpha=0$ )	$v_a=22.9$ km s $^{-1}$	$r_c=0.23$ kpc
Lokas2004	$C = 4.75 \cdot 10^7 M_{\odot} \text{kpc}^{-2}$	$r_b=0.33$ kpc

Table 4.3: Parameters of the DM halo models considered for the Draco dwarf.

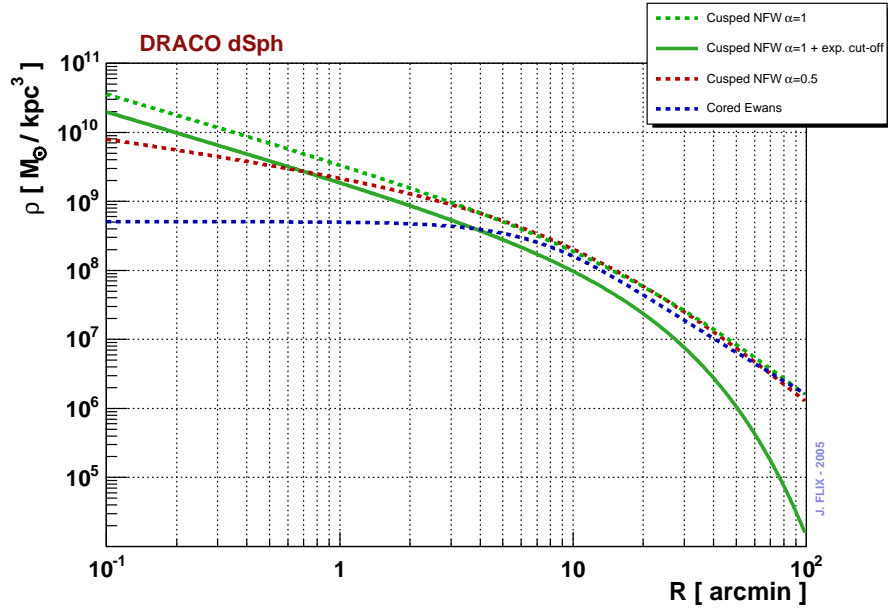


Figure 4.3: Different DM density profiles considered for Draco, as a function of estimated distance to the dynamical center (in *arcmin*, for a Draco distance of 82 kpc).

#### 4.5.1 Evaluation of $J(\Psi)$ for the considered Draco DM density profiles

The averaged l.o.s integration can be calculated for all Draco DM models explained in the previous section. Figure 4.4 shows the different values of the  $\langle J \rangle_{\Delta\Omega}$  while pointing the telescope for different angles  $\Psi$  from Draco center. Approximately, for all models, at  $\Psi \sim 0.25 - 0.3^\circ$  the luminosity of Draco in  $\gamma$ -rays is expected to be reduced by one-order of magnitude. In all cases considered here, the emissivity is not compatible with a point-like source, but would show an extended behavior.

## 4.6 The nearest galaxy: M31 (Andromeda)

M31 is a late-type Sb spiral galaxy, which lies at a distance of about 770 kpc (the nearest galaxy), and is observable from the Northern hemisphere (RA=10.68<sup>0</sup>, DEC=41.27<sup>0</sup>). A study based upon the analysis of HI data and a model-independent reconstruction of the velocity field [167], showed that the star rotation curve arises naturally by considering two optically traced mass components: a bulge, with a total mass of  $(7.8 \pm 0.5) \cdot 10^{10} M_\odot$ , and a disk of  $(1.22 \pm 0.05) \cdot 10^{11} M_\odot$ , within 28 kpc.

Nevertheless, it seems that the star mass-to-light ratios used in this paper,  $Y_{bulge}=6.5$  and  $Y_{disk}=6.4$  (solar units in blue band), were over-estimated, and proper values are considered to be  $Y_{bulge}=3.7$  and  $Y_{disk}=4.5$  [168].

We consider a NFW that accounts for both components, introduced in [169]:

$$\rho_{\text{NFW2}}(r) = \rho_0 \frac{r_0}{r} \left( \frac{r_0 + a}{r + a} \right)^2 \quad (4.7)$$

where  $r_0$  usually stands for a core radius and  $a$  a scale length. From fits to the rotation curve, these parameters are entirely determined by the previous mass-to-light ratios. The fitted values are shown in Table 4.4.

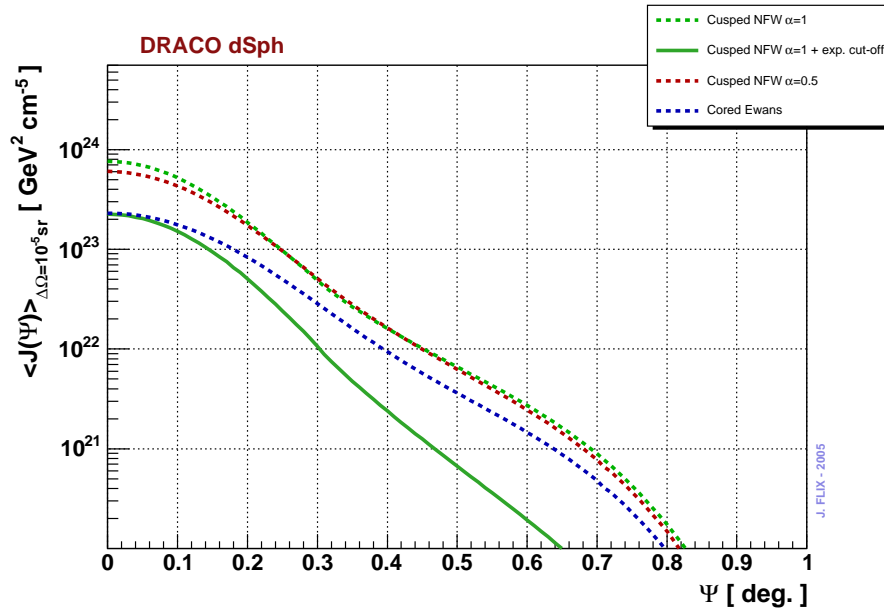


Figure 4.4: The averaged l.o.s integral  $\langle J(\Psi) \rangle_{\Delta\Omega}$  for all DM profiles considered for the Draco modeling.  $\Psi$  is the pointing angle from the dynamical center of the system.

In addition, we consider a single component NFW profile (NFW1) and the recently proposed by Moore and collaborators (M04) profile:

$$\rho_{\text{M04}}(r) = \frac{\rho_s}{(r/r_s)^{1.16}(1+r/r_s)^{1.84}} \quad (4.8)$$

The parameters of both NFW and M04 models are taken from [148] and shown in Table 4.4.

DM profile	Parameters		
NFW1 ( $\alpha=1$ )	$\rho_0=4.2 \cdot 10^6 \text{ M}_\odot \text{ kpc}^{-3}$	$r_0=30.271 \text{ kpc}$	$a = 5 \text{ kpc}$
NFW2 ( $\alpha=1$ )	$\rho_0=0.07 \text{ GeV cm}^{-3}$	$r_0=20 \text{ kpc}$	
M04 ( $\alpha=1.16$ )	$\rho_s=1.55 \cdot 10^6 \text{ M}_\odot \text{ kpc}^{-3}$	$r_s=44.697 \text{ kpc}$	

Table 4.4: Parameters of the DM halo models considered for the M31 galaxy.

#### 4.6.1 Evaluation of $J(\Psi)$ for the considered M31 DM density profiles

As in the other candidates, we compute the averaged l.o.s  $\langle J(\Psi) \rangle_{\Delta\Omega}$  l.o.s integral for all DM models considered for M31 galaxy, while pointing the telescope for different angles  $\Psi$  from its center (Figure 4.5). Like in the Draco case, we do expect DM emissivity not to be compatible to a point-like source, but show an extended behavior. The emissivity falls one order of magnitude at  $\Psi=0.3$ – $0.5^\circ$ .

The M31 is a massive galaxy and the DM might be affected by adiabatic compression effects. The same procedure that we applied to the Milky Way could be in principle applied to M31. We note that for objects that are located outside the Milky Way, and far away, we are 'less' dominated by contributions from the innermost regions of the DM halo, as the emissivity is highly influenced by the large contributions caught from the halo itself. In this scenario, we do expect that the effect of the inner slope has less impact into the  $\langle J(\Psi) \rangle_{\Delta\Omega}$  values as in the GC does.

To illustrate this effect we compute how the adiabatic compressed NFW and the uncompressed NFW profiles derived for the GC behave when we move the heliocentric distance from 8.5 kpc (solar

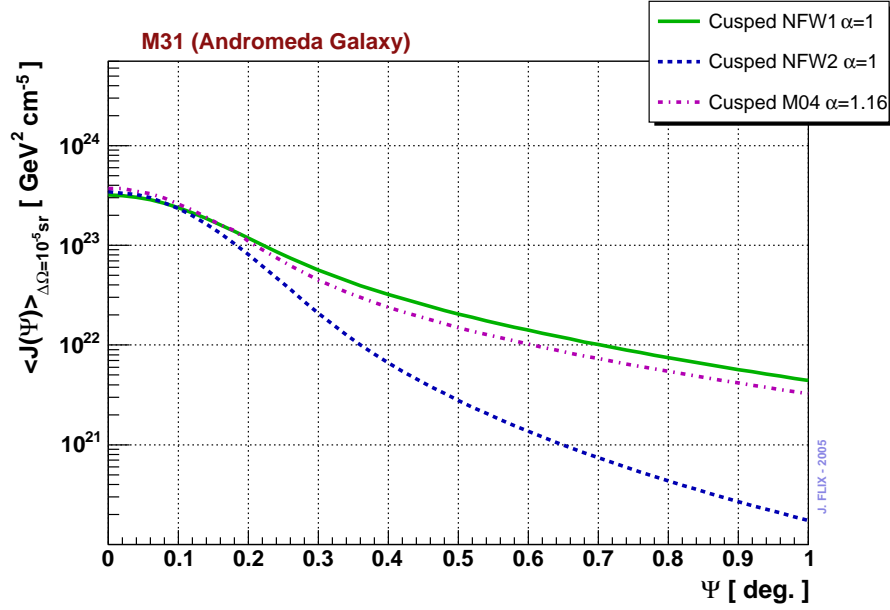


Figure 4.5: The averaged l.o.s integral  $\langle J(\Psi) \rangle_{\Delta\Omega}$  for all DM profiles considered for the M31 galaxy.  $\Psi$  is the pointing angle from the dynamical center of the galaxy.

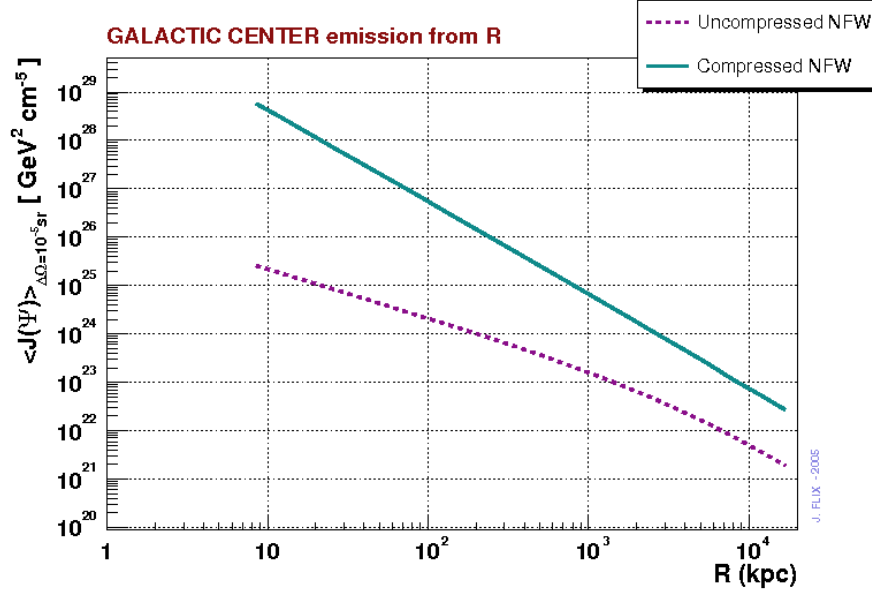


Figure 4.6: Variations of the  $\langle J(\Psi) \rangle_{\Delta\Omega}$  as we vary the heliocentric distance: as farther we are located from a galaxy, we are less affected by the central spiky structure, as the sum more contributions from the halo.

position) up to 10 Mpc. The result is shown in Figure 4.6 and, as expected, the differences are bigger when we integrate less halo contribution, then we are more dominated by the central spike (note that the integral is averaged in solid angle). The integral value spans 3.5 orders of magnitude for  $R=8.5$  kpc and of about 1.5 at  $R\sim 800$  kpc ( $\sim$  M31 distance).

We will not apply the adiabatic contraction prescription to M31 models. The models considered

have to be taken as rather conservative models.

## 4.7 $\gamma$ -ray flux predictions for the selected candidates: MAGIC search strategies

Figure 4.7 shows  $5\sigma$  exclusion limits that we may set with the MAGIC telescope for 30 hours of observation time on the chosen objects. The limits are computed assuming a MAGIC  $E_{\text{thr}}$  of 100 GeV<sup>5</sup>, and the latest instrument sensitivity curve derived from MC studies (in agreement with latest Crab Nebula results<sup>6</sup>). The  $E_{\text{thr}}$  and telescope's sensitivity are accordingly scaled with the culmination ZA of the different sources<sup>7</sup>.

Figure 4.7 displays all 3 possible DM halos considered for the GC, while only the halos that yield the maximum and minimum fluxes are shown for M31 and Draco. The expected fluxes from neutralino annihilations in these objects is predicted to be slow and depends strongly on the innermost density region of the DM halos considered. For example, for a factor  $f_{\text{SUSY}} = 1-10^{-1}$ , and  $\langle J(\Psi) \rangle_{\Delta\Omega} \sim 10^{24}$ , we do expect fluxes of about  $10^{-13}-10^{-14}$  ph cm<sup>-2</sup> s<sup>-1</sup>, i.e. 3 orders of magnitude smaller than for the Crab nebula.

The detection of a DM  $\gamma$ -ray signal from the Galactic Center is possible (or achievable) in case of a very high density DM halo, like the one predicted by adiabatic contraction processes. We consider the Galactic Center as the prime candidate for DM searches, but due to the high ZA for GC observations, MAGIC has an increased  $E_{\text{thr}}$  ( $\sim 650$  GeV), i.e. a penalty to limit to highest neutralino masses, but also an expected large collection area that allows to scan a portion of the SUSY space. Table 4.5 shows the most relevant observational parameters derived for all objects and DM models considered. The value  $\Psi_{10}$  is the pointing angle in which the emissivity is expected to fall by an order of magnitude. It gives an estimation if the source has to be considered extended or point-like (see comments column in Table 4.5). The GC emissivity is expected to be extended for DM profiles with  $\alpha < 1$ , so in this Thesis we developed an analysis technique applied to MAGIC to allow to identify and study extended sources (DISP analysis).

Object	ZA [deg]	$E_{\text{thr}}$ [GeV]	$\langle J(\Psi) \rangle_{\Delta\Omega}$ [GeV <sup>2</sup> cm <sup>-5</sup> ]	$\Psi_{10}$ [deg]	Comments
GC (NFW ad.cont.)	$\sim 60$	$\sim 650$	$5.2 \cdot 10^{28}$	$\sim 0.1$	point,VHE
GC (NFW)	$\sim 60$	$\sim 650$	$2.2 \cdot 10^{25}$	$\sim 0.6$	ext.,VHE
GC (N03)	$\sim 60$	$\sim 650$	$2.8 \cdot 10^{24}$	$> 2.$	ext.,VHE
DRACO (NFW)	$\sim 29$	$\sim 150$	$7.6 \cdot 10^{23}$	$\sim 0.3$	ext.,no VHE
DRACO (NFW $\alpha=0.5$ )	$\sim 29$	$\sim 150$	$6.0 \cdot 10^{23}$	$\sim 0.3$	ext.,no VHE
DRACO (NFW +cut-off)	$\sim 29$	$\sim 150$	$2.3 \cdot 10^{23}$	$\sim 0.25$	ext.,no VHE
DRACO (Cored)	$\sim 29$	$\sim 150$	$2.3 \cdot 10^{23}$	$\sim 0.3$	ext.,no VHE
M31 (M04)	$\sim 13$	$\sim 110$	$3.7 \cdot 10^{23}$	$\sim 0.35$	ext.,VHE
M31 (NFW2)	$\sim 13$	$\sim 110$	$3.5 \cdot 10^{23}$	$\sim 0.25$	ext.,VHE
M31 (NFW1)	$\sim 13$	$\sim 110$	$3.2 \cdot 10^{23}$	$\sim 0.3$	ext.,VHE

Table 4.5: Relevant parameters to evaluate the expected fluxes for all objects and DM halo models considered in this study (ext. = extended emission; VHE = possible  $\gamma$ -ray emitters in the FOV; no VHE = probably, no  $\gamma$ -ray emitters in the FOV).

Draco can also be considered as a plausible candidate for DM inspired observations. Conservative scenarios give low fluxes which are not detectable by MAGIC in a reasonable observation

<sup>5</sup>Conservative, but this is in fact the current analysis energy threshold of MAGIC telescope.

<sup>6</sup>Of about 5% of Crab at 100 GeV and low ZA observations.

<sup>7</sup>The  $E_{\text{thr}}$  deteriorates with ZA as  $100 \cdot \cos(ZA)^{-2.7}$  GeV. The effective photon collection areas increases  $\propto \cos ZA$ , hence the sensitivity is improved (we assume only geometrical effects on the shower development).

time. Low ZA observations preserve the nominal (low)  $E_{\text{thr}}$  of the MAGIC telescope. Moreover, no known VHE emitters in the FOV provides other  $\gamma$ -ray sources in competition to the one predicted in the exposed DM scenario.

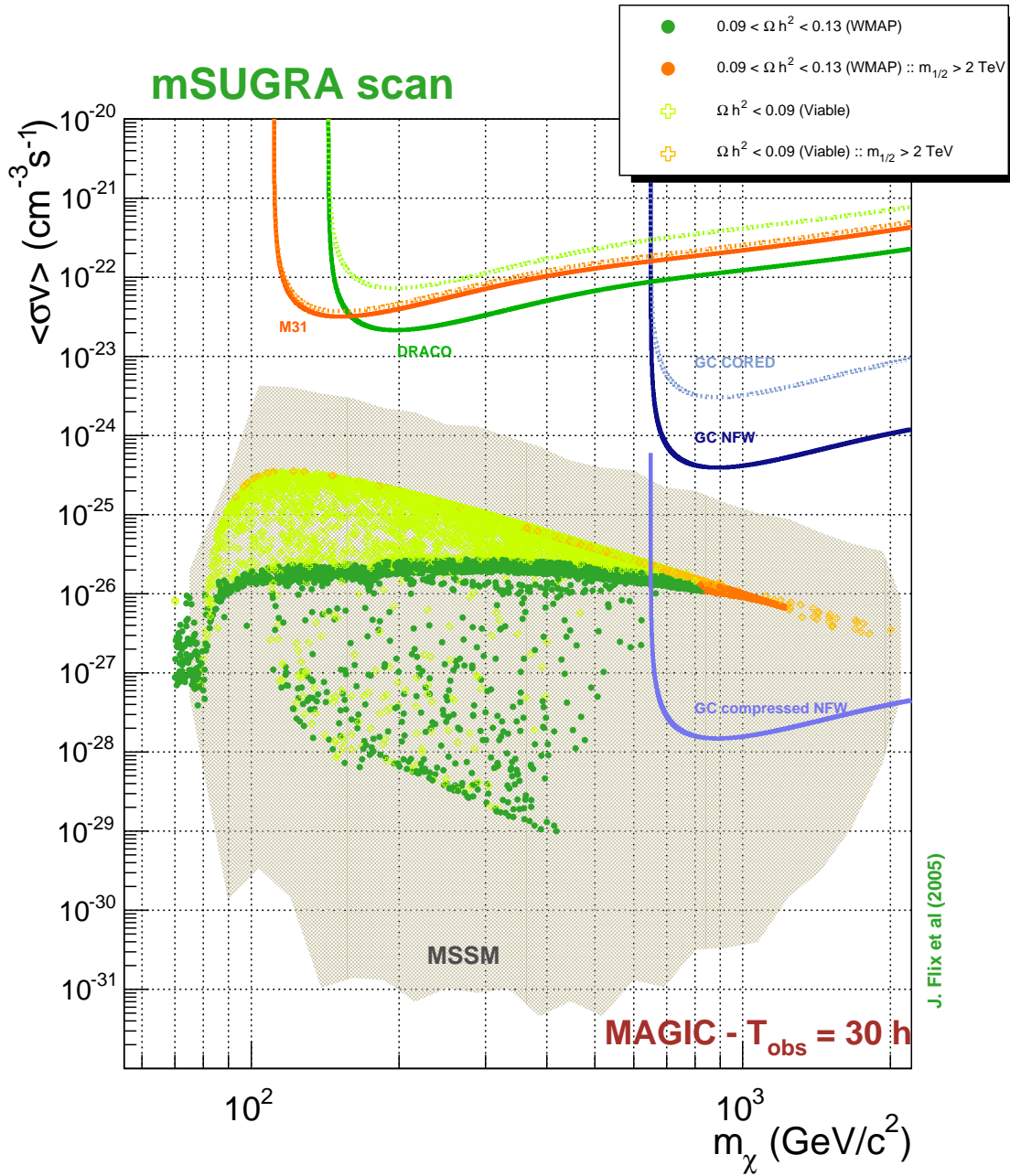


Figure 4.7: Exclusion limits ( $5\sigma$ ) in the SUSY parameter space that can be derived with MAGIC for 30h observation time for each considered source. The curves are obtained for the different DM models considered. The Galactic Center is expected to give the largest flux (lowest exclusion limits) amongst all the sources.

In addition, there are several factors that might enhance the expected flux from neutralino annihilations in the GC and Draco, and in particular for all objects:

- **DM substructures:** the so-called clumps, arise naturally in the hierarchical scheme of galaxy formation, and simulations of the non-linear regime of collapse allow a semi-theoretical study of their statistics and structure. Such local over-densities should induce extra neutralino annihilations, and translate to an additional boost factor to the flux. Although it is rather difficult to estimate how clumpy the galaxies remain today, this enhancement factor was until recently supposed to be smaller than  $\sim 10$  [125]. Nevertheless, a recent study suggests that about 50% of a Milky Way like galaxy mass is possibly bound to dark matter substructures, whose mass range spreads from  $10^{-6}$  up to  $10^7 M_\odot$ . The authors claim that about  $\sim 10^{15}$  of such substructures may have survived against gravitational disruption, leading to a boost factor of over two orders of magnitude compared to the smooth contribution. However, this study has been contested [170].
- **SMBH:** As another possible astrophysical effect, the super-massive black hole at the center of the Milky Way or M31 could raise the central halo profile up due to adiabatic accretion. A possible enhancement of the WIMP annihilation rate due to the presence of intermediate-mass black holes might be expected [171].
- **Quintessence effects:** Beside those astrophysical effects, some recent developments in the frame of theoretical cosmology have focused on the quintessence scheme to solve the so-called coincidence problem (the fact that  $\Omega_\Lambda \sim \Omega_m$  today). Such a quintessential field could undergo a kination regime in the early universe [172], so that its kinetic energy dominates over its potential. In this regime, the expansion rate of the universe is enhanced and the thermal history of neutralinos is consequently modified: the decoupling of neutralinos can take place more rapidly at earlier times. Therefore, the WMAP constraint leads to a higher neutralino annihilation cross-section. This means that this phenomenon rehabilitates SUSY models for which relic densities are too low, when calculated in standard cosmology. According to this cosmology, higher annihilation rate models are required, which therefore means that the  $\gamma$ -ray production is enhanced.
- **Affleck-Dine baryogenesis:** In a SUSY scenario, it yields natural matter-antimatter asymmetry in the early universe [173]. Meta-stable particles result from oscillations in flat directions of the scalar potential, carrying baryon and/or lepton number, namely Q-balls. These Q-balls can have a lifetime long enough to decay after the freeze-out of neutralinos. This induces a non-thermal production of neutralinos, and thus enhances their relic density. This also requires, as previously, higher neutralino annihilation rates to not over-close the universe.

Therefore, although standard conservative predictions are not that optimistic for the considered objects, all these putative contributions may increase the  $\gamma$ -ray flux from the objects significantly. This further motivates observations of such sources with MAGIC keeping in mind that CDM could be something besides SUSY.

## 4.8 Observation proposals

In light of these studies, two observation proposals for GC and Draco were asked for the MAGIC cycle-I observation period:

- **Galactic Center proposal:** Motivated by DM-inspired framework and other scenarios in which VHE radiation is expected, the GC was proposed to be observed for about 40 hours. The 40 hours were splitted into 20 hours ON and 20 hours dedicated OFF data or devoted to observations in the wobble mode. In addition, 60 hours of observation during moonshine

were applied for. **A total of 24 hours of data were taken**, in ON/OFF, Wobble mode and moonshine time. This Thesis focuses in the analysis of the bulk set of this data <sup>8</sup>.

- **Draco proposal:** We proposed the observation of Draco for a total number of 20 moonless hours from May to June 2005 for ZA from 30 to 40 degrees (in Period 30, 72 hours were available). No OFF data was required in this proposal. This proposal was entirely based on DM-inspired framework, and **low priority was given to this source, and no data was taken.**<sup>9</sup>

---

<sup>8</sup>See section 8.4, for a description of the different sets and observation conditions.

<sup>9</sup>At the time of the proposal, we did not know about the CACTUS detection of  $\gamma$ -rays from Draco. We will come back to this issue in the Discussion Chapter.



## Part II

# The MAGIC telescope for $\gamma$ -ray astronomy: description and technical work

## Chapter 5

# $\gamma$ -ray astronomy and the MAGIC Telescope

*This Chapter gives a brief introduction to  $\gamma$ -ray astronomy and recent results, as well as explains the Čerenkov technique for  $\gamma$ -ray astronomy. This technique allows an Imaging Air Čerenkov Telescope (IACT) to indirectly detect  $\gamma$ -rays entering the Earth atmosphere. The main features of Extended Air Showers (EAS) are briefly commented, stressing the differences between EAS induced by primary  $\gamma$ -rays and the several orders of magnitude more numerous EAS induced by charged cosmic ray (CR) nuclei, which constitute the background. The production of Čerenkov radiation in an EAS is described, together with the subsequent detection of the Čerenkov flashes by an IACT. Finally, the MAGIC Telescope, the detector on which the experimental part of this Thesis is based on, is introduced.*

### 5.1 Introduction

This Thesis deals with unresolved questions in the  $\gamma$ -ray band of the electromagnetic spectrum. Being the latter the most energetic end of the radiation emitted by any astrophysical source, the  $\gamma$ -ray field is normally confronted with issues involving the acceleration, production, interactions, and decays of highly relativistic particles. Photons, the carriers of the information that we process from the astrophysical environments, are then inextricably related not only with the parent population of particles that generated them through interactions, but also with the environment within which these interactions proceed. In addition, there are exotic processes that might as well generate  $\gamma$ -ray radiation, like the one we discuss in this Thesis.  $\gamma$ -astronomy, then, is the most adequate vehicle to study non-thermal processes in the universe, from the neighborhood of active nuclei at all scales to diffuse emissions in extended scenarios, such as galaxies, supernova remnants, or the search for exotic physics signatures, which is our goal.

Systems that are able to produce energetic  $\gamma$ -rays are in general also producing photons at lower frequencies. Note that the converse is not true; e.g., thermal radiation can be emitted in narrow bands. This fact makes of  $\gamma$ -ray astronomy essentially a multi-frequency enterprise.  $\gamma$ -rays freely propagate in space, without deflecting in the interstellar and intergalactic magnetic fields, and thus trace back to their original source. This is in fact the major advantage  $\gamma$ -ray (and neutrino) astronomy in front of cosmic ray astronomy. Charged cosmic rays are indeed much more abundant but only those with the highest energy arrive to the Earth without being substantially deflected, and even in that cases, it is hardly possible to correlate the observed flux of particles with a concrete region in the sky. All in all, having yet not sufficiently large collection areas in the existing neutrino detectors so as to compensate the extremely low cross-sections with which



A forthcoming European mission is entirely dedicated to high-energy astrophysics. AGILE (acronym for Astro-rivelatore Gamma a Immagini LEggero), whose expected launch date is within the next two years, has three instruments, which will cover the energy range from tens of KeV to 50 GeV, being the first satellite that will produce simultaneous detections in the X-ray and  $\gamma$ -ray band. AGILE point source sensitivity is comparable to that of EGRET for on-axis sources and substantially better for off-axis sources, but will have a much larger field of view coverage at energies above 30 MeV ( $\sim 1/5$  of the entire sky), to improve background subtraction.

GLAST is a DOE/NASA mission to be launched in September 2007. It will explore the energy range from 30 MeV to 100 GeV with 10% energy resolution between 100 MeV and 10 GeV. The LAT (acronym for Large Area Telescope, the main instruments on-board GLAST) has a field of view about twice as wide (more than 2.5 steradians), and sensitivity at least about 50 times as large, as that of EGRET at 100 MeV, a comparison that improves at higher energies. Its two year sensitivity limit for source detection in an all-sky survey is  $2.4 \cdot 10^{-9}$  photons  $\text{cm}^{-2}\text{s}^{-1}$  (at energies above 100 MeV). GLAST will be able to locate sources to positional accuracies from 30 arc seconds to 5 arc minutes, given a much better point spread function, what would allow better searches of counterparts at other frequencies.

Figure 5.2 is the simulated GLAST sky after 1 year of survey: several thousand sources are expected to be detected with unprecedented resolution.

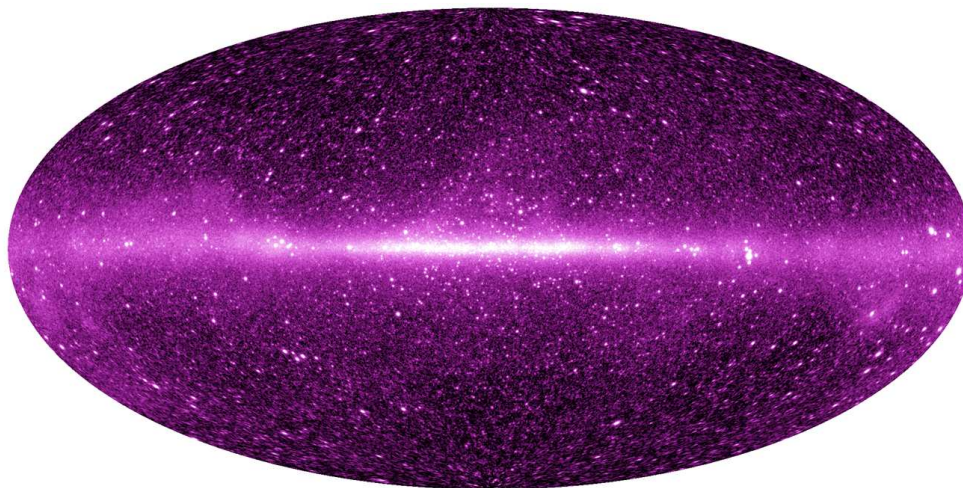


Figure 5.2: Simulated predictions of the one-year all-sky survey of the LAT experiment ( $E > 1$  GeV).

The LAT instrument on-board GLAST is such that just after 1 day of observations it will detect the weakest of the EGRET sources with  $5 \sigma$  confidence level. And after 1 week of observations, GLAST will have reached the same sensitivity and coverage than the whole decade of earlier EGRET operations. With a nominal lifetime of five years, and an expected of ten, GLAST will change the perspective of astrophysics in the GeV energy domain in the early 21st century.

### 5.3 The Universe at TeV energies

One of the last challenges of  $\gamma$ -ray astronomy is the distribution of the sources of GeV and TeV photons. Contrary to the lowest energy  $\gamma$ -ray band, photons in this TeV band are detected using ground-based detectors (as bigger collection areas are needed). To date, almost all the observational results in the energy interval from 100 GeV to 100 TeV have come from observations using the so-called Imaging Atmospheric Čerenkov Technique (IACT). Although considerable effort has been

applied to the development of alternative techniques (solar arrays like STACEE [177], air-shower particle detectors like MILAGRO [178], they are not yet competitive.

The window of ground-based  $\gamma$ -ray astronomy was opened in 1989 by the observation of a strong signal from the first TeV  $\gamma$ -ray source, the Crab Nebula, by the Whipple collaboration. The instrument used was the 10 m diameter Whipple Imaging Atmospheric Čerenkov telescope on Mount Hopkins in Arizona. The breakthrough in the technique was achieved by means of the image parameterization suggested by Hillas [179] allowing separation between the rare  $\gamma$ -ray showers and the background from showers induced by charged cosmic rays, which is orders of magnitude more intense. Since then, increasing progress has been made. The old generation of IACTs operating in the 1990s, Whipple, the HEGRA array and CAT, had an energy threshold of several hundreds GeV to several TeV. The turn of the century has brought a new generation of telescopes and arrays of telescopes which are equipped with larger dishes that bring the energy threshold down to  $\sim 100$  GeV.

The first such instrument was the HESS array [180] of four 12 m diameter telescopes in Namibia. HESS started operation in 2003 and has an energy threshold of about 150 GeV with an unprecedented  $5\sigma$  flux sensitivity around 0.5% crab for a 50 hour observation. Its angular resolution, around  $0.07^\circ$ , and wide field of view turn it into an excellent instrument for sky scans.

The 17 meter diameter single MAGIC Telescope [181] was commissioned one year later in La Palma, Spain. MAGIC is the lowest energy threshold IACT in the world. It combines a huge ultralight reflector with a large number of technical innovations. The camera has a total field of view of about  $3.5^\circ$ . The design of the telescope was optimized for fast repositioning with an eye to perform follow-ups of the prompt emission of Gamma-Ray Bursts (GRBs).

Two more telescope systems are well on their way. The VERITAS array [182] in Kitt Peak, US, and an upgrade of the existing CANGAROO array [183] in Australia. Both HESS and MAGIC have recently announced plans for an extension. HESS is to build a gigantic 28 m diameter single telescope at the center of the existing array and MAGIC is already installing a second 17 m telescope to be operated in coincidence with the first one. It will be commissioned in 2007.

After the Crab Nebula was established as the standard candle at very high energies (VHE) by Whipple, several years elapsed until the discovery of a second source. Mrk 421, an Active Galactic Nucleus (AGN) was claimed in 1994 again by the Whipple collaboration, that subsequently discovered a second AGN also of the BL Lac type, Mrk 501. The progress was slow during the 1990s. By 2003 the number of confirmed VHE sources had crept up to 12. Thanks to the new generation of IACTs the GeV-TeV astronomy has gone through a phase transition during the last two years. The number of sources has almost tripled.

HESS has performed a 112 hour scan [184] of the galactic plane in the range of galactic longitude  $[-30, 30]$  and  $\pm 3^\circ$  latitude. New sources were detected above  $6\sigma$  (see Figure 5.3) and seven tentative ones above  $4\sigma$  have been recently released. Four of the eight high significance sources are potentially associated with supernova remnants (SNRs) and two with EGRET sources. In three cases they could be associated with pulsar wind nebulae (PWN). In one case the source has no counterpart at other wavelengths. Along with two other unidentified sources in this energy band, this suggests the possibility of a new class of 'dark' particle accelerators in our galaxy. Two of the objects in the scan have been recently confirmed by MAGIC [185].

Figure 5.4 shows how the number of detected sources in the TeV energy domain has increased in the last two years as soon as the last generation of ground-based Čerenkov telescopes have started operating. The most recent catalogue of sources claims 32 sources, including 6 unidentified objects.

There are now two consolidated populations of galactic VHE emitters (PWN and SNRs). The VHE catalogue lists six PWN, six SNRs, one binary pulsar, one microquasar, a region of diffuse emission and eleven AGNs. In the last months MAGIC and HESS have detected several new AGNs with redshifts up to 0.19, at distances almost a factor 10 larger than the two first ones detected at

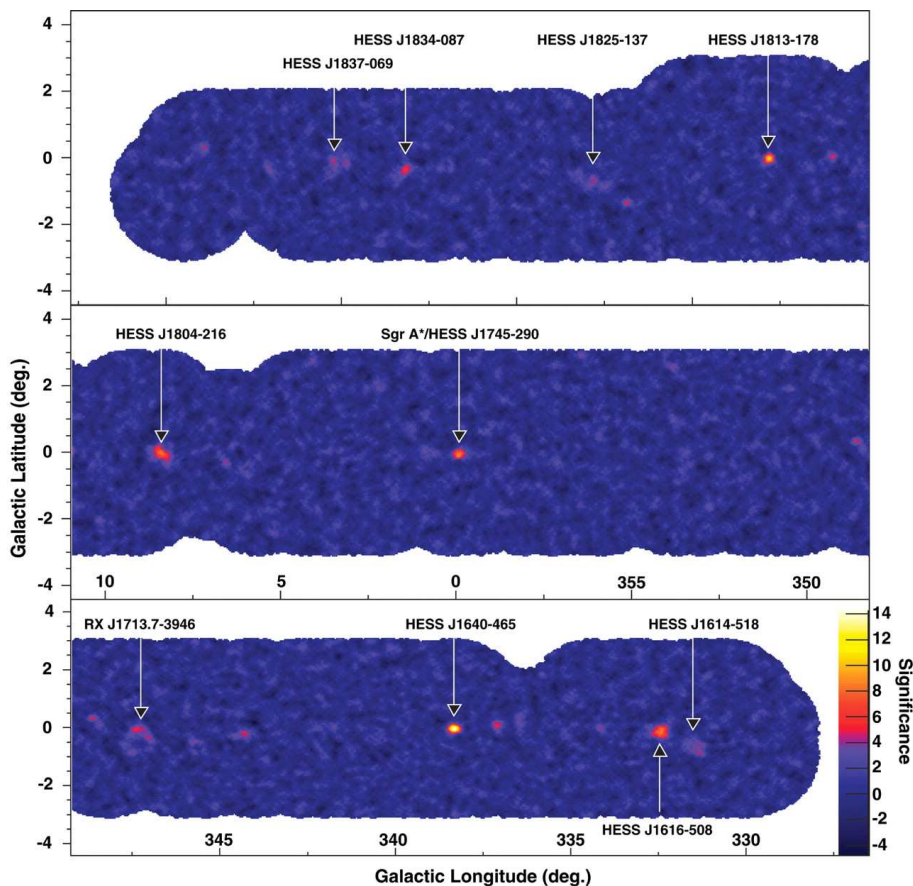


Figure 5.3: Significance map of the H.E.S.S. 2004 Galactic plane scan. 14 sources with  $\sigma > 4$  have been detected [184].

TeV energies.

A recent review of the recent results in HE  $\gamma$ -ray astronomy can be found in [187].

## 5.4 The physics of Extended Air Showers

The physics of EAS is reviewed in detail by [188, 189] among others. CRs –mainly atomic nuclei (98%, from which 87% H, 12% He, 1% C, N, O, Fe), electrons (2%),  $\gamma$ -rays and neutrinos– are emitted by a diversity of astrophysical objects. Some of them reach the Earth. On their way they interact with the interstellar and intergalactic medium and charged CRs are quickly deflected by galactic and intergalactic magnetic fields. Therefore, the distribution of CR incident directions on top of the atmosphere is isotropic, with the exception of the small flux of (neutral)  $\gamma$ -rays and neutrinos. The most energetic ( $> 1$  GeV) among these CRs constitute the primary particles of the EAS that develop in the atmosphere.

An EAS consists of the particles produced by the interaction of a single high energy primary CR on top of the atmosphere ( $\sim 25$  km above sea level). In the first interaction, several secondary particles are generated, which again interact with the molecules and ions of the atmosphere. The secondary products once more interact and generate new particles, and, as this process repeats, an EAS is generated. At the beginning of the process the number of particles in the shower rapidly grows. But, since the energy of the primary particle is distributed over all the generated particles,

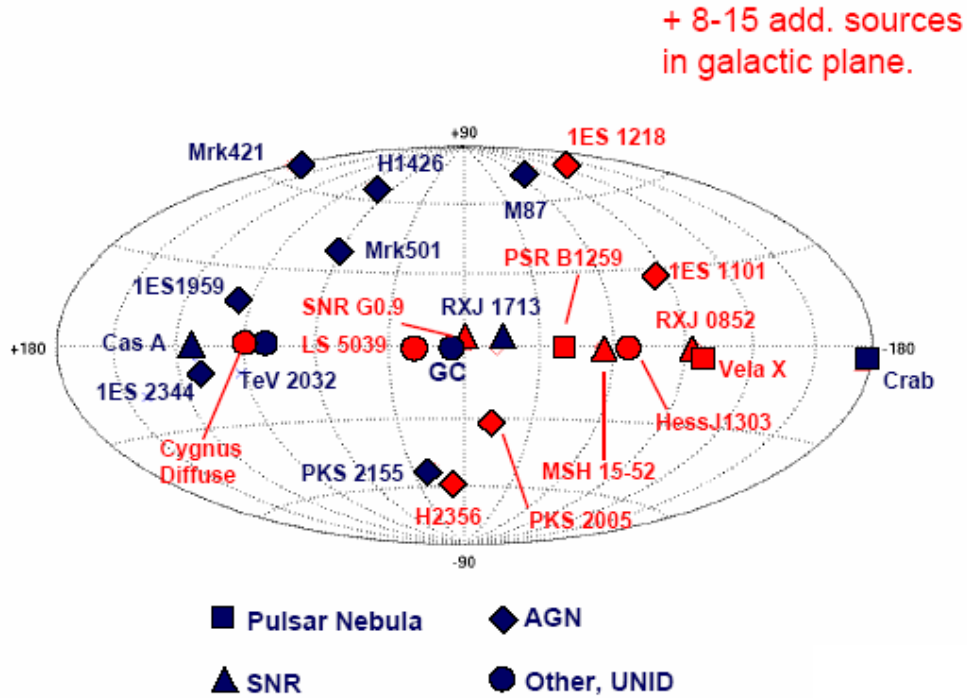


Figure 5.4: The Very High Energy  $\gamma$ -ray sky in 2005. Not shown are 8 more sources discovered by HESS in a survey of the galactic plane. Red symbols indicate the most recent detections, brought during 2004 and 2005 by the last generation of IACTs: HESS and MAGIC. Figure from [186].

at some point their energy falls below the threshold for production of further particles. Eventually energy losses through ionization and Compton scattering dominate and the shower dies out.

#### 5.4.1 Electromagnetic EAS

When a cosmic  $\gamma$ -ray or an energetic electron enters into the atmosphere develops an electromagnetic EAS, that to first order only contains electrons, positrons and photons. The primary  $\gamma$ -ray interacts with the strong Coulomb field of an atmospheric nucleus and, in order to conserve momentum, an electron-positron pair is produced from the emission of a virtual photon. If the energy of the resulting  $e^\pm$  is sufficient, they will be accelerated in the presence of the Coulomb field of other atmospheric nuclei. As a result of this acceleration, a fraction of their kinetic energy is emitted in the form of real photons, i.e., they undergo bremsstrahlung radiation. If the energy of the secondary  $\gamma$ -rays is still higher than 1.022 MeV, they produce again  $e^\pm$  pairs, which in turn can suffer further bremsstrahlung processes. The result of this recursive process is an avalanche of photons, electrons and positrons, which roughly follow the direction of the original  $\gamma$ -ray and share its total energy. A sketch of an electromagnetic EAS is shown in Figure 5.5 left. On the other hand, if a cosmic electron is the primary particle, an electromagnetic cascade, analogous to the one described but starting with bremsstrahlung emission, will develop. Electron-induced EASs are in fact an irreducible background for ground-based  $\gamma$ -ray detectors although their flux is much lower than that of hadronic CRs. For completeness, it should be mentioned that also muon-antimuon pair production and photo-production ( $\gamma + nucleus \rightarrow hadrons$ ) processes may occur in an electro-

magnetic shower. They would lead to a muonic and hadronic component of the shower. However, these contributions can be neglected since the cross section of these reactions are much smaller than that of  $e^\pm$  pair production and bremsstrahlung.

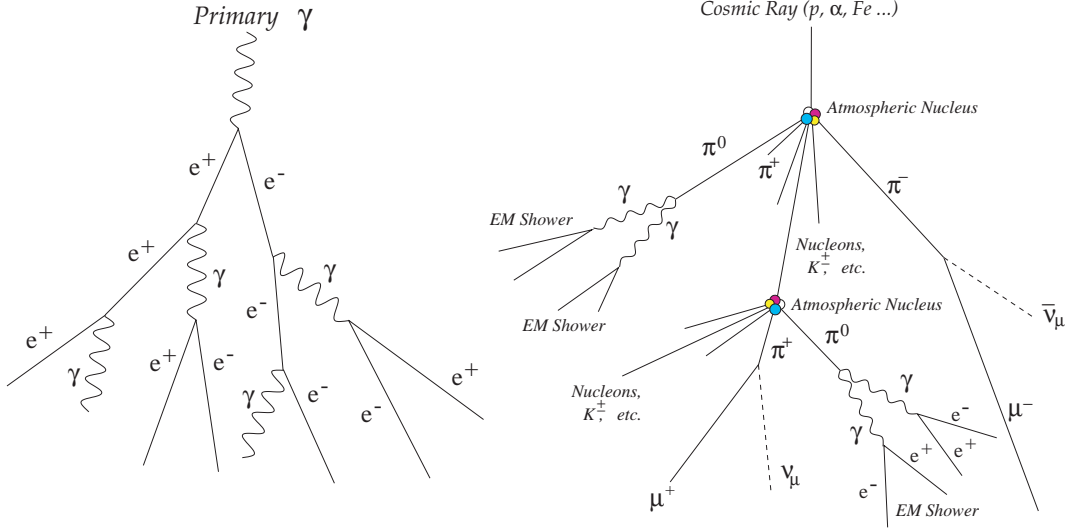


Figure 5.5: Sketch of the structure and the interactions present in an EAS, induced by a cosmic  $\gamma$ -ray (left) and by a charged cosmic nucleus (right).

All the shower particles are strongly collimated along the incident direction of the primary  $\gamma$ -ray, i.e., the shower axis, due to the relativistic energies involved. The main process that broadens the shower transversely is multiple scattering and, in second order, the deflection of the charged particles by the Earth magnetic field. As the EAS develops, the energy of the secondary particles decreases, while the number of particles increases until the shower maximum. This maximum is reached when the mean energy of the electrons and positrons in the shower falls below a critical energy  $E_c$  (about 83 MeV for  $e^-$  in air), which defines the moment when ionization becomes the dominant energy loss process, instead of bremsstrahlung.

At the same time, the mean energy of the shower photons has decreased and the cross section for production of  $e^\pm$  pairs becomes of the same order of the one for Compton scattering and photoelectric absorption (also for energies around 80 MeV). From this stage on, fewer secondaries are produced and the remaining particles rapidly lose their energy in the medium.

The development of electromagnetic EASs was first theoretically modeled by Rossi and Greisen (1941). Assuming several simplifying approximations they found an analytical solution for the longitudinal development of the shower. The Greisen equation (see [190] or [189]) describes the distribution of electrons and positrons with an energy above  $E_c$  as a function of the shower depth (the so-called longitudinal development),

$$N_e(t, E_0) = \frac{0.31}{\sqrt{\ln(E_0/E_c)}} e^{t[1-1.5 \ln(s)]} \quad (5.1)$$

where  $E_0$  is the energy of the primary  $\gamma$ -ray,  $t$  is the depth along the shower axis in units of radiation lengths, and  $s$  is the shower age, which is a dimensionless quantity defined as  $s(t, E_0) = \frac{3t}{t+2 \ln(E_0/E_c)}$  and ranges from 0 to 2. The derivative of the number of  $e^\pm$  with respect to the shower age,  $dN_e(t, E_0)/ds$  is positive, i.e., the number of particles is growing, while  $s < 1$ ; it is zero for  $s = 1$ , at the shower maximum; and becomes negative for older ages as the shower dies out. According

to the definition of the shower age, the depth at which shower maximum occurs  $t_{max}$  only depends on the energy of the primary photon:  $t_{max} = \ln(E_0/E_c)$ .

The lateral distribution of electrons can be modeled using the NKG-formula, which was derived by Nishimura and Kamata [191] and modified by [190]. It describes the  $e^\pm$  density as a function of the distance  $r$  from the shower axis:

$$\rho(r, t, E_0) = \frac{N_e(t, E_0)}{r_M^2} \left(\frac{r}{r_M}\right)^{s-2} \left(1 + \frac{r}{r_M}\right)^{s-4.5} \frac{\Gamma(4.5 - s)}{2\pi\Gamma(s)\Gamma(4.5 - 2s)} \quad (5.2)$$

where  $r_M$  is the multiple scattering Molière radius (about 79 m at sea level), and  $\Gamma$  is the Gamma function.

### 5.4.2 Hadronic EAS

An EAS induced by a charged cosmic hadron has three components, a hadronic, an electromagnetic, and a muonic one. The shower starts with the collision of the incident high energy hadron with an atmospheric nucleus, mainly producing pions, but also kaons and ions lighter than the incident nucleus. If the products of the first interaction have enough energy, they undergo successive nuclear collisions, leading to the hadronic high energy core of the shower.

About 90% of all secondary particles produced in the hadronic core of the shower are pions, out of which 2/3 are charged pions and 1/3 neutral pions. The  $\pi^0$  has a very short lifetime ( $\tau \sim 10^{-16}$  s) and rapidly decays, in most of the cases, into two photons ( $\pi^0 \rightarrow \gamma + \gamma$ ). Each of the resulting high energy photons will initiate an electromagnetic sub-shower, so with each hadronic interaction, approximately one third of the energy goes into the electromagnetic component of the shower. On the other hand, secondary charged pions and kaons may decay into muons and neutrinos ( $\pi^\pm \rightarrow \mu^\pm + \nu_\mu(\bar{\nu}_\mu)$ ,  $K^\pm \rightarrow \mu^\pm + \nu_\mu(\bar{\nu}_\mu)$ ,  $K^\pm \rightarrow \pi^\pm + \pi^0$ ), feeding the muonic component of the shower. Muons only lose their energy via ionization or decay through the channel  $\mu^\pm \rightarrow e^\pm + \nu_e(\bar{\nu}_e) + \bar{\nu}_\mu(\nu_\mu)$ , thus an additional fraction of energy is released into the electromagnetic component of the shower. However, the muon lifetime ( $\tau = 2.2 \times 10^{-6}$  s) is about two orders of magnitude higher than that of the pion and kaon ( $\tau \sim 10^{-8}$  s), and, as many muons are produced with very high energy in the upper layers of the atmosphere, frequently they have high enough Lorentz factors to reach the Earth surface before decaying. These muons, together with the neutrinos, prevent a sizeable fraction (about 5%) of the initial CR energy from being absorbed in the atmosphere [192].

Hence the three components of a hadronic EAS are the electromagnetic sub-showers originated from  $\pi^0$  decays, the hadronic core built up from high energy nucleons and mesons (which usually re-interact and mostly become electrons and positrons whose energy is mostly dissipated through ionization), and a fraction of nearly non-interacting muons and neutrinos.

Figure 5.6 shows a lateral view of a simulated electromagnetic EAS and a hadronic EAS. It can be noticed that hadronic showers are broader, as their lateral spread is mainly caused by the transverse momentum get by the secondary hadrons in the hadronic interactions, which is substantially larger than the scattering angle generated from multiple scattering (the dominant process in the much slimmer electromagnetic showers). It is also worth mentioning that the nuclear interaction lengths of hadrons in air are substantially larger (almost double) than the radiation length for bremsstrahlung and the interaction length for  $e^\pm$  pair production ( $\xi_{nuclear} \sim 83$  g/cm<sup>2</sup>,  $\xi_{brems} \sim 37$  g/cm<sup>2</sup>,  $\xi_{pair} \sim 47$  g/cm<sup>2</sup>), what implies that the starting point and the maximum of the shower of hadron-induced EAS occurs deeper in the atmosphere than in the case of a shower induced by a  $\gamma$ -ray of the same initial energy.

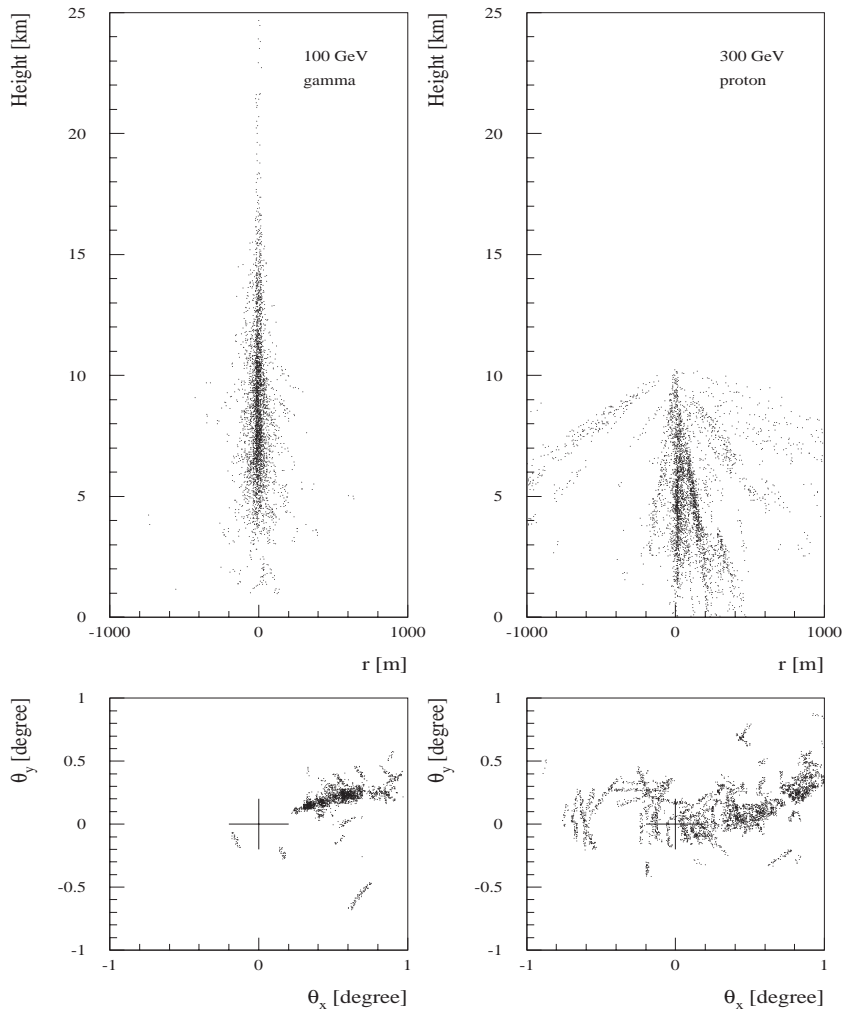


Figure 5.6: Simulation of an electromagnetic (left panels) and hadronic (right panels) Extended Air Showers. The top panels show the development of the shower in the atmosphere and the bottom ones the angular distribution of the Čerenkov photons at ground levels. Evident morphological differences can be seen which are crucial for imaging-based background subtraction methods.

## 5.5 The Imaging Atmospheric Čerenkov Technique

### 5.5.1 Čerenkov radiation in an EAS

When a charged particle travels through a medium with a speed  $v = \beta c$  that exceeds the speed of light in that medium (i.e.,  $v > c/n$ , where  $n$  is the refractive index of the medium), it emits light. This light emission, called Čerenkov radiation, is the result of the reorientation of the electric dipoles induced by the charged particle in the medium molecules. At low velocities, charges around the position of the incident particle are symmetrically distributed so as to cancel out, implying no net effect, and no radiation occurs. Only when the velocity of the charged particle is high enough, a net polarization of the medium briefly remains along the trajectory of the particle and, consequently, short electromagnetic impulses are emitted when the molecules rapidly turn back to their ground state (see a sketch of the process in panels a and b of Figure 5.7).

As a result, the particle suffers a continuous energy loss while its energy is above the Čerenkov

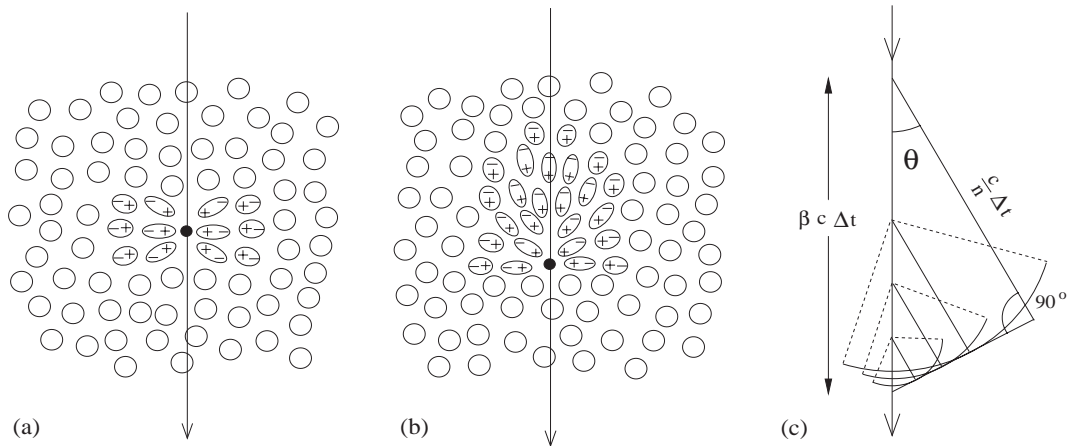


Figure 5.7: Polarization of the medium induced by a charged particle with low velocity (a) and with high velocity (b). Huygens construction of Čerenkov waves that only finds coherence for the Čerenkov angle  $\theta_c$  with respect to the charged particle trajectory (c).

threshold. As the charged particle crosses the medium, a shock-wave is created behind it. The wavefront propagates at a fixed angle  $\theta_c$  with respect to the track of the particle. The reason is that light emitted from different points of the particle trajectory only can add up coherently in Huygens construction for a very concrete angle, as is shown schematically in panel c of Figure 5.7. Requiring coherence, the Čerenkov angle can be deduced only from geometrical considerations:

$$\cos \theta_c = \frac{\frac{c}{n} \cdot \Delta T}{\beta c \Delta T} = \frac{1}{\beta n}. \quad (5.3)$$

Thus, the maximum angle of Čerenkov emission is observed for ultra-relativistic charged particles ( $\beta \simeq 1$ ), and is given by:

$$\cos \theta_c^{max} = \frac{1}{n} \quad (5.4)$$

while the threshold energy of the incident particles to emit Čerenkov light ( $v > c/n$ ) is:

$$E_c^{thr} = \frac{m_0 c^2}{\sqrt{1 - \beta_{min}^2}} = \frac{m_0 c^2}{\sqrt{1 - (1/n)^2}} \quad (5.5)$$

where  $m_0$  is the rest mass of the charged particle.

As the refractive index depends on the density of the medium, it changes with the atmospheric altitude. Therefore, the Čerenkov emission angle and the energy threshold for Čerenkov production take different values along the path of the shower. In order to better understand the evolution of the Čerenkov emission and to compute the Čerenkov radiation parameters for different atmospheric depths, a simplified model of the atmosphere can be used. In what follows, it is assumed an exponential variation of the atmospheric density with height  $h$ , i.e., and isothermal atmosphere,

$$\rho(h) = \rho_0 \cdot \exp\left(-\frac{h}{h_0}\right) \quad (5.6)$$

where  $h_0 = 7.1$  km and  $\rho_0$  is the air density at sea level,  $0.0013$  g/cm<sup>3</sup>. Then, the refractive index of the air as a function of height can be expressed as:

$$n(h) = 1 + n_h = 1 + n_0 \cdot \exp\left(-\frac{h}{h_0}\right) \quad (5.7)$$

where  $n_0 = 2.9 \times 10^{-4}$ . Equations 5.6 and 5.7 show that the refractive index depends linearly on the air density, decreasing at the higher layers where the atmosphere is less dense. Smaller dependencies of the refractive index on other factors, such as the air temperature or the wavelength of the radiation, can be neglected.

Using Equation 5.7 in Eq. 5.4 and Eq. 5.5 and the fact that  $n_h \ll 1$ , the maximum Čerenkov emission angle and the Čerenkov energy threshold can be expressed in terms of the height in the atmosphere:

$$\cos \theta_{\check{c}}^{max} \simeq \sqrt{2n_h} \quad (5.8)$$

$$E_{\check{c}}^{thr} \simeq \frac{m_0 c^2}{\sqrt{2n_h}} \quad (5.9)$$

On one hand, as  $n_h$  decreases with height, the energy threshold for Čerenkov emission is higher in the upper layers of the atmosphere and decreases as the EAS develops on. As an example, at 10 km above the sea level,  $n_h = 7.1 \times 10^{-5}$  and the  $E_{\check{c}}^{thr}$  for electrons, muons and protons is 42.9 MeV, 8.9 GeV and 78.8 GeV, respectively, about two times larger than the threshold values found at sea level ( $h = 0$  km). It is also worth noticing that nearly all the Čerenkov light in an EAS is produced by the secondary electrons and positrons, as they form an overwhelming fraction of the particles in the shower and they are more likely to be above the threshold of Čerenkov emission. At 10 km the Čerenkov energy threshold for electrons is still below the critical energy which indicates the shower maximum ( $E_c \sim 83$  MeV), so most of the electrons and positrons still emit Čerenkov radiation when the electromagnetic EAS is already dying out. Muons from hadronic EAS can also emit a non negligible fraction of the Čerenkov light and occasionally produce a fake light distribution of a  $\gamma$ -ray induced shower. However, as muons travel through the atmosphere undeflected and with almost negligible energy loss, they constitute at the end a very powerful tool to understand the performance and calibrate ground-based  $\gamma$ -ray detectors.

On the other hand, the maximum angle of Čerenkov emission is smaller at the beginning of the shower than in the shower tail due to the change of  $n_h$  with height. This height dependence of the angle is responsible for the fact that the light emitted by shower electrons and positrons at a range of different heights reaches the ground at approximately the same distance from the axis of the shower, an effect that produces a characteristic enhancement of the Čerenkov light density. This effect is illustrated in Figure 5.8. EAS simulations show that this ring structure, also called hump, typically occurs for a radius between 100 and 130 m from the center of the Čerenkov light pool. The Čerenkov light at the ground is the superposition of all the light emitted in cones integrated over the whole shower longitudinal path. However, in a real EAS, due to multiple scattering the trajectories of secondary  $e^\pm$  are slightly deviated from the track of the incoming primary  $\gamma$ -ray, and consequently, the ideal ring light pattern is somehow spread out.

For hadron-induced EAS, the hump structure is less visible as  $e^\pm$  directions are even more dispersed due to the high transverse momentum kick of nuclear interactions and  $e^\pm$  scatter away from the shower axis.

In general, the differences in the shower development between a hadron-induced and a  $\gamma$ -induced EAS, which are reflected in the shape and the time structure of the Čerenkov light distribution at ground level, can be used to distinguish between them with a sensitive enough ground-based instrument. Air showers develop practically at the speed of light, resulting therefore in very short Čerenkov flashes. Typically the front of Čerenkov photons produced in an electromagnetic EAS

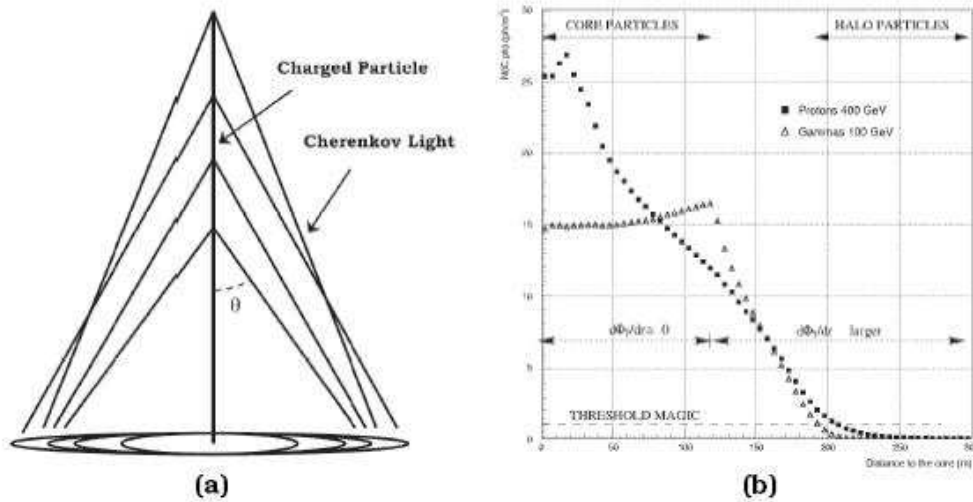


Figure 5.8: Scheme of the Čerenkov light ring produced by an ultra-relativistic charged particle at the observation level. The first two beams on panel (a) hit the ground at roughly the same radial distance even if they are produced at different heights. Panel (b) shows the simulation of the Čerenkov light pool produced by  $\gamma$ -ray and proton showers. The  $\gamma$ -induced Čerenkov light profile is practically constant until a radius of a hundred meters, where the hump occurs, and then decay rapidly for higher radius. Taken from [193].

arrives at the ground in 2-5 ns, whereas hadronic showers have a wider time spread (10-15 ns) due to the development of many electromagnetic sub-showers. As an example, a 1 TeV  $\gamma$ -ray induces an EAS which emit a Čerenkov flash in a cone with an opening angle of the order of  $1^\circ$ , which lasts about 5 ns, and yields about 50 photons per  $\text{m}^2$  on the ground within 100 m around the shower axis.

For detection purposes, it is also important to know the spectrum of the Čerenkov radiation produced in an EAS. The number of Čerenkov photons emitted per unit of path length and per unit of photon energy (or, equivalently, photon wavelength  $\lambda$ ) by a particle with charge  $Ze$  is given by:

$$\frac{dN^2}{dx d\lambda} = 2\pi\alpha Ze^2 \left( 1 - \frac{1}{\beta^2 \cdot n^2(\lambda)} \right) \frac{1}{\lambda^2} \quad (5.10)$$

where  $\alpha = \frac{e^2}{\hbar c}$  is the fine structure constant. Equation 5.10 shows that the emission is restricted to those frequency bands for which  $n(\lambda) > 1/\beta$ . The radiation occurs in the visible and near visible regions of the spectrum, for which  $n > 1$ . In the X-ray band,  $n$  is always  $< 1$ , so the emission is forbidden. The  $1/\lambda^2$  dependency of the spectrum indicates that most of the Čerenkov photons are emitted at short wavelengths, in the ultraviolet range, and that it decreases along the visible region. However, due to the interactions of the Čerenkov photons with the air molecules in their travel through the atmosphere, the spectrum observed at ground level is quite different from the emitted one (see Figure 5.9) and it peaks at around 330 nm. Čerenkov photons suffer the following attenuation processes in the atmosphere:

- Absorption in the Ozone layer, mainly in the upper part ( $\gtrsim 10$  km) of the atmosphere. Practically all photons with wavelength lower than 290 nm are absorbed through this process ( $O_3 + \gamma \longrightarrow O_2 + O$ ).

- Rayleigh scattering, which occurs on polarizable molecules with sizes smaller than the photon wavelength. If the atmospheric conditions are good, this is the process responsible for most of the Čerenkov light attenuation from 15 to 2 km above sea level, with a cross section  $\propto \lambda^4$ .
- Mie scattering, which takes place on polarizable molecules with sizes comparable or larger than the photon wavelength, basically aerosol particles present in the atmosphere. Its effect is especially important when atmospheric conditions are not optimal, i.e., if there is dust, pollution, clouds, fog, etc. The spectral dependence of the cross section is  $\propto \lambda^{-a}$ , with  $1 \lesssim a \lesssim 1.5$
- Absorption by  $H_2O$  and  $CO_2$  molecules, only important for photon wavelengths above 800 nm. These wavelengths are outside the sensitive range of the photo-sensors which are typically used for Čerenkov detection.

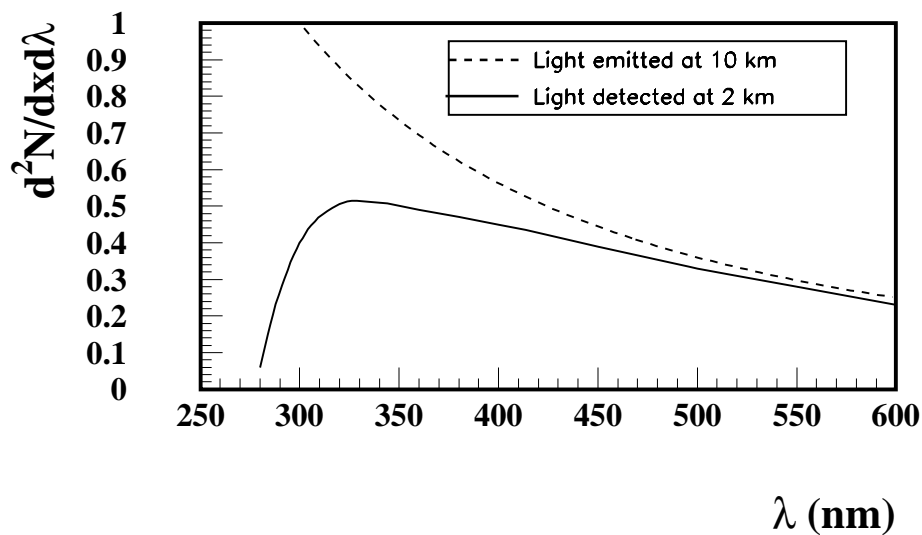


Figure 5.9: Differential Čerenkov photon spectrum in arbitrary units in the ultraviolet and visible wavelength ranges, emitted at 10 km above sea level (dotted line) and detected at 2 km (solid line) after suffering absorption in the Ozone layer and Rayleigh and Mie scattering. Graphic taken from [194].

## 5.6 Imaging Air Čerenkov Telescopes: detection technique

Imaging Air Čerenkov Telescopes (IACTs) are currently the most efficient ground-based experiments for the detection of cosmic  $\gamma$ -rays. As any other optical or radio telescope, an IACT consists of three basic elements: a tracking mechanical system, which counteracts the Earth rotation to track an astrophysical object in the sky; a collecting surface, which gathers the incident electromagnetic radiation and focuses it for its registration; and a receiver element, which converts the collected light in a recordable image of the observed field of view (FOV). A peculiar feature of Čerenkov telescopes is that they do not detect directly the photon flux under study, but instead detect the Čerenkov light which is produced in the EAS that the primary photons gives rise to in our atmosphere.

A mirror surface collects a fraction of the Čerenkov light pool and at the focal plane a set of light detectors converts the incident Čerenkov photons into electric pulses which together conform an

encrypted image of the EAS. The very short time response ( $\sim$  ns) of the light detectors chosen for IACTs is another important characteristic of these telescopes and is key for background rejection.

The image formed in the camera of photo-sensors (generally photomultiplier tubes (PMT)<sup>1</sup>) is a geometrical projection of the atmospheric shower as can be schematically seen in Figure 5.10.

Čerenkov photons emitted at different heights reach the telescope mirror dish with different angles and, therefore, will be focused on different positions in the camera of the telescope. As a consequence, the image contains information of the longitudinal development of the EAS, i.e., the number of particles emitting Čerenkov light as a function of the height in the atmosphere.

Light coming from the upper part of the shower, where the secondary particles are more energetic, has smaller Čerenkov angles and is mapped onto a region close to the camera center, whereas light emitted from the last stages of the shower, from less energetic secondary charged particles, has larger Čerenkov angles and is mapped further away from the camera center (see Figure 5.10). For the larger showers (i.e., the ones induced by more energetic particles) or for showers with high impact parameters<sup>2</sup>, due to this directionality of the Čerenkov radiation, Čerenkov photons from some parts of the EAS may not reach the reflector of the telescope and, therefore, parts of the shower may be not contained in the recorded image.

The Čerenkov technique relies on the shower development information that is contained in the images formed in the telescope to infer the characteristics of the particle that originated the EAS, as will be explained in more detail in the following Chapters on image analysis methods. On one hand, the total amount of light contained in the image is the main estimator of the energy of the primary particle. This is true because, although the fraction of initial energy lost in form of Čerenkov radiation is about 3 or 4 orders of magnitude smaller than the energy lost through ionization, the ratio between the Čerenkov energy losses and ionization losses is in first order constant, so a measure of the Čerenkov light provides a good estimation of the energy absorbed in the atmosphere, which is in fact acting as a calorimeter. On the other hand, the orientation and shape of the image are indicators of the nature and the incoming direction of the primary particle.

With this technique, the first clear detection of a  $\gamma$ -ray source was achieved in 1989, when the Whipple telescope claimed a 9 sigma detection of the Crab Nebula [195]. Since then, much progress has been made, as discussed in the Introduction.

Two main parameters characterize an IACT: its sensitivity, i.e., the minimum detectable  $\gamma$ -ray flux in a given number of observation hours, and its energy threshold, i.e., the minimum energy of the primary particle to which the telescope is able to disentangle the signal from the background. The dispersion of the Čerenkov light generated in an EAS in a large pool over the ground at the observation level crucially influence these two parameters.

On one hand, the light spread allows the IACT to detect EASs over a large range of impact parameters, from  $\sim 30$  to  $\sim 150$  m.<sup>3</sup> This provides IACTs with huge collection areas (of the order of  $10^5$  m<sup>2</sup>).<sup>4</sup> Such collection areas of the IACTs turn into high sensitivities in comparison with  $\gamma$ -ray detectors mounted on satellites, whose dimensions are clearly limited by space-launching requirements to  $\sim 0.01 - 1$  m<sup>2</sup>.

---

<sup>1</sup>Past and current IACTs use PMTs in their cameras, but new higher sensitivity light detectors, like Hybrid PhotoDetectors (HPD), Avalanche PhotoDiodes (APD), or Silicon Photomultipliers (SiPM), are currently under study.

<sup>2</sup>The impact parameter of an EAS is defined as the distance between the telescope location and the point where the shower axis intersects the plane perpendicular to the telescope axis.

<sup>3</sup>Although the efficiency of detection of showers with impact parameters larger than  $\sim 150$  m is quite low, i.e., when the light arriving to the IACT is outside the brightest region of the Čerenkov pool, beyond the hump, the large amount of showers arriving with these larger impact distances makes them to be still a significant fraction of the total amount of detected showers.

<sup>4</sup>It is worth mentioning that the area covered by the EAS light pool and, therefore, also the IACT collection area, depends on the energy of the primary particle and on the zenith angle of observation. At zenith angles  $\gtrsim 60^\circ$  the collection area can increase by one order of magnitude.

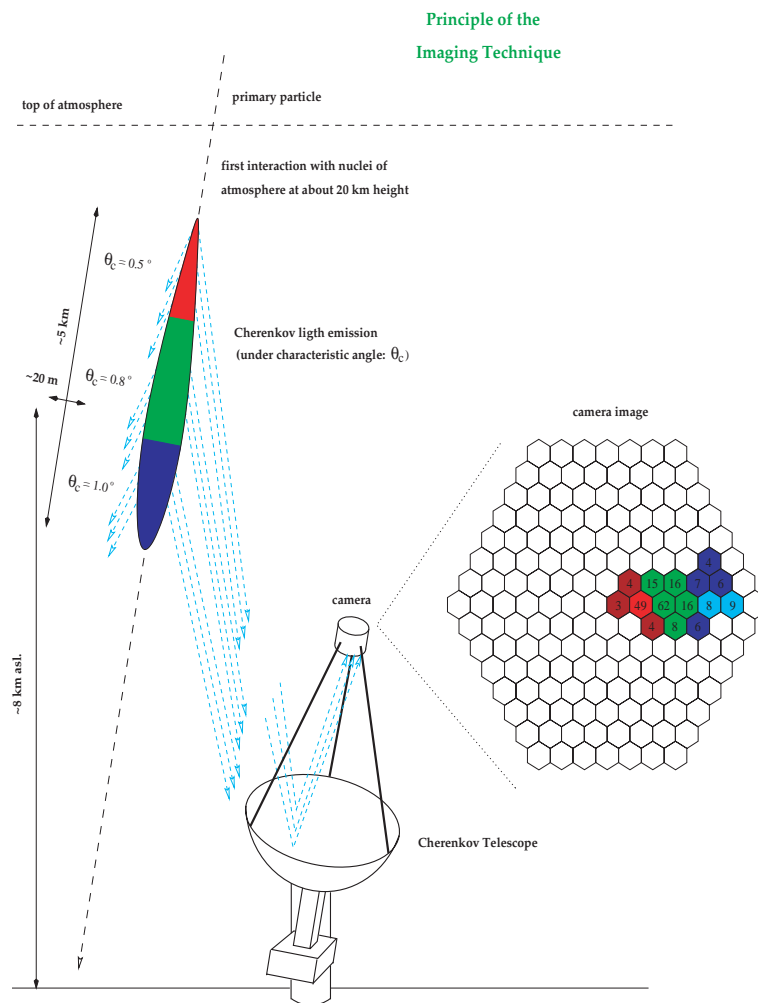


Figure 5.10: Sketch of the principle of the Čerenkov technique, through the formation of the image of an EAS in an IACT pixelized camera. The numbers in the Figure correspond to a typical 1 TeV  $\gamma$ -ray induced shower.

On the other hand, the dilution of the Čerenkov radiation over the large light pool makes its detection more difficult and necessitates large mirrors and high sensitivity photodetectors.

Figure 5.11 shows how the photon density at an observation site at 2 km above sea level diminishes as the energy of the EAS precursor particle is lower, going below 10 Čerenkov photons per  $\text{m}^2$  for  $\gamma$ -rays of less of 100 GeV. An efficient reconstruction of the primary particle characteristics through the image analysis requires a minimum number of detected Čerenkov photons per image (typical numbers are at least 60 equivalent photoelectrons in camera photodetectors). This implicitly means that an IACT is able to recognize  $\gamma$ -ray induced showers only for energies above a given threshold ( $E_{\text{thr}}$ ), which is basically limited by the size of the collection mirror area and the efficiency of conversion from incident Čerenkov photons to detected photoelectrons. As the number of Čerenkov photons is proportional to the energy of the primary  $\gamma$ -ray, the telescope energy threshold inversely depends on the mirror surface,  $A$ , and the light detection efficiency,  $\epsilon$ . It also depends, directly, on the background flux from the night sky,  $\phi$ , the solid angle on the sky subtended by the collection mirror,  $\Omega$ , and the integration time of the signals in the camera,  $\tau$ , as the larger these factors the larger is the amount of background light collected by the telescope

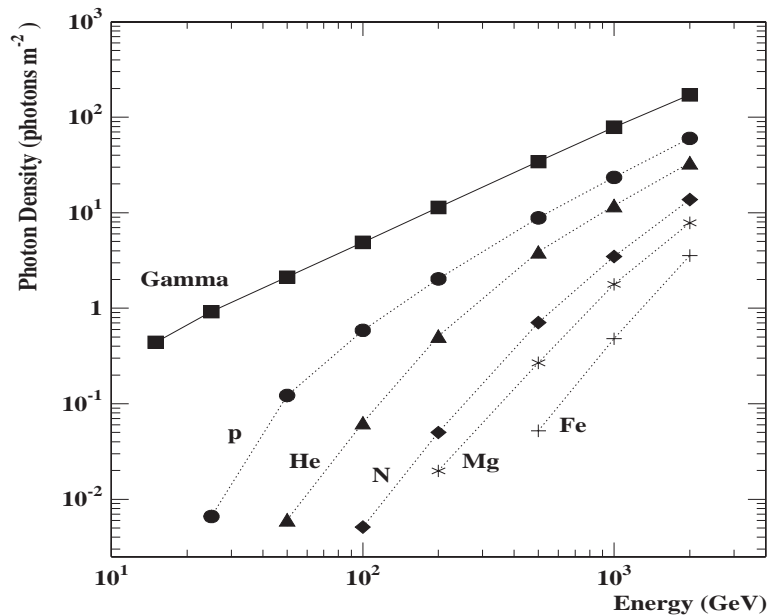


Figure 5.11: Čerenkov photon density at 2km height above sea level for different type of incident primary particles and as a function of their energy. Figure taken from [196].

which makes it more difficult to detect the signal [188]:

$$E_{\text{thr}} \propto \sqrt{\frac{\phi \Omega \tau}{\epsilon A}} \quad (5.11)$$

Although the sensitivity of IACT grows when observing at high zenith angles due to the increase on collection area, their energy threshold moves to higher energies, as the Čerenkov light spreads in a larger area.

The more usual convention for the definition of  $E_{\text{thr}}$  is the  $\gamma$ -ray energy for which the differential trigger rate distribution peaks. As this definition makes the  $E_{\text{thr}}$  dependent on the slope of the  $\gamma$ -ray spectrum coming from the source, a reference object (a so-called standard candle) is needed to compare different IACTs. For northern hemisphere IACTs, the source widely chosen as reference is the Crab Nebula, which is studied in more detail in [197].

Only two years ago, the lowest energy threshold reached with an IACT had been the one obtained by the WHIPPLE telescope, about 300 GeV. Nowadays, a new generation of Čerenkov telescopes are pushing down in energy. Both the HESS array and the MAGIC telescope have reached 100 GeV. Even further progress in lowering the energy threshold is the goal of the MAGIC collaboration, as its mirror collection area is substantially larger than any other existing IACT.

To conclude, observations with IACTs require clear moonless nights if the optimal sensitivity is required. In addition, Čerenkov light attenuation due to Ozone absorption and Rayleigh scattering when propagating from the emission point and through the atmosphere to the detector location is predictable, but the Mie attenuation factor highly depends on the atmospheric conditions which indeed are usually highly variable. Therefore, reliable observations require good weather and atmospheric conditions.

## 5.7 The MAGIC telescope

The name MAGIC Telescope stands for Major Atmospheric Gamma Imaging Čerenkov Telescope and is currently the largest Čerenkov telescope in the world. MAGIC has been constructed to allow, for the first time, detectability of  $\gamma$ -rays in the sub-100  $GeV$  energy domain. MAGIC is located in the Canary island of La Palma (28.8°N, 17.9°W), at the Roque de los Muchachos Observatory (2200  $m$  above sea level), which belongs to the Instituto de Astrofísica de Canarias (same location where the HEGRA stereoscopic system of Imaging Atmospheric Čerenkov Telescopes (IACTs) was installed). This location is considered to be one of the best observation sites in the northern hemisphere<sup>5</sup>.

The first ideas and the initial concept for the MAGIC telescope were developed in 1995 [198]. The Technical Design Report (*TDR*) was completed in 1998 [199] and first prototypes and tests of the telescope systems started right after. Almost all of the total funds for the project were granted at the end of the year 2000, and the construction of the telescope started in September 2001. The telescope was mostly completed at the time of the inauguration in October 2003, although the first light of the telescope was recorded on March 2003. The commissioning of the telescope installation finished in Fall 2004. From then, regular observations are carried out. Nowadays, the MAGIC telescope takes up to more than 100 hours per month of useful observational data.

The original goal of the MAGIC experiment is to cover with high sensitivity the energy gap between 10  $GeV$  and 300  $GeV$  in  $\gamma$ -ray astronomy, by lowering the threshold energy,  $E_{\text{thr}}$ , with respect to current instruments. At the time of the construction, this observation range was inaccessible to the present IACT. It was defined as the range between the upper energy limit from satellite observations and lower limit from IACT observations. The situation has changed recently: the 4 HESS telescopes construction finished in 2004 and the installation has offered to the scientific community lowered threshold observations, down to approximately 150  $GeV$ . This reduces the energy gap (in which no data is available) from 10 to 150  $GeV$ . After the MAGIC commissioning phase, the estimated trigger energy threshold of the telescope is of about  $\sim 60$   $GeV$ , which is not far from the 30  $GeV$  goal  $E_{\text{thr}}$  quoted in the *TDR*. The trigger  $E_{\text{thr}}$  value may be lowered by improving the telescope performance. It is worth to mention that the  $\gamma$ -hadron separation by employing standard analysis techniques below 100  $GeV$  is a critical issue. To solve  $\gamma$ -hadron separation at low energies, new analysis tools are under study and MAGIC would allow, for the first time, for sub-100  $GeV$  observations.

The key elements and goals of the MAGIC Telescope are:

- high Čerenkov photon-to-photoelectron conversion efficiency, and specially, the largest collecting mirror (17  $m$   $\emptyset$ ) in the world to date.
- lowest  $E_{\text{thr}}$  ever obtained with a Čerenkov Telescope, and high sensitivity, to explore the energy gap between 10  $GeV$  and 150  $GeV$ .
- fast movement of the telescope to any position on the sky to observe prompt emission of  $\gamma$ -ray bursts (*GRB*) following satellite alerts.
- capability to operate the telescope under moon shine to increase the observation time by a factor 2.
- Novel technologies and innovations employed; specific *R&D* programs conducted with moderate cost ( $\sim 4$  million Euros).

---

<sup>5</sup>In fact, due to good atmospheric quality, low human-made light background and good weather, it became the European Northern Observatory (ENO).

Figure 5.12 shows a photograph of the telescope after commissioning (autumn 2004), in which most of the relevant systems are indicated. The MAGIC telescope is operated by a collaboration of international institutes from Germany, Italy, Spain, Switzerland, Armenia, USA, Finland and Ukraine.

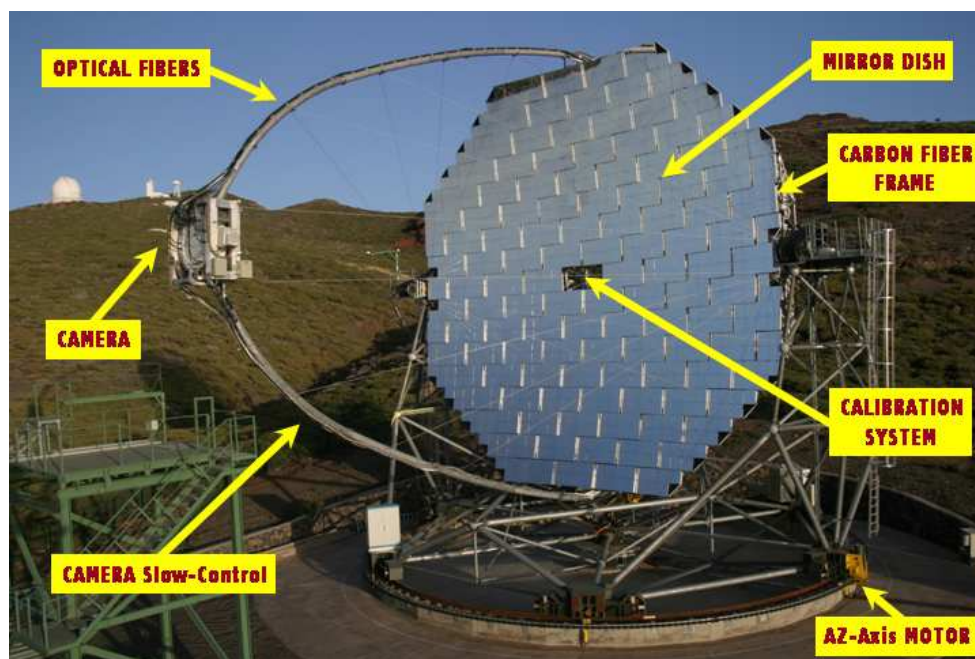


Figure 5.12: Photograph of the MAGIC telescope with main elements labeled.

In the following sections we briefly describe the most relevant elements of the MAGIC Telescope, stressing the technical innovations with respect to contemporary IACT. We pay special attention to the description of the telescope camera and calibration system, since it is the part of the detector in which the Thesis Author contributed technically, mostly related to the slow control system of both systems, including the integration into the Central Control system of the MAGIC telescope. All these technical aspects are explained in a separate Chapter.

### 5.7.1 The frame and the large mirror surface

#### Frame

The frame of the telescope roughly follows the concept of a large (17 m  $\varnothing$ ) solar concentrator with alt/az mount, which was already built and tested a few years ago as part of the German solar power research program. The main mirror support dish consists of a three layer space frame made from carbon fiber-epoxy tubes, which are lighter and more rigid than aluminum. Knots to join the tubes are made from aluminum. The frame assembly took only one month thanks to the simple frame assembly design employed by the German company *MERO*.

The weight of the frame, including the lower drive for azimuthal movement, is about 9 tons (the whole telescope and the undercarriage weights 64 tons). This frame structure keeps the inertia of the telescope low enough for it to be repositioned within 22 s at any position in the sky (below the 30 s that were set as target in the *TDR*, thanks to powerful telescope motors); this allows, for the first time, the capability of fast repositioning to follow-up *GRBs*, which is a extremely valuable

and unique feature among current IACTs. A finite element analysis of the frame has shown that deformations can be held below  $3.5\text{ mm}$  with respect to the nominal curvature at any position. The frame structure guarantees wind resistance up to  $< 170\text{ km/h}$  and stability for complete ice coverage up to  $3\text{ cm}$  thickness.



Figure 5.13: MAGIC telescope pointing upwards. In this position, the carbon fiber frame can be photographed easily. Mirrors were partially installed.

### Drive

The MAGIC Telescope is driven by high precision servo-motors. The azimuth axis of the telescope is equipped with two  $11\text{ kW}$  motors, while the elevation axis has a single  $11\text{ kW}$  motor. The transmission of the signals from the camera to the control house imposes a mechanical constraint on the movement of the telescope (otherwise the cables could be damaged): in azimuth the movement is limited to a range of  $450^\circ$ , while in zenith to  $-10^\circ$ .

The position of the telescope is measured in the mechanical telescope frame by three absolute 14-bit shaft-encoders. With this configuration is possible to monitor the telescope position with an accuracy of  $0.02^\circ$ . By using a high sensitivity CCD camera mounted on the reflector frame, the precision of the tracking system can be verified by monitoring both LEDs installed in the camera frame and stars from the celestial background (Starguider System). With this star-field tracking monitor system it has been measured that the telescope tracks to better than a  $1/10$  of a pixel size.

### Mirrors

The Čerenkov light produced by air showers is collected and focused to the camera by an octagonal shape tessellated mirror reflector of  $239\text{ m}^2$  area. The overall curvature of the reflector is parabolic to minimize the spread in the arrival time of the Čerenkov photons to the camera plane. To assure high optical quality images at the camera, the focal length to diameter ratio ( $f/D$ ) is set to 1 (to lower astigmatism over  $3.6\text{ deg}$  diameter in the focal plane).

The telescope reflector consists of 964 mirror elements of an area of  $49.5 \times 49.5\text{ cm}^2$  each. 892 are placed in panels of 4 mirrors, and the rest in panels of 3 mirrors, located at the rim of the main

reflector. The curvature of the individual mirror tiles is spherical, and, because of the parabolic shape of the main reflector, their focal lengths are increased following their radial position on the dish; from 17 *m* at the center, to 18 *m* at the rim <sup>6</sup>.



Figure 5.14: Left: mirror panels ready to be shipped from MPI to La Palma. Right: a single mirror element.

The construction of the single mirror elements of the main reflector is another of the innovations of the MAGIC Telescope. The technology (adopted from the airplane industry) consists in using an aluminum honeycomb core to confer the panel lightness and stiffness. The front mirror plate is made of a 5 *mm* thick AlMgSi1.0 alloy, machined to spherical shape and polished by diamond milling to achieve the most adequate curvature radius for its position on the parabolic reflector. After the diamond milling, the mirror is coated with quartz to protect it from ageing and scratches. The aluminum plate is glued together with an aluminum honeycomb inside a thin aluminum box; and the final assembly (the so-called raw blank) weights only  $\sim 4$  *Kg*. A photograph of one of these mirrors and assembled panels is shown in figure 5.14. Each mirror panel is equipped with a heating system to prevent ice and dew formation, and to dry them up from condensate water before data taking after periods of high humidity.

The advantages of this mirror structure with respect to the conventional glass mirrors are:

- **Less weight:** which is fundamental for fast repositioning of the telescope.
- **Mirror heating:** the possibility to heat the mirrors to prevent the formation of dew and ice during operation.
- **Fast production technique:** as the diamond milling of the reflective surface takes only about 2 hours per mirror.
- **Cost effective production:** specially when a variety of slightly different curvatures are needed.
- **Longer life:** The dilatations and shrinks produced by temperature changes scratched several glass mirrors per year in the HEGRA telescopes.

The reflecting surface achieved has a mean reflectivity of  $\sim 85\%$  in the wavelength range 300-650 *nm* (the maximum 90% at  $\lambda \sim 450-550$  *nm* and the minimum 80% at  $\lambda \sim 340-360$  *nm*)

---

<sup>6</sup>The reflector is divided in 8 concentric zones with different curvature radii (ranging from 34 to 36 *m*) depending on its distance from the reflector's optical axis. The mirrors are selected for their best position to the dish.

and a roughness below  $10\text{ nm}$ , which produces an excellent image quality: 90% of the light from a parallel beam is focused within a circle of  $1.0 \pm 0.2\text{ cm}$  diameter (less than half of the MAGIC pixel size). During the commissioning of the telescope, the light collection efficiency of the reflector was measured with a high-resolution large dynamic range CCD camera. The active mirror area at time of measuring (including mirror imperfections, temporary defocusing, and all effects of shadowing) was estimated to be  $212\text{ m}^2$ . From several sources with a wavelength spectrum peaking at  $500\text{ nm}$ , the average specular reflectivity was measured to be  $0.77 \pm 0.04$ .

### Active Mirror Control

MAGIC structure is very rigid, but a novel system of Active Mirror Control (AMC) has been developed to allow mirror adjustments and small corrections during telescope turning (due to changes in weight distribution). This re-alignment of mirror elements is used to compensate the small residual deformations of the  $17\text{ m}$   $\varnothing$  frame. This is the first time that such technique is proposed and used in IACTs. The AMC works over lightweight panels of four pre-adjusted mirror elements together with a switchable laser pointer (see Figure 5.15). The panel is tilted by two stepping motors (full step  $1.8^\circ$ , holding torque  $50\text{ Ncm}$ ) while being monitored by a CCD video camera that compares on demand the actual laser spot position on the casing of the camera with the nominal one (defined by 4 reference LEDs located in the camera lids).

The Point Spread Function (PSF) of the reflector can be extracted from the analysis of the width of muon particles ( $\mu$ ) rings and from the comparison of Hillas parameters in real and MC data. The reflector is focused at a distance of  $10\text{ km}$  because this is the typical distance to the shower maximum of low zenith angle  $100\text{ GeV}$   $\gamma$ -ray showers. After AMC reflector adjustment, a point-like light source at this distance produces a Gaussian image at the camera plane with  $\sigma=10.5\text{ mm}$ , which corresponds to  $0.035^\circ$ .



Figure 5.15: Mirror panel lasers switched on during re-alignment procedure. Not all mirror panels were installed at the time of the photograph.

Due to a construction problem in mirror panel tolerances, the mirror panels were touching each other during the AMC mirror re-alignment and the performance was not the expected one, i.e, a fraction of mirrors was blocked and de-focused after the AMC procedure. The solution was to stagger all mirror panels following a chessboard pattern (see Figure 5.12). This prevented the mirror panels to touch each other during AMC re-alignment. After the mirror re-configuration, which took three weeks during the commissioning time, the AMC procedure worked correctly. The re-configuration of the mirror panels increase the time spread of photons focused to the camera. This may deteriorate the  $\gamma$ -hadron separation based on shower timing analysis. Any IACT has a minimal time-spread such as MAGIC, so the collaboration has started some studies on this direction. Up to now any IACT has used timing analysis in the  $\gamma$ -hadron separation and its power is still not demonstrated.

### 5.7.2 The camera

The camera is a vital element for a proper performance of a Čerenkov Telescope. In the camera, the conversion from Čerenkov photons to photo-electrons takes place and this affects the  $E_{\text{thr}}$ , as it depends directly on this conversion efficiency. In addition, the quality of the shower images which are recorded in the camera is relevant for the gamma/hadron separation. Continued dedicated *R&D* on camera design and performance is needed, as well as the incorporation of the latest technological developments available at the moment, to improve the signal to noise ratio.

In the last decade, IACT cameras underwent a development from a single photo-multiplier (PMT) version to cameras with a few hundred pixels. The more pixelized the camera, the better to resolve the differences between the background (hadron showers) and the signal ( $\gamma$  showers). Moreover, other improvements have been accomplished by the community by developing cameras with better trigger efficiencies for  $\gamma$ s, better angular resolutions and a modest noise reduction by decreasing the acquisition time to the short durations of the Čerenkov flashes.

Lowering the  $E_{\text{thr}}$  of an IACT can be achieved by constructing large mirror area reflectors (hence, more Čerenkov light is collected). This is rather expensive and complicated, from the technical point of view. In MAGIC, the mirror area has been increased up to an affordable size and in addition the conversion efficiencies from Čerenkov photons to photoelectrons have been improved in the camera PMTs. Moreover, non-sensitive regions (dead areas) in the camera have been reduced by using dedicated light concentrators.

We were interested to develop a camera which allows the study of showers which have never been observed by an IACT. These low energy showers ( $\leq 100 \text{ GeV}$ ) are rather compact and close to the central part of the MAGIC camera (due to trigger effects). This demands a finer pixelization of the camera in order to properly resolve these images and, quite importantly, to achieve a high-efficiency on photon detectors.

For MAGIC, in which the camera lies at 17 m from the mirror reflector, an important issue is the weight of the camera. To minimize the weight, size and heat dissipation of the MAGIC camera, most of the trigger and readout electronics is not included in the camera housing, but in a central data acquisition building, located 100 m away from the telescope. The very short (2-3 ns FWHM) PMT signals are transferred to the acquisition building by a system based on VCSEL drivers and optical fibers.

The camera of the MAGIC Telescope has been entirely designed and built at IFAE (Barcelona). The light collectors, VCSEL drivers and optical fibers have been developed in MPI (Munich).

#### Layout of the camera

An schematic of the MAGIC camera is shown in Figure 5.16. The inner part of the camera

is equipped with 397 PMTs with an angular diameter of  $0.1^\circ \text{ } \emptyset$  ( $30 \text{ mm } \emptyset$  in the camera plane), whereas the outer part of the camera is composed of 180 larger PMTs of  $0.2^\circ \text{ } \emptyset$  ( $60 \text{ mm } \emptyset$  in the camera plane). The trigger region is formed by the central 325 pixels from the inner zone. The camera in the telescope structure is supported on an aluminum arc reinforced with steel stressor cables to avoid sagging. Total size of the camera is  $1.5 \text{ m}$  in diameter and it weighs  $500 \text{ Kg}$ .

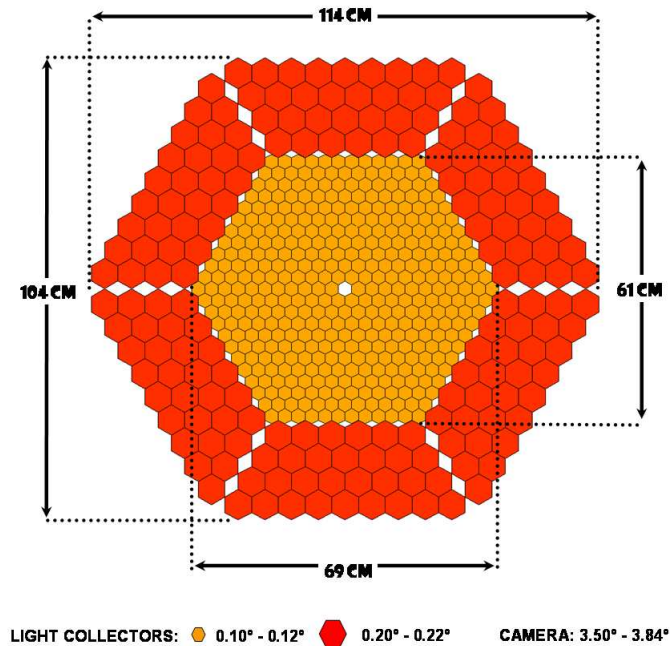


Figure 5.16: Schematic of the MAGIC camera. Inner region (colored orange) is equipped with 397  $0.1^\circ \text{ } \emptyset$  PMTs; outer region (colored red) is equipped with 180  $0.2^\circ \text{ } \emptyset$  PMTs.

The use of two different PMT sizes is mainly due to a compromise between telescope performance and cost. As the goal of the MAGIC telescope is to analyze low energetic showers, which are recorded at the center of the camera, finer pixelization is used. Separately, the outer region of the camera records Čerenkov photons from the shower tails, where the statistical fluctuations in the shower development are larger. This implies more diffuse images in this region of the camera. In addition, the optical quality is degraded by the coma aberration. The outer region is equipped with coarser PMTs of  $0.2^\circ \text{ } \emptyset$ , as the image quality is not deteriorated with respect to a camera entirely equipped with  $0.1^\circ \text{ } \emptyset$  PMTs. The net effect is a reduction of the camera weight (less channels) and specially the total cost of the camera.

The MAGIC camera has the following features:

- **Fine granularity:** as said, allows to resolve the features of low energy shower images and allows for an efficient  $\gamma$ /hadron discrimination. Moreover, the integrated noise per pixel is reduced and trigger threshold at the discriminator level can be lowered. This facilitates the reduction of the  $E_{\text{thr}}$  of the Telescope.
- **Large Field of View:** the  $3.5^\circ - 3.8^\circ \text{ } \emptyset$  camera field of view (FOV) assures recording most of shower images ( $\gamma$ -showers up to  $10 \text{ TeV}$  for low zenith angles).
- **Low noise:** The detection of Čerenkov pulses suffers from a strong background of *Night Sky Background* (NSB) photons. The response of the whole system is fast to reduce the width of

the pulses at trigger level to only a few nanoseconds (i.e, less integrated noise per Čerenkov flash pulse).

- **Low Gain operation:** Low gain operation reduces the noise level recorded by the camera. Since we as well operate the telescope under strong moonlight, we are forced to operate with a relatively low gain around  $1 - 2 \times 10^4$ , in contrast to typical gains around  $10^6$ .



Figure 5.17: The MAGIC camera ready to be shipped from IFAE to La Palma with the light collectors matrix already installed.

### Light Collectors:

Another important element is the light concentrator cones placed in front of the photodetector matrix (see Figure 5.17). PMTs have a sensitive area significantly smaller than their outer dimensions and a sizable fraction of light is lost (also because dead spaces between PMTs). A specially designed light collector is needed to collect as much light as possible into the PMTs. The light collectors were made by the MPI by using plastic material covered with aluminized Mylar foil of  $\sim 85\%$  reflectivity.

These light concentrators provide:

- nearly 100% active area by minimizing the dead space between pixels. Entrance window allows perfect compactness of the camera. Light concentrators output window has circular shape that couples to the round most active area of the PMTs. This increases the photon detection of the PMTs by about 50%.
- a rejection of a large fraction of light coming with an incident angle larger than the one defined by the last ring of mirrors of the telescope reflector (for example back-scattered light from the ground, during moonshine or distant light from human installations, cars, snow in winter, etc...). This considerably reduces the level of background light in the camera.
- an enhancement of the probability of photon double cathode crossing, thus improving the QE of the PMTs by  $\sim 15\%$ : for some incident angles of the photon reaching the cathode, they can cross twice the sensitive area, hence the effective QE increases. Actually, the design of the light collectors is thought to improve the double crossing feature.

### Protective plexiglass cover:

A front cover made by 2 *mm* thick UV transmitting plexiglass protects the PMTs and light collectors from the environmental conditions and hermetically seals the electronic sensors and camera elements from humidity and dust (for typical sand storms or *calima*, thermal isolation and water-tightness). Due to the reflectivity of the plexiglass, the amount of light which arrives to the light collectors is about 95% of the total light focused by the parabolic mirror into the camera plane.



Figure 5.18: Photograph of the MAGIC camera installed in the Telescope frame.

### Camera focus distances

The camera can be shifted along the telescope axis to and away from the reflector to set different focus positions. The camera runs along four guides and it is fixed to its position with two nuts, one at each side of the camera. Using the right wrench one can manually shift the camera along the guides.

The most important positions defined along this axis are:

- **Focus to Infinity/Stars:** if the camera is 17 *m* away from the reflector, i.e. camera is at the reflector focus. Stars should have the minimal spread at this position. This spread actually defines the reflector PSF.
- **Focus to Showers:** when the camera is 3 *cm* further away from the reflector, i.e. 17.03 *m* away from the reflector. For this position the reflector focuses objects that are 10 *km* away into the camera plane. This is the distance to a typical shower and cosmic ray data are taken at this position.
- **Focus to Roque:** when the camera is 30 *cm* further away than the focus, that is 17.30 *m* away from the reflector. For this position the reflector focuses objects that are 1 *km* away into the camera plane. This is approximately the distance from the telescope to the nearby highest altitude site place (“El Roque de los Muchachos”). A lamp installed in this area is used to re-align manually the telescope mirrors once every two or three months.

Camera technical details are given in a separate Chapter.

### Photon-detectors

Several photo-sensors were considered for installation in the MAGIC camera: photomultiplier tubes (PMTs), hybrid photo-multipliers (HPDs) and avalanche photodiodes (APDs). Although HPDs and APDs offered higher quantum efficiencies, the restricted size of the active area and high prices of such devices would have made a deep impact into the total cost of the telescope. Hence, the option of using a special production of PMTs satisfying all MAGIC requirements was adopted and we left the possibility of using HPDs for the camera of the second upgraded MAGIC telescope.

The PMTs were produced in a dedicated R&D cooperation with the English company *Electron Tubes* (ET). The outcome of this collaboration was the design and construction of brand new 9116A and 9117A type PMTs from ET. They differ from conventional produced PMTs and they needed special techniques to be employed in their production.

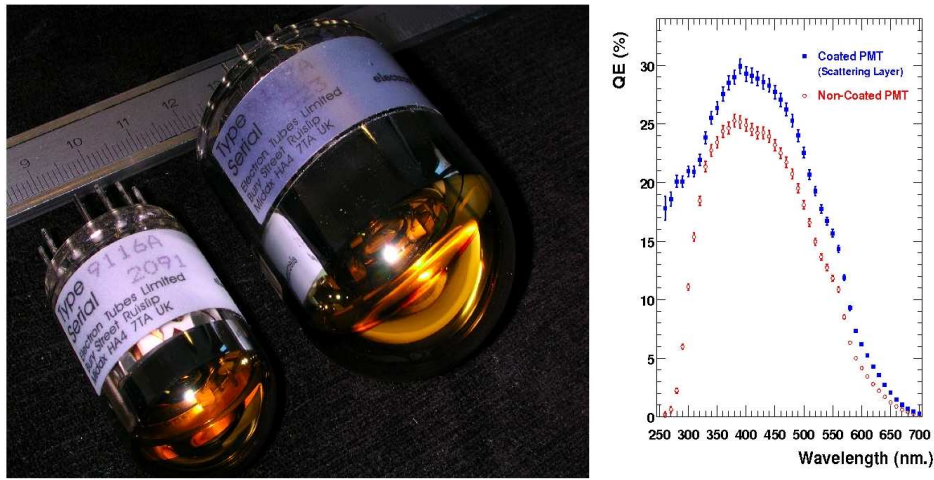


Figure 5.19: Left: the two pixel sizes in the MAGIC Telescope’s camera (without coating). Right: QE of the ET9116A PMT before and after coating with a scattering layer and a wavelength shifter.

These pixels have 6 dynodes (circular focused), as they are expected to work at a lower gain than the usual 10 – 12 dynodes PMTs. Lower dynode developed PMTs allows for a low gain ( $1 - 2 \cdot 10^4$ ) with good inter-dynode electron collection efficiency and a low inter-dynode time spread compared to conventional PMTs. Moreover, the induced noise photo-electron rates is reduced (a few hundred MHz). Their cathode is hemispherical to enhance the probability of *photon double crossing*: a photon arriving with an appropriate angle of incidence to the PMT will cross twice the photocathode, enhancing the response of the PMT through an increase of the probability of generation of photoelectrons. In addition, this cathode design provides better light collection compared with the flat cathode PMTs.

The short path of the electrons through 6 dynodes and the major symmetry of the hemispherical cathode make these PMTs achieve a rise time of 700 ps with a FWHM  $\sim 1 - 1.2$  ns. In addition, because all PMTs have roughly the same path length between photocathode and first dynode, the time jitter is minimized and allows to implement a very fast trigger. This reduces the integrated noise recorded per triggered shower.

The PMTs are coated by a scattering layer and a wavelength shifter that convert the photons in the near-UV range into photons in a range where the PMT have a higher quantum efficiency (QE). This technique enhance the average QE of the PMTs in  $\sim 20 - 25\%$  [193]. Furthermore,

the matrix of *light collectors* installed in the front part of the PMTs is designed to also enhance the probability of double crossing, thus improving the QE of the PMTs by  $\sim 15\%$ . Adding up the effect of all these components a QE of  $\sim 20\%$  between 250 nm to 700 nm has been measured. The peak QE is  $\sim 30\%$  at 400 nm (Figure 5.19 right). This improvement is very important for the telescope performance as it reduces the  $E_{\text{thr}}$  of the telescope. Inner pixels with less QE (low manufactured *Corning Blue*<sup>7</sup> values) were installed in the outmost part of the trigger region of the MAGIC camera, i.e., in the last two rings of inner pixels region.

The voltage applied to each dynode is selected in a way in which the compromise between *single-photoelectron response* and *after-pulsing* is optimized. The single-photoelectron response is the easiest and most direct way of calibrating a PMT. A PMT operates in single-photoelectron mode whenever the HV is tuned so that the distribution of signals in the anode shows a distinctive peak produced by single-photon events, that is, this peak can be separated from the pedestal and the next peak corresponding to two photoelectrons. The single photoelectron mode generally requires a higher voltage in the dynode system. On the other hand, the after-pulsing is an effect of the collision between a generated photoelectron and a free atom in the volume between the photocathode and the first dynode inside the PMT<sup>8</sup>. The collision ionizes the atom with a positive charge. The ion falls in the potential drop and finally collides into the photocathode producing a large amount of electrons. These electrons are amplified and result in a strong signal with a time gap of some hundred ns after the original pulse. In an IACT, the PMT system works in a self-triggering mode. Lowering the  $E_{\text{thr}}$  of the telescope is limited by the after-pulse rate caused by single *phe* pulses produced by the Light Of Night Sky (LONS). Therefore a low after pulse rate is required.

By increasing the HV difference between the photocathode and the first dynode the single photoelectron response improves, but also the probability of after-pulsing. After detailed studies [200], the configuration that maintains the after-pulsing rate below a reasonable level and allows, up to a certain degree, the single photoelectron response is 3 : 1 : 1 : 1 : 1 : 1 (from cathode to anode). It was also found that further increasing the HV difference in the fifth and sixth dynode by 50 V increases the dynamic range of photoelectrons to  $5 \times 10^3$ .

Figure 5.20 shows the scheme of the HV distribution in the PMT. The first five amplification stages ( $HV_{C-1}$ ,  $HV_{1-2}$ , ...,  $HV_{4-5}$ ) are powered through a main HV power supply.  $HV_{C-1}$  is fixed to 360 V by using two Zener diodes and  $HV_{1-2, \dots}$  and  $HV_{4-5}$  are all equal and regulated individually for each pixel. The last two dynodes need an independent power supply in order to get a high current and maintain the voltage difference even when there is a large electron multiplication. The voltage between D5 and the anode ( $HV_{5-6} + HV_{6-A}$ ) is fixed actively using the so-called Active Load power supply to 350 V. The voltage between D6 and the anode is set by an independent power supply to 175 V.

In order to compensate the low gain of the PMT, a 1 GHz bandwidth transimpedance amplifier has been developed. The amplifier output noise is  $\sigma_{\text{noise}} \leq 0.2mV$  for a gain of  $\sim 8$ , which corresponds to an Equivalent Noise Charge (ENC) of  $\leq 0.2$  electrons at a PMT gain of  $2 \cdot 10^4$ , i.e., the amplifier noise is low enough to still resolve single *phe* signals.

### Signal transmission via optical link system

The trigger and readout electronics are not located in the camera but in the telescope control house which is located 100 m away from the telescope. This offers several advantages, like simplified

<sup>7</sup>The *Corning Blue* characterizes the photon sensitivity of the PMT at  $\lambda \sim 400$  nm (i.e., blue region).

<sup>8</sup>The number of free atoms inside the PMTs of the camera of MAGIC is relatively high compared with conventional PMTs, because inside them the vacuum is low in order to allow a more thin glass cover in the photocathode and thus enhance the probability of detection.

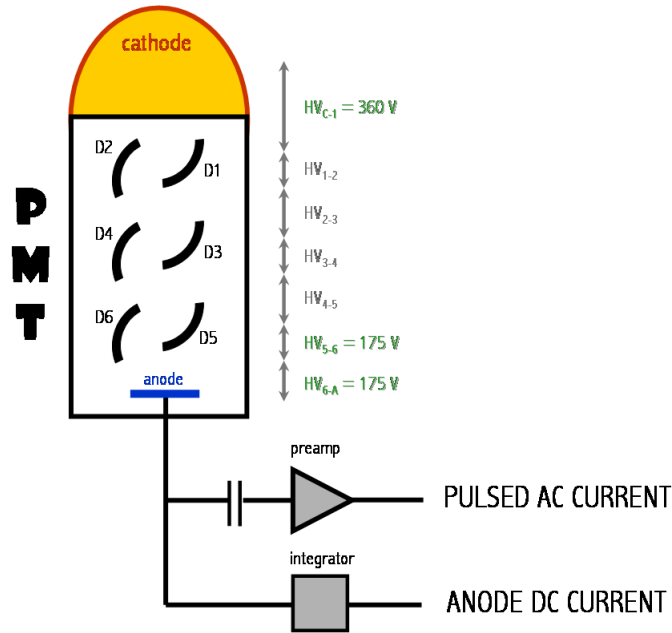


Figure 5.20: Scheme of the HV distribution system in the PMT. The six dynodes are labeled as D1, D2, etc...  $HV_{C-1}$  is the cathode to first dynode voltage,  $HV_{1-2}$  the first to second cathode, etc, and  $HV_{6-A}$  is the sixth dynode to anode voltage.

camera maintenance and a light and small-size camera which reduces oscillations and the need of heavy telescope counter-weights (a requirement for fast telescope movements). The lack of trigger and acquisition systems in the camera helps reducing the pickup noise which affects to the PMT analogue signals. Moreover, the heat dissipation inside the camera is lowered, and a cheaper and lighter cooling system can be used (normally, the MAGIC camera dissipates  $800\text{ W}$ , while the FADC system dissipates  $20\text{ kW}$ ). The electronic pixel chain is modular, allowing for further updates on the trigger system of FADC system without modifying the camera (upgrading tests can be easily made in observation nights).

However, this design has disadvantages. The most important one is the attenuation and distortion of analogue PMT pulsed signals during the transmission to the acquisition building. Although the control house is located at  $100\text{ m}$  from the telescope, the real distance to the camera is  $\sim 162\text{ m}$ , as the cables have to be properly routed through the telescope frame. The degradation of the signal can be significant if we take into account that the pulsed signals produced by the Čerenkov light flashes are very short ( $2\text{-}3\text{ ns}$ ).

In order to minimize pulse degradation, MAGIC uses optical fibers to transfer the analogue PMT pulse signals. Optical signals are obtained by using a *Vertical Cavity Surface Emitting Laser* (VCSEL). These optical signals are transmitted to the control house via multi-mode graded index fibers ( $50\text{ }\mu\text{m}$   $\varnothing$  core,  $125\text{ }\mu\text{m}$   $\varnothing$  cladding). Once the signal is in the control house, the so-called *receiver board* transforms the optical pulses back to electrical pulses by PIN-diodes. Signal can further be processed by the trigger and the FADC system.

This optical transmission system has several advantages with respect to the one based on coaxial cables:

- Dispersion and attenuation of  $ns$  pulses is significantly lower. In a good quality coaxial cable (RG 58 C/U) the attenuation is of about  $24\text{ dB}/100\text{ m}$  at  $200\text{ MHz}$ , whereas for a optical

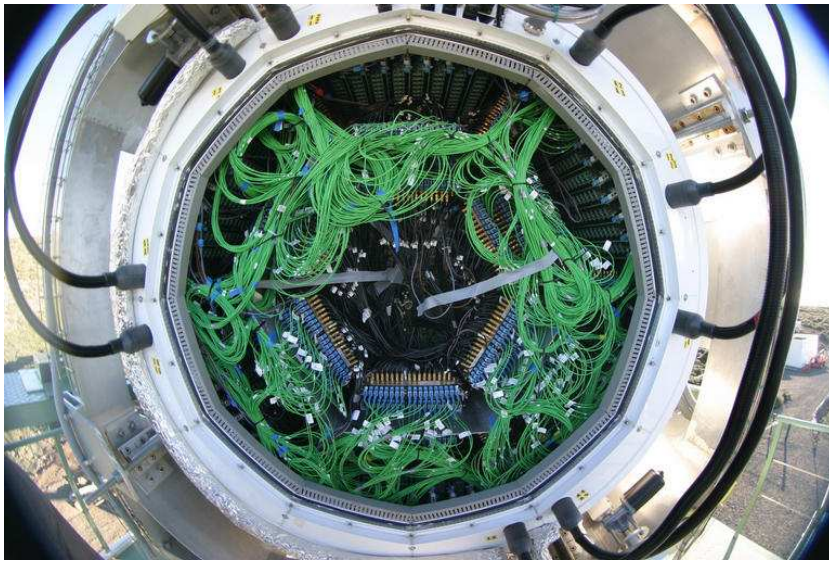


Figure 5.21: Rear part of the PMT camera. Shown are the coaxial cables that connect the pixel base and the Transmitter Boards (black cables in the central part), the VCSELs (inside the metal boxes the blue connectors are attached to) and the optical fibers (green cables).

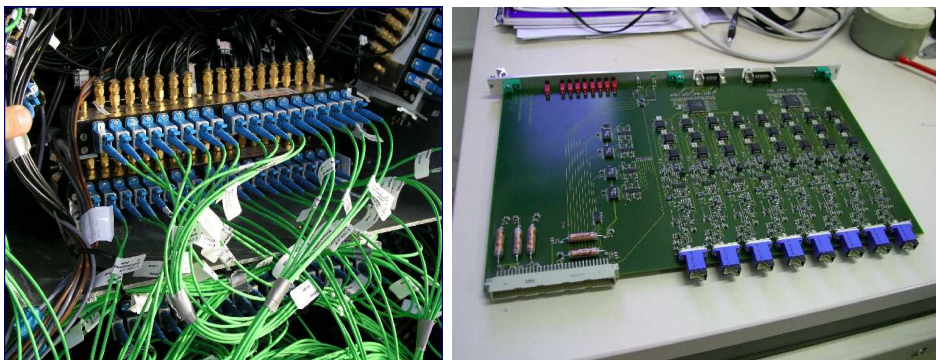


Figure 5.22: Photograph of two transmitter boards installed in the MAGIC telescope camera (left) and a receiver board used to convert the light pulses to electrical ones at the control house (right).

fiber like the one used in the MAGIC telescope this value is  $0.3\text{dB}/100\text{m}$  at  $500\text{ MHz}$ .

- The optical system is more compact and lighter than a system based on coaxial cables. For MAGIC, 72 fibers are packed into a single cable  $16\text{ mm}$   $\varnothing$ . A single coaxial cable has already a diameter of  $5\text{ mm}$ . Optical fibers are a factor 10 lighter than coaxial cables. This reduces the inertia of the telescope, important for fast repositioning.
- There is no cross-talk between channels and any interference due to electromagnetic pickup noise while signal traveling to the control house. Because fibers are made by glass material, which is not conductive, they are immune to lightning strikes. This protects the acquisition system from storms.

It has to be noted that the VCSELs transmitters are quite novel devices, used normally for digital signal transmission. Instabilities in gain and noise performance are present when using

these devices in analogue transmission mode. Special *R&D* was done in order to modify these units to bring the instabilities below the statistical fluctuations of the MAGIC PMT signals [193]. Quality checks were also done in order to reject and to replace VCSEL lasers not fulfilling the strict requirement by the MAGIC collaboration.

In order to transfer the pulsed PMT signals, a total of 36 transmitter boards which contain 18 VCSEL each are installed inside the camera. Figure 5.22 shows a photograph of two transmitter boards already installed in the camera. We use 25 transmitter boards to transfer the signal of the inner PMTs and the remaining 11 to transmit the outer pixel signals. Out of 648 VCSELs installed, only 576 are used. The remaining 72 lasers are spare lasers to allow an easy replacement in case of any VCSEL failure.

The pulsed signal after the preamplifier stage goes through a coaxial cable (RG 174) with gold-plated SMA connector to the *Transmitter Boards*, also inside the camera and fastened to the structure known as *spider*. In the Transmitter Boards the voltage signal from the PMT is converted into current signals which modulate the current flowing through the VCSEL, hence modulating the light output signal. A total of 72 transmitter boards handle the signals of whole camera pixels. Due to AC coupling at the input of the board, the constant light produced by the constant forward current (bias current) flowing through the VCSELs is not amplified; only short PMT pulsed signals are amplified and transmitted to the rest of the acquisition chain. Finally, the optical fibers bring the light signals to the control house, where the optical receivers are installed. Each receiver board contains 8 channels to perform the light-to-electric signal conversion (see Figure 5.22).

Once the optical pulses have been converted to electrical pulses, they are split in two branches; one (the so-called *trigger signal*) goes to a discriminator (located in the same receiver board) which is part of the trigger system. The other branch (so-called *FADC signal*) going to the FADC system, where electric pulses are digitized (see Figure 5.23). Due to digitization speed of  $300 \text{ Msample/s}$  of the current MAGIC FADC system, the signal is stretched in the receiver board to  $\sim 6 \text{ ns}$  FWHM so that at least 4 *samples* can be measured for each pulse. The *FADC signal* is split (also in the receiver board) into *high* and *low* gain channels. The high gain channel is amplified by a factor of 10 and the low gain channel is delayed by  $50 \text{ ns}$ . If the recorded signal exceeds a preset threshold, the delayed low gain signal is combined with the high gain signal using a fast *GaAs* switch, and then digitized consecutively after the high gain signal by the same *FADC* channel. This signal splitting procedure increases the dynamic range of the current 8-bit FADCs by at least 2 bits.

### 5.7.3 The trigger system

The trigger region in the camera of the MAGIC Telescope is restricted to the innermost 325 (out of 397) pixels of the camera. As shown in Figure 5.24, this region is covered by 19 overlapping cells (called macrocells) of 36 pixels<sup>9</sup>.

The trigger system is segmented into three stages or levels; the so-called level 0, level 1, and level 2 trigger:

- **Level 0:** The level 0 trigger is located in the receiver board, and acts on individual PMT signals. The pulses coming from the telescope camera arrive to the receiver board and are split into two branches; the trigger signal and the FADC signal (see Figure 5.23). Whenever the amplitude of the PMT pulses is above a certain predefined value (threshold), the discriminator produces a square pulse of adjustable width. The width is set to  $6.0 \text{ ns}$ <sup>10</sup>. The discriminator threshold is set by an 8-bit DAC that is controlled by the PC in which the Central Control

<sup>9</sup>Topologically, each *macrocell* is formed by 37 pixels; however there is actually one pixel (out of the 37) which is not wired to the trigger logic.

<sup>10</sup>Actually, due to the time reaction of the electronics, the shape of these pulses is distorted and it is not really square. The FWHM of these pulses was measured to be about  $5.5 \text{ ns}$



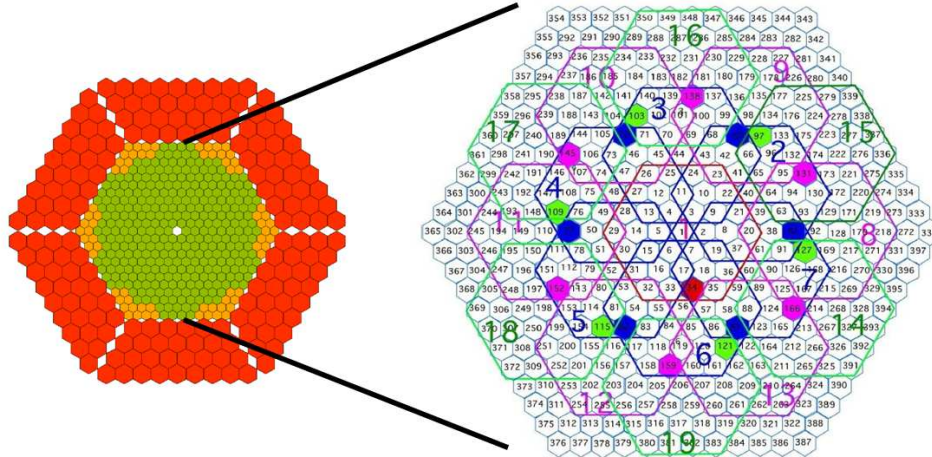


Figure 5.24: The trigger region in the MAGIC camera.

The level 2 trigger communicates directly with the digital boards of the FADC system (see Figure 5.23) enabling the acquisition of the data whenever an event triggers in the above mentioned 3 trigger levels.

It must be pointed out that the level 2 trigger also contains a prescaler board that can prescale the triggers (0-65535) in order not to overcome the maximum (continuous) acquisition rate allowed by the DAQ, which is 1  $kHz$ . However, the level 2 trigger can handle trigger rates up to  $\sim 1 MHz$ . This might be a very valuable feature when performing observations at very low  $E_{thr}$  ( $< 20 GeV$ ), as it is planned for some gamma ray emitting pulsars, and specially, in the case of observation of AGNs in flare state and GRBs, where the trigger rate might go up to several tens of  $kHz$ . In order to keep as much of this additional information as possible, the level 2 trigger is able to send a high frequency trigger (which also can be prescaled) through a second independent line to the digital modules of the FADC system.

The individual pixel rates of the channels included in the trigger region are monitored using 100  $MHz$  scalers and these values are used to dynamically regulate the discriminator thresholds for each individual pixel. This Individual Pixel Rate Control (IPRC) acts only on pixels that are affected by stars brighter than  $4^m$ . In normal observation, the global trigger rate is about 250  $Hz$  for extragalactic sources (standard pixel threshold) and about 200  $Hz$  for galactic sources (increased pixel threshold). According to the full MC simulation this rate corresponds to a trigger threshold around 60  $GeV$ .

#### 5.7.4 The data acquisition system

The data acquisition system (DAQ) of MAGIC consists on 18 crates of 4 FADC boards, and a dual processor PC (the so-called DAQ PC) running a multi-threaded C++ readout program in a Linux operative system. Each FADC board is prepared to digitalize the signals coming from 8 channels. The components of the DAQ for one of the channels are shown in Figure 5.23. There is a 8-bit 500  $MHz$  bandwidth FADC chip which digitalizes at a speed of 300  $MSamples/s$ , a 32  $KBytes$  ringbuffer, and a 512  $KBytes$  First Input First Output (FiFo) module.

The FADC chips continuously digitalize the analogue PMT signals that come from the receiver boards and store them in the ringbuffers. As pointed out, the PMT signals are stretched to  $\sim 6$

$ns$  FWHM in the receiver board (so that the FADC chips can measure the pulse amplitude at  $\sim 4$  points). Then the signals are divided into two branches (high gain and low gain) in order to increase the dynamic range to  $\sim 60$  dB. When a level 2 trigger arrives to the FADC modules, the FADC chip stops digitalizing, the position of the signal in the ringbuffer is determined, and 30 time slices (15 for high gain and 15 for low gain) are written into the FiFo buffer for each pixel. This operation is performed at a maximum rate of  $80$  MBytes/s. The readout of the ring buffer results in a dead time of  $\sim 20$   $\mu s$ , which results in 2% dead time at the design trigger rate of  $1$  kHz. The time and trigger information for each event is recorded by dedicated digital modules, which are read out together with the FADC boards.



Figure 5.25: The DAQ system of the MAGIC camera.

As mentioned, during observations of AGNs in active state, low energy signals from strong pulsars and GRBs, the trigger rate could exceed the  $\sim 1$  kHz data taking capability of the DAQ. Because of that, the DAQ is provided with a separated high frequency data stream which records only the time and trigger information of the events sent by the dedicated high frequency 2 level trigger, that can reach rates of up to  $\sim 1$  MHz. Although the system has been tested, these rates have never occurred up to now during normal data taking.

The FADC data is reorganized and merged into a raw event data format. The data is saved into a RAID0 disk system at a rate of up to  $20$  MBytes/s, which can amount to up to  $800$  GBytes per night. During daytime the data is transformed into ROOT format and written to tape. During normal telescope operation, the complete readout program running in the DAQ PC is controlled remotely via TCP/IP by the Central Control.

### 5.7.5 The calibration system

The analysis of shower images produced in the camera of an IACT is based on the comparison of measured image shape and light content with the MonteCarlo (MC) predictions. The conversion factors between the recorded amount of FADC counts and the amount of photons impinging on the camera must be perfectly known for every individual pixel. This is the only way to properly estimate the energy of the primary  $\gamma$ -ray after  $\gamma$ /hadron separation. Therefore, it is absolutely needed to calibrate the telescope camera with respect to the light flux.

A novel system which allows to perform the optical calibration over a large dynamic range and in an absolute manner, i.e., correcting also for the individual PMT sensitivity (QE and *phe* collection efficiency), and light concentrators efficiency has been built by the MAGIC collaboration [201]. The calibration system design is another innovation of the telescope. It provides ultra-fast light pulses from pulse LEDs (green, blue and UV) with intensities variable by a factor greater than 100 in order to calibrate the whole dynamic range of the camera and the readout chain. At the same time, a continuous light source is provided in four different colors and variable intensities to simulate star and moon light. The absolute light flux is measured with additional devices: three blinded pixels in the MAGIC camera and a calibrated PIN-diode situated between the camera and the pulser box. Moreover, the calibration system provides a sophisticated trigger system which allows to pulse the system up to 4 *kHz*.

Valibration system technical details are explained in a separate Chapter.

#### Calibration methods

The two methods used to calibrate the individual camera pixels with respect to the amount of photons produced in each calibration light pulse are the so-called *blind pixel method* and the *PIN-diode method*:

- The *blind pixel method* compares the signal in the camera pixels with the response of special pixels (blinded pixels), which are illuminated through diaphragms of exactly 1 *cm*<sup>2</sup> and filters that attenuate the signal. The camera pixels record strong signals while the *blinded pixels* resolve single photoelectrons. The single *phe* spectrum of this pixel can be fitted by a sum of Gaussian distributions whose amplitudes are Poisson distributed:

$$f(x) = \sum_{k=0}^N \frac{e^{-\lambda} \cdot \lambda^k}{k!} \cdot \frac{e^{-\frac{(x-\mu_k)^2}{2\sigma_k^2}}}{\sigma_k \cdot \sqrt{2\pi}} \quad (5.12)$$

The fit provides (in addition to the values of  $\sigma_k$ ), the mean number of photoelectrons  $\lambda$ , which is used, together with the *QE* of the PMT used as blinded pixel, the emitted light spectrum of the used LED type, and the geometry of the blinded pixel to calculate the mean number of incident photons per pulse and area at the camera plane.

- The *PIN-diode method* compares the signal in the camera pixels with the one measured by a PIN-diode located at 1.1 *m* distance from the pulser box, and read out with a charge sensitive preamplifier (of 25 *ns* shaping time). The PIN-diode is calibrated with two radioactive sources emitting known gamma emission lines, which generate a precise charge distribution in the depletion region of the silicon diode. The mean number of photons per pulse and area at the camera plane is calculated from the measured number of *phes* in the diode, the *QE* of the diode, the emitted light spectrum of the used LED type, and the geometry of the system.

A third method is also used, the so-called excess noise factor method ( $F$ -factor method), which is a more conventional method (used already in past Čerenkov telescopes like HEGRA and WHIPPLE), to crosscheck the results obtained with the previous two methods. The excess noise factor method provides, for each individual PMT in the camera, the mean number of *phes* ( $\bar{n}_{phe}$ ) reaching the first dynode and being amplified. Such number is given by

$$\bar{n}_{phe} = F^2 \cdot \frac{\bar{Q} - \bar{P}}{\sigma_Q^2 - \sigma_P^2} \quad (5.13)$$

where  $\bar{Q}$  is the mean charge of the distribution,  $\sigma_Q$  the standard deviation of this distribution,  $\bar{P}$  is the pedestal and  $\sigma_P$  the electronic noise.  $F$  is the so-called excess noise factor, and comes from the statistical fluctuations in the amplification of the electrons in the PMT dynode system. The quantity  $F$  is defined as

$$F \equiv \sqrt{1 + \frac{\sigma_G}{\bar{G}}} \quad (5.14)$$

where  $\bar{G}$  is the gain of the PMT and  $\sigma_G$  its standard deviation. A typical way of measuring  $\bar{G}$  and  $\sigma_G$  in a PMT is by studying the response of the PMT to single *phes*. Obviously, these quantities depend on the PMT type and the high voltage settings used to drive the PMT. For the PMTs and the high voltage settings used in the camera of MAGIC, the value of  $F$  is around 1.15.

The advantage of the excess noise factor method with respect to the two previously mentioned methods is its simplicity and robustness. The big disadvantage, however, is that the excess noise factor method does not take into account neither the QE and *phe* collection efficiency of the PMTs (which can vary from PMT to PMT) nor the transmission efficiency of the light guides, whereas the blinded pixel and the PIN-diode methods do.

Note that such a calibration system provides three independent methods (containing different systematic errors) for the calibration of the camera; two methods measure the photon flux and a third one measures the number of *phes* arriving to the first dynode of the PMTs. This design increases the reliability in the calibration procedure, and allows to monitor possible variations in the performance of the pixel chain, as well as in the different light measuring devices of the calibration system.

The calibration box also has a continuous light source whose intensity can be remotely adjusted. Its purpose is to simulate and calibrate the response of the PMTs to different conditions of background light<sup>11</sup>, which could be produced by the LONS and the presence of the moon and/or stars in the camera FOV.

### Current calibration procedure

The calibration system is connected to the trigger system of the telescope, which allows one to perform calibrations even during normal data taking. Calibration of the camera is done once or twice per night. Additionally, interlaced calibration events (UV-pulses) with a frequency of 50 Hz are taken while observing a source. This frequency allows to accumulate enough statistics before reaching the typical time scales of residual short-term fluctuations of the optical transmission gains. At present, the camera is continuously monitored and re-calibrated using the F-factor method. The PIN-diode has been installed and tested recently, as well as the blinded pixels. The light flux from the pulser has been measured, yielding consistent results with the F-factor method. Systematic errors of both methods are above 5%. Blinded pixels are being tested at the moment (2006).

---

<sup>11</sup>The background light increases the DC anode current of the PMTs, and thus, increases the noise in the PMT signal

The calibration system is also used to equalize the gain of all camera channels, i.e, equalize the system response (digitalized signals) when the pixels are illuminated by the same light pulse. The gains must be equalized in order to have the same dynamic range in the digitalizers for all channels and to set the discriminator thresholds to same voltage level for all channels. This equalization of gains is made in a iterative procedure by changing the PMT HVs to compensate for the differences in the channels. This process is generally known as *flat-fielding* and is done once every two or three months.

## 5.8 Status and first results of MAGIC telescope

The performance of the MAGIC telescope has been experimentally evaluated and found in good agreement with the expectations with MC. For the time being, the collaboration is performing regular analyses above 100 GeV. Since fall 2004, the telescope is collecting data from a list of astrophysical objects. Four galactic and four extra-galactic objects have been so far detected by MAGIC, one of which is a new discovery.

The Crab nebula, the excellent calibration candle, was detected by MAGIC soon during the commissioning phase [197]. The data was used for both technical and astrophysical studies. MAGIC has confirmed  $\gamma$ -ray emission from the supernova remnants (SNRs) HESS J1813-178 and HESS J1834-08 [185], shortly after their discovery by HESS [202]. VHE emission from the GC has also been detected [203], which is the observation discussed in this Thesis.

MAGIC has added to the list a new member to the list of VHE  $\gamma$ -ray emitters: the distant AGN 1ES 1218+304 ( $z=0.182$ ) [204]. The AGN 1959+650 was detected in the lowest ever observed emission state [205]. Mrk 501 and Mrk421 have been observed in high state emission [206]. Gamma-ray bursts are also monitored by MAGIC. Particularly, GRB050713a was observed only 40 *s* after the detection by SWIFT satellite. The analysis of the data shows no signal above  $\sim 150$  GeV [207].

Costamante & Ghisellini selected BL Lacs and Blazars detected by the EGRET Telescope were taken into account to perform a catalogue of suitable AGNs to be observed with the MAGIC telescope. The measured EGRET Blazar fluxes were extrapolated to the MAGIC energy detection range by applying the  $\gamma$ -absorption of the radiation by the extragalactic infrared background as well as an intrinsic SSC spectral break at around 50 *GeV*. In case of Costamante & Ghisellini sources, the absorption by the EBL was applied as well. The Thesis Author participated actively in this study [208], which was taken as a reference input for source scheduling.

See [209] for a review of the detected sources and wide observational prospects for the MAGIC telescope.



## Chapter 6

# Camera and Calibration remote control system, and software design

*The MAGIC group at IFAE has been responsible for developing the Camera, Calibration and Central Control systems of the MAGIC telescope. In particular, the Thesis Author was responsible for the development and maintenance of the main control software for the camera and calibration systems, as well as for the insertion of both systems into the telescope's central control system. In addition, the Author participated in the camera instrumentation, electronics testing and camera improvements prior to its installation into the telescope. After the camera installation, special tests were performed to assure the proper performance of the systems integrated into the global telescope system.*

*This Chapter is partially based on the technical papers J. Cortina, J. Flix et al (2006) [210] and J. Cortina, J. Flix et al (2004) [211].*

### 6.1 Camera slow control electronics

This section provides technical information about the design and the implementation of the camera electronics. Among several elements, we describe the PMT electronics base in which the pulsed signal is pre-amplified and the anode DC current is integrated; how the camera low voltage, high voltage and slow control lines are driven by means of mother boards in which all pixels are connected; multiplexed readout electronics for HV and DC currents monitor; camera High Voltage regulators; High Voltage power supplies and Active Loads; camera cooling and lids and camera Low Voltage system.

#### **PMT pre-amplifier base**

Each of the PMTs is equipped with an electronic base in which the pulsed signal and anode DC currents are decoupled. A picture of the electronic base is shown in Figure 6.1. The PMT is connected to the base through a white plastic circular connector placed on its right. The base has the same diameter of the PMT and ends with an 8-pin connector, which allows the pixel to be plugged into its corresponding mother board.

The nearest to PMT printed circuit boards (PCB) are the responsible to distribute the HV in the pixel, split the pulsed and DC signal, amplify the former and integrate the later. The pulsed signal is read through a capacitor (SMD0805 of 100 nF) and the signal is pre-amplified with a high bandwidth transimpedance amplifier. This compensates the low gain in the PMT. The

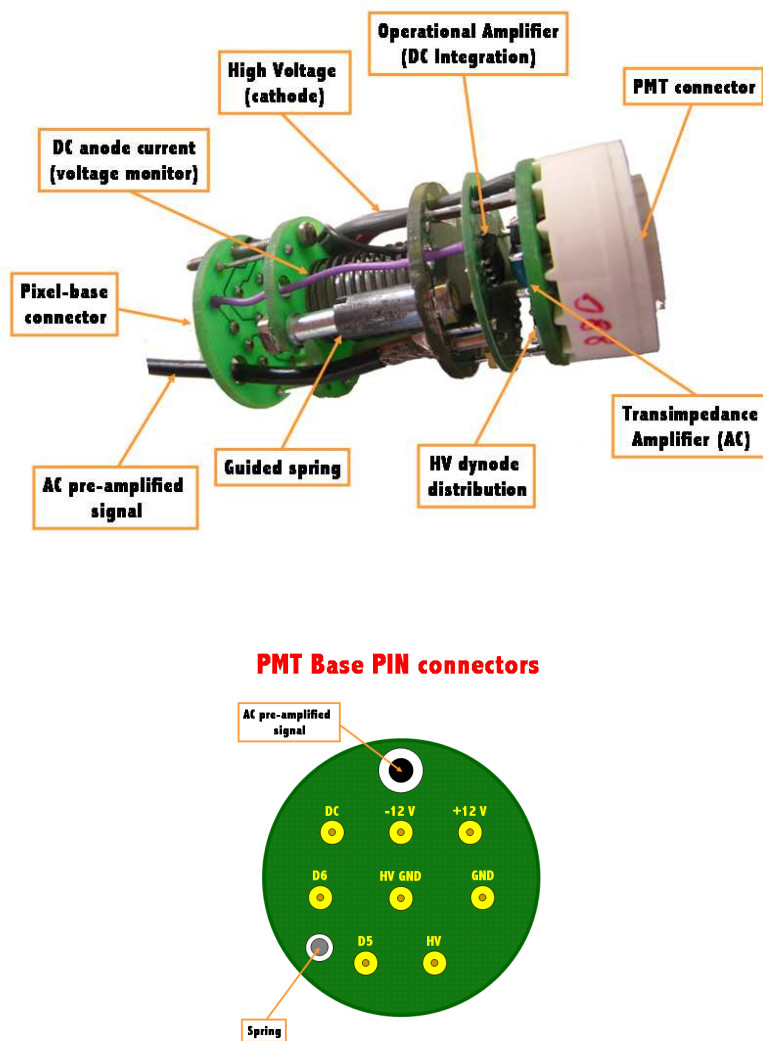


Figure 6.1: Top: an image of the complete electronic base is shown. Bottom: a scheme of the 8-pin connector at the bottom of the base, with a description of the functions of the pins (see text for more details).

DC current is driven from the anode directly to the integrator. The location of the operational amplifier (LF411-SOICB type, used normally for high-speed integration), which takes care of this integration, is indicated in Figure 6.1.

The base 8-pin connectors are used for input and output purposes (see Figure 6.1):

- DC → voltage output of the anode DC integrated signal (0-5 V).
- $\pm 12 V$  → power for the electronics of the base.
- GND → ground for the electronics of the base.
- D6 → HV in the 6th dynode, provided by the independent power supply ( $HV_{6-A} = 175V$ ).
- D5 → HV in the 5th dynode, provided by the Active Load ( $HV_{5-A} = 360V$ ).

- HV  $\rightarrow$  HV applied to the cathode (to be distributed to the rest of dynodes).
- HVGND  $\rightarrow$  ground of the HV.

The pixel base is equipped with a guided spring which allows to mechanically fix the pixel base to the specific mother board. This prevents pixel damage during telescope movements, avoids mechanical stress, and is used to adjust and fix the PMTs positions to contact the light collectors.

### Mother Boards

The camera is divided in 6 sectors (one for each of the equilateral triangles that form the camera hexagon). Each of the sectors is provided with a *mother board* which distributes the low voltage (LV) to all the electronics connected to it, and provides communication lines for HV setting and HV, and anode DC current monitoring for each pixel in the sector (see Figure 6.2). Each mother board (or sector) is separated in an inner and outer part, each containing 66 inner pixels and 30 outer pixels.

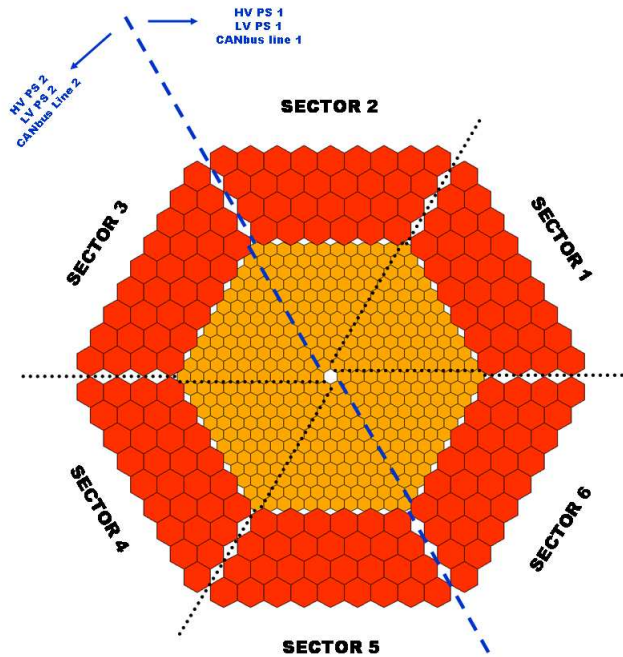


Figure 6.2: Layout of the camera sectors. The two halves of the camera are powered by independent low and high voltage power supplies, as well as two separate slow control communication lines.

The mother board is a PCB composed by 8 layers, in order to avoid crosstalk between lines. The mother board does not process any of the signals. It only acts as a support for transmission channels and is specifically designed to support High Voltage power lines. These lines are separated from the rest of tracks to prevent short-circuits and are located in the two outermost layers, together with the external tracks of the HV for the fifth and sixth dynodes.

The outer mother board hosts the connectors for the low and high voltage power supplies, the HV regulators, the setting of the HV, and the monitoring of HV and DC (see Figure 6.3). The inner mother board is connected to the outer with a flexible PCB terminated with a 128-pin connector and two more 64-pin connectors. The monitor lines (i.e., HV and anode DC currents) are driven to

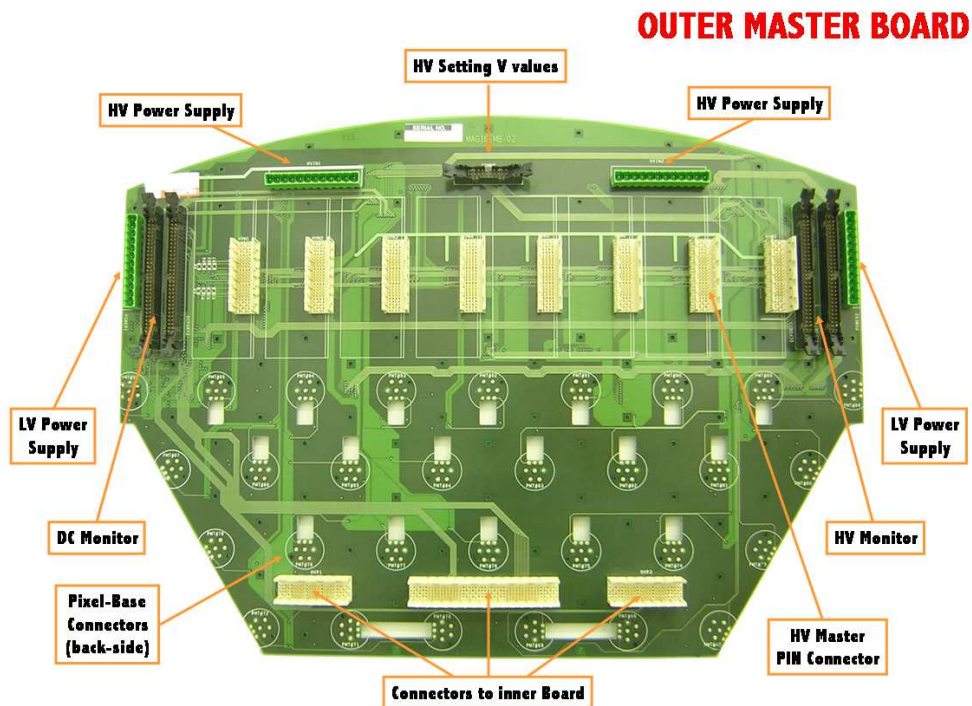


Figure 6.3: The back side of an outer mother board. A short text identifies the functions of the connectors. The PMT bases are plugged into the front part.

proper readout cards via two 60-pin connectors indicated in figure 6.3 (one for each 48 pixels). In addition, these connectors supply the low voltage needed to power the electronics in the monitoring digital cards.

### High Voltage distribution

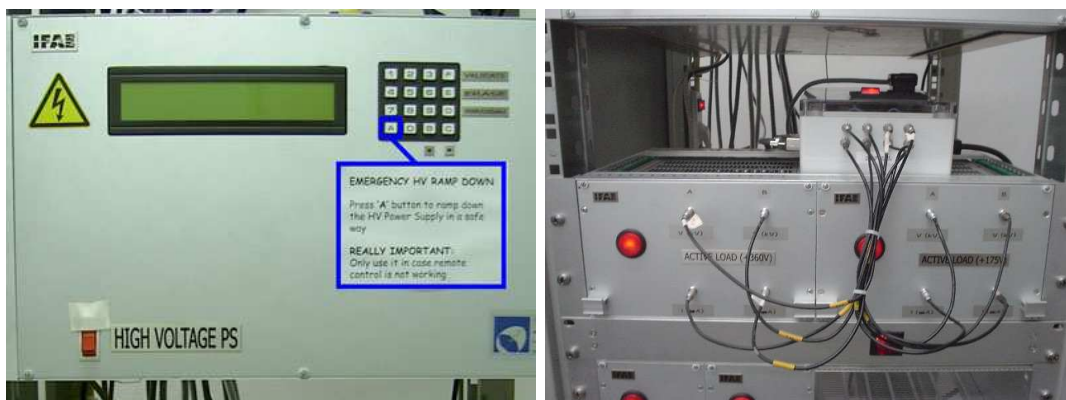


Figure 6.4: High Voltage power supplies of the MAGIC camera. Left: the two High Voltage power supplies embedded in a rack. Right: The Active Load power supplies (350V) and independent power supplies for the 6th PMT dynodes (175V) and their V/I output lines which goes to the monitor ADC board.

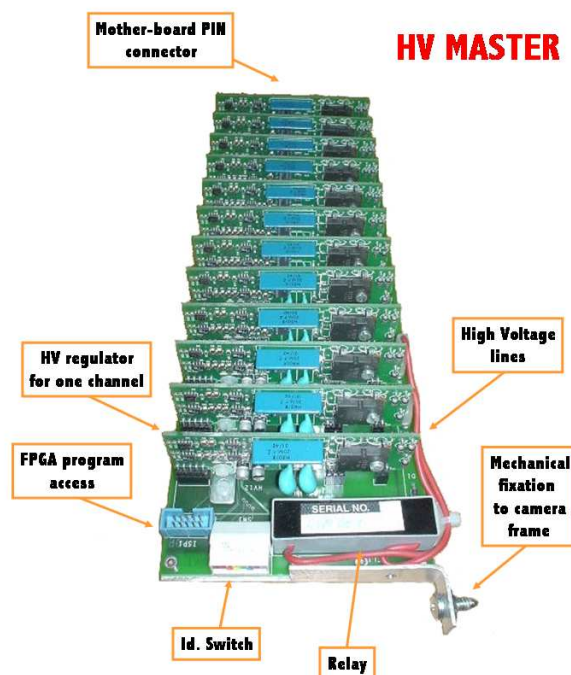


Figure 6.5: Upper view of one of the 48 HV Masters inside the camera, with its corresponding 12 HV regulators.

The High Voltage for the camera PMTs is provided by two external power supplies located at the control house. The High Voltage is transported to the camera through two coaxial cables. These independent lines power the two separate parts of the camera (sectors 1,2,6 and sectors 3,4,5). The power supplies are within a rack and, from the control point of view, are controlled as if they were only one power supply (figure 6.4 left). The control is done via RS-232 and the rack offers a display and a keyboard to manually set High Voltages (all these functionalities were specially designed in an internal microcontroller card). In case of an emergency, a procedure to ramp down the power supplies is also implemented.

The total high voltage provided by the external power supplies for each sector is regulated through 8 “HV Masters”, which are connected to the outer section of the mother board. Each of these HV masters hosts 12 “HV regulators” (figure 6.5), i.e. 96 HV regulators per sector or one per pixel. These HV regulators allow to vary the output voltage in a range from 0 to 2000V (the maximum supplied voltage). At the same time, each of these regulators has a low voltage output proportional to the output voltage. This output is used to monitor the HV applied for every channel.

Every HV master is provided with 3 chips (MAX525BC) each with 4 12-bits DACs. These DACs provide the control values for the HV channel settings. The chips are interconnected in serial mode as this simplifies the HV master hardware design. In parallel, the time to adjust all HV regulators would be reduced, but this improvement does not affect critically to the HV master performance.

Every HV Master incorporates an identifier address by means of a switch incorporated in the PCB board. All HV masters are connected to a common bus from which the control values are sent. A FPGA (VHDL programmed) compares the bus flow with the internal address, and allows to perform the actions in the case the HV channel to be regulated pertains to the particular master.

The communication to the masters is done by CANbus. The communication card which imprints the CAN bus frame format is the same as those used for HV/DC monitoring (but with specially burned FLASH ROM). This card also provides the HV setting interface to the remote control system.

Every HV master is provided with a relay which allows to quickly disconnect the HV in case of an emergency. Moreover, the HV Master incorporates a protection circuit in case of a short-circuit in the PMT base. This prevents the PMT to be damaged since the current flow is limited to 1 mA.

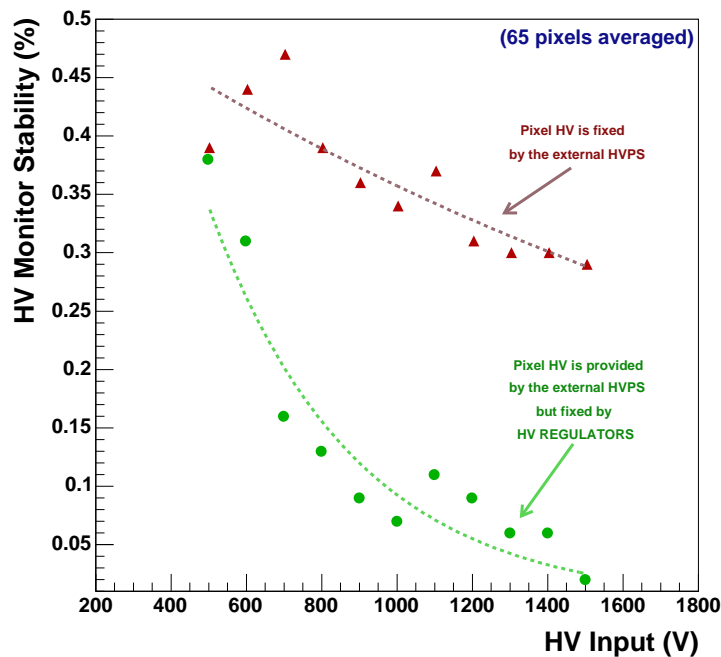


Figure 6.6: Pixel HV stability (for 65 pixels, averaged) when the voltage is directly provided by the HV power supplies and when voltage is controlled by the HV regulators, in which more stable values are obtained.

Figure 6.6 shows the stability provided by the High Voltage system. The high voltage provided by the external power supplies has an stability of 0.45% to 0.3%, depending on the voltage value. When the high voltage is regulated by the HV masters (i.e. the provided external HV is bigger than the maximum pixel regulated HV), the HVs are more stable, of about 0.1% at nominal values. These values were obtained by setting different HVs, waiting for stabilization and acquiring 5 minutes of data at 1Hz rate for 65 pixels. The values show the average stability value (defined as the  $rms$  of the  $HV_{measured}/HV_{applied}$  distribution). There are no differences on the HV stability for outer and inner pixels. When the telescope is taking data and nominal HVs are set, the stability of all camera pixels is a robust less than 0.1%. As above mentioned, the rest of voltages in the PMT are fixed by an *Active Load* (auto-regulated power dissipater that provides a fixed HV) for the 5th dynode to ground (360 V), and an independent power supply for the 6th dynode (175 V). There are two separate lines which powers the same sectors as the ones powered by the High Voltage power supplies. These additional power supplies are in the control room as well (figure 6.4 right) and the voltages are driven by coaxial cables to camera. A monitoring card (same as used for HV and DC monitoring, see below) is used to monitor the voltages and currents provided by these power supplies.

### Multiplexed HV and DC monitor cards

Each sector is equipped with two 12-bits ADC monitor cards to digitalize every pixel anode DC current and applied HV (these are the same boards which are used in the hadronic calorimeters of the ATLAS experiment). HV/DC separated monitor boards prevents losing part of pixel information in case of damages in the monitoring cards coming from an excess of light on some pixels, an accidentally high HV setting, or any short-circuit produced in a card. The camera DC currents and HV slow control is done with 12 monitoring boards in total. The communication between the camera control computer and all monitoring cards is done through two separate CANbus lines (see Figure 6.2). The CANbus frame format has been optimized in order to transfer the minimum quantity of information and get higher rates (for DC monitor purposes). A similar card monitors the currents and voltages in the Active Loads and additional High Voltage power supplies.

The connection between the mother board HV and DC monitor output lines (from 0 to 5 V) and the HV and DC monitoring cards is done through two 60-line flat cables. These lines are also used to power the monitor card electronics.

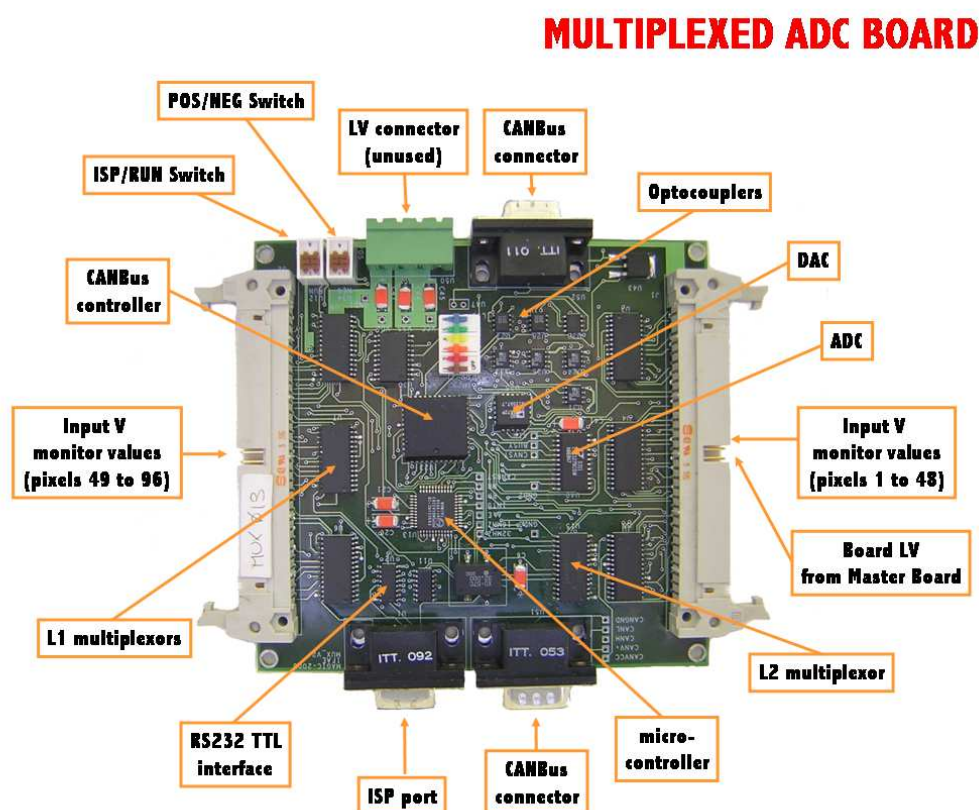


Figure 6.7: Multiplexer card for the monitoring of the DC or the HV. The main elements are pointed out.

Due to the large number of channels to be digitized, a multiplexing approach was considered and a special 4-layer PCB was designed [212]. The size of this board was critical and was reduced as much as possible by using SMD components. The main parts of the multiplexing and digitization (whose physical location on the card is illustrated in Figure 6.7) are [213]:

- A first level of multiplexing: six multiplexers (Intersil DG406DY), each one with 16 selectable

input channels (i.e. one channel per pixel in the sector) and one output (labeled as “L1 mux”).

- A second level of multiplexing: one multiplexer (Intersil DG406DY) with also 16 input channels. Only six channels, one for each of the previous multiplexers output, are actually used (labeled as “L2 mux”).
- A physical switch to choose either positive or negative output (POS/NEG), and thus use it to monitor DC or HV respectively. The monitoring of both signals is done in the same way except for their polarity.
- A Digital-to-Analog Converter or DAC (AD577JP).
- An ADC (Linear Technology ETC1279CSW) to digitalize the HV/DC analog monitor signal.
- A CANbus controller (Siemens Infineon 81C90).
- Two optocouplers (HCPL0501) to optically decouple the CANbus and the camera.
- A microcontroller (Phillips P89C51RC+) to coordinate all the actions between the rest of elements in the board. It is In-System Programming (*ISP*)-capable through a serial port. The conversion is done with a RS232-TTL interface (MAX232E). The software used to program the microcontroller is the “Philips ISP”.
- A CANbus physical interface or transceiver (Philips A82C250) required for the conversion of the digitalized signal after the optocouplers into a differential CANbus message.

There exist three versions of this monitoring card, as they have been upgraded in different camera accesses in order to improve their performance. For example, some capacities, Zener diodes and poly-fuses have been added to protect the card from current spikes in the power supplies or accidental short-circuits.

There is an important value to be set in all these monitor cards: a waiting time value (delay time) prior digitalizing the input value by the ADC. When a channel is selected for digitalizing purposes, due to capacitors which are present at this input stage, the input analog signal needs some time until it stabilizes. If this time is small, we are able to digitalize at high rates but the digitalized values are not stable at all for a stable input signal. This delay time can be changed remotely by software and special tests were done in the laboratory in order to choose the proper delay time. Figure 6.8 shows the deviations of the monitor card readout for a constant input signal for different delay times used on the test. In light of the results, a delay time value of 10 (a.u) was chosen. With this delay time, the anode DC currents for all camera pixels can be read up to 13 *Hz*. Other systems are read through the same bus and a *multi-threading* control program monitor all these systems. The anode DC currents can be read at rate of 6 *Hz* (not stable, if any subsystem is being read by the control program, see Figure 6.9).

All these DC/HV monitoring cards must be calibrated, i.e, the conversion factors from ADC counts to current or voltage. The HV setting of the MAGIC camera is quite reliable. With different HV settings and the monitoring output, the conversion factor from ADC counts to voltage can easily be evaluated for each monitor card. The calibration of a DC current monitoring card must be done in laboratory, injecting well-known current values in the PMT anode pin of the electronic base and reading the output of the monitoring card in ADC counts. Figure 6.10 shows the lineal regressions, which give the calibration factors for HV and DC monitoring cards. Concerning the dynamic range, the anode DC currents can be read up to 30  $\mu A$ , while the HVs make the ADC to saturate at approximately 1500 *V*. The pedestal values are quite stable (pedestal *rms* of about 0.05% for ten hours of data taking). Repeated measurements showed that calibration factors were stable

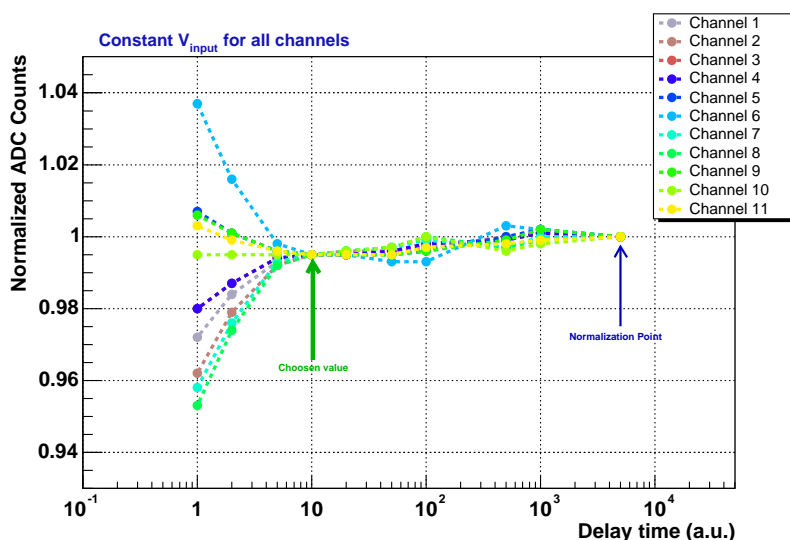


Figure 6.8: Special test to evaluate the optimized delay time for digitalization purposes.

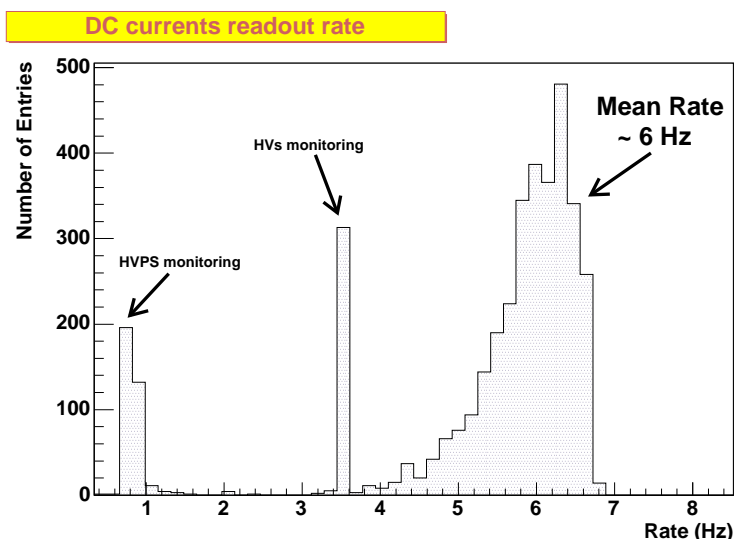


Figure 6.9: Maximum rate for the anode DC currents monitor (up to  $6\text{ Hz}$ ). When another CANbus system is read through the same bus, the rate drops to lower values. The access to the HV power supply is quite slow (because RS232 to CANbus converter) and nearly blocks the bus when is accessed.

and quite reliable, so we decided to make calibration and pedestal runs once every several months to save time during monitor cards initialization. All these calibration factors are taken into account in the slow control software.

All the cards have a six characters identifier (“MUX###”) burned in the microcontroller code. This is necessary for the dynamic assignment of CANbus identifiers and proper assignment for slow control purposes. The software that controls the CANbus elements, relies on a look-up table for cards assignment loaded every time that the CAN bus is initialized [214]. This makes possible to introduce new nodes in the CAN bus line, or to change broken cards without modifying neither

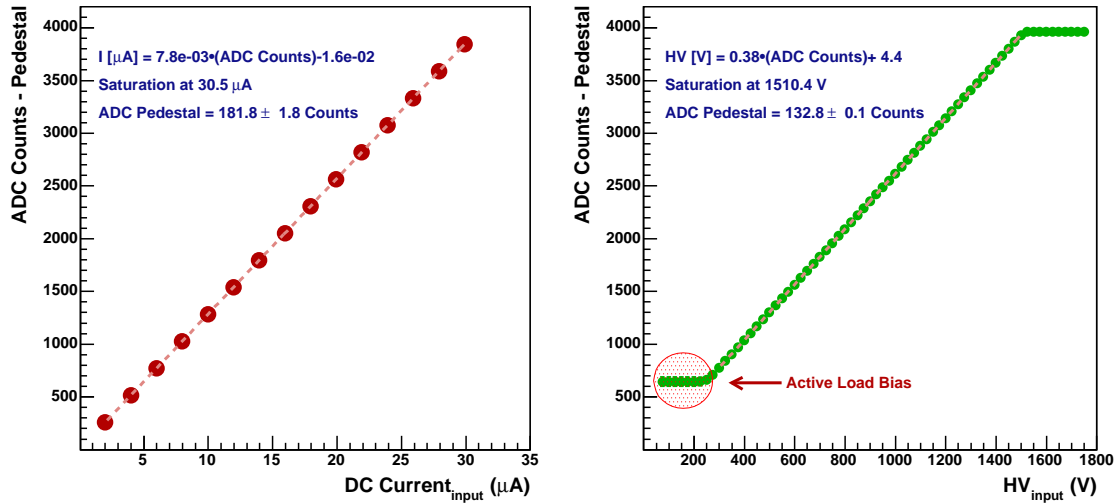


Figure 6.10: Evaluation of calibration factors (ADC counts to Voltage/Current) for HV/DC multiplexed monitor cards.

the CAN bus software nor the code in the micro-controllers.

### The central pixel for optical observations

The installation of a special pixel located at the center of the camera, namely the central pixel, is intended to analyze fast optical signals coming from pulsed  $\gamma$ -ray sources, as pulsars. The PMT used is the 9116A type and the optical variations of astronomical objects are recorded by integrating the slow DC current output of the PMT. The DC branch of the pre-amplifier placed at the PMT base has been modified to have an integration constant of  $0.5\text{ ms}$  and pixel works under  $1.08\text{ kV}$  ( $20k$  gain). The transmission of the signal to the control house is done with one of the optical fibers which are used in pulsed light transmission. Since the expected variations are in the  $10\text{-}100\text{ Hz}$  range, the high-speed VCSEL transmitter has been replaced by a wide dynamic range LED transmitter (sensible to variations of DC currents at the level of  $0.3\%$  and bandwidth of  $1\text{ Hz}$  to  $4\text{ kHz}$ ). An independent readout system is implemented.

## 6.2 Calibration slow control electronics

This section provides technical information about the calibration system. We describe the system, its components, and the slow control.

### 6.2.1 Calibration pulser box

The telescope calibration system is designed to provide ultra-fast light pulses from a calibration watertight box (*pulser box*, see Figure 6.11), located in the center of the main mirror reflector dish. It consists of 16 light pulser slots with LEDs emitting light in three different wavelengths:  $370\text{ nm}$ ,  $460\text{ nm}$  and  $520\text{ nm}$  (UV, blue and green). Every slot is composed of same type LEDs (maximum of 5), i.e., every slot emits at an specific wavelength: four slots contain green LEDs, four slots UV LEDs, and the remaining 8 slots blue LEDs. A scheme of the slots is shown in Figure 6.12. Note

that two slots have an additional filter (diffuser) in front.



Figure 6.11: Calibration pulser box installed in the middle of the telescope mirror dish.

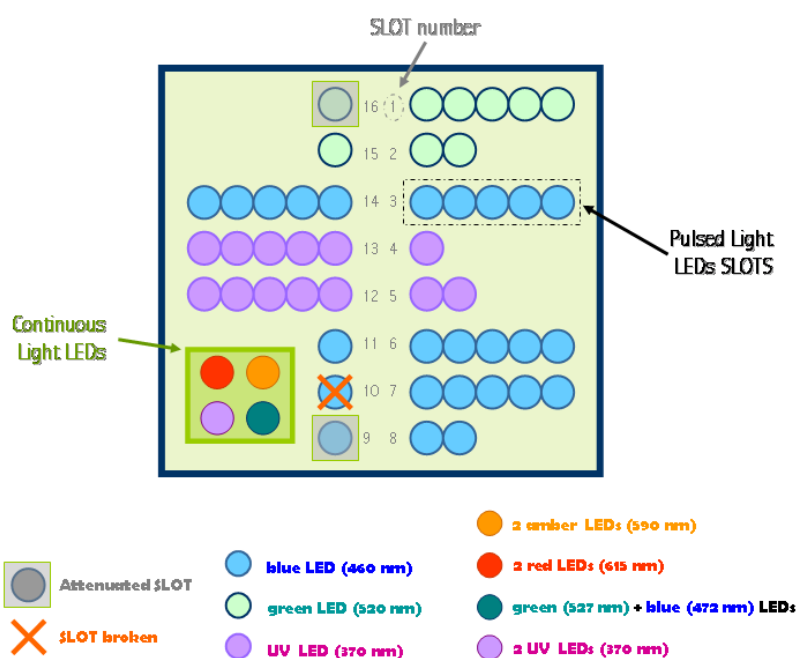


Figure 6.12: Scheme of the calibration LEDs slots available in the pulser box.

The pulsed light is emitted by very fast (3-4 ns FWHM) and ultra bright light emitting diodes of type NISHIA single quantum well. This short time is nearly as short as the pulses produced by the Čerenkov light flashes produced by the air showers in individual pixels. The pulsed light emission is driven by avalanche transistors, which allows very fast and high current flows through the LEDs (6 A in 2-3 ns) with fast recovery times. Slot combinations provides variable intensities (amount of produced light) and different colours, allowing to calibrate the whole readout chain in wavelength and linearity. The pulse slots fire synchronously within 500 ps precision relative to each

slot (with a remotely adjustable pulse rate up to  $4\text{ kHz}$ ), producing a maximum of 2000-3000 *phes* in an inner pixel when all slots are firing. The light output of the LEDs is diffused by a frosted glass plate which allows for homogeneous light of the camera (located at  $17\text{ m}$  distance) with an uniformity of  $\sim 1\%$ , within a cone of  $2\text{ deg}$  from camera center. A glass window protects the electronics against dust and water.

There is also a *continuous light* source in four different colors (blue-green, amber, red and UV) and variable intensities, to simulate different conditions of the star light at different wavelengths (see Figure 6.12). It also serves to flat-field the camera at different wavelengths (useful for star finding algorithms for position accuracy tests). The continuous light LEDs can be set to 256 different current levels from 0 to about  $25\text{ mA}$  (i.e, 256 different light outputs).

The calibration pulser box is powered by an independent LV power supply box (near the pulser box), needed to power the pulser box and PIN-diode electronics. This LV box is fed by a  $230\text{ V}$  line taken from the cooling box below in the telescope, which is switched on/off by the Cooling System PLC (and from the remote control system). An optical trigger carries the trigger line to fire the LEDs from the control house to the pulser box. A  $600\text{ V}$  power supply is installed in the pulser box to provide the collector voltage of the avalanche transistors. Moreover, the pulser box is equipped with a current supply for continuous mode operation. Three 8-bit shift registers are used to switch on/off the 16 pulsed LED slots, the 4 continuous light LEDs, the  $600\text{ V}$  supply and the LV for the PIN-diode counter. The pulser box is steered via CANbus, with a CANbus receiver card similar to the ones used to monitor the camera HV and DC currents. The CANbus card houses a serial line to drive the shift-registers (pulsed emission) and a 8-bit Digital-to-Analog Converter (DAC) to provide the voltage levels to be converted into current levels by the current power supply (continuous emission). The CANbus board has an ADC, which is not used at the moment (i.e, no monitoring of the system is provided).

### Blinded Pixels

Three special inner pixels, the so-called *blinded pixels*, are located in the camera ( $10\text{ cm}$  from the outer ring pixels, each  $120^\circ$  from the two others, see Figure 6.13 left). These pixels have well-known measured Quantum Efficiency curves. Their collection efficiencies are high as they have higher voltage drop from cathode and first dynode than the rest of camera PMTs (here,  $440\text{ V}$ ). The blinded pixels are darkened with absorption filters  $1/100$ ,  $1/1000$  and  $1/10$  and a diafragma of  $1\text{ cm}^2$  is placed in front of the PMT photo-cathodes. The signals at the anode are amplified by a factor 4 more than the rest of camera PMTs and the applied HV is of about  $1450\text{ V}$ . The signals are transported to control house in the same way like normal camera PMTs, i.e, analogue optical transmission.

In this configuration, the blinded pixels are operated in single photon counting mode. These devices are used to measure the absolute quantity of photons contained in the individual calibration pulses, and thus, to allow for an absolute light calibration at the LED emitting wavelengths with great precision.

### PIN-Diode

The calibration system is provided by a PIN-diode located at  $1.1\text{ m}$  away from the pulser box (see Figure 6.13 right). This system provides an independent and complementary way of measuring the absolute light flux. Behind the PIN-diode, radioactive  $^{133}\text{Ba}$  and  $^{241}\text{Am}$  sources provide distinctive gamma emission lines, which are used as precise reference signals in the active region of the PIN-diode for device calibration purposes. The whole setup is housed into two aluminum boxes in order to reduce the pick-up noise.



Figure 6.13: Left: One of the three blinded pixels installed in the camera. Right: Pin-diode box installed in front of the pulser box.

The PIN-diode signal is pre-amplified and converted to an analogue optical signal by a transmitter board. The optical signal is transported to control house and converted back to electrical signal by a modified receiver board. There, the PIN-diode signal gets further delayed ( $60\text{ ns}$ ) in order to match the arrival times of the camera signals to the same pulsed LED light pulses. This PIN-diode signal is able to trigger the system through the digital part of the receiver board. This (delayed) trigger line is led to the calibration trigger box (see next section), which forms a dedicated trigger signal for the L2 system, that fires the whole data acquisition system.

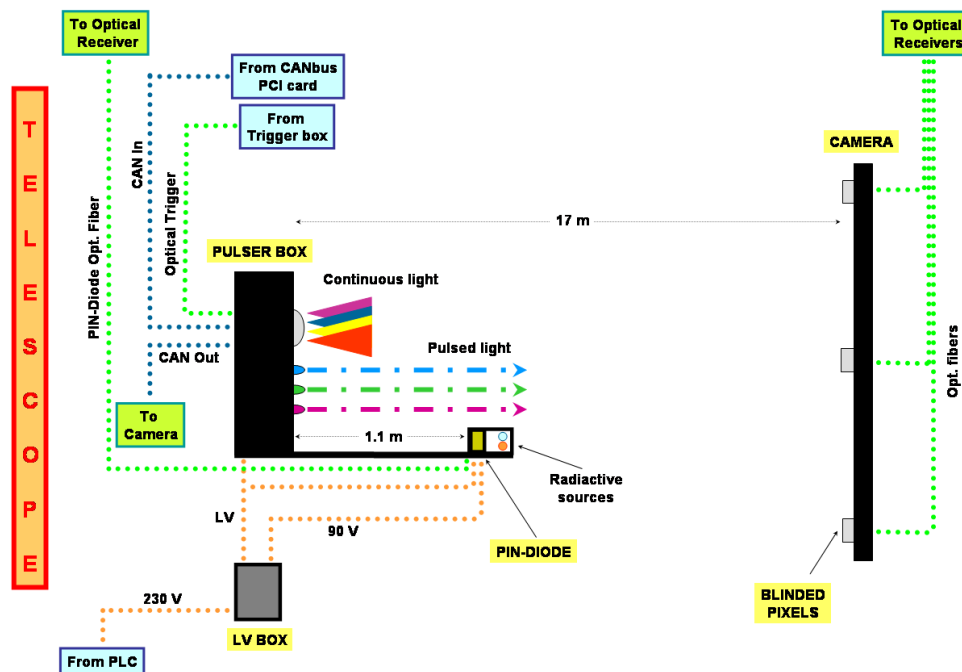


Figure 6.14: Schematic of main calibration system elements installed in the telescope: pulser box, LV box, PIN-diode and Blinded Pixels.

### 6.2.2 Calibration trigger

The calibration system has a dedicated external trigger, meant to avoid cosmic triggers in a calibration run. During a normal calibration procedure the L1 majority trigger is disabled and the calibration triggers the L2 trigger system to read out the events exactly when the pulses from the calibration box arrive from the camera.

An I/O PCI-board with six 10 MHz timers is connected in the control computer. It creates series of software-adjustable pulses which travel to the calibration trigger box system (see Figure 6.15). In this system, an ALTERA chip (MAX7000S) builds four different pulses from the incoming signal. A pulsed signal which is sent to the calibration pulser box to fire the LED slots and three optional pulses, which are sent L2 hardware trigger, triggering the calibration, pedestal or PIN-diode events. The whole system is optically decoupled.



Figure 6.15: Front panel of the calibration trigger board with the test lines and indicator LEDs.

The trigger pulsed signal to the pulser box is translated into optical signal in the trigger box (via optical transmitter) and sent through a 155 m optical fiber. In the pulser box, an optical receiver translates the optical pulses to a TTL-pulsed signal used to fire the LED slots in pulsed mode. The optional calibration L2 trigger signals are delayed and converted to the LVDS standard. Afterwards, they are sent to the general MAGIC L2 trigger. An important feature is the correct time adjustment between the arrival of these trigger signals and the arrival of the corresponding signals from the optical receiver boards. A delay time (in 100 ns steps) can be set from the control software. Finer steps were adjusted by using a cable with proper length and delays introduced in the ALTERA chip (in steps of about 4 ns).

To store all the information of the calibration run configuration, 48 digital output lines from the I/O PCI card are converted into LVDS, sent to the DAQ (via two digital modules), and stored into every triggered event header. This information is very useful for data analysis (for example, to select calibration events inter-spread in raw data).

Figure 6.14 and Figure 6.16 give a sketch of the components of the entire calibration system. The calibration system is used to calibrate the camera since approximately September 2004. The Thesis Author was working in the telescope site when the official MAGIC first light (pulsed emission from the PMTs) was recorded, in March 2003 (before the FADC system was partially installed). At the time, pulses were emitted by a first version of the calibration system and they were firing already installed trigger system. Some of these pulses were recorded with an oscilloscope plugged at the output of the optical receivers (see Figure 6.17). They were the first pulses recorded at the

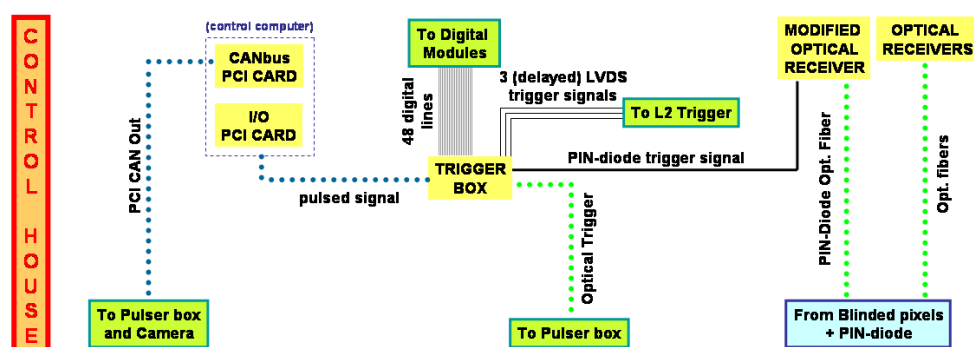


Figure 6.16: Schematic of the calibration system (mainly trigger) elements installed in the control house.

optical receivers output.

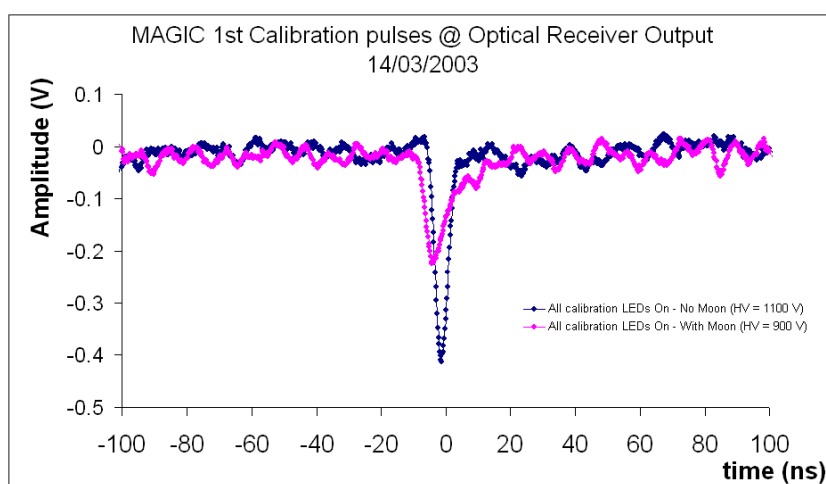


Figure 6.17: First MAGIC pulsed light observations of pulses coming from a first version of the calibration pulser box.

## 6.3 Outline of the MAGIC control system

### Distributed design

The MAGIC control system is split up into functional units which correspond to the independent subsystems of the telescope. A central control (*CeCo*) computer coordinates the subsystems providing a Graphical User Interface (*GUI*) to operate the telescope in daily observation nights. In this sense, the *CeCo* does not manage directly the details of every subsystem but provides a lower level interface between them and the global decision system.

All telescope subsystem control programs run in independent Linux-based standard PCs. Moreover, each of these computers have all the necessary programs and drivers installed, as well as all security resources. In case of a PC failure, a standard spare PC can be equipped with all hardware

communication PCI cards and plugged into the system. By this way, normal situation can be recovered in a quick way minimizing the impact into the observation time. Moreover, independent stations reduce the load of every computer and the one hosting the CeCo. This is helpful in case many resources have to be controlled by the PC, like the case of the camera control computer. Control programs are written in Labview 6.i, C/C++ and CERN root package (mostly for GUI purposes).

The most important subsystems of the MAGIC telescope are listed below (see Figure 6.18 for a outline of the telescope control system):

- Data acquisition (DAQ) system based on 577 FADC channels and designed to acquire up to 1 Kevent/s. For online data quality check, a subsystem monitor and a simple-robust analysis program run over the data which is being taken during observation time.
- Camera and calibration of the camera.
- Drive system: it steers 2 ALT/AZ motors and monitors the telescope position using 2 shaft encoders and 2 rotary encoders.
- Level 2 trigger: a VME system-controlled by a VME CPU allows online loading of new trigger tables. Events can be pre-scaled to optimize event recording at low energies and optionally perform online gamma/hadron separation.
- Active Mirror Control: two motors behind each  $1\text{m}^2$  mirror panel allow to correct any reflector deformation (custom-motor motor steering electronics, CCD and laser pointer).
- Starguider and Camera Oscillation Monitor using 2 CCDs.
- Auxiliary PC: GRB alarm, weather station, GPS reference and future NSB detectors.
- LIDAR: an independent optical telescope equipped with a laser to monitor the light attenuation in the atmosphere.
- Optical telescope: aimed UBVRI photometry down to 18m with 0.01m accuracy, 20'-30' FOV (AGNs, pulsars,  $\mu$ QSR).

### Distributed development

For maintenance, testing and development each subsystem control program has been implemented to allow *stand-alone run mode* without communicating with CeCo or other subsystems. The effect of the distributed development during the telescope comissioning was two-fold: developers easily shared their work due to relatively simple communication protocols with CeCo. This *encapsulation* enabled to fully test the subsystems without having to buy additional hardware or having to transport them to a different site. When the subsystem worked reliably in stand-alone mode, it was integrated into the whole system, the CeCo, and the other systems within a relatively short period of time. This allows easy-to-integrate environment and easier maintenance of the total system once it was implemented at the telescope site. Errors can be located more easily and upgrades of individual hardware or software elements influence only the individual subsystems.

### Communication via Ethernet using TCP/IP sockets and/or file sharing

All subsystem PCs and CeCo communicate with each other via standard TCP/IP socket connections or NFS file sharing in a standard Ethernet network. The Ethernet architecture is based on

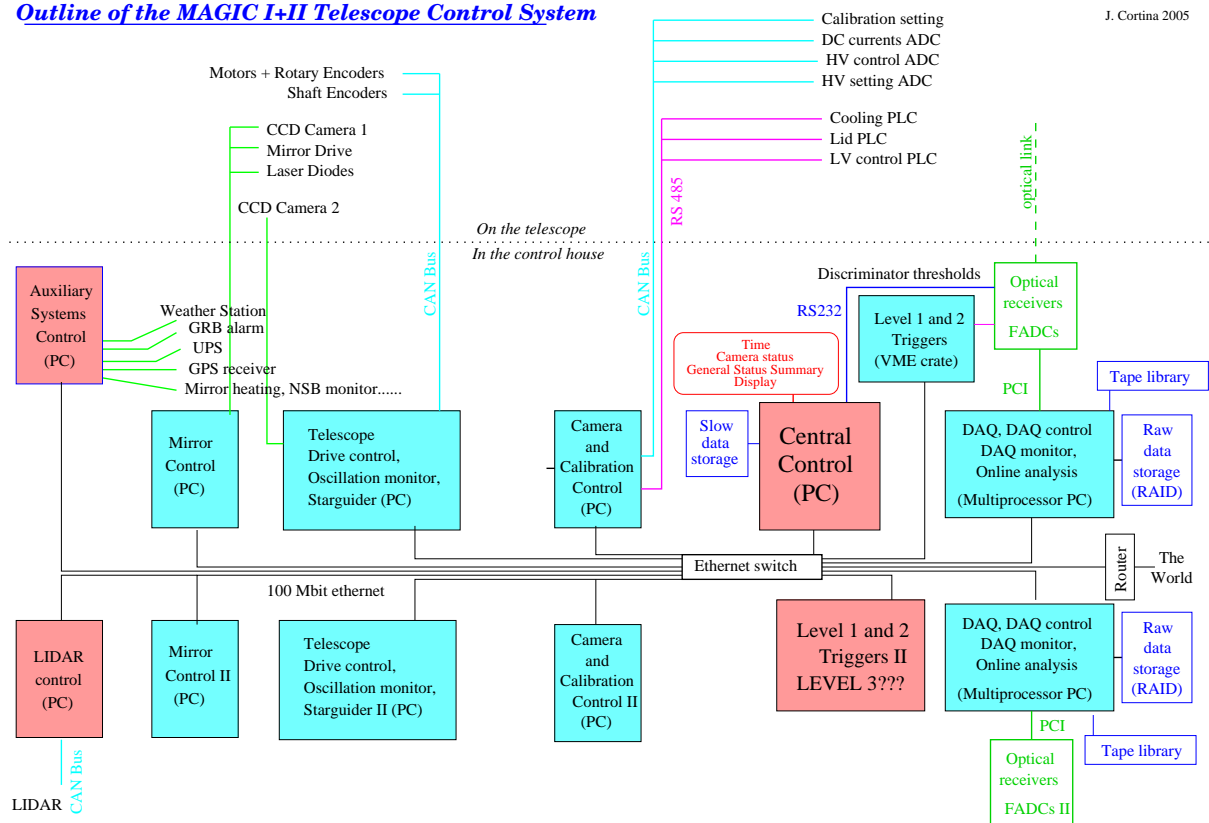
**Outline of the MAGIC I+II Telescope Control System**

Figure 6.18: Outline of the MAGIC telescope control and DAQ system.

simple hub-spokes design, i.e, there is a single Ethernet Switch to which all subsystem computers are connected. If needed, independent control programs interact to the different system hardware programs via internal named *pipes* (UNIX fifos which act as a file sockets).

**Time synchronization**

Synchronous clocks in the computers are important to assure reliable communication. All computers in the control system are synchronized to UTC within  $\sim 100$  ms using the *NTP protocol* implemented through the *xntpd* Linux daemon. Synchronization is based on the standard time server of the Spanish Rediris network (currently *hora.rediris.es*) and on a local time server in the auxiliary systems computer (*wwwint.magic.iac.es*). The computer clock in the auxiliary systems computer is synchronized to UTC directly through a *GPS receiver* and works as NTP time server. This local time server assures time synchronization when the connection to the IAC network is down.

**CANbus communication protocol as standard**

The slow control of the MAGIC telescope camera made extensive the use of the *CANbus* protocol. CAN was strongly encouraged as the MAGIC telescope standard for control subsystems. Even auxiliary instruments normally controlled under RS-232 or RS-485 are linked to CAN over corresponding adapters, if possible.

## Electromagnetic decoupling

All communication with systems outside the control room/house use *optical coupling* in order to keep the control/DAQ computers safe from interference picked up by the long (160 m) cable connections with the telescope. Where possible, *optical fibre* connections have been used. The PCI CAN controller card used for camera control is optically decoupled as well.

## 6.4 Camera and Calibration software control system

Camera and Calibration systems are controlled by the same control program, known as *La Guagua* (that Thesis Author named as a reference to the local word of the island of La Palma to design a typical Bus). This section gives an overview of the system. Full documentation of Camera, Calibration and Central control is available in the MAGIC technical documents.

*La Guagua* is based in the same concept of the Central Control: every functionality in the camera is controlled by independent camera and calibration subsystems, which are managed by a "central" control engine. *La Guagua* consists of *two layers of software* developed using different programming languages:

- C/C++ *Subsystem drivers* developed to communicate with the hardware [214].
- Labview 6.0.2 for GUI (figure 6.19) and *Guagua Decision manager*.

The MAGIC Camera and Calibration systems are controlled accessing the hardware by means of several communication buses and protocols (see Figure 6.20). *CANBus* lines are used to have control over every pixel of the Camera, like set and monitor High Voltages or PMT anode DC current monitor and to access to the calibration system. *RS-232* is used to control the High Voltage power supplies, although they are linked to the CANbus via *CANtoSerial* adaptor. The Camera Cooling, Lid and Low Voltages run in an autonomous way using several *PLCs* (Programmable Logic Controller) [215]. That means, for example, that the Cooling subsystem is able to regulate in standalone mode the temperature inside the camera to avoid water condensation and to ensure constant temperature during operation ( $\sim 37^\circ$  C). The access to those PLCs is done using an standard protocol over *RS-485* called *MODbus*.

### 6.4.1 Subsystem drivers: Control-subsystem interaction

The different functional pieces in the camera (anode DC current monitoring, HV setting, camera lid, ...) and calibration are not so strongly separated in physical or hardware terms. Different purpose items, like the board for HV setting and the calibration board, are connected to the same CANbus line or at least connected to the PC by the same PCI card. A unique program is in charge to communicate to the hardware pieces which, on the camera and calibration control view, are separate Subsystems. To decouple the hardware from upper control levels, whatever is the software combination that drives this hardware pieces, a uniform communication point to *Guagua Decision Manager* for each functional piece is provided, as if a separate software Subsystem were running for each functional item. We call *Subsystem Drivers* the programs that drive the hardware and provide proper initialization to enable a communication point for its subsystem(s) under control.

At the implementation level, to provide the concurrent tasks that attend to each interface, the subsystem drivers have as many threads as functional pieces they host under the same bus. In case of multi-thread drivers, the most stringent requirement is that drivers controlling one of the associated hardware must lock the bus keeping its control. Afterwards, the bus can be unlocked when the action has been processed. To lock and unlock threads, something similar to a file

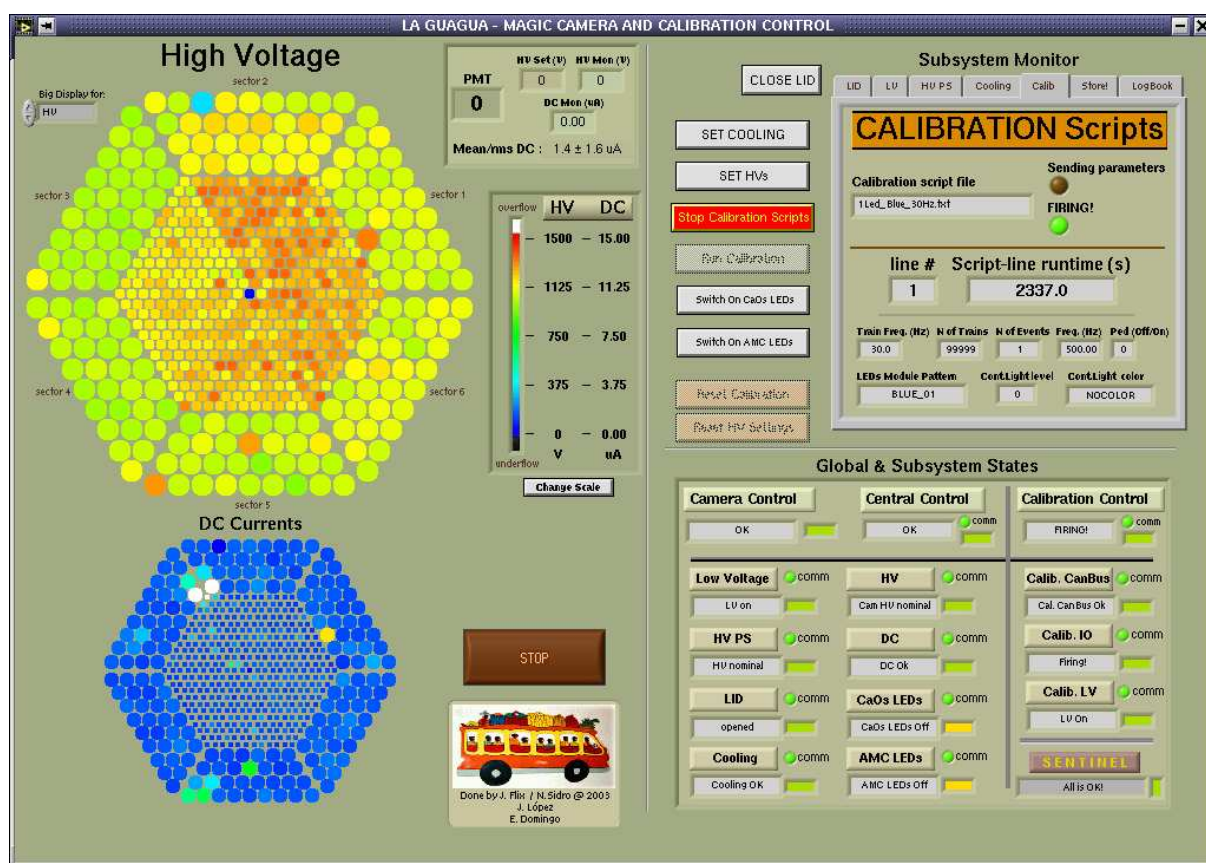


Figure 6.19: GUI of the Camera and Calibration Control (La Guagua).

descriptor is used, but applied to threads using `pthread_mutex_lock` and `pthread_mutex_unlock` functions.

The communication between the *Subsystem Drivers* and the *Subsystem Monitor* and *Subsystem Control* routines in La Guagua resembles as much as possible to the one between CeCo and remote Subsystems. This means that each Guagua subsystem should have its own Driver which uses the libraries containing the specific functions to be called. These functions implement all the possible tasks that the hardware should manage. In this particular case, to deal between the Guagua Decision System and Subsystems, the Ethernet sockets are replaced with internal sockets named *pipes*. The *command channel* and *report channel* distinction and most of the protocol can be used for both cases.

### Control-Subsystem communication channels

Special *pipe* files created in the system allow for the exchange of information between separate running programs, in particular from La Guagua (Labview 6.i) and Subsystem Drivers (C/C++). *Pipes* can be opened by multiple processes for reading or writing purposes. As in Ethernet CeCo-subsystem, two types of separate channels (*pipes*) are used: one to send commands from the Internal Subsystem Monitor to its Driver (specific actions to be executed) and another to send reports on the opposite direction (process monitor of executed actions and real-time monitor). Every Guagua subsystem uses these two named pipes: *subsys\_report*, *subsys\_cmd*.

The main software piece which enables communication between Guagua and subsystem drivers

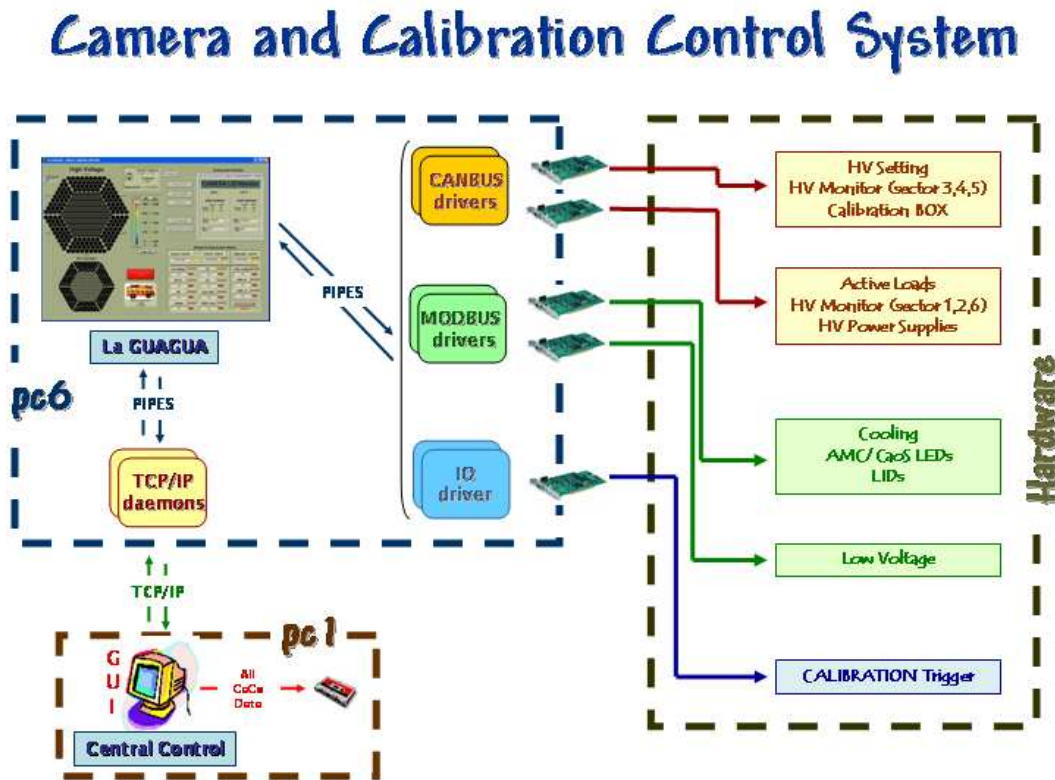


Figure 6.20: Camera and Calibration slow control.

is the `ListenFromDevice` method. When an object of this type is created, the program is able to wait and receive commands through this *pipe* in order to process an action. Once communication is enabled, the subsystem is always pulling into the *pipe* to check if there is a command to be processed. The Driver waits for a time  $\Delta t$  and sends the status report to La Guagua. When a command is received through the *pipe*, it is processed and the Driver waits for a control reaction time, sending a report to La Guagua right afterwards. This assures that last command has been properly executed. Semaphores are implemented in the *Subsystem Control* routine in order to avoid loosing any action if the system is busy processing an action.

Subsystem report contents are shown in Table 6.1. Besides some items for status, error flags, and timestamp, which are common for each subsystem, the reported values and commands are different. This, and the most important commands are exposed in Appendix C.

### 6.4.2 State-machine decision manager

The task of La Guagua is to provide the user a simple user interface to control de camera and the calibration systems. The most important concept behind this control system in the so-called *state-machine core*: the program that evaluates the status of every controlled subsystem from their regular reports. Guagua is not pulling the subsystems to know about their states and parameters. Reports are managed by the Drivers, which are received by Guagua at a given periodicity. This idea of periodical report up to subsystem initiative provides itself a periodical check of Guagua-subsystem connection. Subsystems are expected to change their state as soon as the control system sends a command to be executed. Reports are essential to keep track of all actions asked by La Guagua.

Subsystem	Report contents
HV PS	High Voltages (HV) and Currents (I) for the two camera power supplies
HV	All 577 pixel monitored HVs
DC Currents	All 577 pixel monitored anode DC currents
Active Loads	Voltages and currents (V,I) provided by the +350V and +175V power supplies
LV	(V,I) of camera +5V, +12V and -12V power supplies and Opt. Transmitters +12V. Temperature (T) and Relative Humidity (RH)
LIDs	Motor status and monitored normal/safety switches values
Cooling	4 T for sensors on camera Wall, Center and Opt. Transmitters, and Water on tank. 2 RH values for camera wall and center. Pressure sensors, pump, refrigerator, valve, resistor and fans status

Table 6.1: Main subsystem reported values through `subsys_report` pipe.

Subsystem states are the input for the main *Decision Manager*. Using the updated information of every subsystem a *global state* for the Camera and Calibration system is evaluated by the *Subsystem Monitor* manager. This manager updates the state table whenever a report from a subsystem arrives to La Guagua. This defines different circumstances in which some actions are permitted or forbidden. Figure 6.22 shows all possible subsystem states and global states.

Under special circumstances, the camera enters into an state in which no actions coming from CeCo or User are executed. This corresponds to global BLOCKED! state, which occurs when an emergency happens. Then, Guagua takes an automatic control of the whole system ramping down the pixel High Voltages and closing the camera LIDs. These emergencies can be related, for example, to camera light illumination by a car, bad atmospheric conditions, timeout of an important camera subsystem, etc... All possible states which drive the camera to BLOCKED! state are displayed in red in Table 6.22.

Any subsystem under alarming conditions fires the camera global ALARM state. This happens, for example if one of the two lids has reached a safety limit and cannot be closed remotely from the control house. In many cases, data can still be taken but special actions have to be done to recover the normal situation. These subsystem conditions are displayed in orange in Table 6.22.

The global state HOT is fired when one ore more pixels are quite bright at the anode DC currents level. This may happen if a bright star is present in the FOV. In such a state, La Guagua reduces automatically the High Voltage of the proper pixels (by 5%) to assure they stay into a safe anode DC current region. Due to the ALT/AZ drive of MAGIC telescope, the stars in the FOV rotate in the camera. Automatic recovering of High Voltages is done by La Guagua to bring to nominal values those pixels in which the star is not present anymore because it rotated. This protection was used during the first six months of telescope comissioning with a DC current limit of  $15 \mu A$ . Afterwards, the DC current limit to fire the HOT state was set to  $30 \mu A$  (almost the limit of the monitoring saturation), as special tests showed that MAGIC PMTs gain and performance cannot be deteriorated for such currents (the ageing test was done for an inner PMT in constant  $105 \mu A$  DC current flow for 6 months<sup>1</sup>). With the current upper limit, it is very unlikely that the HVs are modified by the presence of a bright star, as they produce currents of a few  $\mu A$ . In addition, not modified HVs in the pixels in an observation night facilitates the data analysis, as no corrections are needed for PMT gain variations.

---

<sup>1</sup>E. Lorenz, private communication.

## Overview of the Camera & Calib. Control System

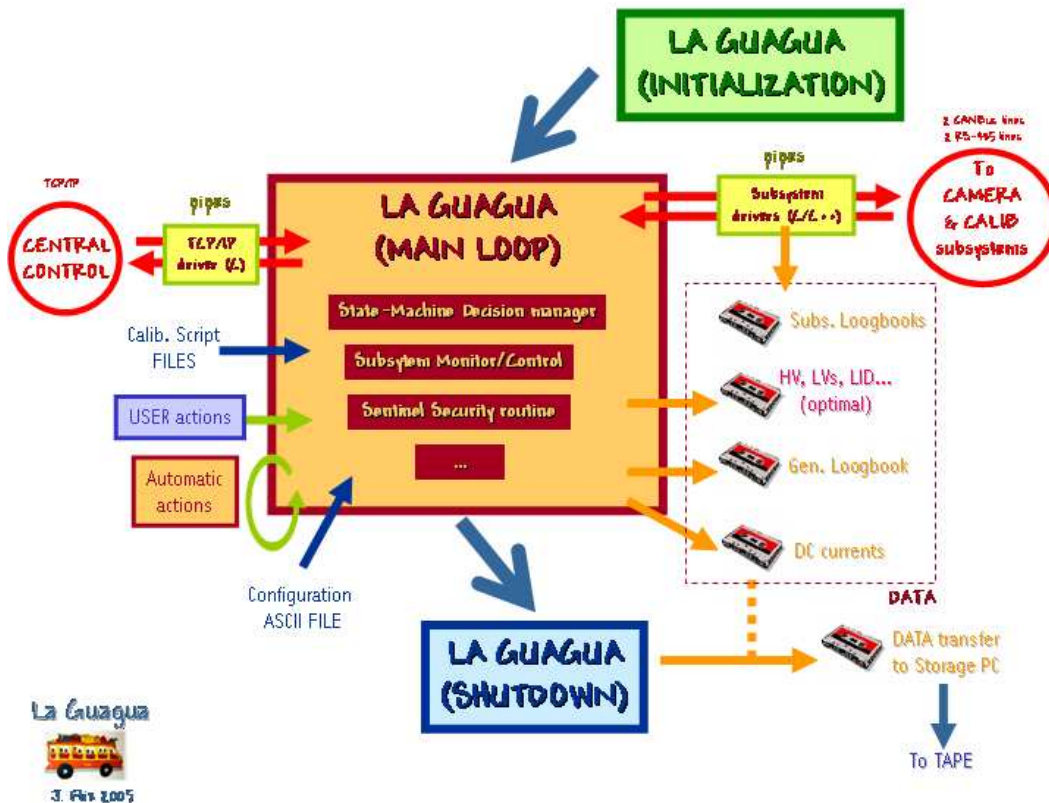


Figure 6.21: Schematic view of La Guagua software architecture.

### 6.4.3 Sentinel routine as security manager

Security is crucial. A routine called *Sentinel* protects the camera against dangerous situations, like restricting the system operation during daytime. Sentinel uses specially created sun time position tables (created with *XEphem*) and checks regularly the MAGIC Weather Station solar irradiation monitor. Moreover, operation is not allowed either in case of bad atmospheric conditions, determined by the Weather Station as well. Only experts are allowed to bypass Sentinel for tests and checks of the system.

In all these situations, La Guagua goes to **BLOCKED!** state, in which CeCo or users cannot operate the camera nor the calibration systems. Nevertheless, Sentinel allows to switch on the camera 2 hours before dusk time, in order to Warm-up the camera (see section). In such warm-up mode, until it is completely dark, the Sentinel does not allow to open the lids. Ramping up the pixel High Voltages is allowed 1 hour before dusk time. Camera Low Voltage system dissipates by itself sufficient power inside the camera to allow the cooling system to reach an stable and proper working temperature for further data-taking during the warm-up period (this is complemented by the latest stage with applied High Voltage).

	System ID	State 0	State 1	State 2	State 3	State 4	State 5	State 6	State 7	State 8	State 9
<b>CAMERA</b>	<b>CamControl</b>	<b>ERROR</b>	<b>ALARM</b>	<b>BLOCKED!</b>	<b>WARM-UP</b>	<b>HOT</b>	<b>HV RAMPING</b>	<b>OK</b>	<b>HIIT</b>	<b>SHUTO</b>	<b>II/A</b>
	Cam.HV.P5	error	HV mismatch	HV Trip	HW ramping	HV Off	HV nominal	Limit Current warning	-	-	n/a
	Cam.LID	error	Safety Limit passed	-	-	closed	opened	moving	stopped	-	n/a
	Cam.LV	error	LV Alarm	LV Trip	-	LV Off	LV On	-	-	-	n/a
	Cam.COOLHIG	error	Cooling Alarm	-	-	Cooling Off	Cooling OK	Temp. warning	Cond. warning	-	n/a
	Cam.HV	error	Cam HV mismatch	HV ramping failed	Cam HW ramping	Cam HV Off	Cam HV nominal	-	-	-	n/a
	Cam.DC	error	DC Alarm	-	hot	-	DC Ok	-	-	-	n/a
	Cam.Act.Load	error	alarm	-	-	Off	On	-	-	-	n/a
	Cam.Central Pix	error	alarm	disabled	-	Off	On	-	-	-	n/a
	Cam. CaOs LEDs	error	-	-	-	CaOs LEDs Off	CaOs LEDs On	-	-	-	n/a
	Cam. AMC LEDs	error	-	-	-	AMC LEDs Off	AMC LEDs On	-	-	-	n/a
	<b>CALIBRATION</b>	<b>System ID</b>	<b>State 0</b>	<b>State 1</b>	<b>State 2</b>	<b>State 3</b>	<b>State 4</b>	<b>State 5</b>	<b>State 6</b>	<b>State 7</b>	<b>State 8</b>
<b>Cal. Control</b>		<b>ERROR</b>	<b>BLOCKED!</b>	<b>WAITING TO FIRE</b>	<b>FIRING!</b>	-	-	-	<b>HIIT</b>	<b>SHUTO</b>	<b>II/A</b>
Cal. CanBus		error	-	-	-	Cal. CanBus Ok	-	-	-	-	n/a
Cal. IO		error	-	Waiting to fire	Firing!	-	-	-	-	-	n/a
Cal. LV	error	-	LV Off	LV On	-	-	-	-	-	n/a	
<b>SENT</b>	<b>Security items</b>	<b>State 0</b>	<b>State 1</b>	<b>State 2</b>	<b>State 3</b>	<b>State 4</b>	<b>State 5</b>	<b>State 6</b>	<b>State 7</b>	<b>State 8</b>	<b>State 9</b>
	<b>Sentinel</b>	<b>ERROR</b>	All is OK!	Sun is present	Bad Attr. Cond.	disabled	-	Only WARM-UP mode	CeCoTimeOut	-	N/A

Figure 6.22: Subsystem states and Guagua camera and calibration global states.

## 6.5 Control operations in observation mode

When camera and calibration control (Guagua) is executed the whole system starts to be operative. First, all subsystems enter into an Initialization phase in which the different subsystems are driven to be ready for further run in combined mode. Once the initialization has finished successfully, the user has full access to control the camera and calibration systems either from Guagua GUI or via CeCo.

### Communication to MAGIC Central Control via TCP/IP

All actions to be executed by the MAGIC telescope are driven by the Central Control. La Guagua is listening to CeCo from a dedicated TCP/IP socket, and waiting for its commands to be executed. The responsables for the TCP/IP communication are two daemon programs `tcp_server_read_socket` and `tcp_client_write_socket`. TCP/IP preserves the command/report channel philosophy. The communication to Guagua is done via *pipes*, like the camera subsystems do. All available commands which can be executed from CeCo, and corresponding actions to be done by La Guagua are shown in Appendix C. Security checks are also implemented at this stage: not all functionalities are available via TCP/IP and checks are done in order to prevent any remote damage of the system.

La Guagua reports periodically (at 1 second rate) to CeCo about the global status of all systems through a special report TCP/IP socket. This information includes the global states, subsystem states, and all subsystem monitored values.

### High Voltage ramping security procedure

The setting of the pixel High Voltages has been programmed to offer a secure ramping up/down procedure. This prevents the pixels to be damaged by rapid variations of applied voltage. This HV ramping is done in the HV power supplies and separately in the camera HV regulators. The High Voltage power supplies ramp up/down in steps of 50 V while the HV regulators ramp up/down in steps of 10 V. The ramping is done until the asked settings have been reached. In case of ramping up the HVs, the total HV provided by the power supplies is always 100 V bigger than the maximum

pixel HV setting of pixel. In case of pixel variations less than 50 V around the final nominal value, we only apply the ramp in the regulators. If variations increase more than 50 V a new ramping in the HV power supplies is done in order to keep the 100 V distance to maximum pixel HV.

The ramping can be stopped from the Central Control at any time. Moreover, if camera enters into HOT state, i.e., the DC currents are larger than expected, the ramping procedure is automatically stopped by La Guagua and, afterwards, if there are too many pixels in HOT state ( $\geq 40pixels$ ), an automatic ramp down and closing the camera lids is done. This prevents the camera to be damaged in case of an operation mistake, like trying to ramp up the camera HVs if some light is present in the telescope.

### Operate calibration system via shell scripts

An easy-to-use method to execute a sequence of light calibration runs using shell scripts is provided (see Table 6.2 for an example). The scripts can be modified as desired and let the user to work using all available functionalities of the calibration system. For example, the intensity and color of pulsed or continuous emission to be sent to camera pixels (combinations are allowed), pulse frequency, train frequencies, L2 vetos(i.e, set of trigger line: pedestal, calibration or PIN-diode) and delay time for the trigger lines to L2 trigger. Special pedestal runs at a given frequency can be started via calibration scripts.

TRAIN-F (HZ)	NR-TRAINS	NR-EVT	F (HZ)	MODULE PATTERN	L2-TRIG LINES	CONT.LIGHT COLOR	CONT.LIGHT-SRC (0-256)
2	3	4	200	UV_ALL	CAL	NOCOLOR	OFF
2	3	6	400	UV_05	CAL	RED	150

Table 6.2: Calibration shell script example: 2 different calibration sequences are defined in the script, which is further processed by 'Guagua'.

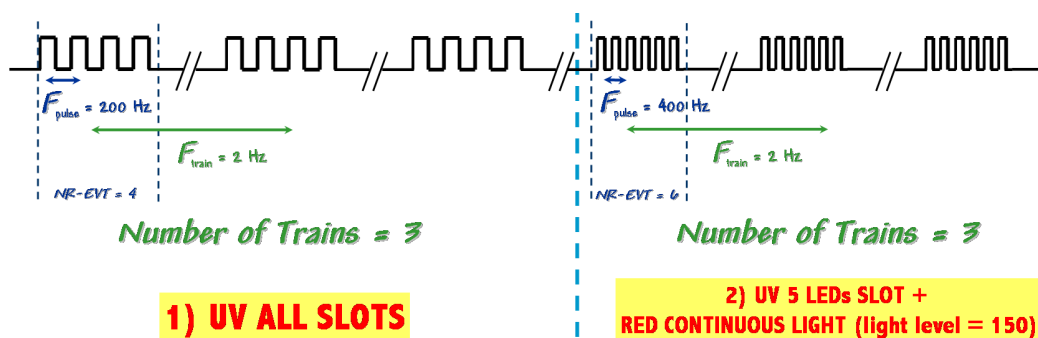


Figure 6.23: 2 calibration sequences defined in the previous script example.

The 600 V of the pulser box are switched ON when La Guagua is launched two hours before data-taking. This output voltage needs one hour to stabilize, i.e, the pulser box has to Warm-up, as well as the camera, in order to produce stable pulsed light emission. The available pulse frequencies supported by the IO Card (up to 4kHz) are: 160, 200, 250, 320, 400, 500, 625, 640, 800, 1000, 1250, 1600, 2000, 2500, 3125, 3200 and 4000 Hz.

La Guagua executes all calibration tasks defined in the sequence by using appropriate commands in an optimized way, i.e, not sending to driver repeated commands (as this would make the execution to be slow). Normally, the file name of a Calibrations script is sent from CeCo to La Guagua,

although calibration scripts can be launched from La Guagua as well.

The conversion factor from phe to ADC counts is obtained by means of the so-called F-Factor method that estimates the number of photoelectrons from the width of the charge distribution of calibration events. The conversion factor in an individual pixel is known to drift by at most 10% in time scales of several minutes due to instabilities in the optical transmission. It drifts coherently for all pixels in the camera by at most 20% in time scales of hours to days, due to thermal effects in the HV regulation and the optical transmission. These fluctuations can be corrected using interleaved calibration events during standard datataking, calibration events with a fixed color (370 nm) and intensity (around 35 phe in the inner pixels) are taken together with cosmic events at a 50 Hz fixed rate. The final precision in the determination of the charge in phe for the individual pixels is about 3%.

### Cooling system operation in daytime and observation night

The cooling system PLC is programmed for the temperature inside the camera to be stable all year round. This prevents extreme low temperatures in the camera during the day-time in winter, which may damage the camera. Moreover, stable interior camera temperature reduces the warm-up time needed to reach data-taking stability temperature point at the beginning of a night.

The camera temperature stabilization is accomplished by the use of hot/cold water which is sent to the camera through the cooling system circuit tubes. When the telescope is not taking data (basically during daytime), hot water is sent through the circuit. La Guagua communicates to the PLC when the camera is about to shutdown (i.e., the end of a night). During this "standby mode" water temperature is in the 40° to 45°C range. This keeps the camera in the 26° to 30°C range during daytime. When Guagua is re-started again (i.e., the next night) water is cooled down to 8° to 10°C. The auto-regulated PLC cooling system allows a stable temperature of  $37 \pm 1^\circ C$  for nights in which the data-taking does not suffer any problem (like HV problem, Guagua re-initializations, etc...). This stable point is reached 2 hours after the LV and HV of the camera have been switched on. This time period corresponds to the camera WARM-UP global state.

Besides some initialization parameters and daytime/night commands, the cooling system is only monitored by La Guagua during data-taking. La Guagua reports to users eventual emergency states of the cooling system while taking data. The cooling system is a very complex system (and dangerous in case of malfunction which may lead to an accident in which humans could be injured) and the system is also monitored during daytime by special scripted programs. The cooling system monitoring values are stored to disk (at 5 minutes rate). In case of system malfunction, an e-mail alert with the monitored values is sent to all responsible persons which are supposed to take an immediate action by calling to the site manager responsible.

### Instrumented lids

Camera lids have been instrumented with several LEDs used to monitor the camera oscillations (CaOs LEDs) and to be used as reference for mirror panels re-alignment procedure (AMC LEDs). Both sets of LEDs can be switched on/off from La Guagua and from Central Control. All these LEDs are accurately placed on the camera frame, since they are used as reference LEDs (see Figure 6.24).

The lids open/close operation takes about 20 seconds. During this interval, the movement can be stopped at any time from the control system. If access is needed to the camera front (due to pixel replacement, for example), lids must be opened manually for safety reasons. When lids are opened manually (through a control panel located in the cooling cabinet in telescope's lower drive), La Guagua is not able to open/close the lids. They are locked and secure. This manual panel must

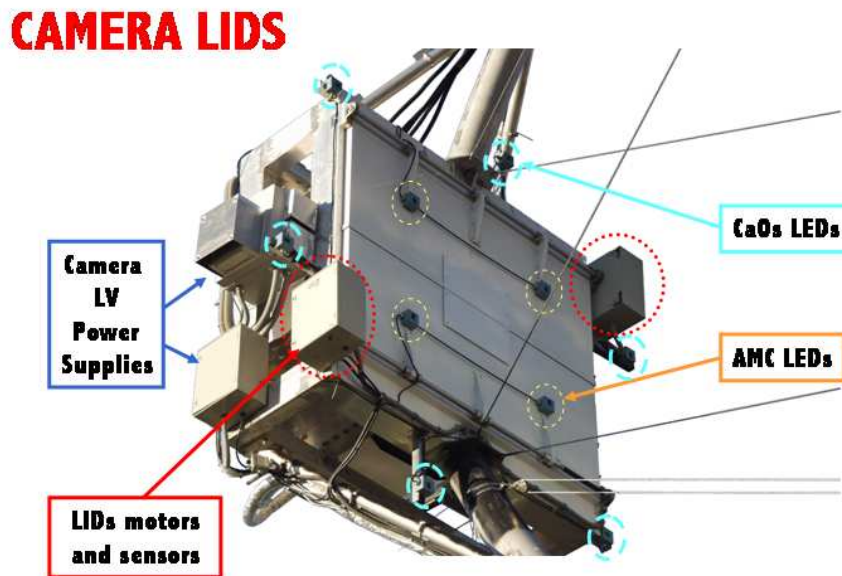


Figure 6.24: Instrumented lids.

be used in case of lids blocked at any position (they have been opened or closed too much due to strong wind, for example).

### La Guagua configuration file

La Guagua provides a configuration file to set the most relevant values which are used in the decision manager, subsystem state reconstruction and other execution subroutines. It comprises: enable/disable Sentinel, camera Warm-up time, High Voltage limit (to prevent trips in the power supply), sleep timers used for all Guagua threads (Subsystem Monitor, Decision Manager, etc.), Cooling System default initialization parameters, etc.

### Control Logbooks and Data Storage

During Guagua operation mode, all camera and calibration subsystems keep track of actions asked by la Guagua and an extensive monitor (debugging level is configurable) is stored into ASCII logbook files. La Guagua produces as well a general ASCII logbook in which all actions and errors encountered during operation are stored (as well displayed in the GUI for easy access). Logbooks have a size of 200 *MBytes/night*.

In an observation night, all 577-pixels anode DC currents are stored into disk at maximum monitored rate ( $\sim 6$  Hz, limited by the CANbus bandwidth) to be used afterwards in observed sources analysis (for example, to find stars in FOV to check for telescope mispointings or correct for camera oscillations). DC currents files have a size of 250 *MBytes/night*. All other subsystem data can be saved, although this is optional. During Guagua shutdown, all DC files and logbooks are transferred to an storage PC via NFS. Afterwards the DC currents are sent to tape together with all raw data files. Tapes are transported to the MAGIC Data-Center, currently in Wuerzburg (Germany).

## Part III

# The detection of $\gamma$ -rays from the Galactic Center with the MAGIC telescope

## Chapter 7

# MAGIC data analysis techniques

*This Chapter describes all the procedures used in this Thesis for the analysis of the data taken with the MAGIC telescope pointing to the Galactic Center region. It covers from checks to ensure the quality of the data to a description of the whole data reduction chain: signal extraction, calibration, image cleaning, image parameterization,  $\gamma/h$  separation technique, energy reconstruction, and final signal evaluation, including differential energy spectra, light-curve and source location.*

*The Thesis Author participated actively in the development of the source location analysis techniques, which were presented in the ICRC 2005 [157].*

### 7.1 Main background sources

The main challenge of any IACT is to cope with the large background of charged particles and background light that trigger the telescope. The characterization and subtraction of the resulting images is one of the most important tasks to be addressed in order to obtain the signals generated by primary  $\gamma$ -rays, in which we are interested.

Two different kinds of background are present in IACTs: a) the cosmic ray showers, that generate undesired images (almost all of the events which are recorded), and b) the background light that increases the noise level in the PMT responses.

- **Cosmic ray showers** As already described, the EAS initiated by cosmic hadrons are much more abundant than those generated by the primary  $\gamma$ -rays emitted from the astronomical object under study. The images generated by hadron showers are similar to those generated by the  $\gamma$ -ray showers, but there are substantial differences in the processes participating in the shower development which are imprinted onto the images, and useful to differentiate both type of images. The method to allow an efficient classification of hadron and  $\gamma$ -like shower images is explained in detail in this chapter. It is worth to mention that the EAS induced by cosmic electrons and positrons creates an irreducible background, as they develop an electromagnetic shower like the  $\gamma$ -showers. This background can be important for very faint  $\gamma$ -ray sources or extended  $\gamma$ -ray sources.
- **Background light** The Čerenkov signal are dim compared to the total light of the night sky, related to stars or human-made light pollution (low near astronomical sites). These sources of light interfere with the detection of the fast Čerenkov EAS light flashes.

Grossly, there are two kind of night-sky background (NSB): a diffuse component, the so-called LONS (Light Of Night Sky), both from artificial and natural origin (like diffuse moonlight,

sunlight scattered by interplanetary dust, zodiacal light, ionospheric fluorescence, etc...); and NSB due to starlight (bright stars present in the FOV). Normally these NSB light contamination depends on the astronomical site location, epoch of the year, the pointing direction (galactic or extragalactic). 'El Roque de los Muchachos', the astronomical site of the MAGIC telescope, is considered to have the best sky conditions for astronomical observations in the world. Specific studies of the LONS were carried out in the MAGIC site, yielding an average value for moonless conditions and pointing outside the galactic plane of  $\sim 0.15$  phe/ns for a  $0.1^\circ$   $\phi$  inner MAGIC-like pixel size [216].

The NSB photons increase the noise level of the EAS signal registered by every PMT signal of the MAGIC camera (the NSB increases the DC current light level of the pixels as well). This makes the detection of faint signals, related to low energy  $\gamma$ -rays. A proper evaluation of the NSB is essential (as we rely on detector simulations), as well as minimizing its effect to the reconstructed PMT signals.

Other source of noise for the PMTs is related directly to the electronic noise of the global DAQ chain, or pickup noise during signal transmission (partially reduced with the use of optical fibers). It is mandatory to keep the electronic noise at a minimum level.

## 7.2 Monte Carlo simulation of MAGIC response to EAS

An IACT is a detector that can be properly calibrated, i.e., the conversion of recorded charge to incident photons for each individual PMT, but it cannot be tested against a controlled flux of known primary particles<sup>1</sup>. A proper knowledge of the IACT is needed as realistic and detailed Monte Carlo (MC) simulations are crucial for the data analysis: from complex processes involved in the EAS to the subsequent detection of the light with the detector.

In any IACT, many of the steps involved in the analysis depend on the MC simulations. The *Crab Nebula* is considered the most important astronomical object for IACT observations, because it provides a high and steady  $\gamma$ -ray flux (it is treated as a standard candle). Once the detector is fully characterized, the most important test is the detection and proper reconstruction of the expected Crab Nebulae flux. Once this is accomplished, and considering how heavily one has to rely on the MC simulations, it is remarkable the good agreement among different IACTs, even in quasi-simultaneous measurements in same sources, like AGNs in flaring state.

In MAGIC, we have developed a chain of different programs to simulate the EAS properties, and the detector parts. Modular programs allow to change parameters either related to the EAS or the detector without the need for generating the full simulation chain again (which is costly, from the computational time point of view).

- **Simulation of the EAS:** The development of the EAS is simulated, either for  $\gamma$ -ray and hadron showers, with the CORSIKA 6.019 package, developed by the KASCADE team [217]. Each particle generated in the shower cascade is treated individually, and all information of the Čerenkov photons arriving at the earth (for the given telescope altitude location) is stored into an output file.
- **Reflector:** This includes the simulation of the telescope's mirror dish. This program takes the output of the CORSIKA simulated showers and simulates the focalization of the Čerenkov photons in the camera plane. The output contains the information of Čerenkov photons hitting the camera.

---

<sup>1</sup>Normally done in particle detectors, like calorimeter tests (the so-called test-beams).

- **FOV Star-field:** Given the telescope pointing position, time of day, the stars position on the FOV are obtained from a star catalogue. Given the spectral data for each star, the photons which impinge into the camera plane are as well calculated (over a given integration time).
- **Response to NSB photons:** Both from stars and diffuse NSB, this program simulates the analogue signal at the entrance of the trigger discriminator and the digitized signal at the output of the FADC. NSB signal is treated independently, in a much longer time window than the one used for EAS, and the result is stored in a database. The output is merged with the signal response to the EAS Čerenkov photons, in a further step. In this way, computing time is saved, as the background has not to be generated for each event.
- **Camera:** This program simulates the electronic chain response to the EAS Čerenkov photons. The PMT, trigger and FADC system is simulated. The output of this program is in the same format as the real data raw files, which allow to test the whole analysis chain with the use of MC  $\gamma$ -rays and hadrons.

Some parameters involved in the MC chain have to be measured with certain precision, like the mirror reflectivity, efficiency of light collection, quantum efficiency of the PMTs, noise introduced by the electronics, etc... This was the main task of the collaboration during the telescope commissioning phase. Regular checks are done in order to keep a monitor on most of these parameters.

An important parameter, with a great impact imprinted into the data, is the width of the Point Spread Function (PSF) distribution of the light collected by the mirror dish and focused into the camera. Although the AMC corrects for mirror element deviations, about three times per year a major access is done to cure mirror panels which cannot be properly adjusted. Progressive loose of the mirror alignment capability means wider and less concentrated Čerenkov images in the camera. This has several disadvantages, maybe the most important is that low energy  $\gamma$ -rays are much more difficult to observe. In addition, the difference between  $\gamma$  and hadron images diminishes, affecting the efficiency in the  $\gamma$ -hadron separation, hence deteriorating the sensitivity of the telescope (which is quite bad if we observe expected faint sources, or new discoveries whose emissions are nearby the nominal  $E_{\text{thr}}$ ). The MC simulations should take this effect into account.

Several independent methods are carried out to monitor the PSF of the telescope:

- **PSF from strong  $\gamma$ -ray signal:** strong  $\gamma$ -ray emissions, like the Crab Nebula and AGNs in flaring state, are useful as high  $\gamma$ -ray statistics are accumulated, and the MC PSF can be adjusted until the best agreement of simulated  $\gamma$ -showers and  $\gamma$ -like events is reached.
- **PSF from muon images:** the width of ring-shaped real muon images is a good measure of the telescope PSF, used to tune the PSF of the MC for the best match.
- **PSF from stars:** direct measurements of the bright starlight in a panel placed in the camera plane with a CCD camera.

In [215] the three methods have been used to check for the degradation of the telescope focusing during 2005, by using the strongest  $\gamma$ -ray signals. The PSF which we use in this Thesis derives from these measurements, resulting in a mean value of  $\sigma \sim 14$  mm.

### 7.3 Selection of the data sample

The raw data is stored in the MAGIC data-center. The selection of the data is done through the type in which we are interested (calibration data, raw data, etc...). The *project name* usually relates the files contents with an observation tag that contains information of the type of data present in

the file and the astronomical position tracked. At present, all data is stored in the database, so we will explain which kind of selection criteria we made in order to skip a few corrupted files.

### 7.3.1 Types of data runs

The raw data files contain the digital information of the recorded events. These files are later merged with other telescope subsystem information, so all necessary information for correct processing of the data is given (like event time stamp, tracking position, Starguider information, camera temperature, etc...). During the observation, the DAQ subsystem manages the raw data files, creating new files when they exceed a fixed number of recorded triggers, and assigning a run number to each of these files.

Normally, three type of data files are available:

- **Data runs:** contain events that trigger the system when the telescope is tracking a particular position in the sky. Interleaved calibration events are present in these data files, at a fixed rate of about 50 Hz (they are needed to correct small fluctuations of the signal readout chain).
- **Pedestal runs:** while tracking the particular position in the sky, the trigger is activated randomly and 1000 events are taken at a rate of 500 Hz. Given the MAGIC characteristics and the rate of hadron showers, the probability of a random trigger from any signal coming from a real shower is small. This provides information about the NSB and the noise present in the readout chain, in particular is used to determine the signal baseline and its fluctuations. A pedestal run is used before a calibration run sequence is started.
- **Calibration runs:** the light emitted by the calibration system is recorded after a synchronized trigger line activates the DAQ. Normally, prior to observing a source, a calibration run with the 10 UV LEDs configuration is a must. There are as many calibration runs as sources tracked per night.

The raw files (either pedestal, calibration or data files) are tagged with the *project name*, that indicates the source and in which observation mode the data has been taken:

- **ON data runs:** telescope tracks and points to the source.
- **OFF data runs:** telescope tracks a position of the sky in which presumably no  $\gamma$ -ray source is present (this is based on cataloged probable VHE emitters), but with similar zenith and background conditions as for the ON runs. This data is used for background estimation purposes.
- **Wobble mode data runs:** The source is tracked at fixed angular distance off-axis from the pointing direction. The source position is used as ON data, while the symmetric positions with respect to the camera center are treated as OFF data.

### 7.3.2 Run selection

Once the data sample is chosen, the runs are subjected to first selection checks based on the quality of the data:

- **Event rate:** the rate of events that trigger the telescope, the *trigger rate*, monitored during the data taking, is a good indicator for bad atmospheric conditions or for deficient data taking due to telescope system misbehavior. The trigger rate depends on the ZA of observation (Čerenkov light is more absorbed in the atmosphere at large ZA), but comparisons night-to-night for similar observation conditions allow to search for these problems.

- **Weather conditions:** the weather station located in the MAGIC site is a good instrument to check about the weather conditions and the connection to low trigger rates. This is checked every night during the observation time. Moreover, the atmospheric extinction coefficients, provided by the MERCATOR telescope are used<sup>2</sup>. High extinction coefficient values ( $c > 0.2$ ) are normally traduced to low trigger rates. With naked-eye the night seems to be perfect, but the presence of 'calima' or dust in the atmosphere affects drastically the quality of the data which is being taken.
- **Online run-books:** the telescope operators fill these run-books, in which all technical incidents that appeared during the data taking are written, like DAQ or calibration failures, PMT HV reduction for safety reasons, due for example to the nearby passage of a car during the observation night, etc...
- **General database:** The day after the observation, a database is filled with all important parameters. It is useful to discard runs with a few events, runs tagged as test or defective, wrong trigger discriminator values set, wrong trigger condition, etc...

## 7.4 Signal extraction

Once the raw data selection is completed, the data is processed in order to treat the pixelized digital image showers, and extract the relevant results. In the following sections we explain the steps to be done to accomplish this objective.

### 7.4.1 Signal extraction method

A 300 MHz FADC system is used to digitize the air shower signals. A total of 30 FADC samples are stored per event and channel. The first 15 slices are reserved for a high gain chain, while the last 15 for low gain chain. Normally, the digitized pulse is totally contained in the first 15 slices, and in case of saturation in the high gain region (i.e. the signal overpass a certain FADC counts level), the low gain chain is switched and the last 15 slices contain a copy of a low amplified pulse, as can be seen in figure 7.1.

Several methods have been implemented to extract the charge and the arrival time information of the recorded pulses, all of them with the aim of minimizing the impact of the NSB in the signal reconstruction. As the pulse shape is known, the procedure that we applied is the *digital filter* algorithm that extracts the total charge and pulse arrival time [218]. The signal is evaluated from a weighted sum of  $n$  FADC samples within a given window position, and the weights are estimated from the expected shape and with the help of dedicated MC simulations. This signal extractor has proven to give better results than other conventional signal reconstruction algorithms. For large signals, a timing resolution of about 200 ps can be obtained. The *digital filter* reduces the noise contribution to the error of reconstructed signal.

In order to reduce the bias introduced by the signal extractors due to the search of the signal maximum prior applying the extraction algorithm (since positive fluctuations of the background are then favored), a pulse position check is done before extracting the signal. The first 1000 events of the run are readout and the mean position of the pulse maximum is evaluated. We do expect some spread in the arrival times of the different regions of the image shower, hence a searching window of limited width around the determined mean pulse position is defined for the signal extraction,

---

<sup>2</sup>Mercator Telescope web page: <http://www.mercator.iac.es/extinction/extinction.html>, the extinction coefficient data is only available for few days as it is tabulated on-line only when the photometer is used for the observations and the sky presents photometric conditions.

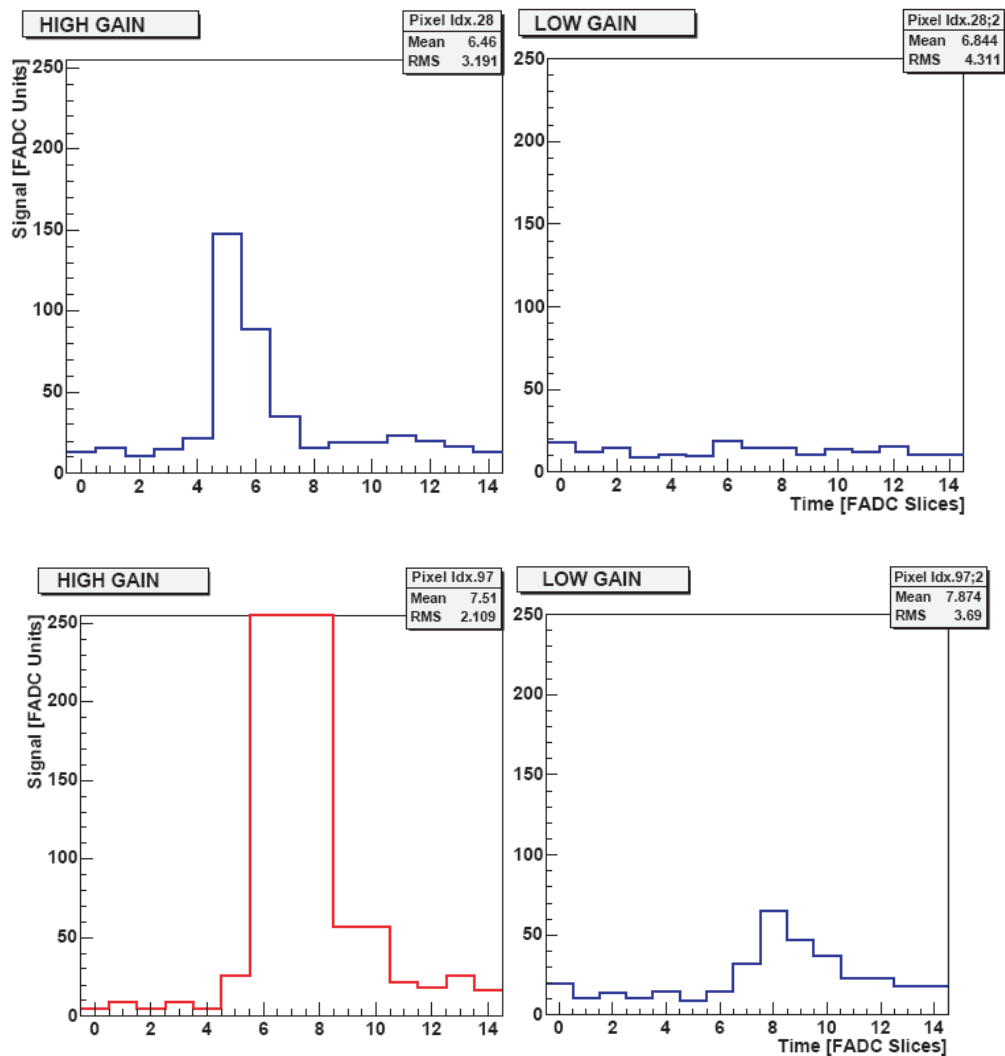


Figure 7.1: FADC sampling of a small and a large signal from one pixel of the MAGIC telescope. Left: high gain signal. If signal reaches the maximum of 250 FADC digital counts (bottom), the same signal is recorded after a certain delay and with a reduced amplification. Note that the high gain signal is amplified by a factor 10 with respect to the low-gain signal. If no saturation occurs, the low gain branch is not activated (top).

and remains fixed for all the events and pixels. The digital filter extractor evaluates the signal only for the FADC slices included in this fixed searching window.

A disadvantage of the digital filter signal extractor is that it can not properly adjust pulses which are out of range of the recorded window. A hardware problem in the time delay setting of one of the trigger macro-cells affected most of the MAGIC 2005 data. The consequence is that those events triggered by the misbehaving macro-cell tagged the starting point to register the pulses too late and the position of the pulses appeared shifted to the left even by two FADC time slices [219].

### 7.4.2 Pedestal evaluation

Two ways are used to compute the pedestal level for the MAGIC data analysis: from a dedicated pedestal run, as the mean signal (with its corresponding RMS) per FADC slice recorded (no cosmic signals are expected to be caught by the random trigger, as the probability is quite low); or directly using the events in the data runs, from the registered FADC slices in the low-gain region (last 15 slices) if no saturation occurs in the high-gain channel (as happens for most of the events). In this case, no switch to add up the low-gain pulse is done, and the average mean pedestal for each pixel is evaluated in the low-gain region from 2000 events with no saturated high-gain.

Since the output of the PMT is AC-coupled, the NSB does not modify the level of the FADC pedestal, but alters the size of the fluctuations. These fluctuations are proportional to the square root of the NSB phe rate. The noise fluctuation is characterized through the pedestal RMS, and only pulses whose charge is significantly above the level of noise fluctuations will be interpreted as signal. This procedure is referred to as image cleaning, and we will explain it in detail later.

### 7.4.3 Calibration of the data

The integrated charge of the extracted signal is given in units of FADC counts. It has to be converted to number of photoelectrons arriving to the first dynode of the PMT. The PMT pulsed signals of each channel  $i$  are calibrated basically by multiplying the recorded charge in this channel  $Q_i$  (measured in digital units of FADC counts) by its corresponding calibration factor  $C_i$ , thus obtaining the signals in units of Čerenkov photo-electrons  $S_i$ . The calibration factors  $C_i$  can be computed using a calibration system that illuminates the camera with homogeneous (and/or known) light pulses (during the so-called calibration runs). The calibration provides a relative calibration among the different pixels, but not an absolute energy calibration.

The calibration constants are calculated using the excess noise factor method. The mean number of *phes* produced per calibration pulse is estimated using formula 5.13 (section 5.7.5), with  $F = 1.15$ . Then, the conversion factor  $C_i$  from FADC counts to *phe* for each pixel is directly obtained from

$$C_i = \frac{n_{phe}}{Q_i - \bar{P}_i} = \frac{\bar{Q}_i - \bar{P}_i}{\sigma^2} F^2 \quad (7.1)$$

where  $\bar{Q}_i$  is the mean charge from calibration pulses in FADC counts for the pixel  $i$ ,  $\bar{P}_i$  the mean pedestal to be extracted, and  $\sigma^2$  is defined as the reduced variance calculated from the charge distribution and corrected by the contribution of the pedestal variance ( $\sigma^2 \equiv \sigma_Q^2 - \sigma_P^2$ ).

The calibration system can be fired in multiple wavelengths to calibrate the whole readout chain in wavelength and linearity. The 'standard' procedure used to obtain the calibration factors during data-taking is through the very fast light (3-4 ns FWHM) emitted with 10 UV LEDs located in the calibration system. The spectral emission of the LEDs is centered at 370 nm, i.e, close to the QE peak of the PMTs and the median of the spectrum of the Čerenkov light reaching the telescope. In addition to the calibration runs described previously, special runs used to compute the signal pedestals are also taken. The pedestal and the RMS of the pedestal extracted from the pedestal runs are also converted into Čerenkov *phe* equivalent values using the same calibration constants to calibrate the *data runs*.

The conversion factor in an individual pixel is known to drift by at most 10% in time scales of several minutes due to instabilities in the optical transmission, and coherently for all pixels in the camera by at most 20% in time scales of hours to days due to thermal effects in the HV regulation and the optical transmission. These fluctuations can be corrected out using *interleaved calibration events*: during standard data-taking, 10 UV LEDs calibration events, with intensity around 30 phe in the inner pixels, are taken together with cosmic events at a 50 Hz fixed rate. The calibration factors, which are evaluated with the initial calibration run, are adjusted with the help of these

interleaved calibration events, which minimizes the effect of possible drifts in the electronics. The final precision in the determination of the charge in phe for the individual pixels is about 3%.

Apart from the central (id. 0) and the calibration blind pixel (id. 560), some pixels are excluded by the calibration routines during the calibration of the different nights. Those pixels have to be recognized to diagnose the hardware problem and repair it, but also to treat them in the more convenient way to avoid biases in the analysis. They are the so-called *bad pixels*. The software can proceed in two ways with bad pixels: they can be completely excluded from the calculation of the image parameters, i.e. their signal is ignored in the following analysis steps; or the signal can be interpolated, i.e., their signal, pedestal and pedestal RMS values are substituted by the average quantities from their neighbor pixels. By default, a pixel is interpolated if none of the neighbor pixels has been tagged as unsuitable, and the pixel with its new content is once again included in the regular analysis data chain.

## 7.5 Image cleaning

To trigger the telescope readout channel, the recorded event should have passed the L1 trigger criteria, i.e. that at least 4 next neighbor (4NN) pixels have signal above the discriminator levels. If this is the case, the trigger gate is opened and the event is digitized. Most of the camera pixels do not contain Čerenkov signals, but fluctuations from the NSB. A procedure is needed to determine which pixels should be considered part of the recorded image, with the goal of keeping those pixels which contain information about the EAS and rejecting those ones whose signal is more likely due to NSB fluctuations. This procedure is called *image cleaning*, particularly important because the 2nd moment calculation of the shape image parameters does not take into account the errors (fluctuations) in the pixel signals, but only the calibrated signals.

The selection of the 'meaningful' pixels in a given image can be performed by comparing their calibrated signals ( $S_i$ ) with their calibrated noise, which is estimated by the calibrated pedestal RMS ( $\text{RMS}_i^{\text{ped}}$ ). This is the so-called *scaled-cleaning*. Another way of estimating which pixels do contain a signal is to set a fixed level of 'signal' in terms of *phes* for cleaning purposes (i.e. signal  $> N_{\text{phe}}$ ). This is the so-called *absolute-cleaning*.

The disadvantage of relative image cleaning is that the pedestal RMS noticeably depends on the NSB conditions. For example, it is different for galactic and extragalactic sources. If the same levels of relative image cleaning are applied to data taken with different background conditions, the resulting images can present large differences. This problem can be partly avoided with the absolute image cleaning, which does not take into account the magnitude of the pedestal fluctuations, but which is in turn sensitive to pixels with especially high pedestal RMS (e.g. those affected by stars). The method which we use in the analysis that is presented in this Thesis is the *absolute cleaning*, as it has shown to give better agreement when comparing ON and OFF Hillas parameters distributions, even better agreement to MC, compared to the *scaled-cleaning* procedure.

The arrival time of the signal in each pixel can also be used to define an image cleaning method. Presently several timing based cleanings are under study and are already giving promising results specially for the smaller images. The analysis of the islands of pixels of the resulting image to discriminate if they are from noise origin or not is also another possible tool to improve the image definition. Neither the arrival time nor the islands will be considered in this analysis.

The image cleaning is grossly done in four steps:

- **Correction of 'bad' pixels:** The signal content of 'bad' pixels which had at least 3 neighboring 'live' pixels is interpolated from the light content of the neighboring pixels.
- **Selection of core pixels:** The pixels fulfilling the condition  $S_i \geq 10 \text{ phes}$  (*absolute cleaning*),

and having at least a neighboring pixel fulfilling the same requirement are tagged as core pixels.

- **Selection of boundary pixels:** The pixels (which are not core pixels) fulfilling the condition  $S_i \geq 5 \text{ phe}$  and having at least a core pixel as a neighbor are tagged as boundary pixels.
- **Removal of the noisy pixels from the image:** The signals of the pixels which are neither core pixels nor boundary pixels are set to zero.

The resulting cleaned event should contain only the pixels considered to have the Čerenkov photons coming from the EAS. From here, the set of Hillas parameters are evaluated. Figure 7.2 shows the same event before and after images cleaning.

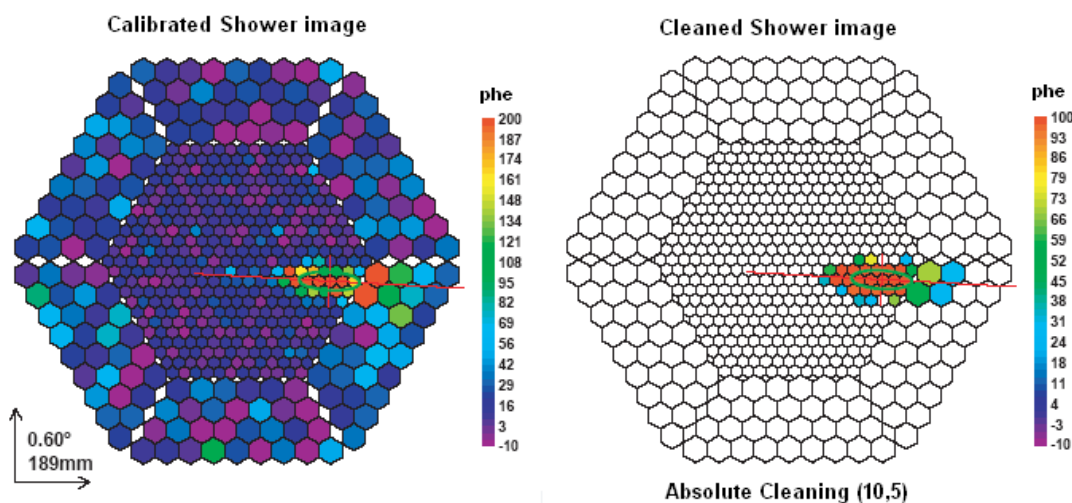


Figure 7.2: Example of image cleaning procedure: an event recorded by the MAGIC telescope after calibration (left) is cleaned with the absolute cleaning method (10,5) (right).

## 7.6 EAS shower image characterization: the Hillas parameters

After calibration, pedestal subtraction and rejection of pixels only affected by the NSB, the resulting image contain valuable information about the EAS shower, and hence can be used to estimate the energy, the direction and the type of primary particle responsible for the camera illumination. This is another major task of the *Imaging Technique*.

The parameterization analysis is based on the use of the Hillas parameters as image parameters that describe the light distribution of the shower images recorded by the camera [179]. Hillas parameterization is based on the first, second and third moments of the two-dimensional distribution of the signal along the image. For the moment calculation, the position of each pixel included in the image is weighted with the fraction of the image signal content in it,  $\omega_i = \frac{N_i}{\sum_k N_k}$ . The shower image is parameterized as an ellipse and the moments are estimated with respect to a system of coordinates with center at the center of gravity of the image, x-axis along the major axis of the ellipse, and y-axis along the short axis.

This analysis technique has been extensively used by most of IACTs<sup>3</sup>, but we have learnt with

<sup>3</sup>These analysis techniques have been successful for IACTs with  $E_{\text{thr}} > 150$  GeV. MAGIC telescope poses a lower  $E_{\text{thr}}$ , but these techniques can safely be applied for moderate to high energies.

the MAGIC telescope that the use of the 'classical' Hillas parameters imposes a kind of limitation to enter into the sub-100 GeV domain (accessible at low ZA observations), as the shower images start to behave different. With current capabilities of the MAGIC telescope, and low ZA observations, the trigger energy threshold is estimated to be about 60 GeV, estimated from the background trigger rate. This means that low energy  $\gamma$ -showers may trigger the telescope, although it is difficult to disentangle them from the background with the Hillas approach.

New analysis techniques are under development, and first satisfactory results have been obtained when analyzing a huge  $\gamma$ -ray flare of the Mrk501 Active Galactic Nuclei, with significant excesses detected in the sub-100 GeV regime [201]. The purpose of this Thesis is to measure, confirm or discard HESS/CANGAROO results and, if possible, extend the spectra measurement of the GC VHE emission to higher energies. Hence, we have not made any attempt trying to improve and lower the energy threshold, at least on this dataset, as in case of confirmation (that is the case) the spectra in this low energy window is already measured by HESS.

The Hillas parameters are grouped into three classes; namely image parameters that depend on a) the shape and light content of the shower, b) a reference direction, c) and a reference point. The image parameters are shown in Figure 7.3, and are defined as follows:

- *Shape parameters*

**SIZE:** the total number of *phe* in the shower image.

**LENGTH:** the *phe* distribution RMS value along the main axis of the shower image.

**WIDTH:** the *phe* distribution RMS value along the minor axis of the shower image.

**ASYM:** asymmetry of the *phe* distribution along the shower major axis.

**M3LONG:** 3rd moment of *phe* distribution along the shower major axis.

**DISP:** Distance that estimates to expected source position along the shower major axis, from the CoG of the image. This is the distance estimated from the DISP method (that will be explained in separate section). Ideally,  $DISP \sim DIST$  for a source observed on-axis.

**CONC:** fraction of signal contained in the 2 brightest pixels of shower image.

**LEAKAGE1, LEAKAGE2:** fraction of photons contained in the pixels close to the last ring or last two rings of pixels, at the edge of camera outer region.

**NUMISLANDS:** Number of 'images' which remain in the shower image after image cleaning.

- *Parameters that depend on a reference direction*

**DELTA:** The angle  $\delta$  between the shower axis and the x-axis of the camera.

- *Parameters that depend on a reference point*

**DIST:** the distance between the reference point (*RP*) and the center of gravity (*COG*) of the shower image.

**ALPHA:** the angle between the shower major axis and the line connecting the *COG* of the shower image with the *RP*.

The parameters WIDTH and LENGTH are basically the Čerenkov light projections onto the camera plane of the geometrical length and width of the EAS. The differences between pure electromagnetic showers and hadronic showers have a great impact into these two parameters, this is an important feature to distinguish  $\gamma$ -showers from *hadron*-showers.

The parameter SIZE is directly related to the total amount of Čerenkov photons produced in the *EAS*, and is proportional to the total amount of energy of the primary particle, at first

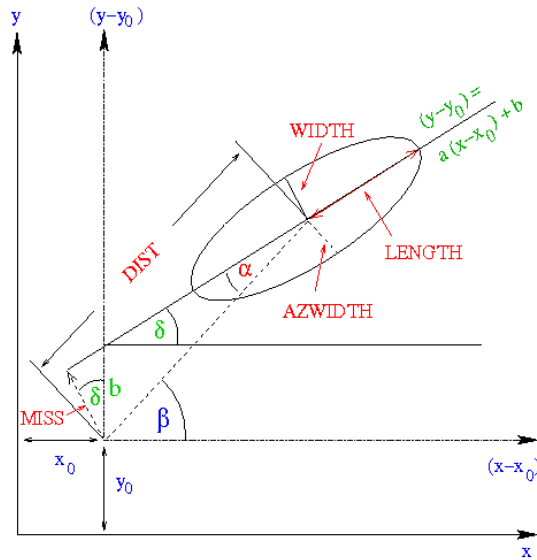


Figure 7.3: Definition of the Hillas parameters.  $(x, y)$  are the coordinates in the original camera system and  $(x_0, y_0)$  are the coordinates of a reference point, like the source position or the camera center position.

order (assuming a certain uniform illumination of the shower image cone at ground level). This parameter is quite useful for energy determination. The energy estimation can be improved by combining SIZE to other parameters, like DIST, which gives an estimate of the impact parameter of the shower, or the ZA, etc... These corrections improve the energy resolution.

The ALPHA parameter is related to the angle between two planes: the plane formed by the telescope axis and the CoG of the shower, and the plane formed by the shower axis and the reflector center. ALPHA is close to zero if the two planes coincide, i.e. if the telescope axis and the shower axis lie within one plane. This is the particular case when the direction of the primary particle is parallel to the telescope axis.

The ASYM and M3LONG<sup>4</sup> Hillas parameters are useful as shower 'head-tail' determinations, i.e. to decide which part of the shower ellipse corresponds to the Čerenkov light emitted in the initial EAS development. Either ASYM or M3LONG are proven to be useful parameters for determining the  $\gamma$ -ray arrival direction with the DISP method. However, M3LONG is most affected by the shower LEAKAGE effects, losing its powerness, so only ASYM is considered for 'head-tail' determinations.

The image parameters are influenced by the limited Čerenkov angle, the statistical fluctuations in the shower development, and (specially at  $\gamma$ -ray energies below 100 GeV and observations at zenith angles  $> 30^\circ$ ) the Earth magnetic field. The typical distributions of LENGTH, WIDTH, DIST and ALPHA for gamma-induced showers and hadron-induced showers are discussed in next section. The Hillas parameters formulation is given in Appendix E.

### 7.6.1 Hillas parameters: implications for $\gamma$ -hadron separation.

The Hillas approach turns out to be quite useful to characterize the shower images, as this set of parameters mostly parameterizes the information from the EAS. In particular there are clear

<sup>4</sup>Technical: M3LONG in the MARS software has to be signed with the  $\cos(\text{COSDELTAALPHA})$ .

differences on some of these parameters for  $\gamma$ -showers and *hadron*-showers. To evidence these differences, we made use of the outcome of the standard MAGIC simulation programs to show the typical set of Hillas parameters for both cosmic hadrons and  $\gamma$ -rays in the telescope camera<sup>5</sup>.

To show the differences imprinted into the Hillas parameters from different primary particles we use a MC data sample formed by 5.2 million gammas (for a point-source located at the center of the camera field of view) and 28.5 million protons<sup>6</sup>. The gammas are simulated in the energy range from 10 GeV to 30 TeV with an energy distribution that follows a power law spectrum with a spectral index of -2.6. The protons are simulated in the energy range from 30 GeV to 30 TeV with a spectral index of -2.75. All showers are simulated in the zenith angle (ZA) range 0-30°, and at two fixed azimuthal angles  $\phi=0^\circ$  and  $\phi=90^\circ$ , which correspond to showers coming from the South and from the East, respectively. The impact parameters are distributed uniformly in the circle defined by a radius (with respect to the telescope axis) of 300 m for gammas and 400 m for protons. In the MC simulations, the MAGIC Telescope trigger is set to the standard one, i.e, coincidences of four closed-packed 'pixels' whose signals' amplitudes are above 4 mV. The image cleaning applied to the MC data was an *absolute cleaning* (10,5).

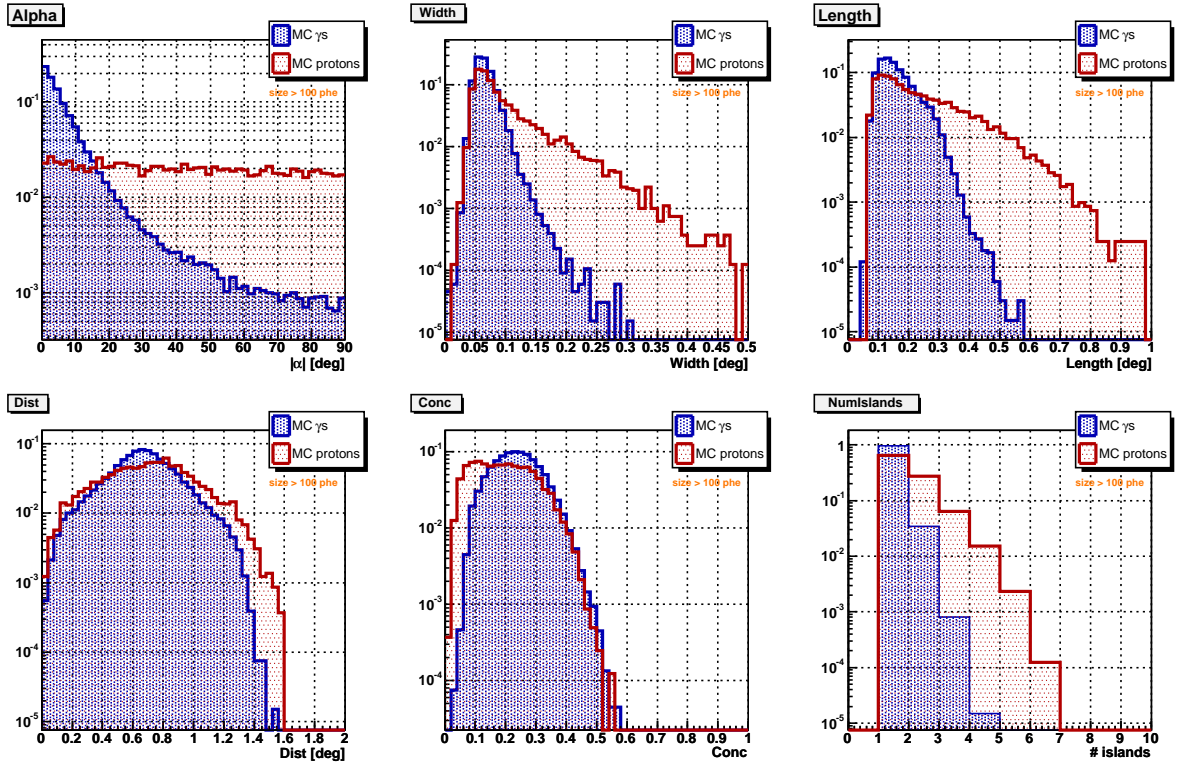


Figure 7.4: Distribution of ALPHA, WIDTH, LENGTH, DIST, CONC and NUMISLANDS parameters for simulated  $\gamma$ -induced showers (blue filled histograms) and proton-induced showers (red filled histograms), after trigger and image cleaning procedure. All distributions are normalized to unit area for a better comparison (a cut in SIZE > 100 *phes* is applied to both samples).

<sup>5</sup>These set of MC files are generated at low Zenith Angle (ZA), and they do not correspond to the simulation files used for the specific analysis presented here. We make use of these files to make a comprehensive view, as there is a lack of simulated protons below 30° Zenith Angle (due to computational power needed to simulate them).

<sup>6</sup>Helium nuclei could be added, as it is the second important contribution to the hadron sample, but the outcome of the comparison does not change drastically.

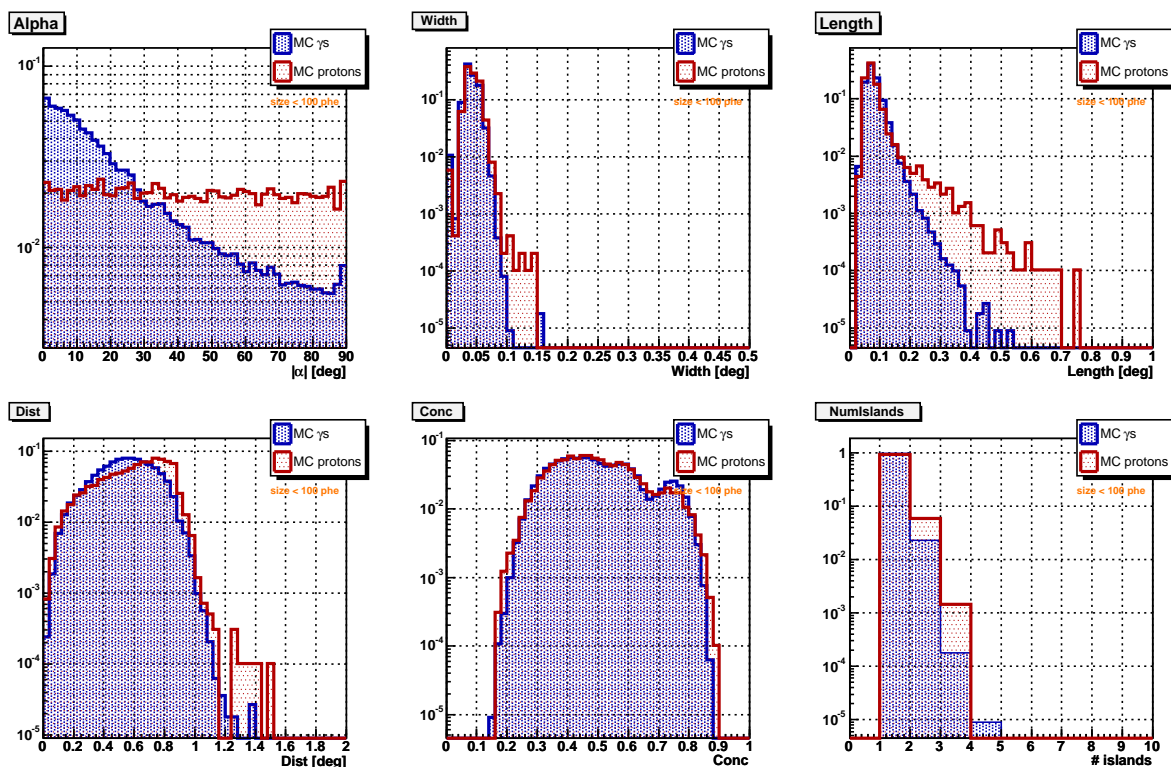


Figure 7.5: Same caption as Figure 7.4, but a cut in SIZE  $< 100$  phe is applied to both MC samples.

The use of the Hillas parameters for  $\gamma$ -hadron separation has been extensively reported in the literature. Figure 7.4 shows the most important parameters in which the differences between  $\gamma$ s and hadrons are visible. These distributions are done for SIZE  $> 100$  phe, that corresponds, roughly, to a cut in  $\gamma$ -energy of about  $> 100$  GeV. Note, that the differences from the two samples start to vanish for size  $< 100$  phe, Figure 7.5, i.e, for  $\gamma$ -energies  $< 100$  GeV, hence the  $\gamma$ -hadron separation based on the Hillas parameters turns out to be a difficult task. This is the typical case for low ZA observations. At large ZA, the scenario is almost the same, but due to the light absorption in the atmosphere, the  $E_{\text{thr}}$  increases and this deterioration of the  $\gamma/h$  separation starts to be visible at higher energies (in particular, around 650 GeV for  $60^\circ$  ZA observations).

Static cuts on these variables can be used to optimize the  $\gamma$ -hadron separation. Nevertheless, we make use of the Random Forest method, based on the Hillas parameters, as a powerful technique to separate  $\gamma$ s and hadrons, making use of the full power that supposes to search for correlations and separation regions in a multi-dimensional parameter space. We will explain this method in a separate section.

To summarize, the most relevant differences for images generated by  $\gamma$ -showers and hadron-showers, characterized by the Hillas parameters, are:

- At a given energy,  $\gamma$ s produce more Čerenkov light than hadrons. Every primary particle has its own energy-to-size dependence.
- $\gamma$ -images are more compact than those produced by hadrons. This is visible in the WIDTH and LENGTH parameters. In particular, the images from hadron cascades are more fragmented than those coming from  $\gamma$ s, as seen from NUMISLANDS histogram.

- As pointed out, in the most favorable observations, the  $\gamma/h$  separation in the sub-100 GeV region is a difficult task. Moreover, one of the most powerful parameter, ALPHA, loses its peakness power in this domain (see Figure 7.6), in which new separation techniques should be developed.
- Hillas parameters are quite sensitive to the impact parameter of the primary particle and the ZA, important for  $ZA > 30^\circ$ . This dependences can be included in the  $\gamma$ -hadron separation techniques, in particular by means of the DIST parameter, as it is highly correlated to the impact parameter<sup>7</sup>.

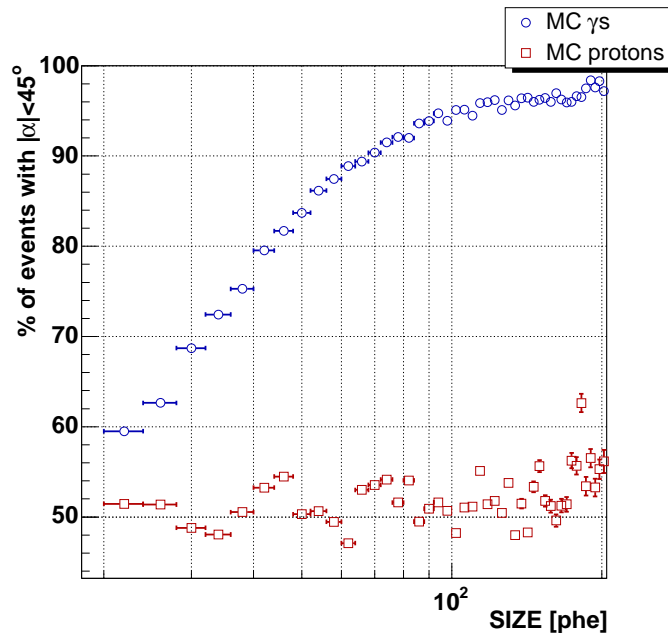


Figure 7.6: Percentage of events with  $|\alpha| < 45^\circ$  for both  $\gamma$  and proton MC described in the text. For  $\gamma$ s, the ALPHA peakness starts to lose its power at about 100 *phes*, which corresponds to a  $\gamma$  energy of about 90 GeV. Note that *hadrons* are quite flat distributed in ALPHA, as expected for isotropic showers in the field of view.

## 7.7 Data quality checks and filter cuts

By the time of the telescope observations, there can be some problems on its performance that directly affect the quality of the data, hence the quality of the results. In this section we briefly explain the problems we encountered when analyzing the GC data set, at least the most relevant ones, and we leave the methods we used to try to recover them, to the Analysis Chapter.

The major problems were:

- **Non-operative pixels:** About 28 pixels are non-operative for the analysis. These pixels are excluded at the calibration level, as they show no charge, fluctuating signals, etc... as a response to the calibration system pulses. The charge in these pixels is then interpolated from the neighbor pixels.

<sup>7</sup>The correlation is higher for  $\gamma$ -showers, rather than *hadrons*.

- **Corrupted runs:** Some data runs were corrupted. This happens from time to time because the heat dissipation in the electronic racks that contains the receiver boards and the FADCs, and many other reasons. A total of 8 runs, out of 436, are excluded from the GC analysis. These runs are not tagged as bad runs previously, but they are recognized easily as the Hillas parameters corresponding to these runs is not compatible with the rest of the data.
- **Rate instabilities:** The data acquisition rate is a good measure of the night sky quality. Two observation nights were excluded from the analysis due to low data acquisition rates. These low rates are not related to ZA variations, as almost all data is taken near the GC culmination ( $ZA \sim 60^\circ$ ), but due to higher light absorption in the atmosphere.
- **'Spark' events:** Noisy events related to some fast-light-sparks that appears regularly in the camera PMTs. These 'special' events trigger the whole acquisition data chain and these events have to be excluded from the analysis. This will be explained in detail in separate section.
- **Camera inhomogeneity:** The different L1 trigger cells suffer from synchronization. These differences in the timing windows affect the pulse positions which are recorded at the FADCs. The events which are triggered in one specific region of the camera are particularly affected. The outcome is that the signal extractor is not able to reconstruct the charge properly for the individual channels of the image, and the event is discarded, affecting to the total amount of events after image cleaning. This creates an inhomogeneous distribution of events in the camera.
- **Problems in telescope tracking position:** Pointing (Moving) to a position on the sky is not very accurate ( $\pm 10$  Shaft-encoder (SE) Steps). The reposition is done two, three or four times until the correct SE step is reached on both axis (which has an accuracy of  $\pm$  one SE step). When tracking starts, one gets a further improvement as soon as the movement crosses the edge of one SE, i.e. changes its value. The time needed depends on the ZA of observation (for HZA this might be a few minutes at the beginning of source tracking). When the source passes through its culmination, the tracking on one axis changes direction and some SE steps are lost. The outcome is that the source is not at the camera center anymore, but  $\sim 0.12^\circ$  away, until the movement crosses the edge of one SE and the pointing procedure starts to be corrected. In addition, in an ALT-AZ mount, the source located off-axis rotates in the camera. In case of the data analyzed in this Thesis, almost 35% of the data is affected by the so-called 'culmination' effect.

## 7.8 $\gamma$ /hadron separation

Emphasis has to be put on the differences between hadronic and photon extended air showers, as we are interested to measure the properties related to the later. It is particularly important to reject as much hadron-showers as possible, as they trigger the telescope by 4-orders of magnitude more than the photons, which are the minimal component of the acquired data. Even though there are large differences between hadronic and photon images, not all hadronic events will be removed from the data after the  $\gamma/h$  separation algorithm, but most of them will, while retaining almost the whole signal in which we are interested.

A high background rejection can be obtained with the use of statistical learning methods, preserving a high  $\gamma$ -efficiency. All these methods are applied to the data after image cleaning and are based on the Hillas approach. The most used  $\gamma/h$  separation methods are the use of *Static Cuts* or the use of the so-called *Super-cuts* [220], in which a set of dynamical cuts are defined, i.e. cuts on

the Hillas parameters which depend on the Hillas parameters as well. Normally these dependencies are parameterized and optimal values are found, by the use of a strong  $\gamma$ -ray source, with ON and OFF subset of the data (maximizing the significance of the  $\gamma$ -signal from the pair ON and OFF datasets after  $\gamma$ /h separation) or with the use of MC simulations.

The analysis of the MAGIC data offers many possibilities to test many statistical learning methods for  $\gamma$ /h separation. We apply the *Random Forest* method as the statistical learning method for  $\gamma$ -hadron separation [221]. This method is based on random set of subspaces in the Hillas multi-parameter space as a method to learn how to classify the  $\gamma$ -showers from the background. The outcome of the *Random Forest* is based on a variable, the so-called HADRONNESS ( $h$ ), which resumes the likeness of an event to be from a  $\gamma$ -shower ( $h \rightarrow 0$ ) or from hadron shower ( $h \rightarrow 1$ ).

One of the pillars of the statistical learning is based on the use of a *train* sample of both signals to be distinguished. This is the feed of the algorithm, which is used to identify in which regions of the multi-parameter space our signal resides. As this is a 'supervised' learning, in order not to bias the results (i.e, over-training of the method), the use of a train sample is crucial. Of course, this training of the method assumes that both underlying physics and the detector response is well understood, as it is normally used a train sample of pure MC  $\gamma$ -rays, while MC or even OFF data are used as hadron train sample. With the use of MC simulations as train samples, one has to be careful, as small deviations of the simulation from reality may result in a trained method that handles simulated events perfectly, but not satisfactory results when applied to the real data. In the current status of the MAGIC telescope, this method has been applied giving satisfactory results, even when comparing with other  $\gamma$ /h methods.

Technically, the *Random Forest* (RF) consist:

- **Train sample:** Two samples of data are selected, each of them corresponding to the categories to distinguish. In this case, pure MC  $\gamma$ -events and real OFF data for hadron-events.
- **Training variables:** Classification of events is done using a certain number of Hillas parameters. The parameters should be at least partially independent.
- **Decisional trees:** The RF is composed of 100 decisional trees, each of them using 3 Hillas parameters, randomly chosen among the selected ones. Interactively, these trees grow, and the events are classified into the random subsamples on the Hillas multi-parameter space, based on a nodes approach, until each of them contains a minimum number of events or the final subsample is totally populated of one of the two categories (terminal node).
- **Optimizing the  $\gamma$ /h separation:** During the tree grow, the cuts on each variable are tested and a coefficient that accounts to the powerness of every Hillas parameter involved in the cuts is computed (the so-called *Gini Index*). The optimal cut is chosen to maximize the Gini index. The use of multiple trees is done to test as much as possible all possible combinations of the multi-parameter space and increase the chance of finding better  $\gamma$ /h separation regions.
- **Output of the RF:** Finally, the HADRONNESS parameter is evaluated for each terminal node of each RF tree, which expresses the probability of an event to be classified in the terminal node  $i$  to be a hadron. By definition, all train MC  $\gamma$  events have HADRONNESS distribution peaking to 0 and all train hadrons have HADRONNESS peaking to 1.
- **Testing the RF input variables powerness:** The RF provides a tool to quantify which are the used image parameters that provides better  $\gamma$ /h separation. For each tree and each node the increment of gini-index,  $\Delta g$ , is defined as the difference of gini-index of the node before and after cutting the population of the events with the analyzed variable. Summing up all the gini-index increments, a test of the separation power assigned to each of the training Hillas parameters can be obtained.

- **Application to data:** After the training procedure, this trained algorithm is applied to the data and a HADRONNESS value is assigned to each event of the real data being analyzed by passing it through the RF classification trees.

All the data analysis presented in this Thesis make use of the Random Forest as  $\gamma/h$  separation procedure. Therefore a cut in only one parameter is applied to the events, a HADRONNESS cut, doing the work of dynamic cut in each of the image parameters used for the RF training. A full review of the RF technique applied to MAGIC can be found in [221], which concludes that RF gives comparable results as neural networks in terms of  $\gamma/h$  separation power, and improved results compared to static and dynamic cuts, especially at low energies. The results when applying this algorithm to the analyzed data is explained further.

## 7.9 Energy estimation of primary $\gamma$ -candidate showers

The energy associated to the  $\gamma$ -like events well after the  $\gamma/h$  separation turns to be an important quantity, as it will be used to determine the shape of the differential energy spectrum of the primary  $\gamma$ -ray candidates associated to the source of emission. The energy of the primary particle is not measured directly and has to be derived from the shower image parameters. This has to be done as accurate as possible, in combination with an efficient set of  $\gamma/h$  separation cuts.

At first order, the total amount of Čerenkov photons within an EAS is directly proportional to the shower energy, and therefore to the energy of the primary particle. Although, the energy resolution is quite poor if using only the dependence on SIZE. Second order corrections arise from the fact that the Čerenkov light distribution on the ground depends on the distance to the EAS maximum, losing part of the signal because leakage effects, changes in Zenith Angle, changes on the atmospheric conditions, etc... All these factors have to be taken into account in order to accurately determine the primary  $\gamma$ -ray candidate energy.

Normally, complex parameterized relations between the energy of the primary and a subset of the Hillas parameters are used in the  $\gamma$ -ray community. In contrast, we would use the set of the MC events for training purposes to feed a special developed RF as a learning method to estimate the energy of the primary particle, as we do know from MC the correspondence of the 'true energy' of primary and the rest of the Hillas parameters. Instead of minimizing the parameters associated to a complex parameterization, the method which we use focus on a different approach, based on the RF technique.

## 7.10 Source position reconstruction: The DISP method

In the standard operation mode (ON mode), an Imaging Air Čerenkov Telescope (IACT) points to the source under study. It is assumed that the source position is at the center of the camera. However, many observations involve conditions that prevent us from using an standard analysis, based on the ALPHA parameter and assuming that the source is point-like, located at the camera center or some other specific known point in the camera. These analysis methods which assume that the position of the source in the camera is known a priori can not be used for many other observations, like observations of extended sources or unknown sources within the FOV. This includes extended sources, as Galactic Supernova Remnants or dark matter searches; sources whose position is poorly known, as is the case of unidentified EGRET sources or Gamma Ray Bursts; or new sources in the camera FOV, for example when doing a sky scan or serendipitously found in the FOV of another source.

For all these cases the Hillas image parameters dependent on the source position can not more be well determined (as no reference position can be defined) and, thus, an ALPHA-based analysis

makes no longer sense. Analysis methods which reconstruct the individual  $\gamma$ -ray arrival direction are essential to treat these particular cases.

As we are interested to study if the detected emission detected from the GC direction is extended or compatible with a punctual source, the Thesis Author participated in the development of an analysis method, called DISP, that uses the information of the shower image shape to reconstruct the position of the source for each detected shower. Starting from the previously successful application by the WHIPPLe Collaboration, the DISP method has been improved and adapted to MAGIC [157].

Here, we will briefly report about the method, and some tests on its performance achieved when applying it to 5.5 hours of Crab Nebula observed on-axis.

### The DISP method

The DISP method uses the information of the shower image shape to reconstruct the position of the source on an event-by-event basis. The source position lies on the major axis of the Hillas ellipse that fits the shower image in the camera, at a certain distance (DISP) from the image center of gravity. Fomin et al. [222] were the first to propose the use of the 'ellipticity' of the shower images (defined as WIDTH/LENGTH) to infer the position of the source of individual showers using a single IACT:

$$\text{DISP} = \xi \left( 1 - \frac{\text{WIDTH}}{\text{LENGTH}} \right) \quad (7.2)$$

where the  $\xi$  parameter has to be determined from a pure sample of  $\gamma$  events (commonly MC  $\gamma$  simulations). The method was applied by the Whipple Collaboration and provided a good angular resolution for single IACTs ( $0.12^\circ$  above 500 GeV). This technique was also adopted by the HEGRA Collaboration when analyzing the data of the stand-alone HEGRA telescope CT1, and by other IACTs.

Because of the different features of the MAGIC Telescope, such as its parabolic reflecting surface and low energy threshold, we adopted a more general parameterization. This describes better the correlation between the shower elongation and the distance shower/source and improves the angular resolution. Additionally, we have added a dependence of the parameters with the total charge (SIZE) of the shower image:

$$\text{DISP} = A(\text{SIZE}) + B(\text{SIZE}) \cdot \frac{\text{WIDTH}}{\text{LENGTH} + \eta(\text{SIZE}) \cdot \text{LEAKAGE2}} \quad (7.3)$$

We have also included a correction term in LENGTH to account for images truncated at the edge of the camera, similar to the correction introduced by D.Kranich et al. [223] for the CT1 HEGRA telescope. The LEAKAGE2 parameter is defined as the ratio between the light content in the two outermost camera pixel rings and the total light content of the recorded shower image.

The optimal values of the DISP parameters can be determined from MC simulations or real data from a well known point-like source. In the work we did for testing the method with real Crab Nebulae data taken at low ZA, we optimized these values with a MC simulated  $\gamma$ -ray sample (zenith angle  $< 30^\circ$ ) by minimizing the average angular distance ( $\theta^2$ ) between the real and estimated source position. This minimization procedure is used elsewhere when applying the method.

The distributions of reconstructed arrival directions are described, in a first approximation, by a bidimensional symmetric Gaussian, so that  $\sim 40\%$  of the events lies within a radius of  $1\sigma$  and  $\sim 85\%$  within  $2\sigma$ . We adopt  $\sigma$  as an angular resolution estimator.

## Head-tail information from shower images

The DISP calculation, eq. 7.3, provides two possible source position solutions along the shower major axis. Therefore, a method to select the correct source position is needed. Images in the telescope camera carry some information about the longitudinal development of the shower in the atmosphere. The 'asymmetry' charge distribution in the images contains the 'head-tail' information of the recorded shower, i.e, which image edge is closer to the source position in the camera plane. Čerenkov photons from the upper part of the shower create a narrower section of the image with a higher photon density ('head') than photons arriving from the shower tail. The photons from the shower tail should normally generate a much more fussy and more spread end of the image.

An image parameter, the so-called ASYM, is defined as the direction between the center of gravity of the charge distribution image and the position of the maximum signal pixel. It allows one in most cases to determine the 'head-tail' assignment to a shower, providing the selection efficiency for the photon density in the image is high. This is normally the case for high energy showers (>70% for SIZE>180 *phe*s). In addition, we introduced new image asymmetry parameters have been defined to improve the 'head-tail' discrimination, like applying different set of weights to pixel charge contents. By combining them, through a multidimensional events classification algorithm, the achieved ratio of correct 'head-tail' assignment improves to up to 85% for SIZE>180 *phe*, but the study is not completed<sup>8</sup>. Here, we use the ASYM as discriminator, leaving the improved variable combination for further studies.

## Test of the DISP method on Crab Nebulae data at low ZA

In order to assess the angular resolution provided by the DISP method, we analyzed 5.5 hours of Crab Nebula taken on September and October 2004, at zenith angle below 30°. The source was observed on-axis. Also, we took 3 hours OFF data for background estimation. These results were presented at the ICRC conference, 2005 [157].

After data calibration and image cleaning, we have used the Random Forest method to discriminate  $\gamma$ -ray from hadron events. As RF training parameters for the  $\gamma$ /h separation we used those Hillas parameters which are basically 'independent' of the source position in the FOV of the camera, i.e., WIDTH, LENGTH, CONC, and SIZE, as we are interested to determine the emission location and in particular the angular resolution. We selected the background sample such that its SIZE distribution resembled that of the MC sample in order to avoid dependences on the MC generated spectrum. With a test sample, we optimized the HADRONNESS cuts (maximizing gamma/hadron separation while retaining at least 80% of gammas and sufficient OFF events for background estimation) for the different SIZE bins. The size of the remaining OFF data sample used for the analysis (1.4h) was of about 25% compared to the ON sample. Therefore, in order not to be dominated by the OFF fluctuations we have adopted models to fit the background in the excess region.

We approximated the distribution of the reconstructed arrival spots by a 2-dimensional bell-shaped Gaussian function leaving the sigma as a free parameter. The values of  $\sigma$ , obtained from fits to the MC gamma data and to the Crab Nebula data are shown in Figure 7.7. The global  $\sigma$  for SIZE>180 photo-electrons ( $\sim 140$  GeV) is  $0.102^\circ \pm 0.008^\circ$ . The results show a significant improvement in the angular resolution of the MAGIC telescope when compared to the results of Lessard et al [224].

In order to compare our bidimensional analysis to the standard ALPHA-based<sup>9</sup> analysis we have

<sup>8</sup>V. Scalzotto, private communication. Study in progress.

<sup>9</sup>ALPHA-analysis contains in the RF training a set of Hillas parameters that may depend on the source position (like DIST, for example), while the DISP-analysis only uses Hillas parameters that do not depend on source position.

computed the number of excess events and significance (i.e. the signal and statistical significance of the detection) for different SIZE bins obtained using both ALPHA and DISP analysis. To make them comparable, we use for the ALPHA-analysis those images that points to the center (based on the ASYM parameter). This adds an additional cut, like the one introduced in the DISP-analysis with the 'head-tail' discrimination, which reduces in the ALPHA-analysis the background in the excess region by 50% as well as 20% of the excess events. The results are shown in Table 7.1. The  $\alpha$ -plot and  $\theta^2$ -plot above 180 phe are shown in Figure 7.8. The used bidimensional DISP-analysis gives a better sensitivity (higher significance) compared to the standard ALPHA-analysis.

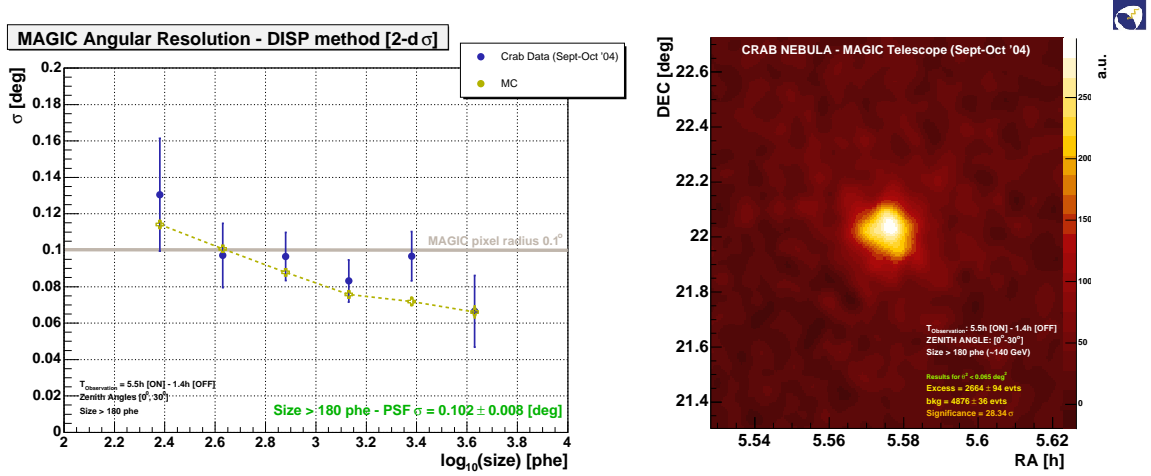


Figure 7.7: (*left*) Results of 2-dimensional Gaussian fits to the distribution of reconstructed arrival directions, both for MC and Crab Nebula, for the different SIZE bins considered. The PSF obtained for SIZE > 180 phe is displayed in lower-right text. (*right*) Smoothed sky-map for Crab Observations using the DISP analysis method.

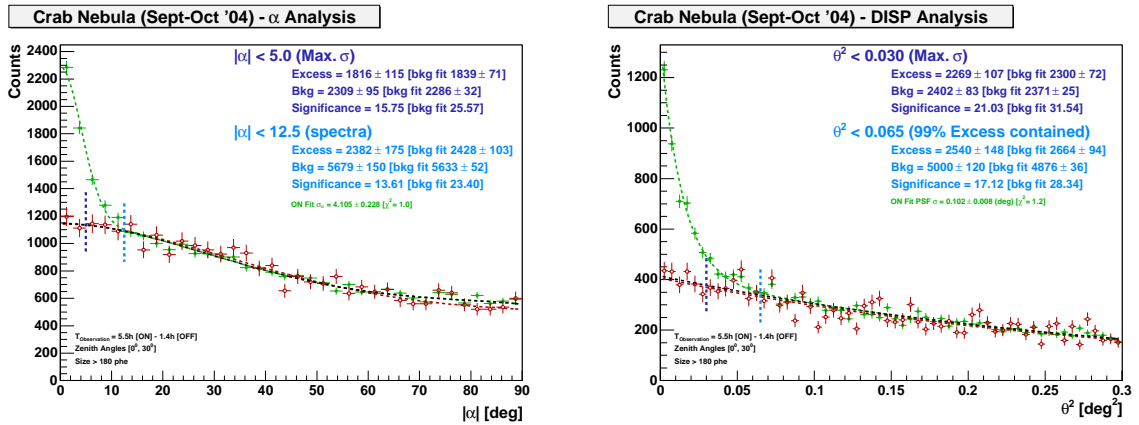


Figure 7.8: Crab Nebula  $\alpha$ -plot and  $\theta^2$ -plot for SIZE>180 phe. Two cuts applied: the one which maximize significance and the one which retain 99% of the excess signal. Results for ON-OFF  $fit$  are displayed in brackets.

The DISP method for the reconstruction of the  $\gamma$ -ray arrival directions has been successfully used to analyze the MAGIC Telescope data. For energies above 140 GeV both MC and real data

SIZE [phe]	Excess Counts	Background Counts	Significance	2-d $\sigma$ [deg]	$\theta^2(\alpha)$ [deg <sup>2</sup> ]/[deg]
(180,320)	316 $\pm$ 73 (248 $\pm$ 78)	4158 $\pm$ 29 (3688 $\pm$ 47)	4.33 $\sigma$ (3.16 $\sigma$ )	.130 $\pm$ .031	<.115 (<17.5)
(320,570)	738 $\pm$ 48 (794 $\pm$ 71)	1219 $\pm$ 19 (2062 $\pm$ 46)	15.31 $\sigma$ (11.17 $\sigma$ )	.097 $\pm$ .018	<.070 (<20.0)
(570,1010)	801 $\pm$ 42 (676 $\pm$ 45)	737 $\pm$ 17 (861 $\pm$ 22)	18.72 $\sigma$ (14.94 $\sigma$ )	.096 $\pm$ .013	<.095 (<15.0)
(1010,1800)	511 $\pm$ 27 (432 $\pm$ 29)	198 $\pm$ 7 (331 $\pm$ 10)	18.41 $\sigma$ (14.62 $\sigma$ )	.083 $\pm$ .012	<.045 (<10.0)
(1800,3200)	312 $\pm$ 23 (275 $\pm$ 23)	205 $\pm$ 6 (218 $\pm$ 8)	13.14 $\sigma$ (11.60 $\sigma$ )	.097 $\pm$ .014	<.065 (<10.0)
(3200,5690)	72 $\pm$ 10 (128 $\pm$ 14)	30 $\pm$ 3 (67 $\pm$ 4)	6.79 $\sigma$ (8.81 $\sigma$ )	.066 $\pm$ .020	<.015 (<7.5)

Table 7.1: Results for the DISP-analysis to Crab Nebula compared to ALPHA-analysis (numbers in brackets)

measurements yield angular resolutions better than  $0.1^\circ$ . The studies show that the performance does not dramatically degrade for lower energies, but the lack of statistics excluded a possible MC/data comparison. The application of the method to Crab Nebula on-axis data shows that this bidimensional analysis is competitive, respectively slightly superior compared to the standard ALPHA-based analysis for point-like on-axis sources. The DISP method provides a promising tool for new source discoveries, and it is widely used now within the MAGIC Collaboration [181, 185, 203, 205, 207, 225, 226].

## 7.11 Cuts optimization

Generally the higher the energy the higher the chances to extract a more pure sample of  $\gamma$ -ray images from the initial sample of events, as the differences between  $\gamma$ -rays and hadrons are more visible. Images generated from low energy induced showers contain only a few pixels and the distinctive features between hadron and  $\gamma$  showers are diluted. Therefore, in the final steps of the analysis it is convenient to classify the sample in bins of the primary particle energy, and optimize the cuts dynamically, to improve as much as possible the signal extraction.

To quantify the powerness of the cuts to be applied, some methods have been tested. The idea is to find a set of cuts in order to maximize the hadron suppression, without cutting away part of the signal. The first cut to be optimized are the energy-dependent HADRONNESS cuts:

- **Quality factor:** it is considered the use of the quality factor  $\mathcal{Q}$ , defined as

$$\mathcal{Q} = \frac{\epsilon_\gamma}{\sqrt{\epsilon_h}} \quad (7.4)$$

where  $\epsilon_\gamma$  and  $\epsilon_h$  are the acceptance values for  $\gamma$ s and hadrons respectively, and are defined as the ratio of the number of events after the HADRONNESS cut to the number of events before cut. This factor evaluates the  $\gamma/h$  separation efficiency after the telescope trigger, and image cleaning. The set of HADRONNESS cuts (energy-dependent) that maximizes both the  $\mathcal{Q}$ -factor and the  $\gamma$ -acceptance are considered the optimal cuts. Generally, the optimal HADRONNESS cut per energy bin is that which provides the maximum  $\mathcal{Q}$ -factor, but a minimum  $\gamma$  acceptance (typically 80%, or at least not less than 50%) is usually required in order to keep enough statistics of  $\gamma$  events for the signal evaluation.

- **Maximizing the significance with a known source:** The set of HADRONNESS cuts can be optimized to get the best sensitivity (or maximum significance) from a known strong source. The ALPHA parameter distribution for the ON data sample is then compared with the ALPHA distribution of the OFF data sample, cutting the events above different values

of HADRONNESS cuts, per energy bins. The procedure consists in evaluating the signal obtained from the so-called ALPHA plots, i.e. the excess events that may show up in the ON data distribution above the normalized OFF data distribution for low values of the ALPHA parameter. Changing the HADRONNESS cut between 0 and 1, the cut value that provides the maximum significance can be selected.

Additional cuts can be applied to the data in order to improve the sensitivity. The most important is the cut in ALPHA which defines the region in the ALPHA plot considered as signal region, where the number of excess events is extracted from the subtraction of the OFF ALPHA histogram to the ON ALPHA histogram. As it is expected, and as it can be seen in the several ALPHA plots presented in the following Chapters (and the one shown in Figure 7.8), the peak at 0 of the ALPHA distribution for  $\gamma$  events is narrower for higher energies of the primary  $\gamma$ -ray. This effect is due to the fact that showers induced by lower energy  $\gamma$ -rays are subject to more fluctuations and, therefore, their subsequent images in the camera present a larger dispersion in the orientation of their major axis. For this reason, it is generally convenient to extract the signal with a smaller cut in ALPHA for higher SIZE bins than for lower ones. A similar approach of the one explained for the optimization of the cut in HADRONNESS can be followed to optimize the cut in ALPHA. The combination of HADRONNESS cut and ALPHA cut are set. In addition, another cuts can be applied, like dynamical DIST cuts, low SIZE cut, etc...

We note that normally the set of cuts that maximizes the sensitivity are not the optimal cuts to get the energy spectrum. The best sensitivity cuts are those that maximizes the chances of observing a signal out of the background, with high significance. These strong cuts, cut away part of the signal, while improves the chances for new source detections. To get the energy spectrum of a source, it is more convenient to keep as much signal as possible, i.e. maximize the  $\gamma$ -acceptance. In addition, if the MC does not reproduce the reality with certain precision, the MC efficiencies can be badly evaluated and this affects directly to the differential energy spectra determination. This errors on the efficiencies are not so important when one relaxes the cuts. For example, in the case of the Crab Nebulae analysis (see table 7.1), these two cuts on the ALPHA parameter are chosen: the one that maximizes the significance and the one that keeps 99% of the  $\gamma$ s.

## 7.12 Evaluation of the detected signal

The data analyzed in this Thesis follows the most common procedure of IACTs, taking consecutive ON/OFF observations. The excess events after cuts is normally evaluated from the ALPHA or  $\theta^2$  plot, as the signal resides in a region of small ALPHA or  $\theta^2$  values<sup>10</sup>. Two standard ways are used to determine the irreducible background in the signal region: one consists on the extrapolation from a smooth function fit of the ON ALPHA values outside the signal region and another extracts the signal from ON but evaluating the irreducible background from the OFF data. The fitting method has proven to give good results if the signal is quite large (like for the Crab Nebulae or Active Galactic Nuclei in flaring state). The fitting procedure has been already shown in Figure 7.8, when analyzing the Crab Nebula data at low ZA. But, for the case of the GC data the fits the obtain the irreducible background are not convenient.

The ON and OFF data are taken to evaluate the excess events in the signal region. Normally, ON and OFF observation times are different, so the OFF data has to be scaled to the ON distribution in the ALPHA plot as

---

<sup>10</sup>This is the case for on-axis observations, i.e., the source is located exactly at the pointing position, and the signal peaks towards  $\text{ALPHA} \rightarrow 0$ . Another possibility is to determine the arrival direction of every single  $\gamma$ -ray event candidate to find the signal in the  $\theta^2$  plot.

$$\langle N_{off} \rangle = \Gamma \cdot N_{off} \quad (7.5)$$

where  $\Gamma$  is the ratio of the ON to OFF events in the ALPHA region from 40 to 85 degrees, i.e, both distributions are scaled in the region in which the signal is not expected. This normalization has sense in case of consecutive ON and OFF observations, in which neither the telescope response or the atmospheric conditions changes drastically. The same scaling procedure can be done in the  $\theta^2$  variable.

The number of excess events in the signal region, located at low ALPHA or low  $\theta^2$  values, is evaluated as

$$N_{exc} = N_{on} - \langle N_{off} \rangle \quad (7.6)$$

### Significance calculation

In  $\gamma$ -ray astronomy the calculation of significance is an important topic. Since the detector sensitivity and the signal to noise ratio is limited, the significance of a detection, i.e. the probability that the observed signal is due to a genuine source and not produced by the background fluctuations must be carefully derived. Assuming that  $N_{on}$  and  $\langle N_{off} \rangle$  follow a Poisson Distribution (PD), the probability that a background fluctuation generates an excess equal or larger than the observed excess can be calculated.

Following Li & Ma [227], the significance of a signal can be derived as

$$S = \sqrt{2} \left[ N_{on} \ln \left[ \frac{1 + \Gamma}{\Gamma} \cdot \left( \frac{N_{on}}{N_{on} + N_{off}} \right) \right] + N_{off} \cdot \ln \left[ (1 + \Gamma) \cdot \frac{N_{off}}{N_{on} + N_{off}} \right] \right]^{1/2} \quad (7.7)$$

where  $N_{on}(N_{off})$  are the number of events from the ON(OFF) sample after the  $\gamma/h$  cuts and within the signal region. As more background data, the smaller the value of  $\Gamma$ , and consequently the higher the value of the significance. The ideal and desired observation condition should be to have as much ON data and much more OFF data, in order to reduce the fluctuations of the background on the analysis results. In reality, and due to the limited time of observation per source, and weather conditions, this is not possible, and the dedicated OFF data is not larger nor even equal to the quantity of ON data. Normally,  $\Gamma \sim 1$ , i.e. almost the same quantity of ON and OFF data are taken, like the case presented in this Thesis.

Another way of estimating the significance of the detection is the following. Since ON and OFF data are results of two independent measurements, the variance of the excess signal can be calculated by:

$$\sigma^2(N_{exc}) = \sigma^2(N_{on}) + \sigma^2(\Gamma N_{off}) = \sigma^2(N_{on}) + \Gamma^2 \sigma^2(N_{off}) \quad (7.8)$$

Then, the standard deviation of the excess signal, where both the fluctuations of the ON and the OFF samples contribute (which, from the poissonian law, are given by  $\sigma(N_{on}) = \sqrt{N_{on}}$  and  $\sigma(N_{off}) = \sqrt{N_{off}}$ ), can be estimated from:

$$\sigma(N_{exc}) = \sqrt{\sigma^2(N_{on}) + \Gamma^2 \sigma^2(N_{off})} = \sqrt{N_{on} + \Gamma^2 N_{off}} \quad (7.9)$$

Defining the significance  $N_\sigma$  as the ratio of the excess counts above background to its standard deviation, it is given by:

$$S = \frac{N_{exc}}{\sigma(N_{exc})} = \frac{N_{on} - \Gamma N_{off}}{\sqrt{N_{on} + \Gamma^2 N_{off}}} \quad (7.10)$$

Results from Equation 7.10 have been used for the next steps of the analysis presented in this Thesis. Equation 7.7 has only been computed for a check, in all cases giving consistent results.

A significant detection is considered when  $S > 5$ , marginal source detection if  $3 < S < 5$ , and no detection if  $S < 3$ .

### 7.13 Effective area and flux evaluation

For a significant detection ( $S > 5$ ), like the one that is presented here, the differential *energy spectra* of the emission can be determined from the excess events  $N_{exc}$  and the efficiencies of the hardware selections and analysis cuts, for different energy bins. The differential flux of the source is determined as

$$\frac{d\Phi(E; ZA)}{dE} = \frac{N_{exc}(E; ZA)}{E \cdot A_{eff}(E; ZA) \cdot T_{eff}(ZA)} \quad (7.11)$$

where  $A_{eff}$  is the effective  $\gamma$ -ray collection area,  $T_{eff}$  is the effective ON time (i.e. the observation time corrected for the dead time of the detector as explained in [228]), and E the energy of primary  $\gamma$ -ray.

As we cannot calibrate the detector with a known test-beam we have to evaluate the selection  $\gamma$ -ray efficiencies and collection areas from MC simulations. From the number of simulated showers  $N_{sim}$  and the number of selected events  $N_{sel}$  surviving the whole analysis chain, we can obtain the total efficiency), as a function of energy, ZA and  $\gamma$ -ray impact parameter:

$$\epsilon_{total}(E; ZA; I) = \epsilon_{trigger}(E; ZA; I) \cdot \epsilon_{cuts}(E; ZA; I) \quad (7.12)$$

$$= \frac{N_{sel}(E; ZA; I)}{N_{sim}(E; ZA; I)} \quad (7.13)$$

This is the  $\gamma$ -ray efficiency after the hardware selection criteria (the trigger selection) and analysis cuts.

The effective area  $A_{eff}$  takes into account the cuts selection, i.e. the  $\gamma$ -ray acceptance and it is one of the most important parameter of the IACT. As a function of energy and ZA, the  $A_{eff}$  can be calculated in the impact parameter range ( $I_{up}, I_{low}$ ) as:

$$A_{eff}(E; ZA) = \pi \sum_{i=1 \dots N} \frac{N_{sel}(E; ZA; I)}{N_{sim}(E; ZA; I)} \cdot (I_{up}^2(i) - I_{low}^2(i)) \quad (7.14)$$

The  $A_{eff}$  is properly averaged in the energy bin depending on the MC input spectrum slope, and always evaluated after cuts. The effective collection area accounts then for the  $\gamma$ -efficiency.

The dependence on the ZA is useful if the data spans a wide region of ZA as the Hillas parameters slightly change, and the effective areas changes considerably (hence the  $E_{thr}$ ). This is not the case of the GC data, in which all data is taken nearby the source culmination, and it is not needed to bin the data in ZA.

#### Evaluating the mean energy value of the energy bin

In the differential energy spectra distribution, for every energy bin, the mean energy values  $\langle E_i \rangle$  has to be evaluated. As the data point has to be placed in a bin of finite width and we

want to fit the spectra and compare to theoretical models, neither the central value of the bin nor the weighted mean value (barycentre) of the abscissa within the bin is the appropriate place to plot the data point, which are usually the most common procedures.

$$x_c = x_1 + \frac{\Delta x}{2} \quad (7.15)$$

$$\bar{x} = \frac{\int_{x_1}^{x_2} xg(x)dx}{\int_{x_1}^{x_2} g(x)dx} \quad (7.16)$$

where  $g(x)$  is the distribution function measured in the data.

In [229] it is shown that *none* of these methods are strictly correct and they rather propose that the data points ought to be placed where the predicted distribution function is equal to its mean value over the wide bin:

$$x_{lw} = \frac{1}{\Delta x} \int_{x_1}^{x_2} g(x)dx \quad (7.17)$$

This is the procedure which we use in this Thesis. The mean energy values for each bin  $< E_i >$  are obtained in a recursive process in which the differential energy spectra is recursively fitted by a function, the so-called  $g(x)$  (in the case of this Thesis a power-law), to find the proper mean energy values, the so-called  $x_{lw}$ .

### Spill-over corrections

As the energy spectra is evaluated with the use of the  $E_{rec}$ , a second step has to be applied in the calculation of the energy spectra in order to derive the proper deviation factors (the so-called spill-over corrections) which affect to the different energy bins due to the energy resolution and bias of the energy estimator. In an iterative way, in which the spectral index of the input MC is changed recursively until stabilizes, a set of proportional constants  $\kappa_i$  are calculated as

$$\kappa_i = \frac{N_{sim}(E_{i,true})}{N_{sim}(E_{i,rec})} \quad (7.18)$$

i.e, the ratio of MC events in the  $i$ th energy bin used for spectra calculations evaluated with the true energy and the number of events evaluated with the reconstructed energy.

### Unfolding the differential energy spectra

The measured differential energy spectra is a convolution of the true spectra of the source with a response function, that describes the finite energy resolution of the telescope. The procedure to determine the true distribution from the measured differential energy spectra, by inverting the convolution, is called differential energy spectra 'unfolding'. Several unfolding methods are present in the literature, and some of them have been tested for MAGIC [230], in order to get the unfolded differential energy spectra.

The unfolding formalism is still being tested in MAGIC to date. Nevertheless, first satisfactory results have been obtained when applying the so-called 'forward' unfolding, in which in an iterative way and with the help of using as ansatz the known solution, the spectra can be unfolded. The differential energy spectra shown in the first preliminary article of the GC data is unfolded with this method [203], although we only have applied the spill-over correction procedure in the analysis presented in this Thesis, as we consider the unfolding methods in MAGIC to be still in a preliminary stage.

### Evaluation of the effective observation time

For measuring the differential energy spectra (i.e. fluxes) of the  $\gamma$ -ray candidates, we do need to know the effective observation time  $T_{eff}$ , i.e. the observation time  $T_0$  corrected by the dead time of the telescope.

The distribution of cosmic ray events in time follows a Poisson distribution. In a Poisson process, the probability distribution for time differences for successive events should follow an exponential distribution:

$$P(t) = \lambda \cdot \exp(-\lambda \cdot t) \quad (7.19)$$

where  $t$  is the time difference between the successive events and  $\lambda$  is the average event rate.

In the ideal case in which the detector has no dead time, i.e. all successive events are registered by the system, the total observation time is simply evaluated as  $T_0 = N_0/\lambda$ , where  $N_0$  are the total number of events recorded. But, in reality the measured distribution deviates from the ideal exponential expected as the detector sometimes loses events as it is still busy processing a previous event.

In [228] is shown a procedure how to correct the observation time by the dead time: the effective event rate  $\lambda_{fit}$  is obtained from an exponential fit of the event time difference distribution, in the region which is not affected by the dead time, i.e. avoiding the low  $t$  values region. The effective observation time  $T_{eff}$  is shown to be

$$T_{eff} = N_{events}/\lambda_{fit} \quad (7.20)$$

The fraction of lost observation time can be computed from the average rate value  $\lambda_m$  and the rate value derived from the exponential fit as:

$$r_{dead} = \left(1 - \frac{\lambda_m}{\lambda_{fit}}\right) \quad (7.21)$$

This is the method which we used in this Thesis, applied to **all recorded** ON events used in the analysis. The method can be safely applied for samples in which the event rate does not change dramatically (if not, the  $\lambda_{fit}$  is not a good estimator), i.e. samples in which the majority of events come from the hadron background.

### Evaluation of the stability of the source: Light-Curve

The integral flux of the recorded signal is evaluated in an analogous way like the differential spectra is evaluated, but the signal is integrated above a energy  $E_0$ :

$$\Phi(E_0; ZA) = \int_{E_0}^{\infty} \frac{N_{exc}(E; ZA)}{E \cdot A_{eff}(E; ZA) \cdot T_{eff}(ZA)} dE \quad (7.22)$$

The data is binned in different time intervals, as much as the strength of the emission allows. This let to check for emission variations in time, which is an important measure, in particular to constrain the nature of the emission.

These analysis techniques have shown to be robust when applied to the Crab Nebula data taken with MAGIC. See [197] for observational results on Crab Nebula, and Appendix D.



## Chapter 8

# Analysis of the GC data taken with MAGIC

*In this chapter we will review the GC region properties, and we will report about the significant detection of  $\gamma$ -rays obtained with the MAGIC telescope in the direction of the GC. In particular, we explain in detail all procedures applied in order to derive the differential energy spectrum, light-curve, source location and checks for emission extension.*

*The results obtained in this Chapter are partially published on the paper J. Albert et al (MAGIC Collaboration) [203].*

### 8.1 The center of the Milky Way

The Galactic Center (GC) region is a very dense and complex sky region of approximately  $4^\circ$  in projection that contains many remarkable objects which may be responsible for high-energy processes. The GC is located at about 8 kpc and is a region rich in massive stellar clusters with up to 100 OB stars, immersed in a dense gas. It contains up to 10% of galactic interstellar medium, in form of giant molecular clouds. There are young supernova remnants, e.g. Sgr A East, molecular clouds, and non-thermal radio arcs. The dynamical center of the Milky Way is associated with the compact radio source Sgr A\*, hypothetically assigned to a super-massive black hole (SMBH). Figure 8.1 shows a radio image of the GC obtained with the VLA at 90 cm, in which all the complexity of the region is shown.

The central GC region,  $\sim 0.2^\circ$ , forms the so-called *Sgr A complex*. The objects within this region are particularly important as there are many objects that might emit in the VHE regime (see [231] for a review). As the MAGIC angular resolution is about  $0.1^\circ$ , it is important to know their properties in order to elucidate the origin of the emission observed:

- **Molecular clouds:** Two molecular clouds present (M-0.02-0.07, and M-0.13-0.06). Cosmic rays impacting to MC might generate emission of VHE  $\gamma$ -rays.
- **An expanding SNR:** *Sgr A East*, a non-thermal radio source, with diffuse emission (7pc x 9pc,  $3' \times 4'$ ), located  $50''$  (2 pc) from the central SMBH (Sgr A\*). The shell appears to be compressing M-0.02-0.07, probably creating substructures which are visible in the shell. A SNR shell interacting with a dense medium might creates VHE  $\gamma$  - rays.
- **Thermal diffuse SNR:** *Sgr A West*, *IRS16*, which seems to be ionized by a cluster of young and massive stars. Stellar winds interact with the medium and the shell probably feeds the SMBH. It is centered  $2''$  from Sgr A\*.

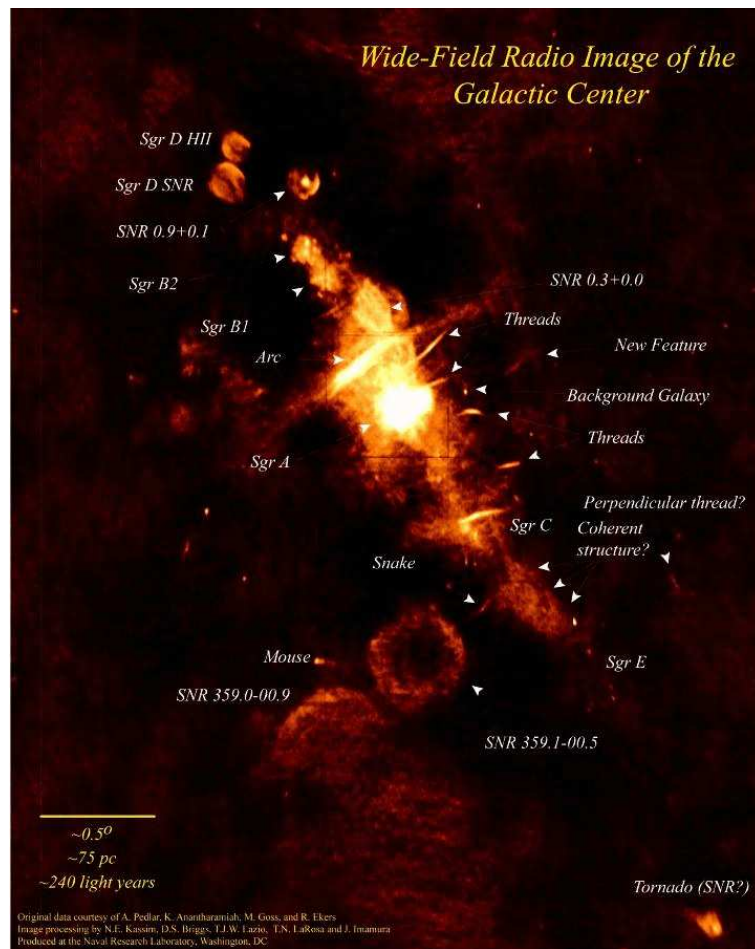


Figure 8.1: The GC region seen by the VLA at 90 cm.

- **Central compact radio source:** *Sgr A*\*, surrounded by a central HII region, is the radio manifestation of the central SMBH. From matter dynamics, the SMBH mass is about  $3\text{--}4 \cdot 10^6 M_{\odot}$ , with  $R_s \sim 0.06$  AU.
- **Densest dark matter region:** If the GC is the dark matter densest nearby region it would appear to be the most brilliant object in  $\gamma$  - rays from hypothetical neutralino dark matter annihilations.

The GC, an extreme environment, provides a unique laboratory for HE and VHE astrophysics. The GC is totally obscured in the optical by the galactic plane, and it can be only observed from radio to infrared (IR) and at high energies. Hence, multi-wavelength information from the region is quite valuable. From 2004, valuable measurements have been provided by *Chandra* (X-rays), XMM-Newton (X-rays), INTEGRAL (GeV  $\gamma$ -rays) and HESS (GeV-TeV  $\gamma$ -rays).

### 8.1.1 The GC in the X-ray band

A SMBH immersed in a dense environment is a priori a good place to produce accreted powered X-ray emission. However, the measured X-ray emission is steady and weak, with a luminosity of about  $5 \cdot 10^{36}$  erg  $s^{-1}$  from radio to X-rays. Very inefficient accretion flows theories emerged at the time of these measurements, with the IRS16 stellar winds as the feed (ADAF models) [232].

### Flaring activity of Sgr A\*

In 1999, *Chandra* measured the luminosity and spectral index in the 2-10 keV band, and the results were not compatible with the ADAF models. In 2000, a dramatic discovery from *Chandra* revealed for the first time a powerful X-ray flare from Sgr A\*, that lasted for 3h with luminosity increase by a factor 50. Later, from 2003 to 2005, these X-ray flares have been confirmed by XMM-Newton, with the most prominent flare detected with 200s duration and 200 luminosity enhancement [233].

The X-ray flare frequency is estimated to be of about 1 flare per day with durations from 200 s to 30 min. From flare durations, the radiation seems to be emitted within  $20R_s$ . This is not compatible with ADAF models, in which the X-ray emission is emitted from the whole accretion flow. Alternative models have been developed to accommodate the observed flares in the X-ray band, e.g. accreting matter circulating around the SMBH where IC radiation is generated by the circulating electrons (changes in the magnetic field generate flares), the presence of a relativistic jet, modified ADAF models, etc...

### Diffuse X-ray emission

Hard diffuse X-ray extended emission (few hundred pc) is present centered at Sgr A\* and elongated along the galactic plane. *Chandra* detected about 2000 point-like sources in this region, but only account to 10% of the observed diffuse emission. To explain this emission, non-thermal nature is considered, in which scenarios where Cosmic Rays (CRs) interact with the interstellar medium or even the molecular clouds. The effect of the SN ejecta in the Sgr A\* dense region is as well considered.

### Sgr A East

Sgr A East is a mixed morphology SNR, in which a non-thermal radio shell surrounds a centrally peaked thermal X-ray emission. Recently, *Chandra* has detected the central neutron star relic from the SN explosion. It seems not to be an exceptional SNR, maybe a product of a typical SN II or SN Ia, with an age of only about 1700 yr [234].

The shell is expanding against a very dense medium, and given the distance from the neutron star to Sgr A\*, the shell could have reached the SMBH triggering an outburst of hard emission (this is reinforced from the detection of emission from Sgr B2, supposed to be the reflection of this emission [235]).

## 8.1.2 The GC in the HE-band

From 2003-2004 INTEGRAL observed the GC region in the 20-600 keV (HE) band. INTEGRAL detected a faint, persistent and steady HE emission compatible with Sgr A\* (1' error radius, see Figure 8.2). But, INTEGRAL has  $\sim 13'$  FWHM angular resolution, and no clear association to SMBH or other specific source can be attributed. In particular, the central source IGRJ17456-2901 is located 1.1' from center of Sgr A\* and 0.9' from center of Sgr A East.

A multi-wavelength campaign with XMM-Newton was scheduled to search for flares in the HE-band and check for correlations with the X-ray band. The result was not conclusive, as the flares in X-rays coincided with the INTEGRAL passage through radiation belts (i.e. INTEGRAL switched off and no data was taken). In the rest of the data, no flares were detected in the HE-band.

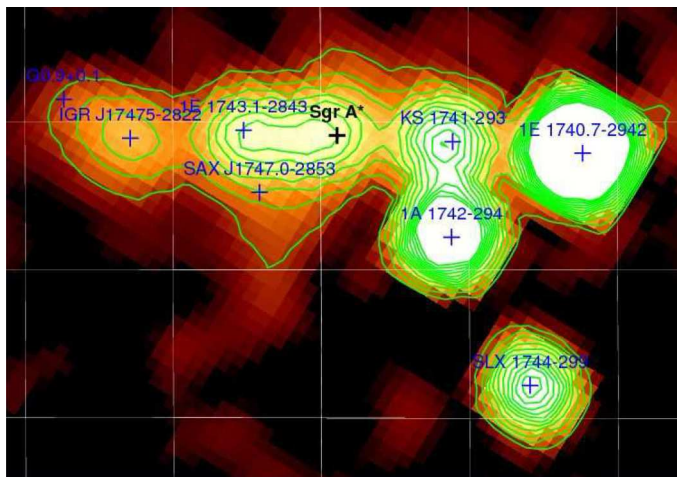


Figure 8.2: The 20-40 keV INTEGRAL/IBIS image of the GC region showing the central source IGRJ17456-2901, labeled as Sgr A\*.

### 8.1.3 The GC in the VHE-band

The EGRET satellite detected a strong source in the direction of the GC, namely 3EG J1745-2852, which has a broken power law energy spectrum extending up to at least 10 GeV, with a spectral index of 1.3 below the break at a few GeV. Assuming a distance to the GC of about 8.5 kpc, the  $\gamma$ -ray luminosity of this source is very large, up to  $2.2 \cdot 10^{37}$  erg/s, which is equivalent to about 10 times the  $\gamma$ -flux from the Crab Nebula. An independent analysis of the EGRET data indicated a substantial difference in the observed flux (mainly due to bad background subtraction) and that the emission was compatible with a point-source whose position is different from Sgr A\* at a confidence level beyond 99% [236]. This has been recently sustained by Pohl [237]. None of these studies were officially made by the EGRET collaboration, but the EGRET detected emission seems not to be the counterpart of the INTEGRAL central source emission.

The GC has been recently a source of debate in the VHE, as  $\gamma$ -radiation above a few hundred GeV has been detected by VERITAS, CANGAROO and HESS collaborations. The energy spectra measured by these telescopes show substantial differences, as one can see in Figure 8.3. This might be due to different sky integration regions of the signal or a source variability at a time scale of about a year. The later seems not to be the reason of the discrepancy, as the accumulated HESS data of two years observations in the direction of the GC shows no sign of variability [238].

HESS has provided the most sensitive and precise measurement, in which the VHE emission is constant, displaying a power-law spectra from 160 GeV to 30 TeV (the most recent results). The emission has a point-like core with an extended tail. Within the errors, IGRJ17456-2901 seems to be linked to the VHE emission. This VHE emission is hardly explained by dark matter annihilation products, and the acceleration mechanism that generate the VHE radiation is still unknown. Like in the case of INTEGRAL, the limited angular resolution makes the identification to Sgr A\* or Sgr A East difficult. We will discuss this issue in the Discussion Chapter.

## 8.2 Motivations for GC observations with MAGIC

In this context, the main motivations for the observation of the GC with the MAGIC telescope are:

- Measure the  $\gamma$ -ray flux and its energy dependence. As the GC culminates at high ZA, MAGIC has the penalty of a higher  $E_{\text{thr}}$  ( $\sim 650$  GeV) compared to CANGAROO and HESS telescopes,

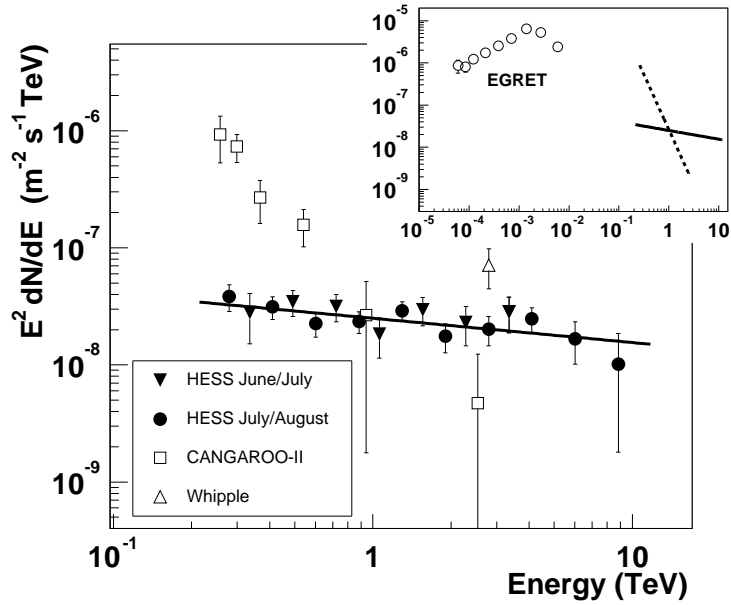


Figure 8.3: The VHE gamma flux from the Galactic Center as observed by Whipple, Cangaroo, HESS and by the EGRET experiment (figure from [239]).

but the benefit of higher energies up to about 20 TeV to be accessible, because it is expected an increase of telescope sensitivity at high ZA.

- Help resolving the main differential energy spectra discrepancies between HESS, CANGAROO and VERITAS.
- Study if the emission is extended or compatible with a point-like source.
- Check for variability of the  $\gamma$ -ray emission.
- Gain information about the nature and production mechanism of  $\gamma$ -rays in the direction of the GC. Particularly, set constraints on models for dark-matter-particle annihilation.

It is worth to notice, indeed, that the mechanisms which generate such VHE  $\gamma$ -rays have still to be identified. This is maybe the most fundamental open question related to this emission, apart from the flux discrepancy between CANGAROO and HESS.

### 8.3 GC observational constrains with MAGIC

At La Palma, the GC [(RA, Dec) = (17<sup>h</sup>45<sup>m</sup>36<sup>s</sup>, -28°56′)] culminates at about 58° zenith angle (ZA). It can be observed with MAGIC at up to 60° ZA, between April and late August, yielding a total of 150 hours without moon per year. The expected integral flux above 700 GeV derived from the HESS data is  $(3.2 \pm 1.0) \cdot 10^{-12} \text{cm}^{-2} \text{s}^{-1}$ , suitable enough to get a positive detection with MAGIC telescope in a few hours of observation.

In order to collect a data sample comparable in size to those of the other experiments and to be able to measure the energy spectrum, 40 hours of observation time during 2005 were requested to the *MAGIC Observation Committee*. The observations were conducted in the wobble mode, ON/OFF mode, with a total of 24 useful hours of GC data to be analyzed. In addition, 60 hours



have involved many observation modes (Wobble, Moonshine, ON/OFF), and it requires a careful treatment.

Period	date	ZA [°]	time [h]	events [10 <sup>6</sup> ]	obs. mode	note
I	Sep. 2004	62-68	2	0.8	ON	commissioning phase
II	May 2005	58-62	7	2.8	wobble	-
III	Jun./Jul. 2005	58-62	17/13	7.3/5.6	ON/OFF	-
IV	July 2005	58-62	7	-	ON	moonshine

Table 8.1: Data set per observation period of the GC. The column 'time' states the effective observation time, the column 'events' states the events after image cleaning. Colored is the data analyzed in this Thesis.

Figure 8.5 shows the star-field present in the field of view of the GC region and the different observation modes pointing directions. One can clearly see that the star field around the GC is non-uniform. In the region west of the GC ( $RA > RA_{GC} + 4.7^m$ ) the star-field is brighter, but this has a small impact in the analysis, as the noise in those pixels which are illuminated in this area is slightly larger than for the rest (this can be seen in the pedestal RMS values, which are shown in Figure 8.6). All observation directions were chosen so these group of stars are always located in the outer camera region (i.e, outside the trigger region), and the trigger rate is not drastically affected with the use of standard galactic discriminator threshold levels ( $DT = 40$  DAC counts)<sup>1</sup>.

In particular, within a distance of  $1^\circ$  from the GC there are no stars brighter than  $mag = 8.4$ , and there are 16 stars with  $8 < mag < 9$ . At distances between  $1^\circ$  and  $1.75^\circ$  from the GC the total number of stars with  $4 < mag < 9$  is 26. The brightest ones are Sgr 3 with  $mag = 4.5$ , GSC 6836-0644 with  $mag = 6.4$  and GSC 6839-0196 with  $mag = 7.2$ .

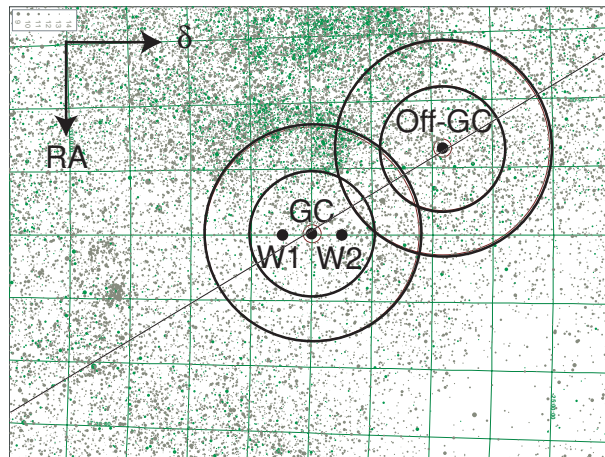


Figure 8.5: Star field around the GC region. Stars up to a magnitude of 14 are plotted. The 2 big circles correspond to distances of  $1^\circ$  and  $1.75^\circ$  from the pointing directions (GC and GC-Off), respectively. The grid spacing in the declination is 20 arc-minutes. The Galactic Plane is given by the line.

<sup>1</sup>Stars make the pedestal RMS increase, then the probability to trigger the telescope only with noisy events increases. In some cases, the trigger rate can be well beyond the capability of the detector. Then the discriminator thresholds have to be adjusted, and consequently affects the  $E_{thr}$ , that increases.

The data analysis has been carried out using the standard MAGIC analysis and reconstruction software<sup>2</sup> [181], the first step of which involves the calibration of the raw data [201]. The analysis is done night-by-night for ON and OFF data. ON and OFF pedestal, calibration, and data files used for the analysis which is carried out in this Thesis are shown in Appendix A. Dedicated MC files and dedicated runs to understand about special kind of noisy events will be explained in separate sections.

## 8.5 Dedicated MC simulations at large ZA

Dedicated MC  $\gamma$ -ray simulations were generated in order to obtain a significant number of triggered events at high ZA, generated in the same ZA range of the ON data. These dedicated files, generated at higher energies and with different spectral index (labeled HE MC), were mixed with the standard MC files. Only  $\gamma$ -rays were simulated, as the simulation at such high ZA of proton and helium could have been hard in terms of computing time. We use a fraction of the OFF data for training purposes.

Table 8.5 displays the most important parameters regarding to the standard and the *HE* MC production.

MC simulation parameter	standard MC	HE MC
primary particles	$\gamma$ -rays	$\gamma$ -rays
energy range	20 GeV - 30 TeV	500 GeV - 30 TeV
Spectrum	$E^{-2.6}$ (*)	$E^{-1.0}$ (*)
Zenith angle	$57.3^\circ$ - $62.3^\circ$	$57.3^\circ$ - $62.3^\circ$
Impact parameter	0 m - 400 m	0 m - 400 m
Nr. simulated showers	$\sim 7$ M	$\sim 23$ k
Nr. events after trigger	$\sim 100$ k	$\sim 19$ k
diffuse NSB level	0.178 phe/ns (**)	0.178 phe/ns (**)
$\sigma$ of PSF	14 mm	14 mm

Table 8.2: Most important parameters of the simulations used in this analysis. (\*) For flux calculations, the energy spectra is weighted to properly derive the results, i.e. the MC is generated following  $E^{-\delta}$ , and  $\delta$  is changed recursively. (\*\*) NSB level for  $0.1 \times 0.1$  deg<sup>2</sup>, i.e. inner pixel size.

## 8.6 Preprocessing of the data: Online Analysis

The first preprocessing of the data is done automatically in La Palma by running a version of the standard code used for the analysis (the so-called *MARS*), in dedicated computers. The output of this first step gives a preliminary, but useful, set of processed files which allows to know about how the data which is being taken performs. This is done in a daily basis and, in addition, an *Online Analysis* runs automatically to know about the data quality and the outcome of the observations.

This first preprocessing of the data consist on the following steps:

- Raw data is converted to ROOT format for further processing, including several subsystem data, like the information from the drive. This arrange of the data is done with the *merpp* program.

<sup>2</sup>MARS, Magic Analysis Reconstruction Software

- The recorded FADC counts (together with the pedestal and pedestal RMS) are converted into Čerenkov photons, for each pixel. This is the main task of the *callisto* program, which uses the information coming from special calibration files and calibration events inter-spread at the data. Here, some pixels can be excluded from the analysis if misbehaviors are seen (tagged as 'bad pixels').
- Pixels with non-significant light content are removed from the analysis (*image cleaning*) and the Hillas parameters are computed. Signal interpolation for 'bad pixels' is also assigned. This is done with the *star* program.
- Basic filter cuts are applied to remove unusable events, very preliminary procedures for  $\gamma$ -hadron separation and energy estimation are applied, and some basic plots are provided.
- These preliminary processed files and results are transferred via *scp* automatically to the data center, located in Wuerzburg (Germany). The raw data is stored into tapes and sent periodically to the data center as well.

These are the main tasks of the *Online analysis* program, a fully automatized analysis but not optimized source-to-source, even not capable to handle some problems that need special actions. Moreover, the *Online Analysis* runs for every night data, not for a large dataset, so it is useful to check the quality of data that is being taken and to spot changes in the emission for the bright objects, like a flare in an AGN, for example.

In case of the GC analysis, these files were not useful to carry out a consistent and sensitive analysis, as some corrections to the data were needed: corrections of telescope mispointing, correction of the signal extractor, re-calibration of whole data, etc... The data which is presented in this Thesis was further processed at the data center, with all appropriate corrections, explained in the following sections.

## 8.7 Calibration of the GC data

The calibration is done via the *callisto* software. In [201] a detailed description of the calibration system and calibration procedures is available.

Apart from the central (id. 0) and the calibration blind pixel (id. 560), some pixels were excluded by the calibration routines during the calibration of the data for the different nights. For ON and OFF data, there are a total of 32 independent sequences of analysis, each one starting with a *pedestal run* and a *calibration run* (mainly one analysis sequence per night and data type). The list of pixels, the reason why they are excluded from further analysis, and exclusion frequency (i.e. in how many sequences the pixel is excluded from the analysis) are shown in Appendix A. These pixels are tagged as *bad pixels*, which need special treatment (charge interpolation) when evaluating the Hillas parameters. A total of 28 pixels are at some point excluded from the sequence analysis. All these pixels were cross-checked with the camera experts and found to be quite compatible with already known list of pixels<sup>3</sup>.

Figure 8.6 shows the most important summary plots from *callisto* program. The pedestal RMS (top, left) reinforces that there is no important bright star in the inner part of the camera (a gradient on the RMS is seen towards the most star populated region in the camera FOV). The most brighter star is located in the bottom right region of the outer camera (Sgr 3 with mag = 4.5). Note that a few outer pixels appear to be quite a bit noisier than the rest. The mean calibrated signal to the calibration pulses is also shown (top right). The 'bad pixels' charge assignation is

---

<sup>3</sup>In particular, some of these pixels were replaced in a camera technical access in September 2005.

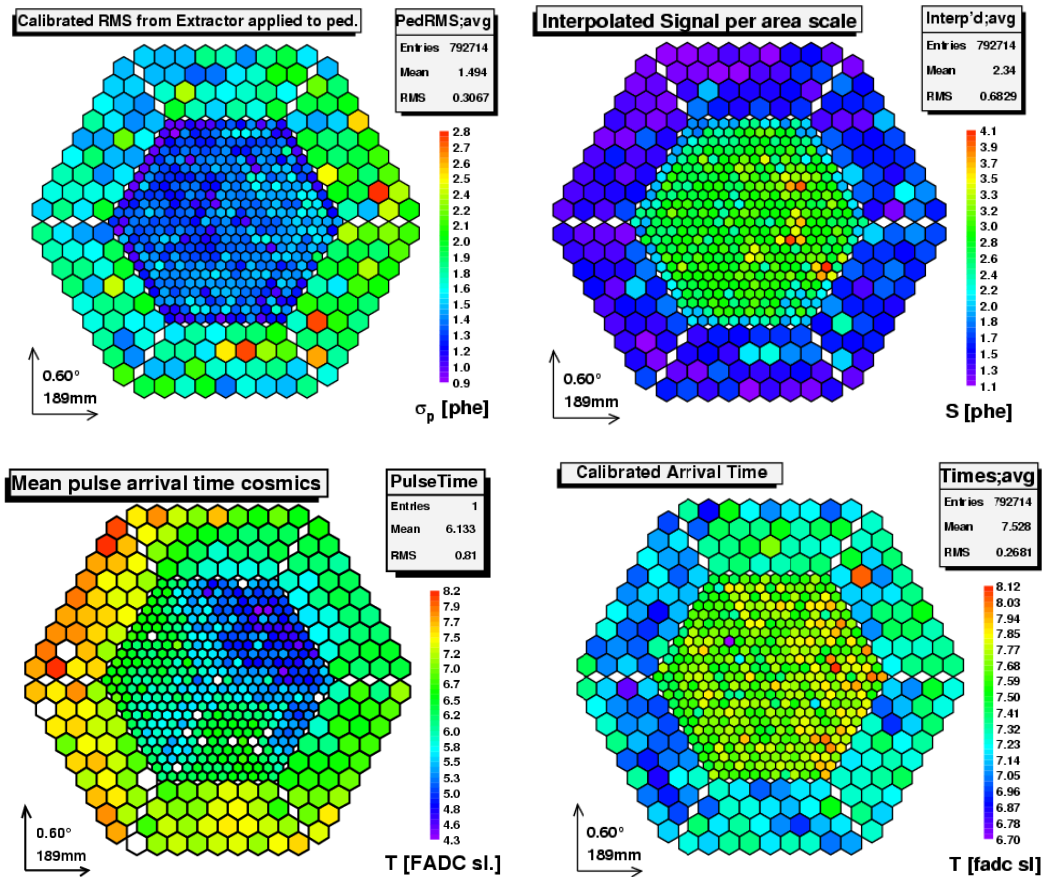


Figure 8.6: Results from the calibration *callisto* program. From left to right: average pedestal RMS, mean interpolated signal in *phes*, mean signal pulse arrival time, and mean calibration signal pulse arrival time.

done via interpolation (as explained in the next section), and outer pixel signal is multiplied by a factor .25 in order to get the camera response in pixel area unit. From this Figure, we can see that the camera response, after calibration, is quite flat for the calibration homogeneous camera illumination events, except for some pixels which are affected by the 'sparks' events which also triggers the system (special type of noisy events which needs special treatment).

Figure 8.6, top-right plot, shows the calibrated mean charge for the calibration pulses. A small deficit of  $\sim 5\%$  at the lower right part of the inner camera is seen. This deficit will remain until the end of the analysis and will constitute a true inefficiency, which will have to be corrected for. The bottom right Figure shows the mean pulse arrival times for cosmic pulses with  $S_i \geq 15$  *phes*. The differences in average Čerenkov signal arrival times are probably due to a time offset of one of the trigger cells at the upper right part of the camera [219]. The trigger lines for both the calibration and EAS shower images are independent, and this difference in the camera for the mean pulses arrival time turn to be important, with a clear impact into the homogeneity of recorded images distribution (see Figure bottom/right that calibration pulses do not suffer from this effect). In order to cure this effect, the signal extractor procedure has to be slightly modified.

## 8.8 Image cleaning and Hillas parameters calculation

The use of an *absolute cleaning* of 10 *phes* for core and 5 *phes* for boundary pixels, the so-called absolute (10,5) cleaning, is a rather strong image cleaning cut. As the pedestal RMS for inner pixels is of about  $2.3 \pm 1.5$  *phes*, this corresponds approximately to a *scaled-cleaning* of about  $(5\sigma, 2\sigma)$ , when normally  $(3\sigma, 2\sigma)$  is commonly used by  $\gamma$ -ray IACT community. This strong cut minimizes the differences between ON and OFF samples, as they are taken in different FOV regions, with slightly different pedestal RMS values. Moreover, this minimizes the bias introduced by the charge extraction method, which slightly overestimates small signals. This image cleaning could in principle be optimized, so the chosen has to be taken as a conservative image cleaning, which has shown to give very good results.

The resulting cleaned event should contain only the pixels considered to have the Čerenkov photons coming from the EAS. From here, the set of Hillas parameters are evaluated. Figure 8.7 shows the most relevant Hillas parameters evaluated for the whole ON and OFF samples, and evidences the good agreement between both samples, once some corrupted runs are excluded (see Appendix A for a list of excluded runs).

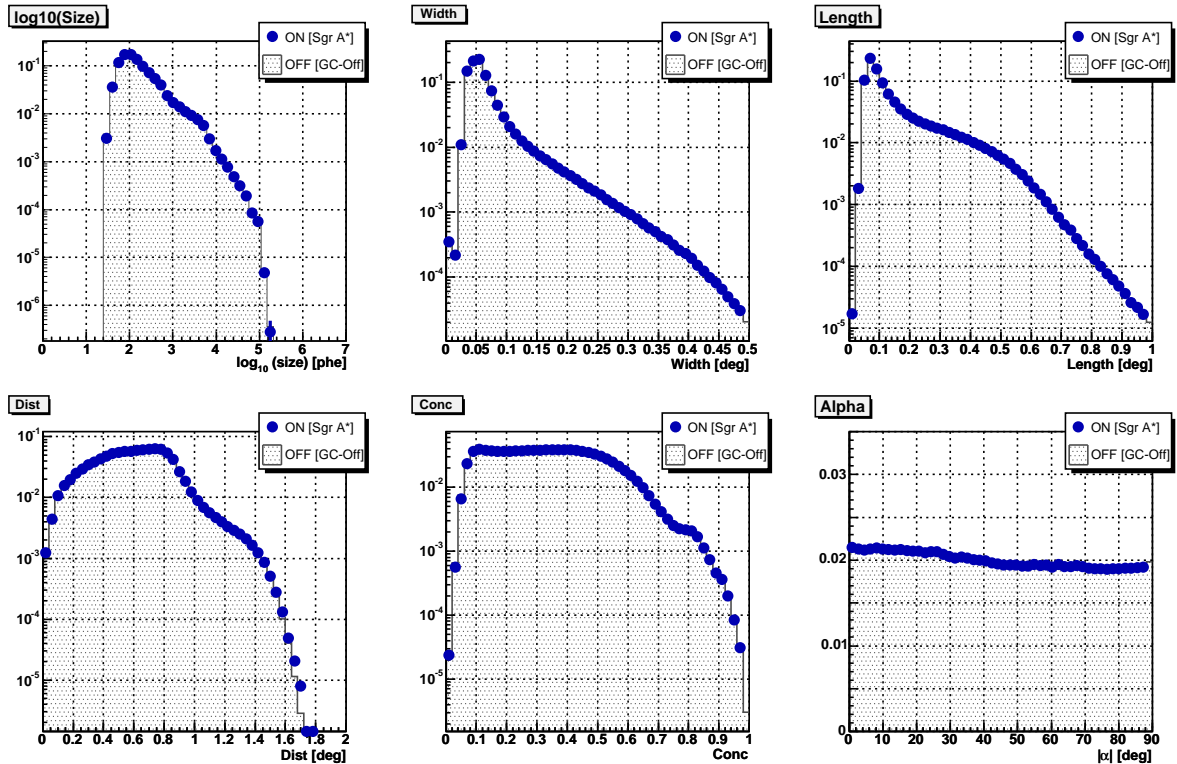


Figure 8.7: Hillas parameters distributions for ON (blue points) and OFF (black dashed) data samples, obtained well after image cleaning. No  $\gamma/h$  separation cut, or any quality cut, is applied.

## 8.9 GC Data Quality

By the time of the GC observations, there were some problems on the performance of the telescope that directly affected the quality of the data, hence the quality of the results. In this section we

explain the methods we used to try to recover as much as possible these problems, at least the most relevant ones.

### 8.9.1 ON and OFF event rate after image cleaning

The data acquisition rate is an important measurement. Assuming any telescope malfunction, low rates normally indicate the presence of high clouds or dust in the atmosphere, which cannot be seen with the naked eye, neither with the help of the 'normal' atmospheric detectors. If the Čerenkov light is much more absorbed in the atmosphere then less light is focused into the camera. This affect the Hillas parameters of the shower image, in particular the SIZE, which is related to the energy of the primary particle. The event reconstruction turns out to be difficult, as corrections due to the absorption losses should be applied (still missing the LIDAR measurements, and specific studies on how to include these effects into the MC simulations).

All observation nights had a good sky quality (in terms of relative humidity or presence of clouds). Figure 8.8 shows the acquisition rates for all different nights, and for GC ON and OFF data separately. Different nights are plotted in different colors, separated by red lines, and the rates are evaluated in an event average every 2 minutes. These rates are evaluated after the image cleaning, i.e. excluding the 50 Hz inter-spread calibration events, as well as the events which do not fulfill the image cleaning criteria (about 10%). The trigger acquisition for the GC data was about 180 Hz, and, although not shown, highly correlated to the one which is plotted here.

Two nights show significant low rates compared to the others: 07/06/2005 and 15/06/2005. The Northern Optical Telescope (NOT) facility measures regularly the atmospheric extinction coefficient in the site. For the night of 07/06/2005, this coefficient was a factor 2 bigger than the measured for the rest of the nights. In particular, that night was tagged by NOT as 'bad night for observations'. For the night 15/06/2005, the NOT data is not available, but our data acquisition rates were also very low. Both nights were excluded from the analysis (see Table A).

### 8.9.2 Subtraction of spark events

The so-called 'spark' events refer to roundish events ( $WIDTH/LENGTH > 0.7$ ) that trigger the system and appear spread in the data, but with the peculiarity that they are not coming from any EAS. These noisy events seem to be related to some fast-light-sparks that appears regularly in the camera PMTs<sup>4</sup>. The light emitted by these sparks is reflected in the camera plexiglass front window, and neighbor pixels are illuminated by the reflected spark light generating roundish images. These 'special' events trigger the whole acquisition data chain and have to be excluded from the analysis.

In order to know more about how to extract them from the data, we took about 30 minutes of data with the camera closed, during a shift period the Author Thesis was taking data in La Palma. With the camera closed we forced that all triggered events are related to the sparks occurrences. This data was calibrated with a calibration run taken prior to the 30 minutes of data taking. Of course, no inter-spread calibration events were possible to be taken, and the analysis software chain was slightly modified.

From these special runs, we derived that the total rate of sparks is about 0.34 Hz. It is interesting that all these events are normally centered at the same position in the camera reference frame. This can be seen by plotting the Center of Gravity (CoG, the mean charge  $x, y$  values of recorded image) of the spark events. From Figure 8.9, we can clearly see that the sparks are mostly centered in four

<sup>4</sup>At moment, there two plausible hypothesis: (a) discharges between the PMT anode and the aluminum cover that protects the PMT against the earth magnetic field or (b) discharges within the PMT due to free moving particles, residuals from the cathode, which were detected on some PMTs prior installation into the camera. These PMTs were replaced by the company, but it may turn out that not all of them were detected.

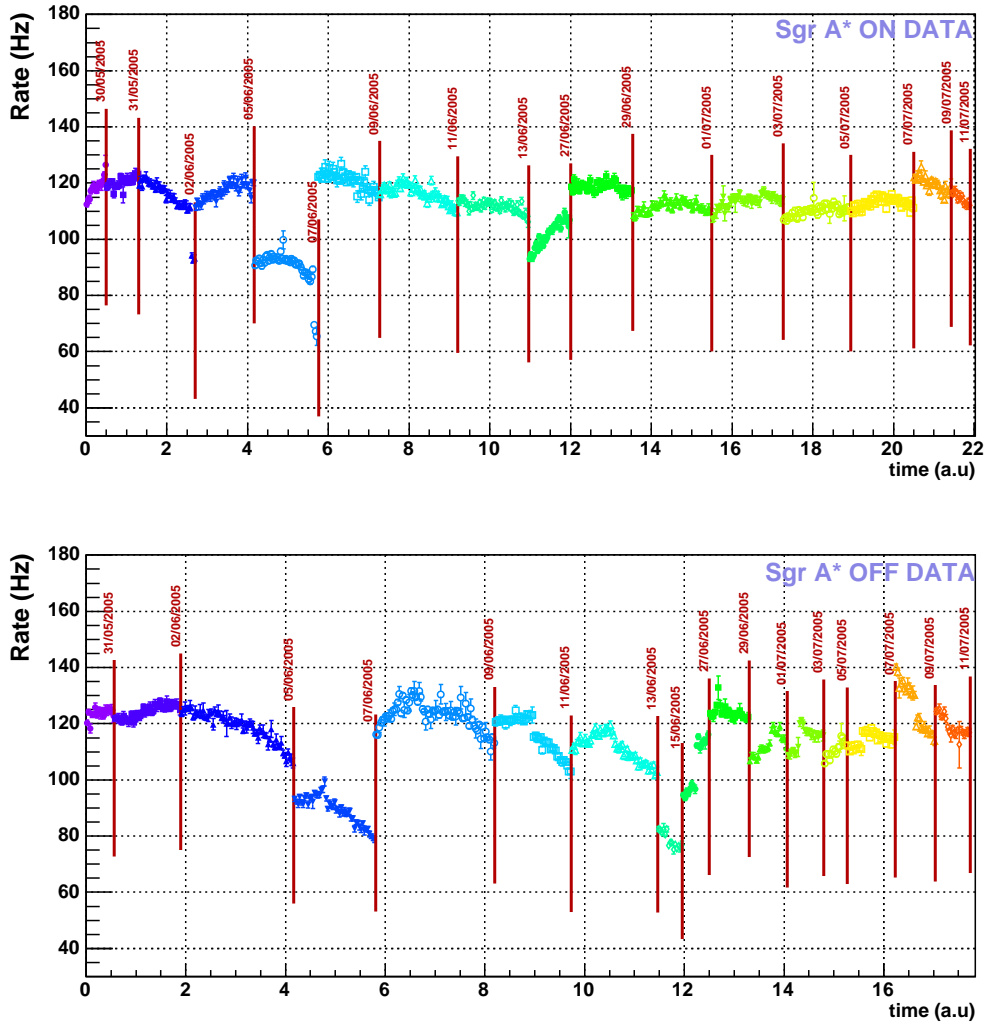


Figure 8.8: Event rates after image cleaning for both GC ON and OFF samples (see text for details).

specific locations. This reinforces the hypothesis that the sparks are related to some PMTs, with some particular problems<sup>5</sup>.

In order to extract the spark events from the data, a special filter cut has to be found. A cut on  $W/L < 0.7$  to get rid of them is not useful, as this cuts real signal. As these events are quite bright, we see in Figure 8.10, a cut in SIZE vs. CONC plane almost cut all of the spark events, without cutting away the signal,

$$\log_{10}(CONC) < -0.28 \cdot \log_{10}(SIZE) + 0.46 \quad (8.1)$$

With this cut the spark events rate is reduced to  $\sim 0.09$  Hz. In addition, after quality cuts and  $\gamma/h$  separation cuts, all these remaining spark events are completely removed from the data.

<sup>5</sup>These problems were reported to camera experts.

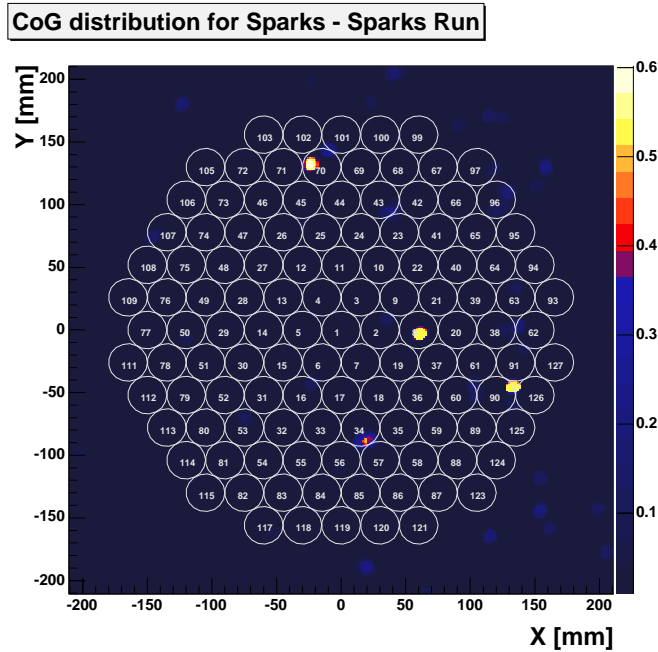


Figure 8.9: Center of Gravity (CoG) for the shower images plotted in the camera reference system. These special runs taken with the camera closed shows the camera pixels that most likely generate the light sparks.

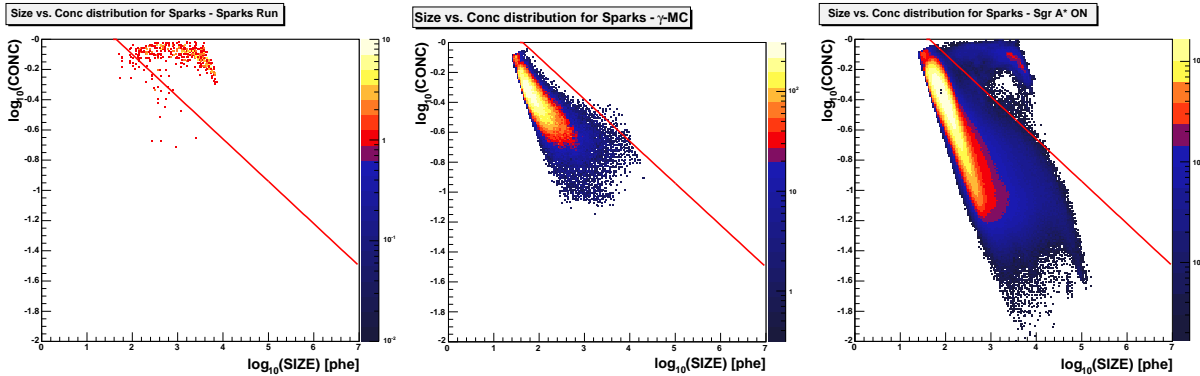


Figure 8.10: Events in a SIZE vs CONC plot. (left) These are events from special camera closed runs, i.e., only the spark events trigger the DAQ; (center)  $\gamma$ s from the MC sample; (right) the whole GC ON data sample. The 'spark cut' is displayed with a red line.

### 8.9.3 Curing camera inhomogeneities: modifying the signal extractor

The different L1 trigger cells synchronization affected the pulse positions which were recorded at the FADCs, and some events were not properly reconstructed with the *Online Analysis*. The pulse positions in the FADC channels were slightly displaced from the nominal value when the shower image was triggering in a particular region of the camera [219]. As the charge extractor is based on a set of default values, the charge assigned to most of these pulses was failing, and these events were automatically removed by the image cleaning from the rest of the analysis.

To cure this effect, the whole GC ON and OFF data sample were re-calibrated and processed

with an extraction window larger in the FADC slices than the one employed in the *Online Analysis*. The digital filter fitting 4 FADC slices is set. To partially cure the misbehavior of the trigger macro-cell number 19, the size of the window for pulse searching around the determined pulse position has been increased from the standard values of 2.5 slices to the left and 4.5 slices to the right to the values of 4.5 slices to the left and 5 slices to the right. This slightly enhance the bias as the region for maximum signal searching is larger, but it is still expected to be lower than the case when no position check is performed.

In Figure 8.11 it is shown the Center of Gravity (CoG) of the images for the ON data before and after correcting the signal extractor. The upper right region on the camera is the one most affected by the trigger cell timing problem, which is recovered after the correction.

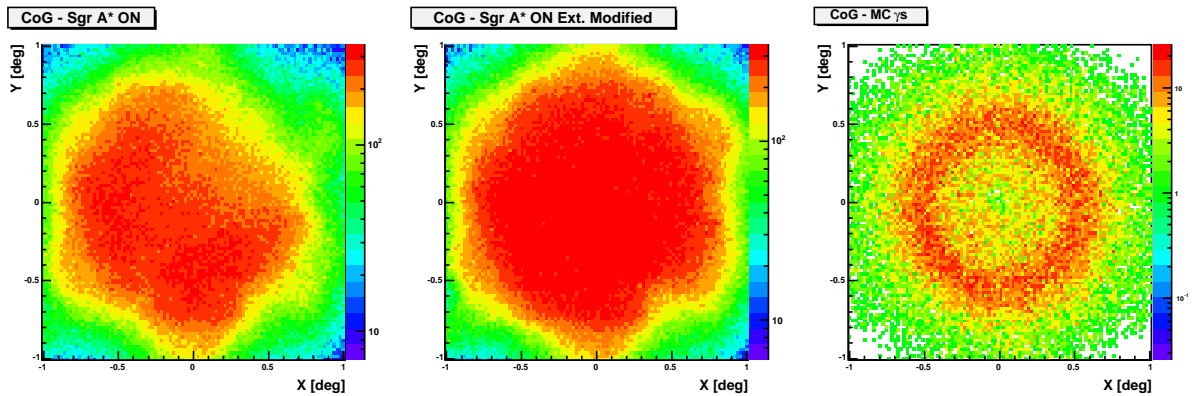


Figure 8.11: CoG of image showers after image cleaning. (left) GC data from the *Online Analysis*, (middle) GC data processed with modified extractor parameters, (right)  $\gamma$ -MC.

The expected  $\gamma$ -shower distribution is homogeneous in the camera, as can be seen in Figure 8.12, that shows the number of events which lie in a line that crosses the center of the camera with an angle  $\phi$  to the x-axis. We see that, if this effect is not corrected, up to 15% of signal is lost in the region from 0 to 2 radians. This affects the detection efficiency of the system (which should have to be corrected afterwards by hand, as of course this is not visible in the MC). With the correction, more homogeneity of events distribution in the camera is obtained, and the signal also increases adding more statistics to the further analysis.

#### 8.9.4 Mispointing corrections with the Starguider

Pointing (Moving) to a position on the sky is not very accurate ( $\pm 10$  Shaft-encoder (SE) Steps). The reposition is done two, three or four times until the correct SE step is reached on both axis (which has an accuracy of  $\pm$  one SE step). When tracking starts, one gets a further improvement as soon as the movement crosses the edge of one SE, i.e. changes its value. The time needed depends on the ZA of observation (for HZA this might be a few minutes at the beginning of source tracking). When the source passes through its culmination, the tracking on one axis changes direction and some SE steps are lost. The outcome is that the source is not at the camera center anymore, but  $\sim 0.12^\circ$  away, until the movement crosses the edge of one SE and the pointing procedure starts to be corrected. In addition, in an ALT-AZ mount, the source located off-axis rotates in the camera. In case of the data analyzed in this Thesis, almost 35% of the data is affected by the so-called 'culmination' effect.<sup>6</sup>

<sup>6</sup>To date, solving this problem is under investigation by the Collaboration.

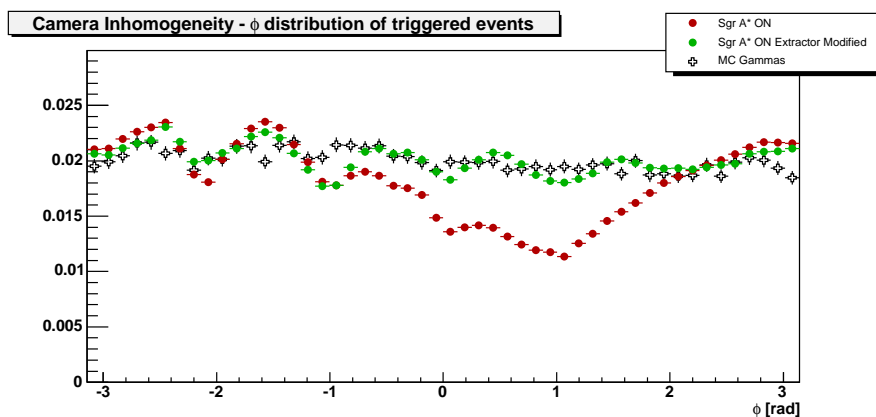


Figure 8.12:  $\phi$  distribution of CoG of shower images for GC data from the *Online Analysis* (red), GC data processed with modified extractor parameters (green), and  $\gamma$ -MC (black).

In case of GC, the observations were carried out near the culmination ( $ZA \sim 60^\circ$ ), otherwise the data would have been taken at very large zenith angles. Almost 36% of the data is affected by the so-called 'culmination' effect. This mispointing affects the source dependent Hillas parameters, in particular DIST and ALPHA, which are powerful parameters to distinguish between  $\gamma$ s and hadrons. In this sense, an uncorrected mispointing results in losing part of the signal, as the  $\gamma/h$  technique cannot recognize the mispointed  $\gamma$ -images accurately. In addition, we want to know if the emission from GC is extended in nature or compatible with a point source, so the mispointing has to be corrected as much as possible.

Data can be corrected for the mispointing of the MAGIC telescope in two ways:

- Using bright stars in the field of view and identifying them in the pixels, which are brighter than the rest at the DC currents.
- Using the star-field CCD camera to identify the stars in the field of view to get the pointing position comparing to the camera reference frame, with the so-called *Starguider system*.

Both methods present some problems. In the field of view of the GC, two bright stars can be used to correct the mispointing by identifying them in the DC currents. We know a priori at which position we are pointing at any time, i.e., the correspondence of the center of the camera to celestial coordinates, then using the star field information in the camera plane one can correct the mispointing from the DC currents. The problem presented here is that these two bright stars are located in the outer region of the camera which is equipped with pixels of about  $0.2^\circ$  diameter. The two stars only illuminate one outer pixel each, and the pointing position is badly determined (see Figure 8.14). The method to correct the mispointing with the DC currents has shown to be useful when the stars are in the inner part of the camera [214]. In this case, several pixels are illuminated by the star (note that we point to 10 Km, not to infinity) and the pointing position can be accurately determined.

The case of the mispointing correction with the use of the Starguider yield other problems. The Starguider at the time of observations was installed but not calibrated. This means that an absolute mispointing correction cannot be done, but only a relative correction<sup>7</sup>. By comparing the stars in the field of view (around 25-30 stars are identified in a CCD frame for the GC FOV) with

<sup>7</sup>Note that the Starguider does not take into account any mispointing created by bad alignment configuration of the mirrors. We assume that the AMC works properly, as its performance results indicate.

the reference frame defined by the MAGIC camera, the Starguider provides the deviation in  $ZA$  and  $Az$  to the current pointing position.

Figure 8.13 shows the 'culmination-jump' as seen by the Starguider when the source is in culmination (i.e, reaches  $Az = 180^\circ$ ). At this time, the pointing position jumps in  $ZA$  about  $0.12^\circ$  (at top-left figure), and it is almost recovered when the GC has passed the culmination region (when  $Az \sim 185\text{--}190^\circ$ ). Note that at the beginning of the observations we are still not tracking properly the source, as expected from the current pointing algorithm. This happens for about 3-5 minutes every night, i.e, the data taking starts and the telescope is still approaching the source. This problem is nowadays taken into account in the standard data-taking procedure.

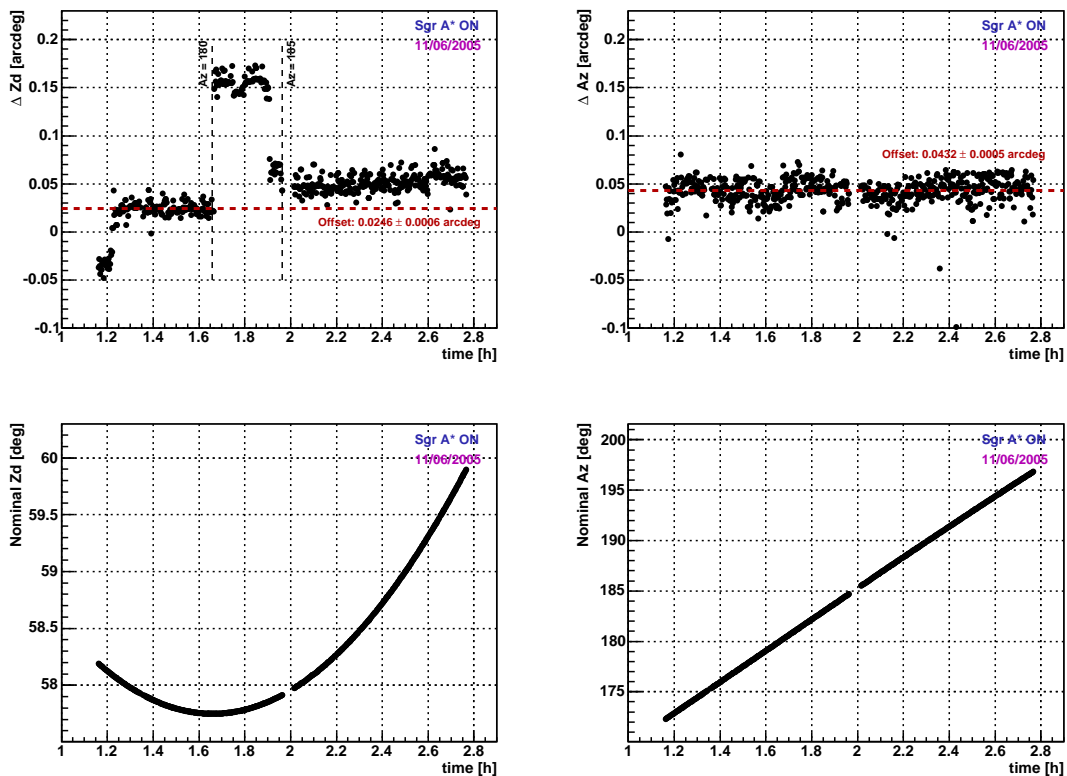


Figure 8.13: Plotted are the tracking  $ZA$  and  $Az$  values, and deviations in  $ZA$  and  $Az$  provided by the Starguider system, for night of 11/06/2005 and GC ON data-taking period. The mispointing when source passes trough culmination is clearly seen in upper-left panel. The calibration  $ZA$  and  $Az$  offsets for the Starguider data are shown with the red dashed lines.

At the time of the GC observations, the Starguider CCD camera was installed, but not calibrated. In order to calibrate the Starguider we proceeded in the following way:

- **Calibration of  $ZA$  and  $Az$  deviation offsets:** here we assume that before source culmination we are pointing accurately to the source (at least, only dominated by the telescope pointing accuracy, see Figure 8.15). The Starguider offsets in  $ZA$  and  $Az$  are evaluated and all the Starguider data is corrected by these offsets (plotted with a dashes red line in Figure 8.13). These corrections are done for every night independently, as these values differ from

night-to-night<sup>8</sup> (see Appendix A).

- **Calculate the pointing position:** once the Starguider is calibrated, the pointing position can be calculated at any time. Also, the GC position in the camera reference frame can be as well calculated. Here, one has to be careful to apply proper source location algorithms, as in an ALT-AZ mount a source located off-axis rotates in the camera [240]. This effect is not very important at high zenith angles, as the rotation velocity of an off-axis source is very small. Figure 8.14 shows the GC position in the camera reference frame evaluated with the DC currents (star finding algorithm, that clearly fails) and the calibrated Starguider (which is in good agreement with the uncorrected GC excess sky-maps shown in Figure 8.15).
- **Re-evaluation of the Hillas parameters:** those that depend on the source position, like DIST, ALPHA, etc... are re-evaluated taking as a reference point the one corresponding to the GC position in the camera reference system. The reference point is evaluated in a run-by-run basis.

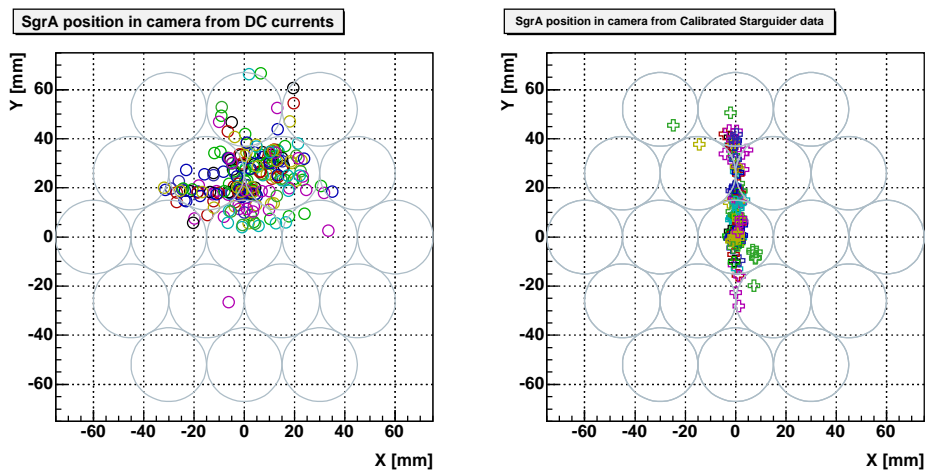


Figure 8.14: GC positions in the camera reference system evaluated with the DC currents (left) and the Starguider (right) methods. These positions are evaluated in a run-to-run basis. The different colors correspond to different GC ON nights.

Figure 8.15 shows the GC sky-maps, after  $\gamma/h$  separation and obtained with the DISP method (both will be explained in a separate section), for 3 different regions of Azimuth, that correspond to before, during and after mispointing (i.e.  $Az < 180^\circ$ ,  $180 < Az < 190^\circ$ , and  $Az > 190^\circ$ ). These plots are done before correcting the mispointing and clearly show some of the assumptions made: a) before the culmination, in average, we are pointing accurately to the source, which is at the center of the camera frame; b) during culmination, the source is clearly detected off-axis, the expected distance and in the expected direction; c) after the culmination the source is nearby the center, but not so close as before the culmination.

With the mispointing corrections we solve some of these telescope tracking problems: we correct for small residual mispointing which are seen at the beginning of every observation night, and we correct the 'culmination-jump' effect in Zenith. Unfortunately, we do not correct the small residual mispointing which are seen after culmination. This residual mispointing can be related to a badly

<sup>8</sup>To date, the reason of these differences is still unknown.

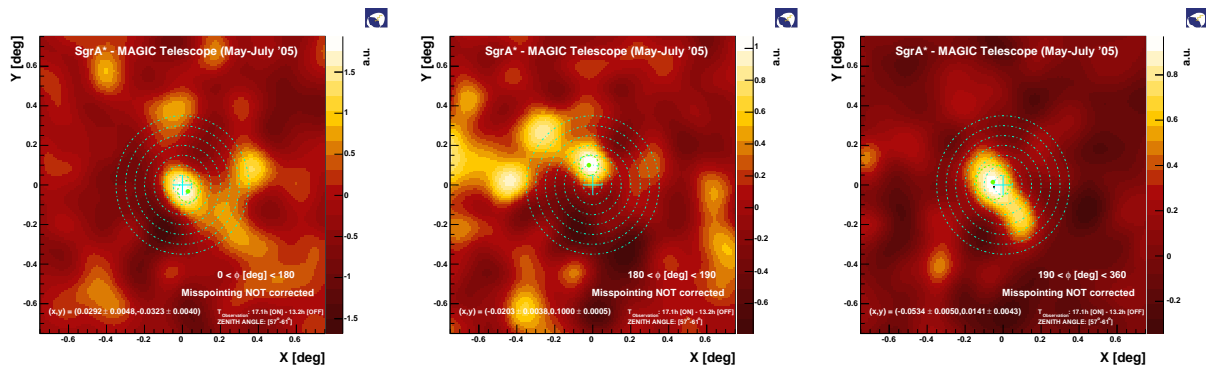


Figure 8.15: DISP-sky-maps in a camera reference system for GC data before (left), after (right), and during the culmination culmination jump (middle). The data is not corrected by the mispointing effects, and GC is detected off-axis while the culmination problem is present.

assigned bending corrections in the drive system<sup>9</sup>. Table 8.9.4 shows the distance of the GC signal to the camera center, resulting from a bi-dimensional Gaussian fit to the signal excess in the DISP-skymaps, before and after source correction. We improve the source position correction, except for 10% of data that is taken after the culmination effect. At present Starguider status, this result is far from satisfactory.

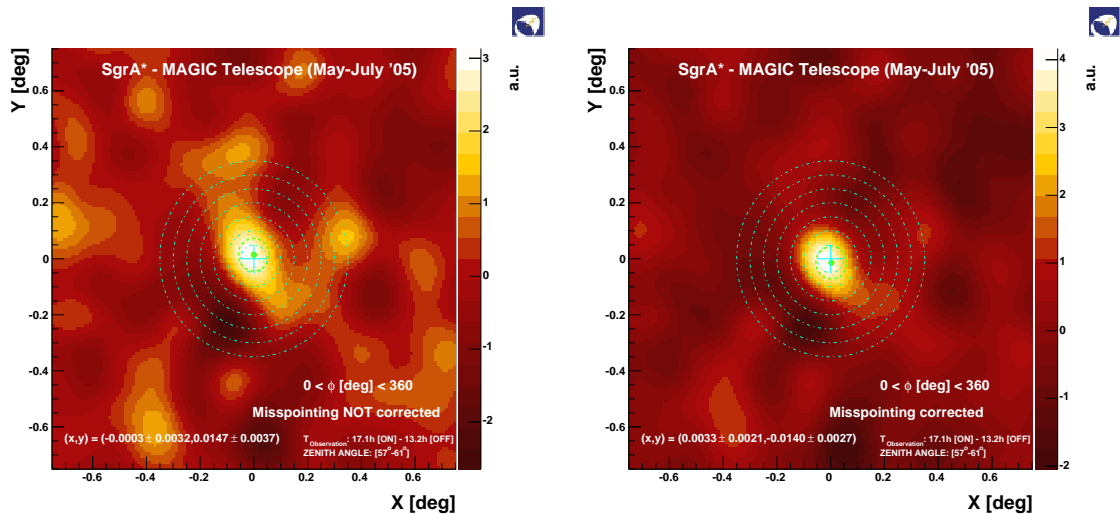


Figure 8.16: Global DISP-sky-maps in a camera reference system for GC data with mispointing not corrected (left) and corrected(right).

The net effect of the source correction is shown in Figure 8.16. More excess is obtained, as expected, with the use of these corrections. Although a more careful treatment of the mispointing should be addressed, this method presented here improves the analysis in terms of integrated

<sup>9</sup>The bending corrections are needed to compensate deviations of the camera frame due to its weight. These corrections are normally evaluated tracking bright stars in different  $ZA$  and  $Az$  regions, stored into a database which is further used by the drive control system (Tpoints data).

signal, sensitivity, and quality. The 15% effect related to the inhomogeneities and the 20-25% improvement in the signal-to-background with the mispointing corrections are crucial to be able to get an spectra extending to the highest possible energy bin (where there is of course lack of statistics for a power-law type spectra).

Az range [deg]	mispointing not corrected $d_{center}$ [deg]	mispointing corrected $d_{center}$ [deg]	% of data
$0 < Az < 180$	0.0435	0.0211	54.8%
$180 < Az < 190$	0.1020	0.0154	35.5%
$190 < Az < 360$	0.0552	0.0571	9.7%

Table 8.3: Distance of the GC signal to the camera center, resulting from a bi-dimensional Gaussian fit to the signal excess in the DISP-skymaps, before and after source correction.

## 8.10 Random Forest for $\gamma$ -hadron separation

To train the RF method for  $\gamma/h$  separation we have used a train of the large ZA  $\gamma$  MC sample of about 100 kEvts and of about 100 kEvts of OFF events as *hadron* sample, randomly selected from the whole OFF sample. The use of real data is mainly due to the lack of simulated proton and helium induced showers at high zenith angle. It is indeed convenient, as the OFF data is supposed to be entirely composed by background images.

Two separate RF methods are used, as we are interested to perform two separate kind of analysis: (a) one to calculate the flux (labeled *ALPHA-analysis*, with RFStd RF) and (b) one to evaluate the emission location and possible extension of the emission (labeled *DISP-analysis*, with RFDisp RF). The methods are different, as in (a) we make use of source-dependent parameters (as we assume the source is located exactly at the pointing position), which improves the  $\gamma/h$  separation, and in (b) we exclude all source-dependant Hillas parameters in the RF training, resulting in a slightly different  $\gamma$ -hadron separation efficiency, but without including a bias when determining of the emission location.

<i>ALPHA-analysis:</i>	SIZE, WIDTH, LENGTH, CONC, DIST, M3LONG	(RFStd)
<i>DISP-analysis:</i>	SIZE, WIDTH, LENGTH, CONC	(RFDisp)

Table 8.4: Set of variables used in the RF training procedures for the two separate analysis chains: ALPHA-analysis and DISP-analysis.

The variables used to train the RF for both analysis are shown in Table 8.10. We note that in the training of the RF, the OFF events are selected such as the SIZE distributions of both  $\gamma$  MC train sample and train OFF sample coincide. We do know that intrinsic SIZE distribution of hadrons and  $\gamma$ s are different, because their different energy spectra and because of the effect of the trigger on the different shapes of  $\gamma$  and hadron images. We do not want the SIZE to be a full power separation parameter, only a parameter that guides the rest of the Hillas parameters in the multi-parameter space. Otherwise, the algorithm would select  $\gamma$ s with a given SIZE distribution fixed by the MC, which is directly related to the spectral power index in which the MC has been

generated, with high probability of being different of what we would measure from the observed source.

Figure 8.17 shows the mean decrease in Gini index, obtained for the two different optimizations. This variable is a measure of the efficiency that the given cut parameter obtains in rejecting background if the other cut parameters are present. We can clearly see that the parameter LENGTH results to be the strongest cut parameter, and that the DIST parameter adds an improvement on the method for the ALPHA-analysis, when comparing to the DISP-analysis method.

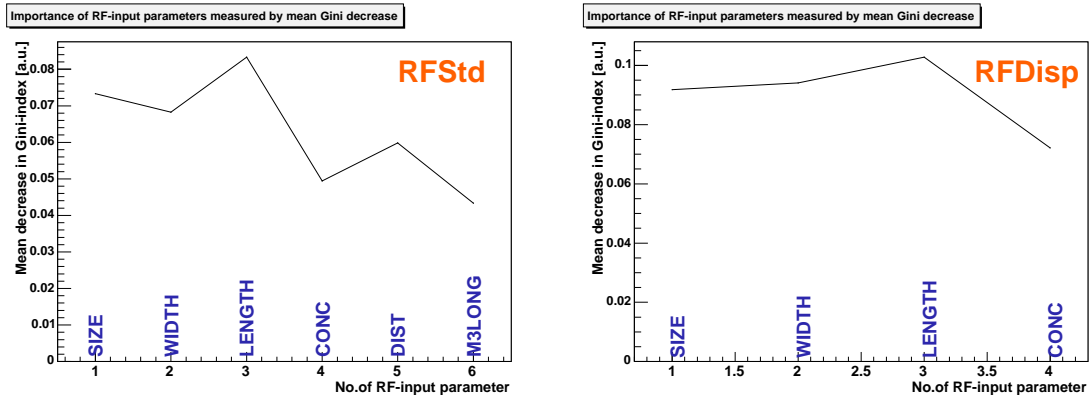


Figure 8.17: Mean decrease in Gini index for the training variables used in the RFStd and RFDisp RF training methods.

By the use of a separate *test sample* of MC  $\gamma$  and OFF events, the HADRONNESS parameter, the quality factor  $\mathcal{Q}$  and the selection efficiencies can be evaluated as a function of the HADRONNESS cut (i.e,  $h < a$  given value) for both MC and OFF samples. Figure 8.18 shows these variables, in different SIZE bins and for the two RF methods, i.e, the RFDisp (red) and RFStd (black). The distribution for the  $\gamma$  MC events is plotted as a solid line, while the OFF events are plotted with dashed lines.

From this Figure we can extract quite some interesting remarks. We can clearly see that the  $\gamma$ -showers are identified to have low HADRONNESS values (as expected peaking to 0 value), while the hadrons have HADRONNESS distributions peaking at value 1. We see that the RF method does not identify all the hadrons to be 'hadrons'. This irreducible background has to be estimated by other means (in particular, the signal is obtained by subtracting ON to 'scaled' OFF distributions, the so-called excess signal). In general, the  $\gamma/h$  separation worsens when going to low SIZE values. We see that below a SIZE of about 180 *phes*, the two peaked-like distributions for hadrons and  $\gamma$ s start to loose its peakness. This evidences that the  $\gamma/h$  separation below 180 *phes* turns out to be a difficult task with the use of the standard Hillas parameters. This effect is visible for both RFDisp and RFStd  $\gamma/h$  separation methods, and limits the energy threshold in which the measured spectra would contain any significant signal (at such high zenith angle, 180 *phes* corresponds to an energy threshold of about 650 GeV).

RFStd method provides better  $\gamma/h$  separation than RFDisp method (bigger  $\mathcal{Q}$  factors), as the DIST parameter is a powerful parameter for  $\gamma$  identification, as seen in Figure 8.17. Normally, HADRONNESS cuts are around 0.1 to 0.2.

## 8.11 Random Forest for energy reconstruction

The energy associated to the  $\gamma$ -like events after the  $\gamma/h$  separation turns out to be an important quantity, as it will be used to determine the shape of the energy spectrum of the primary  $\gamma$ -ray

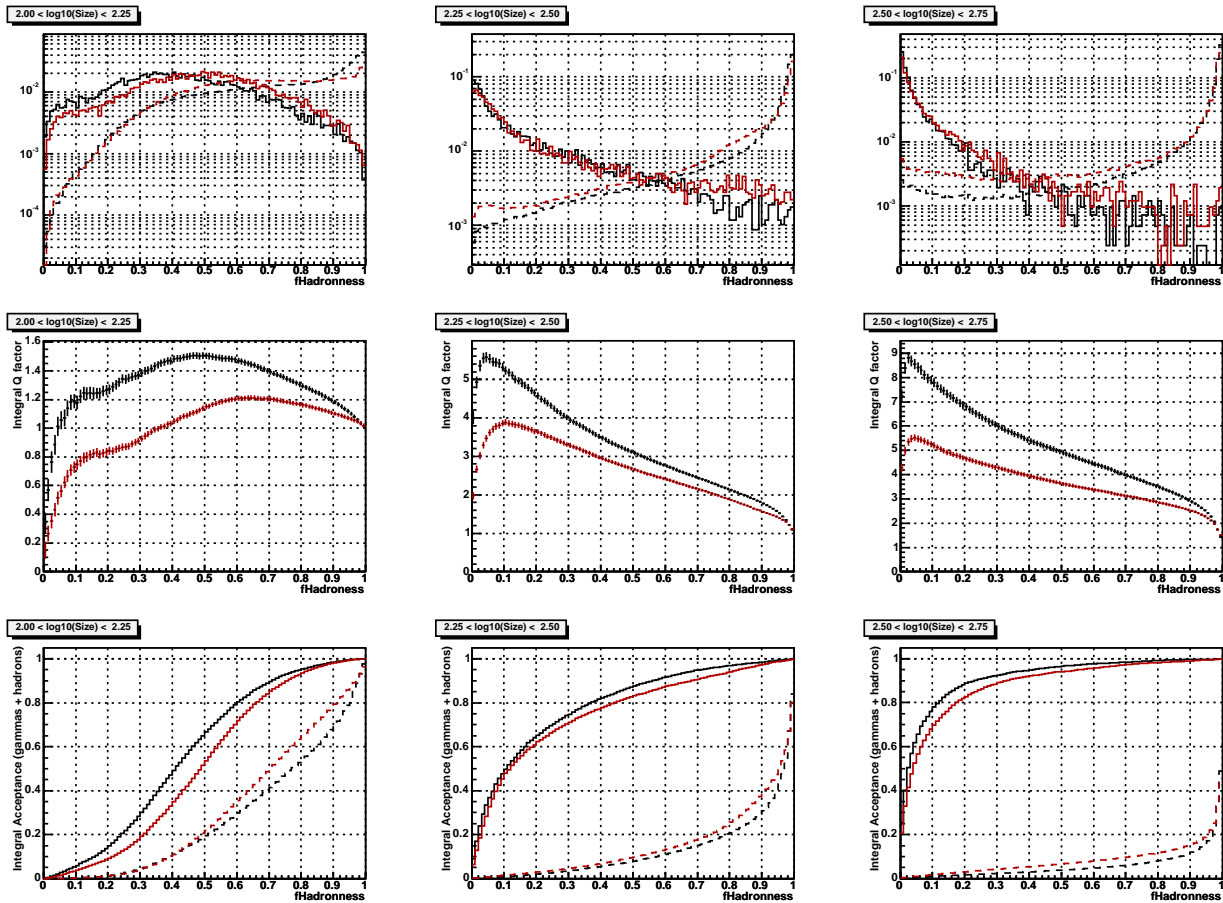


Figure 8.18: For different SIZE bins [phe], the HADRONNESS distributions (top),  $Q$ -factors (middle), and  $\gamma$ -acceptance (bottom) for  $\gamma$ s (solid lines) and hadrons (dashed lines). The RFStd (RFDisp) training method applied to the test sample is displayed in black (red).

candidates associated to the source of emission. The energy of the primary particle is not measured directly and has to be derived from the shower image parameters.

In first order, the total amount of Čerenkov photons within an EAS is proportional to the shower energy, and therefore to the energy of the primary particle. We can see in Figure 8.19 the strong correlation between the SIZE and the energy of the primary  $\gamma$ -ray for the MC set. However, the energy resolution is quite poor if using only the dependence on SIZE, and we need second order corrections for a better determination of the primary  $\gamma$ -ray energy.

Normally, complex parameterized relations between the energy of the primary and a subset of the Hillas parameters have been extensively used. In contrast, we would use the set of the large ZA MC events for training purposes to feed a specially developed RF as a learning method to estimate the energy of the primary, as we do know from MC the correspondence of the 'true energy' of primary and the rest of the Hillas parameters.

The input variables for the RF training on the energy estimator are: ZA,  $\log_{10}(\text{SIZE})$ , WIDTH, LENGTH,  $\log_{10}(\text{SIZE}/(\text{WIDTH} \cdot \text{LENGTH}))$ , DIST, CONC, LEAKAGE1, and the TRUE\_ENERGY (quoted here as  $E_{mc}$ ). The energy estimation is done by training different classifiers in several energy bins (with a logarithmic binning). Each classifier is constructed by training the contents of

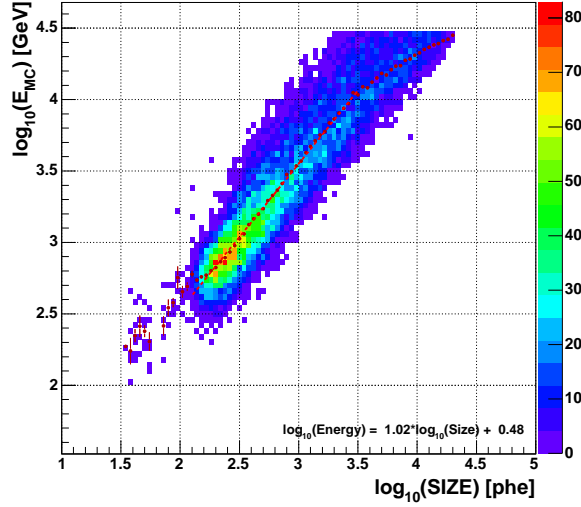


Figure 8.19: Correlation of the image shower SIZE parameter to the energy of the primary  $\gamma$ -ray, from the large ZA MC- $\gamma$  test sample.

one energy bin against all others, hence each classifier should recognize a specific energy region. The evaluation of the energy is done by weighting the output of each classifier by the respective energy (center of the bin)<sup>10</sup>

$$E_{rec} = \frac{\sum E_i \cdot out(i)}{out(i)} \quad (8.2)$$

The results obtained with this RF method are shown in Figure 8.20, with  $\Delta E$  defined as:

$$\Delta E = \frac{E_{mc} - E_{rec}}{E_{rec}} \quad (8.3)$$

The left plot of Figure 8.20 shows the *mean* and *RMS* values of the distribution  $\Delta E$  in bins of the true energy ( $E_{mc}$ ). This has the advantage to plot the behavior of the reconstruction method against an objective value. Nevertheless, from the calculational point of view, it is interesting to plot these values as a function of the reconstructed energy ( $E_{rec}$ ), shown on the right plot, since this is the energy resolution and the bias that is given by the method to the  $\gamma$ -rays when estimating their energy spectra<sup>11</sup>.

We see that this energy estimation method provides biases (mean values) near 0, and an energy resolution of about 25% RMS value. The deviations at higher energies might be related to the lack of MC statistics. All these values are evaluated after  $\gamma/h$  separation, with HADRONNESS < 0.125, and with the use of the RFStd method. The overall picture does not change substantially if no  $\gamma/h$  is done, neither with the use of the RFDisp method.

Some other methods have been tested for the MAGIC Telescope results, but the energy estimation with statistical learning methods (shown here the RF method) gives better results than the classical parameterization with resolutions that improve from 40% to 25% *RMS* values. See [221] for full comparisons and improvements of the method presented here.

<sup>10</sup>The *output* of each classifier goes from 0 to 1. This output is analogous to the so-called HADRONNESS in the RF for  $\gamma/h$  separation, but here we have as many RF (classifiers) as energy bins defined in the training.

<sup>11</sup>This is the case presented in this Thesis, in which spillover corrections are applied as unfolding method.

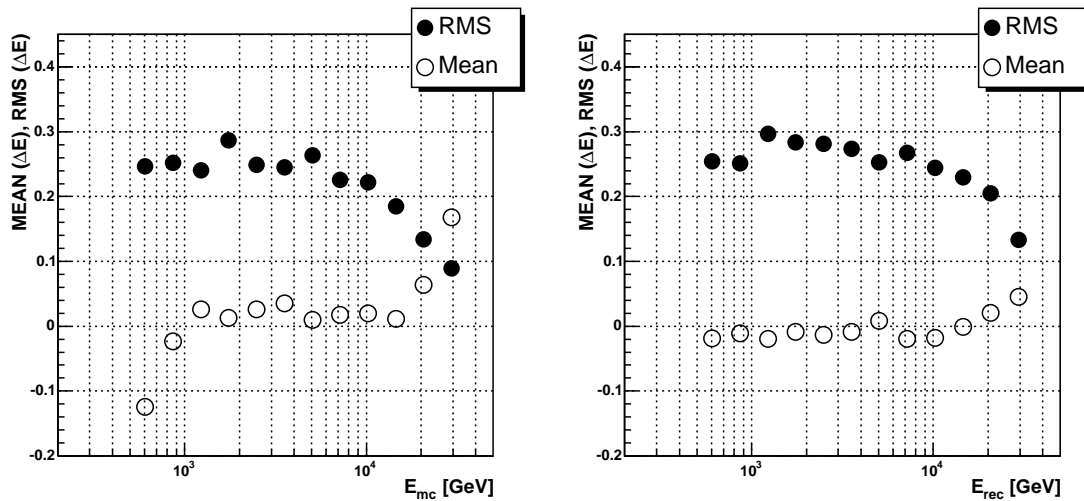


Figure 8.20: Mean  $\Delta E$  and RMS of  $\Delta E$  for different energy bins: (left) against true energy, and (right) against reconstructed energy. From the large ZA MC- $\gamma$  test sample, with HADRONNESS $<0.125$  (RFStd method used).

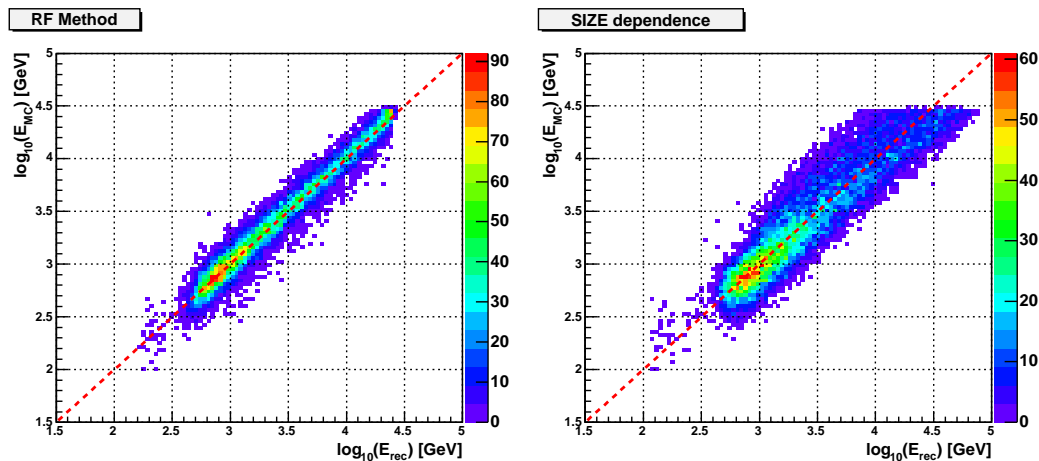


Figure 8.21: Comparison of the reconstructed energy  $E_{rec}$  with the simulated shower energy  $E_{mc}$  for the large ZA MC- $\gamma$  test sample, with HADRONNESS $<0.125$  (RFStd method used). (left) Applying the RF Energy estimation algorithm and (b) applying the SIZE dependence shown in Figure 8.19.

## 8.12 Cuts applied to the data

Additionally to the HADRONNESS cut, further quality cuts are applied to the GC data in order to maximize the hadron suppression without cutting away a significant part of the signal. These set of cuts can be obtained either from MC or better from a strong signal like observations of Crab Nebula or an AGN in flaring-state.

In this Thesis, we will not apply a set of optimum cuts obtained from the analysis of a strong source by several reasons:

- At the time we did not have Crab Nebula data at such large ZA and with the same telescope conditions. About 2 hours of Crab Nebula were available in same observation conditions, but the PSF of the telescope was not the same as that considered in the GC dataset. As the PSF affects drastically the results, we decided not to use a set of data with different telescope conditions to get optimum cuts.
- No other intense source was observed at such large ZA with the same telescope conditions.

So, we decided to apply a set of 'relaxed' cuts, rather than the optimal (i.e. the ones that give better sensitivity), trying to keep most of the signal, based exclusively on the MC  $\gamma$ -set. These 'relaxed' cuts translates on much more statistics in the signal region, but bigger errors and less significance than that obtained in an optimum analysis (as more background is as well retained).

The set of the cuts that are applied to the data are:

- **Spark-events cut:** A cut is used to cut away the sparks events.

$$\log_{10}(CONC) < -0.28 \cdot \log_{10}(SIZE) + 0.46 \quad (8.4)$$

- **SIZE cut:** A cut is applied, to avoid the region in which the  $\gamma/h$  separation method starts to fail.

$$SIZE > 175phe \quad (8.5)$$

- **HADRONNESS cut:** we choose an intermediate HADRONNESS value that keeps about 80% of the signal (after size cut, see Figure 8.22). For higher energies, this HADRONNESS cut does not allow to have a residual background, which is necessary to determine the amount of signal over the background. For the largest energy bin considered in the analysis the HADRONNESS cut is increased to 0.3. This HADRONNESS cut reduces the background images by a factor 1000.

$$HADRONNESS < 0.125(0.3) \quad (8.6)$$

- **ALPHA cut:** The optimum value for the ALPHA cut in order to get the best significance is around  $ALPHA < 5^\circ$ . But, this is the best significant point, which is quite useful to make discoveries. Once a source is detected, the ALPHA cut can be relaxed in order to keep the maximum quantity of signal. We choose a cut in ALPHA that at least retain 95% of the signal (after size cut).

$$ALPHA < 15deg \quad (8.7)$$

- **Lower DIST cut:** For the ALPHA-analysis we apply a lower DIST quality cut, that cuts 5% of signal events when applying the SIZE and ALPHA cut.

$$DIST > 0.42deg \quad (8.8)$$

- **Upper DIST cut:** we apply an additional upper quality cut of DIST depending on SIZE, in order to keep 85% of signal, per SIZE bin.

$$DIST < 0.22 + 0.25 * \log_{10}(SIZE)deg \quad (8.9)$$

Figure 8.22 displays the effects of the cuts over the MC  $\gamma$ -sample. OFF data is also shown for comparison purposes.

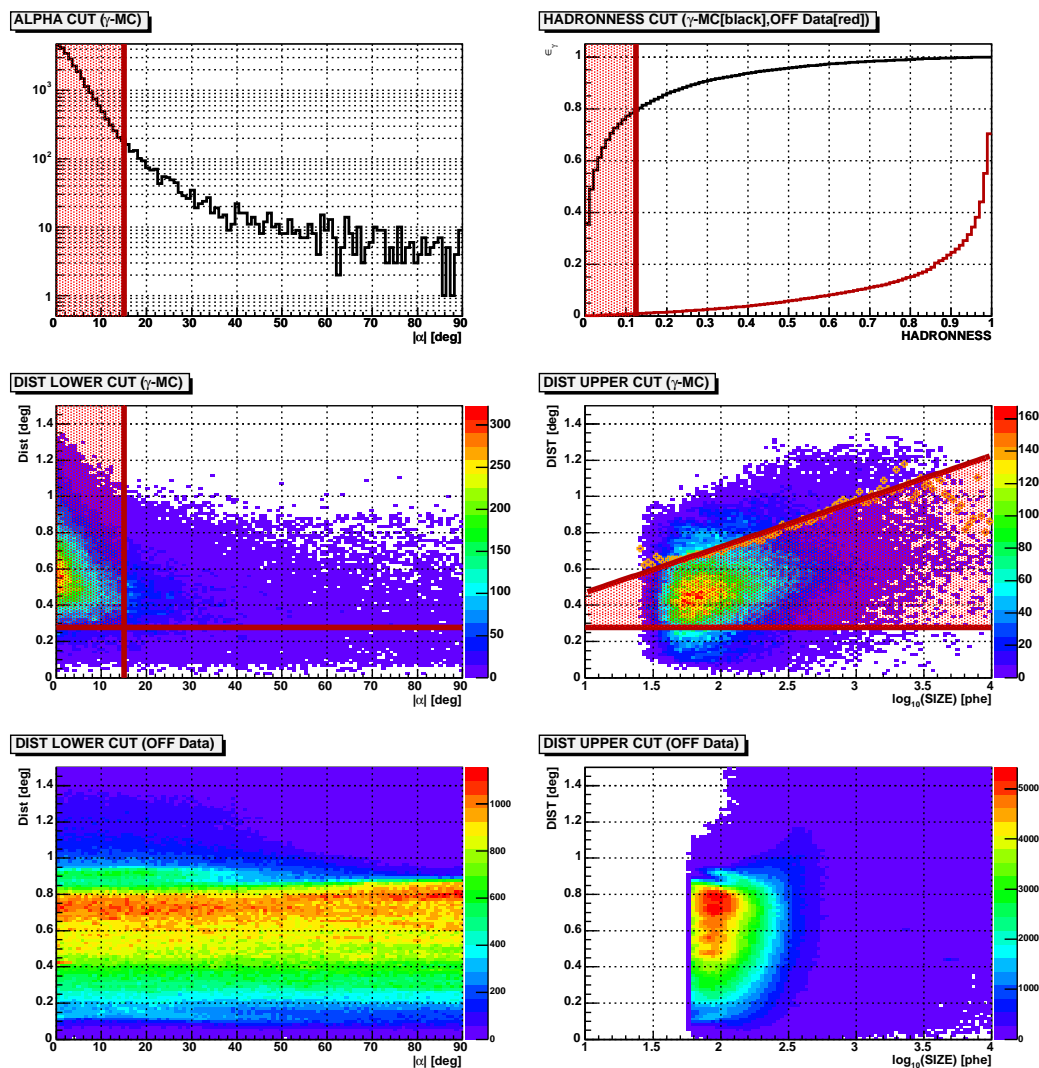


Figure 8.22: Cuts used on the analysis, obtained from the MC test sample. The behavior of OFF data (background) is also shown (see text for details).

### 8.13 ALPHA analysis: differential energy spectra determination

After data quality pre-processing, RF training for  $\gamma/h$  separation and energy estimation, we are ready to evaluate the differential energy spectrum, with the ALPHA-analysis (RFStd).

#### Effective observation time

The effective observation time is calculated, and is of  $59202.4 \pm 27.0$  s for the ON sample, while the effective OFF observation time is  $42881.6 \pm 22.7$  s (see Figure 8.23). This results on about 16.4h of GC ON data and of about 12 h of OFF data available for the analysis.

#### ALPHA-plot: detection significance

The global ALPHA plot after cuts is shown in Figure 8.24. As the ON and OFF observation

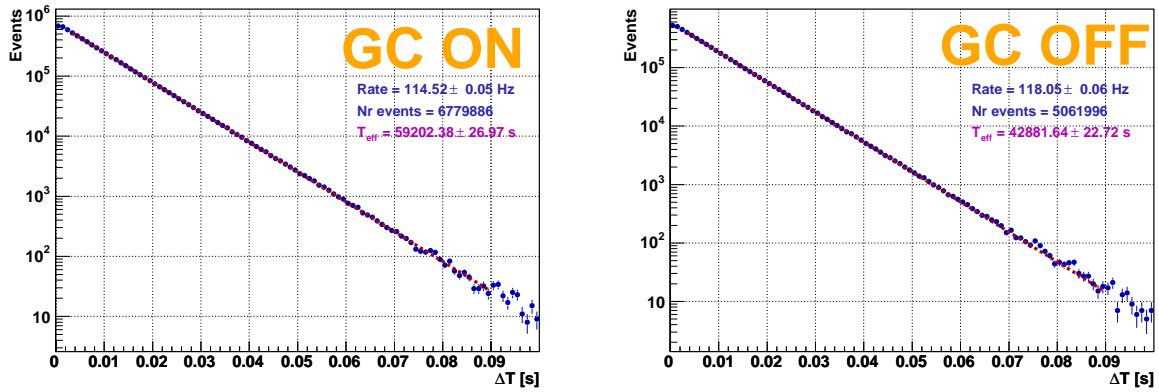


Figure 8.23: Effective ON and OFF times.

times are different, the OFF data is scaled to the ON distribution as as the ratio of the ON to OFF events in the ALPHA region from 40 to 85 degrees, i.e, we scale both distributions in the region in which the signal is not expected. The scale factor is  $\Gamma \simeq 1.61$ . Note, that this normalization takes into account the little differences present for both type of observations (like different weather conditions, sky brightness, etc...) that affect the Hillas parameters. Ideally,  $\Gamma$  should be the ratio of observation times, but we note that  $\Gamma$  is slightly different from it ( $\Gamma_t \simeq 1.38$ ).

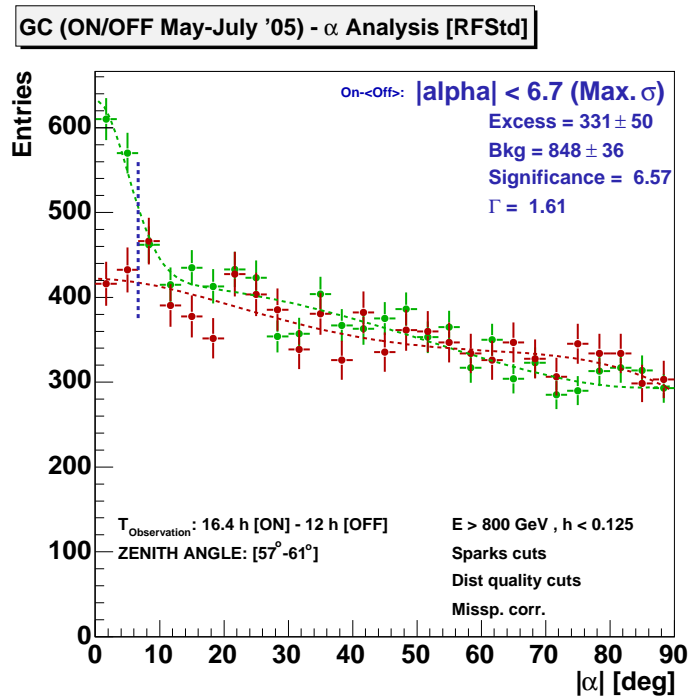


Figure 8.24: ALPHA-plot for SIZE&gt;275 phe (corresponding to an energy threshold of 1 TeV, approximately). See text for details.

After cuts, and with slightly bigger SIZE cut of 275 phe ( $\sim 1$  TeV) and with the use of the most significant ALPHA cut, the total number of excess events is  $338 \pm 53$ , resulting in a significant

6.36 $\sigma$  detection (see figure 8.24). For the spectra calculation, we relax the SIZE cut down to 175 phe and the ALPHA cut to 15 $^\circ$ .

### Differential energy spectrum

The differential energy spectra is derived. The results of all relevant parameters involved in spectra determination are shown in Table 8.13, and the differential energy spectra is shown in figure 8.25 (the ALPHA plots for every bin are placed in Appendix B). The flux above 1 TeV corresponds roughly to  $\sim 10\%$  of the Crab Nebula flux.

The differential energy spectrum is consistent with a power-law fit  $dF/dE = \Phi_o * E_{TeV}^{-\delta}$  from 1 TeV to  $\sim 15$  TeV ( $\chi^2/NDF = 1.5/4$ ):

$$\frac{dN_\gamma}{dAdT dE} = (2.0 \pm 0.6_{stat} \pm 0.7_{syst}) \cdot 10^{-12} (E/TeV)^{-2.0 \pm 0.2_{stat} \pm 0.2_{syst}} \text{ cm}^{-2} \text{ s}^{-1} \text{ TeV}^{-1} \quad (8.10)$$

This derived differential energy spectra is highly consistent to the one derived by 2 year observations of the GC region by the HESS telescope over two-decade of energy range from 160 GeV to 30 TeV [238].

$E_{lw}$ [GeV]	$N_{exc}$	$\langle N_{off} \rangle$	$S$	$\Gamma$	$\epsilon_\gamma$	$A_{eff}^{after\ cuts}$ [cm $^2$ ]	$\kappa$	dF/dE [cm $^2$ s $^{-1}$ TeV $^{-1}$ ]
1049.1	92.6 $\pm$ 51.3	968.4 $\pm$ 39.6	1.8 $\sigma$	1.62	$\sim 0.37$	(1.49 $\pm$ 0.02) $\cdot 10^9$	0.82 $\pm$ 0.02	(1.5 $\pm$ 0.8 $_{stat}$ ) $\cdot 10^{-12}$
1808.6	66.0 $\pm$ 38.0	460.9 $\pm$ 30.3	1.8 $\sigma$	2.00	$\sim 0.50$	(2.33 $\pm$ 0.03) $\cdot 10^9$	1.05 $\pm$ 0.02	(5.0 $\pm$ 2.9 $_{stat}$ ) $\cdot 10^{-13}$
3117.9	67.1 $\pm$ 23.3	157.9 $\pm$ 17.9	2.9 $\sigma$	2.02	$\sim 0.51$	(2.56 $\pm$ 0.04) $\cdot 10^9$	1.03 $\pm$ 0.03	(2.6 $\pm$ 1.0 $_{stat}$ ) $\cdot 10^{-14}$
5375.0	38.9 $\pm$ 10.4	26.1 $\pm$ 6.5	3.8 $\sigma$	1.63	$\sim 0.54$	(2.86 $\pm$ 0.06) $\cdot 10^9$	1.02 $\pm$ 0.03	(7.9 $\pm$ 2.2 $_{stat}$ ) $\cdot 10^{-14}$
9266.2	15.2 $\pm$ 7.3	13.8 $\pm$ 4.9	2.1 $\sigma$	1.73	$\sim 0.54$	(2.95 $\pm$ 0.06) $\cdot 10^9$	1.05 $\pm$ 0.04	(1.8 $\pm$ 0.9 $_{stat}$ ) $\cdot 10^{-14}$
15974.4	10.5 $\pm$ 4.7	4.5 $\pm$ 2.6	2.3 $\sigma$	1.50	$\sim 0.48$	(2.75 $\pm$ 0.06) $\cdot 10^9$	0.87 $\pm$ 0.03	(6.4 $\pm$ 3.0 $_{stat}$ ) $\cdot 10^{-15}$

Table 8.5: Parameters involved in the differential energy spectra calculation:  $E_{lw}$ , mean Energy for the bin (according to [229]);  $N_{exc}$ , excess events in signal region;  $\langle N_{off} \rangle$ , normalized background events in signal region;  $S$ , significance;  $\Gamma$ , normalization factor;  $\epsilon_\gamma$ ,  $\gamma$ -efficiency;  $A_{eff}^{after\ cuts}$ , effective area after cuts;  $\kappa$ , spill-over correction factors; dF/dE, differential energy spectrum value. Only statistical errors shown.

All errors in the differential energy spectra shown in Figure 8.25 and Table 8.13 are statistical ( $1\sigma$ ). They are carefully propagated, taking into account that the errors of the spillover corrections and the effective areas are correlated. In particular, the most important error for every bin comes from the excess events. The error from the effective time and effective areas is small.

Besides statistical errors, the results are also affected by systematic errors, which are quoted in the result shown in 8.10. Although it is difficult to know all the systematic uncertainties that can affect the final results, at least with the present understanding of the telescope, one can nevertheless make in most cases reasonable guesses to get a coarse estimate<sup>12</sup>:

- **Atmospheric transmission:** atmospheric conditions are still not monitored during data taking. In the MC simulations, an standard atmospheric model is used, that can slightly differ from the real observation conditions. In particular, the non-ideal conditions result in an underestimation of the real flux. This estimated uncertainty can be as high as 15%.
- **Calibration in absolute scale:** At the moment, still missing is a complete study of the systematics of the calibration system. Among several effects, due to temperature drifts the

<sup>12</sup>E. Lorentz, MAGIC internal talk.

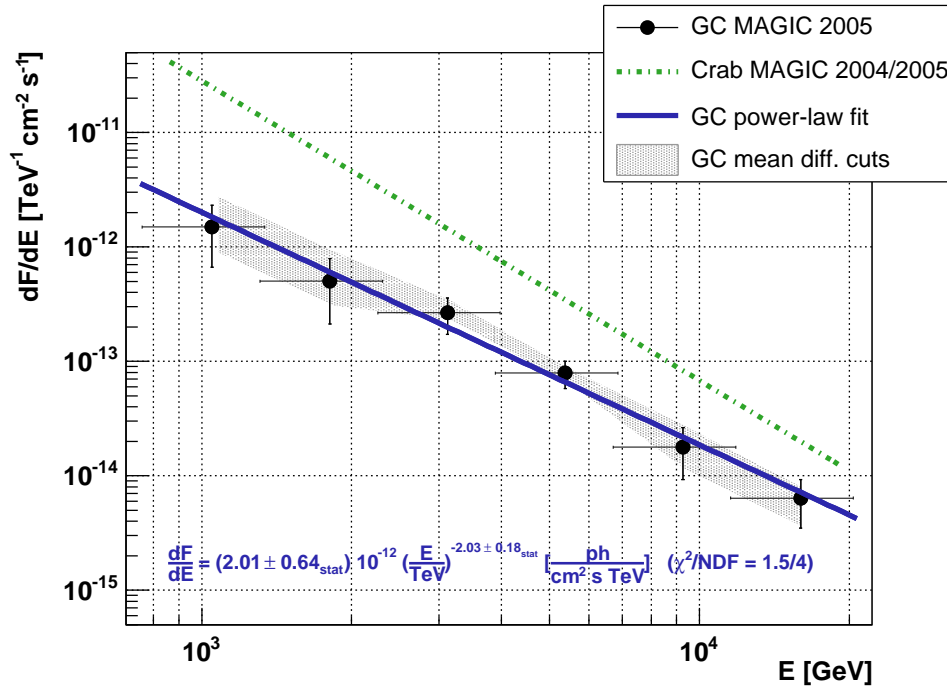


Figure 8.25: Reconstructed VHE  $\gamma$ -ray spectrum of the GC (statistical errors only). The full line shows the result of a power-law fit to the data points. Dashed line shows the energy spectrum of the Crab Nebula as measured with MAGIC. The grey shaded-region shows the spread from several realizations changing the analysis cuts (see text for details).

light outcome from the calibration system can vary. In addition, the F-factor method may as well introduce a systematic error due to the poor knowledge of the PMTs signal-to-noise ratio. The QE uncertainties are estimated to be about 5%. A conservative uncertainty in the charge-to-phe conversion factors is estimated to be about 10%.

- **Light losses:** The mirror reflectivity was estimated to be about 77%, from measurements done before summer 2005 [181]. This value is fixed in the MC simulations, but it might have changed from the time of measurement by the presence of dirt, dust, etc... The telescope PSF has shown to be an important parameter, which shows degradations (and even fluctuations night-to-night) until a major access is done to fix some AMC hardware problems. The telescope PSF is fixed in the MC simulations at an average value (namely  $\sigma \sim 14\text{mm}$ ). The presence of dust in the camera window plexiglass can also be added. All these effects might result in light losses to about 5%.
- **Camera (trigger) inefficiency:** We have seen that the distribution of events in the camera is not as homogeneous as expected. The residual inhomogeneity after the re-processing of the data with modified extractor algorithm parameters is estimated to be around 10%.
- **Analysis method:** The parameters adopted in the analysis can be as well a source of systematic uncertainty. The systematic error resulting from the analysis has been investigated by changing the HADRONNESS cut for every energy bin ( $\Delta\epsilon_\gamma \sim 10\%$ ). The mean flux value resulting from 100 realizations is displayed as the grey shaded-region in Figure 8.25. It is difficult to judge the importance of the analysis systematic errors with the statistical errors

that are present in this analysis, but we can conclude they are not the dominant source of systematic error. Different spectral fits of all realizations make changes the spectral slope  $\sim 0.16$ , and to about 25% in the  $\Phi_o$  parameter. This is compatible with the errors estimated from the original fit.

At present telescope situation the total systematic error is roughly estimated to be 35% in the estimation of flux level, and roughly 0.2 in the spectral index [241]. This is a coarse and conservative estimation of the systematic errors that can affect the data. These are the values that today the MAGIC collaboration quotes on all their results, although, a robust analysis to estimate the systematics is certainly needed. The dominant systematic uncertainties are the atmospheric model used in the MC simulations (15%), camera (trigger) inefficiency (10%), and absolute light conversion (calibration) (10%) error.

## 8.14 Flux stability: light-curve

The flux stability has been studied for energies above 1 TeV. For the analysis of time variability, the sample is divided into 13 sub-samples, taking every observation night as an un-separate block, resulting in time intervals for the different bins of about 1 to 1.5 hours, approximately.

For energies above 1 TeV, the mean effective area (for an spectral index of 2.0) is

$$A_{eff}^{aftercuts}(E > 1TeV) = (2.14 \pm 0.02) \cdot 10^9 cm^2 \quad (8.11)$$

with  $\epsilon_\gamma \sim 0.46$  and  $\kappa = 0.95 \pm 0.01$ .

Figure 8.26 shows the integral flux above 1 TeV and Table 8.14 shows all relevant parameters of each of the considered time bins<sup>13</sup>. Within the statistical errors, we obtain a constant flux ( $\chi^2/NDF = 9.1/12$ ) of

$$F(> 1TeV)_{MAGIC} = (1.8 \pm 0.3_{stat} \pm 0.6_{syst}) \cdot 10^{-12} ph cm^{-2} s^{-1} \quad (8.12)$$

The flux level is consistent to a steady emission within errors and within 1 hour time-scales considered here (see Figure 8.26). This is consistent with the results published by the HESS collaboration, in which no indication for flux variability is found in a two year time-span:

$$F(> 1TeV)_{HESS} = (1.84 \pm 0.10_{stat} \pm 0.30_{syst}) \cdot 10^{-12} ph cm^{-2} s^{-1} \quad (8.13)$$

## 8.15 DISP Analysis: location and possible extension of the GC emission

For each event, the arrival direction of the primary in sky coordinates can be estimated by means of the DISP method. To perform an unbiased DISP analysis, only source independent image parameters are considered in the RF training (RFDisp). In addition, to evaluate the energy of the primary we have made use of the source-dependent DIST parameter. To be consistent, no cut in energy will be applied in the DISP-analysis, neither the quality DIST cuts. Only a SIZE cut  $> 300$  phe (that corresponds roughly to an energy threshold of  $\sim 1$  TeV), HADRONNESS  $< 0.125$ , and the so-called spark-cut are applied.

For ON and OFF data, the DISP positions event by event are evaluated. As MAGIC is equipped with an ALT/AZ mount, the DISP positions have to be properly de-rotated and the results given

---

<sup>13</sup>We note that all OFF data is used for every bin, and this could result in some correlation between the different time bins.

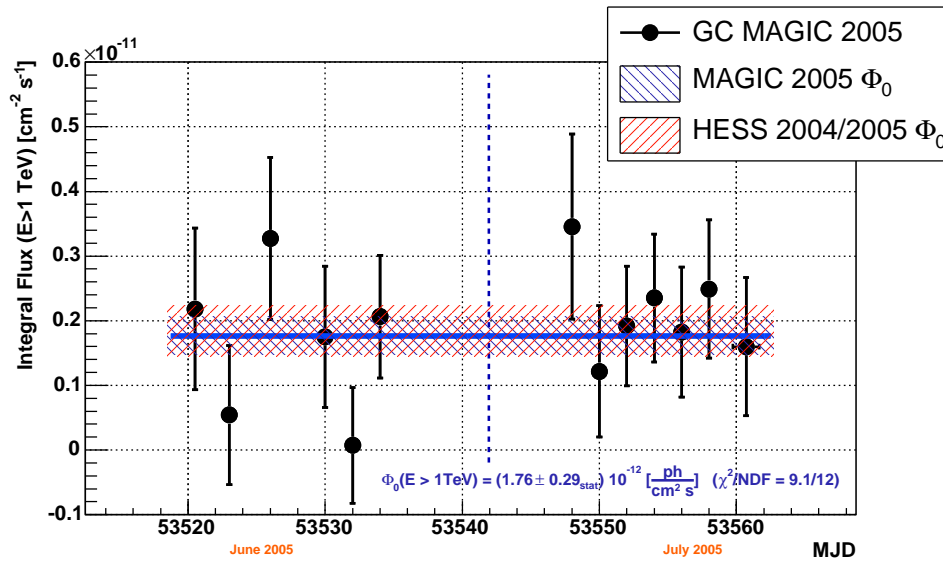


Figure 8.26: Light-curve: Reconstructed integral VHE gamma-ray flux above 1 TeV as a function of time. Within errors ( $1\sigma$ ) the data are consistent with a steady emission.

in a reference time. The rotation angles used for the ON sample are taken as the reference rotation angles for the OFF data (to reduce the systematics influenced by camera inhomogeneities) and every DISP position is folded with a two-dimensional Gaussian with a standard deviation of  $0.075^\circ$ . The folding of the skymap serves to increase the signal-to-noise ratio by smoothing out statistical fluctuations. However, it somewhat degrades the spatial resolution, much more if the  $\sigma_{folding}$  is close to the MAGIC PSF  $\sigma_{PSF} \sim 0.10^\circ \pm 0.01^\circ$ . The excess skymap is evaluated with similar procedure that the one used for the ALPHA-plot: from the  $\theta^2$ -plot, the normalization factor  $\Gamma$  is evaluated in the region in which no signal is expected (i.e. in the region located between  $0.45^\circ$  and  $0.7^\circ$  from camera center), and the excess map is obtained from the ON- $\Gamma$ ·OFF subtraction in celestial coordinates. Determining the excess extension from a fit to the folded (smoothed) skymap needs to subtract the folding sigma in quadrature and compare what it is expected from the MAGIC  $\sigma_{PSF}$  (subtracting the PSF in quadrature from the resulting value would then be used to estimate possible source extension).

Figure 8.27 shows the excess events (a.u.) resulting from the DISP-analysis in celestial coordinates, for the data with  $Az < 180^\circ$ , that corresponds to the subset that is not affected by the culmination mispointing effect. No correction of the mispointing is done, and this is the most conservative skymap that can be obtained, as no 'important' mispointing is present<sup>14</sup>. The maximum excess bin is located at (RA,Dec) = ( $17^h 45^m 40^s$ ,  $-28^\circ 59' 41''$ ). Compared to what is expected from a point-like source emission (2d-Gaussian,  $\sigma_{PSF} \sim 0.1^\circ$  for SIZE > 300 phe and large ZA -  $\sigma_{PSF} \sim 0.125^\circ$  when folded), the excess emission is compatible with a point source but with small but significant elongation in the direction of the galactic plane. This elongation may result from: a) a systematic error on the DISP method, b) residual telescope mispointing or c) the emission is in fact extended. We will come back to these points in the next lines. The results from the uncorrelated and correlated Gaussian fit to the excess signal are shown in the Figure. The fit errors are typically  $\Delta RA \sim \Delta Dec \sim 15''$  and  $\Delta\sigma \sim 0.01^\circ$  for all GC skymaps produced so far.

Adding the resulting statistics to the skymaps, mispointing corrections must be applied. The

<sup>14</sup>The data is only affected by the drive system pointing accuracy.



atic error of the mispointing correction procedure and the present systematic telescope pointing uncertainty is estimated to be roughly of about  $3'^{15}$ .

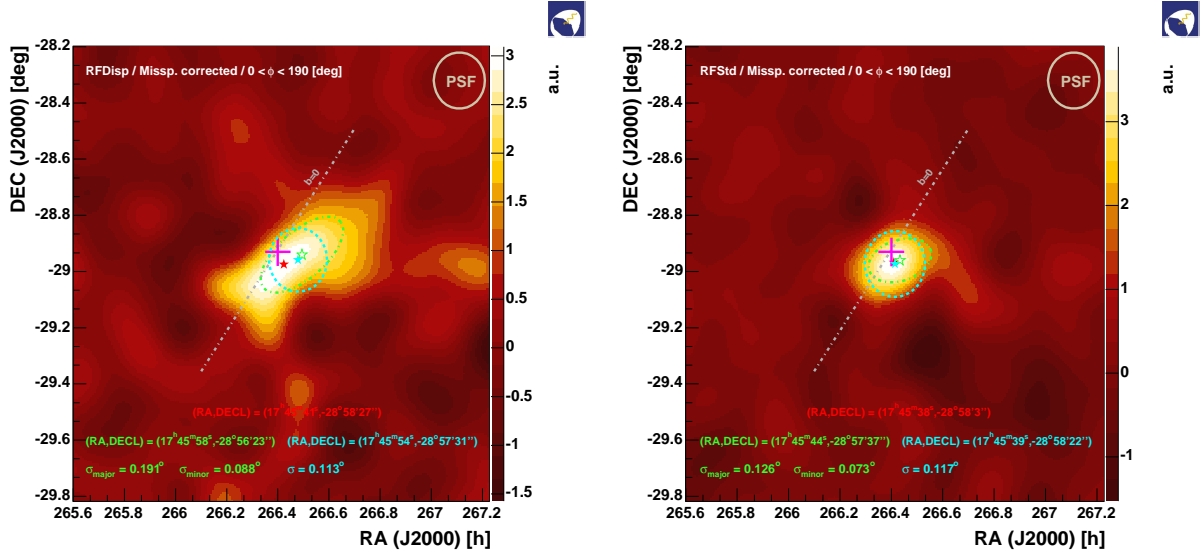


Figure 8.28: Smoothed skymaps of  $\gamma$ -ray candidates (background subtracted) in the direction of the GC for SIZE>300 phe (corresponding to an energy threshold of about 1 TeV), and Az<180 degrees. (left) RFDISP RF method applied. (right) RFSTD RF method applied. Overlaid are shown the best fit values for source location: the maximum excess (red), and the location from correlated and uncorrelated Gaussian fits (green and blue, respectively).

From the results, the elongation feature remains with and without mispointing corrections. In order to check for possible systematic uncertainties of the DISP method, the same skymap as shown in Figure 8.28(left) is produced by using the RFSTD Random Forest method, i.e., the  $\gamma/h$  separation method used for the ALPHA-analysis, which is normally used for point-like source analysis that includes source dependant parameters. The result is shown in Figure 8.28(right), in which no significant elongation is seen and emission is compatible to a point source. This is indeed expected: if the elongation excess comes from a real signal, the RFSTD  $\gamma/h$  separation method would treat it partially as background, as it does not fulfill the conditions of a point-source. This is what happens, hence the systematic uncertainties due to the DISP method itself are negligible. In addition, the Crab nebula was analyzed with the use of the two analysis chains, namely RFSTD and RFDISP, resulting in skymaps both compatible with a point-source emission. This evidences that for this low ZA, the residual mispointing were small. This might not be the case for large ZA, but it turns to be unlikely.

The most probable scenario is that the observed emission is indeed compatible with a point-source but with an small faint excess elongated along the galactic plane. With the present telescope mispointing, preliminary corrections, and present excess statistics, this statement has to be considered with caution. This scenario is reinforced by the HESS observations of the GC region, in which a point source is detected nearby the dynamical center of the galaxy and a faint emission is present along the galactic plane. We will come back to these particular HESS results in the Discussion

<sup>15</sup>Taking the Tpoint data (tracking to known stars and recording the position on camera plane with a CCD) it is possible to give an estimate of the systematic tracking uncertainty in the period the GC data was taken. The uncertainty is estimated to be  $3.0' \pm 1.5'$  (T. Bretz, priv. communication).

Chapter.

Summarizing, the excess maximum for the observed emission is located  $2.7' \pm 0.3'_{stat} \pm 2.0'_{syst}$  from Sgr A\* (see Figure 8.28). Although the DISP-method provides a rather good PSF for a single telescope ( $\sim 0.1^\circ$ ), future improvements in the pointing determination are certainly needed.

## Part IV

# The nature of the observed Galactic Center emission

# Chapter 9

## Discussion

Prior to the observations of the GC carried out by MAGIC, several IACTs have reported about VHE  $\gamma$ -rays from the GC region: CANGAROO [242], VERITAS [243], and HESS [239]. All these measurements have shown unresolved differences, in particular the CANGAROO differential energy spectra differs substantially from the one derived by the HESS system of telescopes. The discrepancies between the measured flux spectra could indicate: (a) inter-calibration problems between the different IACTs, or (b) variability of the the source, or (c) that the signal is integrated in different regions.

Before addressing these topics, first we will put into context the results which have been obtained in this Thesis, and right afterwards we will discuss the DM annihilation origin of the detected signal, accompanied by many other explanations of VHE origin of the signal. At the end of the Chapter, we will give a view of the indirect DM searches and which could be the future directions.

### 9.1 Galactic Center VHE emission: observational results

At present date, the published VHE data on the GC region is quite complete: we already have available data coming from 4 different IACTs. Most of this data has been analyzed and published during the last 2 years and a number of interpretations of the signal origin has been provided by several authors.

Almost all these publications have appeared while this Thesis was developed. Here we list the most important results collected so far in the VHE regime in the GC direction, in historical order, to put into context the results obtained in this work:

- **VERITAS [astro-ph/0403422] [243]:** In 2004, Whipple 10m  $\gamma$ -ray telescope reported a marginal detection of TeV  $\gamma$ -rays from the GC. A total of 26 hours of data (1995→2003) results in a total significance of  $3.7\sigma^1$ . The measured excess corresponds to roughly 40% of the integral flux from the Crab Nebula above 2.8 TeV. The 95% confidence region has an angular extent of  $0.25^\circ$ , including the position of Sgr A\* and Sgr A East. The detection is consistent with a point source and shows no evidence for variability. (see Figure 9.1)
- **CANGAROO [astro-ph/0403592] [242]:** The same year, the source was confirmed by the detection of sub-TeV  $\gamma$ -ray emission from the direction of the GC, reported by CANGAROO-II IACT. A statistically significant excess ( $9.8\sigma$ ) above 250 GeV was detected (66h data). The first differential energy spectra of the GC VHE emission was derived, estimated to be 10% of Crab flux at 1 TeV, with a soft spectrum with slope  $-4.6 \pm 0.5$ . The signal centroid is consistent with SgrA\* and consistent with a point-like source.

---

<sup>1</sup>If significance is  $3 < \sigma < 5$ , the detection is considered to be marginal.

- **HESS [astro-ph/0408145] [239]:** At the end of the year 2004, HESS reported the GC VHE detection, coincident within 1' of Sgr A\*. The data consisted of 4.7 h ( $6.1\sigma$ ) with 1 HESS telescope ('June/July 2003' dataset) and 11.8 h ( $9.2\sigma$ ) with 2 HESS telescopes ('July/August 2003' dataset). The energy threshold was typically of 165 GeV (255 GeV for the 'June/July' dataset).

The observed  $\gamma$ -rays exhibit a power-law energy spectrum with a spectral index of  $-2.2 \pm 0.09_{stat} \pm 0.15_{syst}$  and a flux above 165 GeV of  $(1.82 \pm 0.22) \cdot 10^{-7} m^{-2} s^{-1}$ . The measured flux from this dataset differs substantially from results reported previously by the CANGAROO collaboration. The apparent point-like nature of the emission derived from this dataset does not exclude the possibility of non-azimuthally symmetric tails in the emission. The source is consistent to SgrA\* and Sgr A East.

- **MAGIC [astro-ph/0512469] [203]:** At mid-end of 2004, The GC is firmly considered to be a source of VHE  $\gamma$ -rays from VERITAS, CANGAROO and HESS experiments. Triggered by these observations, MAGIC observed about 2h the GC during the commissioning phase (Sept.-Oct. 2004). The analysis of this data was not straight-forward, and the resulting integral flux above 1 TeV was in agreement with HESS results<sup>2</sup>.

In parallel, dedicated MAGIC GC observations were carried out during MAGIC observation cycle-I, in 2005, resulting in a significant detection of the source. A preliminar analysis of the GC data was submitted late 2005 as a letter to ApJ [203]. The differential gamma-ray flux is consistent with a steady, hard-slope power law:  $(2.9 \pm 0.6) \cdot 10^{-12} (E/\text{TeV})^{-2.2 \pm 0.2} \text{ cm}^{-2} \text{ s}^{-1} \text{ TeV}^{-1}$ .

The MAGIC result confirms the existence of a VHE source at the GC, favouring the HESS differential energy spectra measurement. The results indicate a steady source of TeV gamma-rays, point-like, consistent with Sgr A\* and SgrA East.

- **HESS [Nature 2006 - 'Discovery of very-high-energy  $\gamma$ -rays from the Galactic Centre ridge'] [244]:** A more sensitive exposure of the GC region during 2004 revealed a second source nearby the GC: the supernova remnant/pulsar wind nebula G0.9+0.1. Due to the deep observations in the GC region, the HESS Collaboration subtracted these two sources and searched for much fainter emission. Two significant features are apparent after subtraction: extended emission spacially coincident with the unidentified EGRET source 3EG J1744+3011 and emission extending along the Galactic plane for roughly  $2^\circ$ . The latter emission is not only very clearly extended in longitude  $l$ , but also significantly extended in latitude  $b$  (beyond the angular resolution of HESS) with a characteristic root-mean-square (r.m.s.) width of  $0.28^\circ$ , as can be seen in Figure 9.1.

The reconstructed  $\gamma$ -ray spectrum for the region is described by a power law with photon index  $2.29 \pm 0.07_{stat} \pm 0.20_{sys}$ . This  $\gamma$ -ray emission seems to be spacially correlated with a complex of giant molecular clouds in the central 200 parsecs of the Milky Way. The hardness of the  $\gamma$ -ray spectrum and the conditions in those molecular clouds indicate that the cosmic rays giving rise to the  $\gamma$ -rays are likely to be protons and nuclei rather than electrons.

- **HESS 2006 [Phys. Rev. Letters - submitted] [238]:** The GC observations during the 2004 are analysed as a whole (49h, 1863 excess events,  $38\sigma$ ). The analysis reveals a stable point source with an extended asymmetric tail, compatible with SgrA\* and SgrA East. The

---

<sup>2</sup>Although not significant ( $\sigma \sim 3$ ), this result came by mid 2005, with integral flux above 1 TeV of  $(3.0 \pm 1.9) \cdot 10^{-12} \text{ cm}^{-2} \text{ s}^{-1}$  (S. Commichau, October 2005, MAGIC Collaboration meeting).

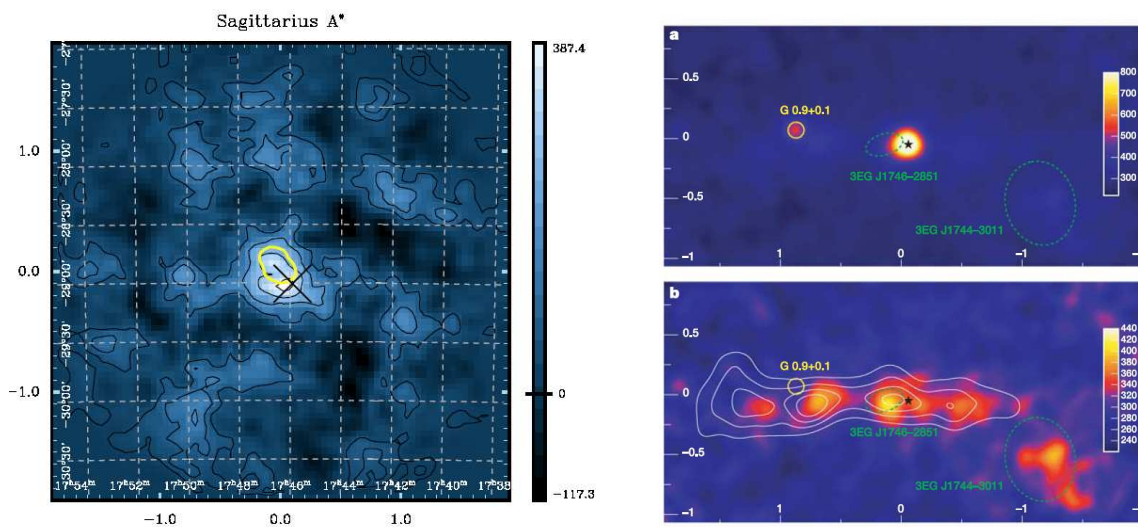


Figure 9.1: (*left*) Excess map as published by Whipple: marginal detection of the GC VHE emission. (*right*) Latest HESS excess maps on the GC direction: (a)  $\gamma$ -ray count map; (b) the same map after subtraction of the two dominant point sources, showing an extended asymmetric band of  $\gamma$ -ray emission. The 95% confidence region for the positions of the two unidentified EGRET sources in the region are shown as dashed green ellipses.

spectra is determined over two decade in energy range (160 GeV – 30 TeV), characterized by a power-law with slope  $2.25 \pm 0.04_{stat} \pm 0.10_{sys}$ .

In that letter, the asymmetric tail (which is associated to the faint emission along the Galactic plane in the HESS nature paper) and the spectra are intended to be explained within a DM scenario<sup>3</sup> (we will come back to this issue later).

- **MAGIC 2006 [This Thesis]:** This Thesis re-analyses the bulk of the MAGIC GC observations carried out so far, trying to correct and make a robust analysis. The results which are obtained in this Thesis are compatible to the previously published but slightly different.

(a) The detected emission shows an extended emission along the galactic plane. (b) The energy spectrum from this analysis is described by a power law  $f_0 E^{-\alpha}$ , where  $f_0 = (2.0 \pm 0.6) \cdot 10^{-12}$ , and  $\alpha = -2.0 \pm 0.2$ . These results slightly differ from the MAGIC ApJ letter, where  $f_0 = (2.9 \pm 0.6) \cdot 10^{-12}$ , and  $\alpha = -2.2 \pm 0.2$ . This substantial differences maybe due to the corrections which are applied to the data. (c) The emission is stable.

The MAGIC results favour the HESS measurements, but unfortunately does not add anything significantly new (apart from solving the flux discrepancies among several IACTs). This was obvious: HESS was designed to map the GC region in the VHE regime, as a key-scientific goal. In this sense, the results presented in this Thesis cannot compete (at the level of detected signal) but complement the HESS results, with an independent measurement. We expected to measure with accuracy the highest possible energies of the energy spectra, although, the observed signal indicates that we overestimated our sensitivity for high ZA observations. This problem is under investigation [246]. About the pointing accuracy, we indicate that some further work should be

<sup>3</sup>First interpretation of the HESS data in a dark matter scenario was previously done by [245].

done in MAGIC to improve it. The source location is a difficult analysis with present MAGIC pointing accuracy.

We want to note that the GC is a suitable source to be observed from the southern hemisphere. The observation and the analysis of the GC data taken with MAGIC can be considered a challenge observation carried by the telescope, as the source is very close to the horizon (high ZA).

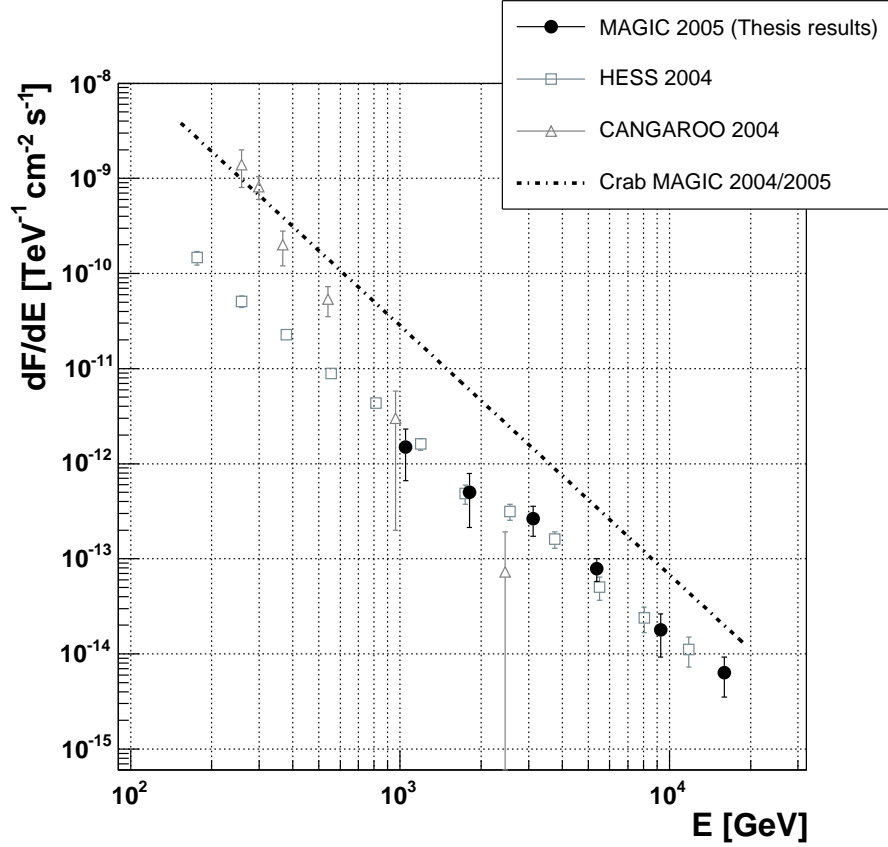


Figure 9.2: Observed VHE  $\gamma$ -ray differential energy spectra derived from different GC observations by IACTs: HESS results as presented in the ICRC 2005 conference, CANGAROO results published in [242], and MAGIC results obtained in this Thesis.

## 9.2 Interpretations of the results in a DM paradigm

For a DM interpretation of the detected signal, both the source morphology and energy spectra impose strong constraints:

- **Source morphology:** The DM halo density profiles that we have discussed follow a power-law  $\rho(r) \sim r^{-\gamma}$ , with  $\gamma$  between 0 for cored profiles and  $\geq 1$  for cuspy profiles. We have seen that either a point source or an extended source is expected, but centered at the Sgr A\* position. The fact that the emission shows an asymmetric and elongated feature along the Galactic plane, discards that it could come from an extended DM halo, which should give a symmetric distribution nearby Sgr A\*. The bulk point-like emission can be interpreted in a DM scenario with a cuspy DM density profile, like the one we have derived by using an

adiabatic contraction of the DM during the Milky Way formation. Assuming a point-source, the HESS results indicate a lower limit  $\alpha > (1.0)1.2$ , at (90)95% C.L (see [245] and [238], respectively). The cuspy adiabatic contracted profile discussed in this Thesis [77] has  $\alpha=1.45$ .

- **The energy spectra:** The energy spectrum provides another crucial test concerning a possible DM origin for the detected VHE emission. The extension of the spectrum beyond 10 TeV requires masses of DM particles which are uncomfortably large for minimal supersymmetric models (MSSM). In addition, the annihilation spectra derived from neutralino annihilations exclusively from pure bosons final state or from from Kaluza-Klein dark matter particle do exhibit a curved spectrum. Such a spectral shape is inconsistent with the measured power-law in two energy decades (165–30 TeV) [238].

The option of mixed  $\tau^+\tau^-b\bar{b}$  final state, viable in some SUSY models, remains open in order to interpret the data, as discussed in [247] (see Figure 9.3). Although, this seems to be highly inconsistent with the most recent HESS accumulated data [238].

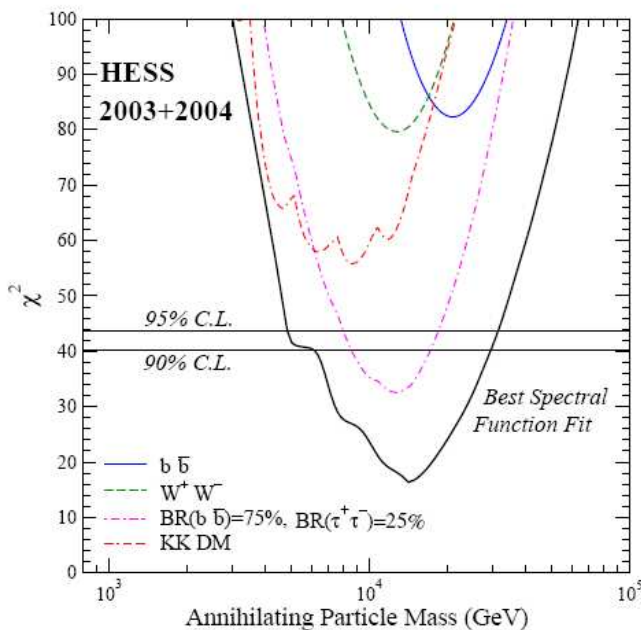


Figure 9.3: The minimal  $\chi^2$  resulting from fits to the 2003+2004 HESS data set (right panel) on the  $\gamma$ -rays flux from the Galactic Center, as a function of the annihilating Dark Matter particle mass, for different final state channels (Figure extracted from [247], check therein for details). The two horizontal lines in each panel indicate the 90% and 95% C.L. exclusion limits corresponding to the set of data under consideration.

On the other hand, if the bulk of the VHE emission has non-DM origin, there is still the possibility of a DM signal hidden under an astrophysical spectrum. Fitting the HESS spectrum as a sum of a power-law with free normalization and index, and a MSSM  $\chi$ -annihilation spectrum yields no significant DM component in the spectrum [238].

Considering the GC discussed cuspy profiles (NFW and adiabatic contracted DM density profiles), exclusion limits on the velocity-weighted annihilation cross section  $\langle\sigma v\rangle$  vs  $m_\chi$  can be derived, if we consider the detected emission to have a non dark matter origin. For both DM halo shapes,  $3\sigma$  HESS and  $1\sigma$  MAGIC exclusion limits are set, from the measured differential energy spectras (see Figure 9.4). Only the HESS measurements exclude a portion of the available MSSM parameter space, if the adiabatic contracted dark matter profile is considered. In addition, the recent exclusion region from CELESTE measurements on M31 are plotted in the Figure [169]. Obviously, the data constrains neutralino masses larger by the minimal energy probed by the experiment.

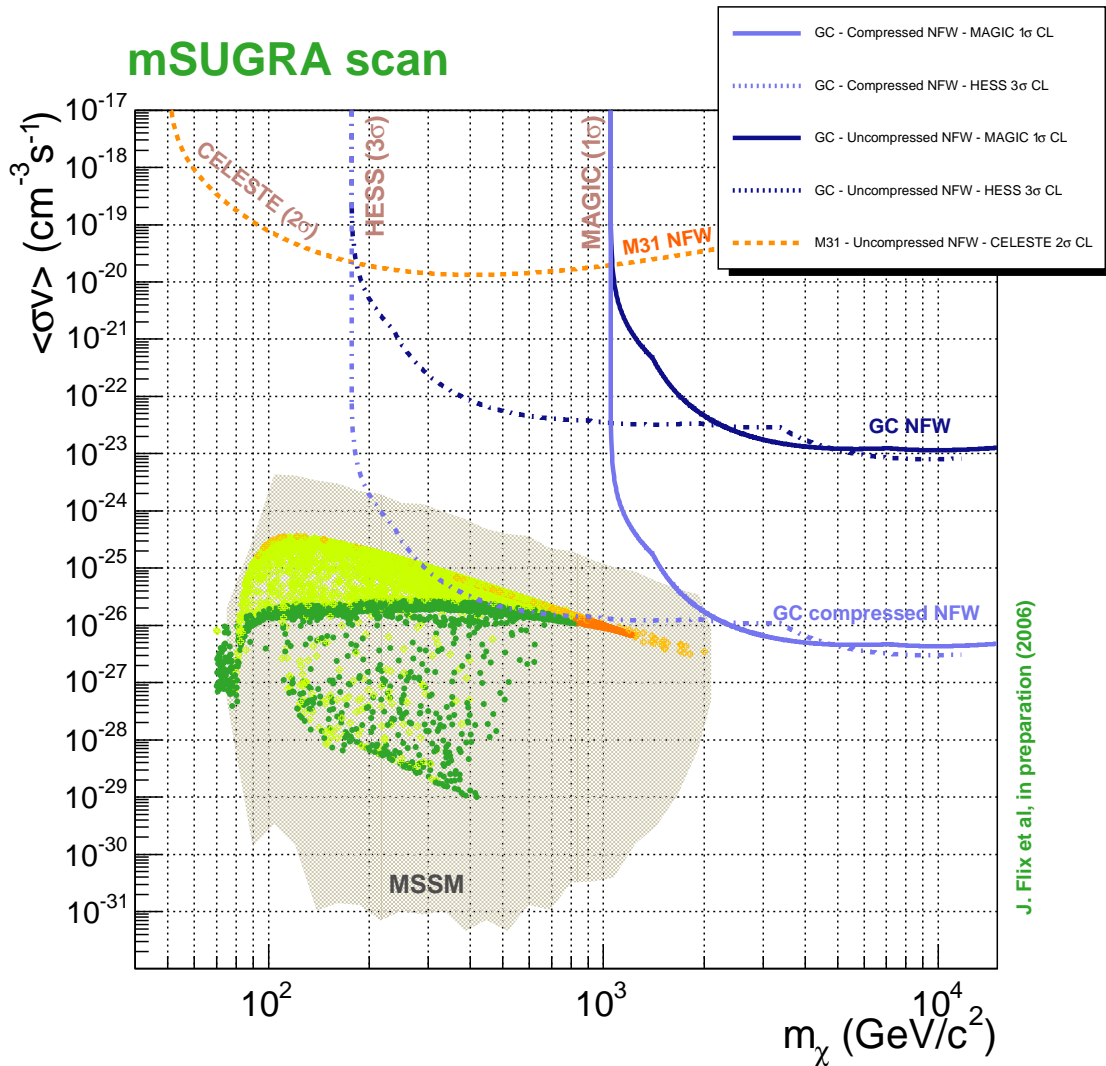


Figure 9.4: Exclusion limits from HESS and MAGIC measurements of the GC VHE emission for the two cuspy profiles discussed in the Thesis ( $3\sigma$  HESS and  $1\sigma$  MAGIC).

In conclusion, the source morphology and energy distribution of TeV  $\gamma$ -rays detected from the direction of the GC impose strong constraints on a possible DM interpretation (in the unlikely case where all the VHE  $\gamma$ -rays are attributed to DM annihilation), requiring a radial DM profile with a DM-halo  $\gamma$  index higher than 1.2 and DM particles with a mass of at least 11 TeV whose

annihilation spectrum mimicks a flat power-law spectrum over two decades in energy, which is very unlike.

### 9.2.1 Other proposed (and most probable) production mechanisms for the VHE emission

Other VHE generation mechanisms in the GC region have been proposed in the literature. The number of publications is huge, but the most relevant are:

- **Interactions in the vicinity of the SMBH:** At least three gamma-radiation scenarios are proposed in [248] that can explain the TeV observations without apparent conflicts with observations of Sgr A\* at lower frequencies. (a) Hadronic models based on photomeson or  $pp$  interactions are considered, as well as an (b) electronic model (CRIC), based on the curvature and synchrotron radiation channels, that allows an economic way of conversion of energy of electrons to  $\gamma$ -rays. (c) In addition to the  $\gamma$ -rays emitted in compact regions in the vicinity of the massive black hole, one should expect also a diffuse (extended) component of radiation associated with interactions of the runaway protons with the surrounding dense interstellar gas. However, these models predict relatively fast variability, while the TeV emission seems to be stable.
- **Non-thermal HE emission from stellar wind shocks in the GC:** The central parsec of the Galaxy contains dozens of massive stars with a cumulative mass loss rate  $\sim 10^3 M_{\odot} \text{yr}^{-1}$ . Shocks among these stellar winds produce the hot plasma that pervades the central part of the galaxy. In [249] it is argued that these stellar wind shocks also efficiently accelerate electrons and protons to relativistic energies. The relativistic electrons inverse Compton scatter the ambient ultraviolet and far infrared radiation field, producing high energy  $\gamma$ -rays with a roughly constant luminosity from  $\sim \text{GeV}$  to  $\sim 10 \text{ TeV}$ . This can account for the TeV source seen at the GC.
- **Capturing stars by the central BH:** In [250] it is suggested that Sgr A\* can become active when a captured star is tidally disrupted and matter is accreted into the BH. As a consequence the galactic BH could be a powerful source of relativistic protons. This scenario might explain the current observed diffuse gamma-rays and the very detailed 511 keV annihilation line of secondary positrons by  $p - p$  collisions of such protons.
- **Stochastic Acceleration in the GC:** In [251], stochastic acceleration of charged particles in a small accretion torus is considered as the mechanism responsible for much of  $mm$  and shorter wavelength GC spectrum. The longer wavelength radiation is produced at larger radii by electrons either diffusing from smaller scales or accelerated *in situ*. An important prediction of this model is the ejection of a significant flux of relativistic protons from a magnetic-field-dominated acceleration site into the wind-shocked medium surrounding the black hole, that accounts for the high-energy emission while retaining consistency with Sgr A\*'s well-studied  $cm$  and  $mm$  characteristics.
- **SNR Sgr A East as the emitter:** Several arguments point the Sgr A East as the natural source of hadrons and the possible VHE emitter. The shell of this SNR is interacting with a very dense medium and the observed VHE spectrum is very similar to other SNR spectra as measured by HESS, and other IACTs. This VHE energy spectra is in good agreement with the expected from decay of neutral pions produced in hadronic collisions of UHE shock accelerated protons by a SNR with the same characteristics as Sgr A East [252].

In addition, some observations suggest that strong magnetic fields may be present in the GC region allowing the acceleration of composite nuclei in Sgr A East beyond the EeV. In [253] it is shown that, if this is case, EeV neutrons should be effectively produced by the photo-disintegration of Ultra High Energy nuclei onto the IR photon background (with temperature  $\sim 40$  K) in which Sgr A East is embedded. Neutrons with such an energy can reach the Earth before decaying and may be detectable under the form of a CR point-like excess in the direction of the GC (this is a recent field called *neutron astronomy*). This signal might be measurable by the AUGER observatory.

### 9.3 Outlook for dark matter searches

Complementary to developments on the *direct detection* technique, the *indirect detection* of annihilation products is still a live-field.

This Thesis has shown the results for the GC, and the difficulties to explain the HE emission in a dark matter scenario, but still the IACTs can collect HE data on other dark matter candidates, like nearby dwarf spheroidal satellites. Very recently, CACTUS has shown  $\gamma$ -ray excess above 50 GeV from Draco, and this has fired preliminary dark matter interpretations of the signal (see [254], for example). MAGIC observations pointing to Draco are needed and expected. Moreover, GLAST will be launched in 2007 and it would bring light into this dark matter scenario in which HE photons are expected (see for example [158] for the expectations). In addition, planned future low energy IACTs will also provide valuable measurements (see for example [255], where we discuss the potential of a low energy IACT in indirect dark matter searches).

Concerning neutrinos, the expected neutrino fluxes from the GC might be also detectable by neutrino experiments for about 2 years of data-taking, according to [256] and some models.

Studying the neutralino annihilation phenomenology is complex and requires to account and fit the several product expectations with the available data. Very recently, de Boer et al. [257] have proposed an halo model to explain the excess of diffuse galactic  $\gamma$ -rays observed by the EGRET experiment. Any model based on dark matter annihilation into quark jets, such as the supersymmetric model proposed by de Boer et al., inevitably also predicts a primary flux of antiprotons from the same jets. Bergstrom et al [258] argue that since propagation of the antiprotons in the unconventional, disk-dominated type of halo model used by de Boer et al. is strongly constrained by the measured ratio of boron to carbon nuclei in cosmic rays, and find that this model is excluded by a wide margin from the measured flux of antiprotons.

Further and more complete studies and measurements will come and the dark matter scenario which has been discussed in this Thesis will be more constrained.



## Chapter 10

# Concluding Remarks

The study herein presented is intended to evaluate the possibility of the detection of  $\gamma$ -rays from neutralino annihilations in high dense dark matter regions with new generation of  $\gamma$ -ray detectors, in particular with MAGIC, both from a theoretical and an experimental point of view.

After a phenomenological evaluation of the most brilliant objects in  $\gamma$ -rays from neutralino annihilations, the center of the Milky Way is considered as the prime candidate. At the time of proposing the observation to the *telescope's time allocation committee*, the Galactic Center (GC) was reported by several IACTs to exhibit VHE  $\gamma$ -ray emission. Dedicated observations of the GC region were carried out in 2005 with MAGIC. The observations were taken during the first year of telescope regular observations.

The bulk of data analyzed in this Thesis consists of a dataset of 17h useful data, yielding a positive detection of VHE radiation from the GC, with significant emission ( $6.5\sigma$ ,  $\sim 330$   $\gamma$ -ray candidates). The observation and the analysis of the GC data taken with MAGIC can be considered a challenge observation, as the source is faint (10% of Crab flux at 1 TeV) and very close to the horizon (high ZA).

The MAGIC observations confirm the VHE  $\gamma$ -ray source at the GC. Prior to the observations carried out by MAGIC, several IACTs have reported VHE  $\gamma$ -rays from this region: CANGAROO, VERITAS, and HESS. All these measurements have shown unresolved differences, in particular the CANGAROO differential energy spectra differs substantially from the one derived by the HESS system of telescopes. The flux derived in this Thesis is compatible with the measurement of the HESS system of telescopes, within errors. The VHE  $\gamma$ -ray emission does not show any significant time variability; our measurement rather affirms a steady emission of  $\gamma$ -rays from the GC region. The excess is point-like source, with an faint extended feature along galactic plane, and the location is spatially consistent with SgrA\* as well as SgrA East.

The HESS results from the GC direction are quite more complete and sensitive than those derived with the MAGIC data analyzed in this Thesis. This was expected, if we think that the major scientific goal of the HESS system of telescopes was to perform a deep scan of the GC region. A sensitive exposure of the GC region with HESS revealed a second source nearby the GC, the supernova remnant/pulsar wind nebula G0.9+0.1, and in particular a much fainter extended emission, spatially coincident with the unidentified EGRET source 3EG J1744+3011 and extending along the Galactic plane for roughly  $2^\circ$ .

The morphology and energy spectra are crucial for the dark matter interpretation of the signal as neutralino self-annihilations. The morphology of the GC source at VHE excludes the possibility of non-cuspy dark matter halo profiles: if dark matter is present in the Galactic Center, and 'shines' in the VHE regime, its distribution has to be cusped at the center. This result is consistent with our results of detailed Milky Way dark matter models, developed in this Thesis, accounting for the effect of the baryons on the dark matter particles in the central galaxy region. Assuming a

point-like source, the HESS results indicate a lower limit  $\alpha > 1.2$ , at 95% CL, for DM density profiles as  $\rho^{-\alpha}$ .

The measured energy spectrum provides another crucial test concerning a possible DM origin for the detected VHE emission. Unfortunately, the extension of the spectrum beyond 10 TeV requires masses of DM particles which are uncomfortably large for minimal supersymmetric models (MSSM). In addition, the annihilation spectra derived from neutralino annihilations exhibit a curved spectrum. Such a spectral shape is inconsistent with the measured power-law in two-energy decades (165–30 TeV).

The detected signal considered as a whole does not fit within the dark matter scenario exposed in this Thesis. Considering all bounds from measurements (morphology and spectra), exclusion regions in the SUSY parameter space defined by  $\langle\sigma v\rangle$  and  $m_\chi$  can be derived, regardless of the large uncertainties that exist on the dark matter and neutralino properties. This is the main result from the attempts to detect, in an indirect way, the neutralino particle with observations of VHE radiation from the GC. The adiabatic contraction prescription poses some constraints on the SUSY parameter space.

The nature of the source of the VHE  $\gamma$ -rays has not yet been identified. Future simultaneous observations with the present Čerenkov telescopes, GLAST, and in lower energies will provide much better information on the source localization and variability of emission. This will shed new light on the nature of the high energy processes at the GC. At present, it seems plausible that the VHE radiation could be generated from the SgrA East SNR or even from ongoing processes nearby the super-massive central Black Hole.

In light of the results obtained in this Thesis, we consider the GC not to be a candidate source for further observations with MAGIC-I to set constraints in a DM scenario. We would like to emphasize the interest in devoting deeper observations with the MAGIC telescope of the Draco source, recently reported by the CACTUS detector to exhibit extended VHE emission, at the energy range 50–250 GeV (see [254]). This source cannot be observed with the HESS telescopes, and MAGIC can bring valuable results to the  $\gamma$ -ray community. We consider this to be the natural extension of DM searches with MAGIC-I.

MAGIC-II is expected to be operative in 2007. The new telescope will be provided with a larger trigger area and the outer camera region will be equipped mostly with small pixels. This will increase the sensitivity for high energy showers and reduce the systematics. Maybe with MAGIC-II we can precisely determine the energy spectra of the GC at higher energies (the search for a cut-off in the energy spectrum has important consequences for the signal interpretation).

Keeping faith that a modest contribution to the understanding of  $\gamma$ -ray production from neutralino annihilations in high dense dark matter regions has been made, and hoping that at least this effort will motivate further and more complete studies, this Thesis ends here.

Part V  
Appendix

# Appendix A

## Analysis of the data: Technical details

Date	Excluded Runs	Date	Excluded Runs
30/05/2005	56651 [ON]	31/05/2005	-
02/06/2005	-	05/06/2005	-
07/06/2005	whole night	09/06/2005	-
11/06/2005	58127 [ON]	13/06/2005	58359 [OFF]
15/06/2005	whole night	27/06/2005	-
29/06/2005	59727/28 [OFF]	01/07/2005	-
03/07/2005	-	05/07/2005	60325 [ON]
07/07/2005	-	09/07/2005	60776 [ON] 60768 [OFF]
11/07/2005	-		

Table A.1: Runs which are excluded from the analysis. The individual runs correspond to corrupted runs. Two nights excluded from the analysis are due to bad atmospheric conditions.

Date	$\Delta ZA$ [arc-deg]	$\Delta Az$ [arc-deg]
30/05/2005	-0.0064±0.0005	0.0244±0.0008
31/05/2005	-0.0183±0.0002	0.0303±0.0008
02/06/2005	0.0205±0.0005	0.0196±0.0006
05/06/2005	-0.0024±0.0003	0.0207±0.0005
07/06/2005	-0.0264±0.0006	0.0228±0.0004
09/06/2005	-0.0715±0.0008	0.0473±0.0008
11/06/2005	0.0246±0.0006	0.0432±0.0005
13/06/2005	-0.0158±0.0001	0.0466±0.0009
27/06/2005	0.0379±0.0004	0.0164±0.0008
29/06/2005	0.0340±0.0003	0.0177±0.0005
01/07/2005	0.0316±0.0003	0.0230±0.0004
03/07/2005	0.0431±0.0004	0.0251±0.0004
05/07/2005	0.0290±0.0002	0.0212±0.0005
07/07/2005	0.0313±0.0003	0.0211±0.0005
09/07/2005	-0.0088±0.0003	0.0103±0.0008
11/07/2005	-0.0772±0.0025	0.0108±0.0006

Table A.2: Estimated offsets for  $\Delta ZA$  and  $\Delta Az$ , corresponding to the different GC observation nights.

id.	Exclusion reason	nr. seq.	id.	Exclusion reason	nr. seq.
0	central pixel	32	53	dead	32
54	fluctuating arr. times	2	115	very low signal	17
150	very low signal	2	157	dead	32
160	~dead	30	162	very low signal	30
209	dead	32	211	dead	32
220	~dead	1	239	fluctuating arr. times	25
312	fluctuating gain	32	334	fluctuating arr. times	5
345	dead	32	372	~dead	1
395	no signal	31	420	fluctuating arr. times	26
432	fluctuating arr. times	5	475	~dead	2
485	fluctuating arr. times	2	497	fluctuating arr. times	21
511	fluctuating arr. times	1	525	fluctuating arr. times	1
544	no signal	8	551	fluctuating gain	32
560	blind pixel	32	574	fluctuating gain	9

Table A.3: Excluded pixels for the 32 sequences of ON and OFF GC data analyzed. In red are marked the most frequent excluded pixels. The categories are **dead**: already known dead pixels; **~dead**: Pedestal RMS is 4.5 smaller than the average pedestal RMS; **Fluctuating gains**: fluctuating charge response; **Fluctuating arr. times**: RMS of arrival times is bigger than 1.7 FADC counts. **Very low signal**: mean reconstructed charge is smaller than half the mean charge average of the camera; **No signal**: mean reconstructed signal of the calibration light pulses is smaller than 3.5 pedestal RMS.

Date	Analyzed Runs	$T_{obs}$ [h]	ZA [deg]
30/05/2005	56647 56648 56649/50 56652/53 56655	0.313	58.67-60.03
31/05/2005	56784 56785 56786/90 56792/95	0.614	57.75-58.45
02/06/2005	57093 57094 57095/99 57101/04 57106/109 57111/112	0.995	57.75-60.42
05/06/2005	57416 57417 57418/22 57424/28 57430/34 57436/37	1.068	57.75-60.18
07/06/2005	57730 57731 57732/35 57737/40 57743/46 57748/51 57753	1.363	57.75-59.34
09/06/2005	57885 57886 57887/902	1.126	57.75-58.57
11/06/2005	58115 58116 58117/26 58128/37	1.548	57.75-59.88
13/06/2005	58361 58362 58363/80	1.215	57.75-59.41
27/06/2005	59631 59632 59636/41 59643/47	0.865	58.30-61.67
29/06/2005	59731 59732 59733/48	1.207	57.75-58.55
01/07/2005	59859 59860 59861/80	1.722	57.75-59.47
03/07/2005	60058 60059 60060/81	1.375	57.75-60.02
05/07/2005	60307 60308 60309/12 60314/17 60319/22 60324 60326/28 60331/32	1.435	57.75-59.81
07/07/2005	60540 60541 60542/57	1.254	57.75-59.36
09/07/2005	60772 60773 60774/75 60777/84	0.712	57.75-58.18
11/07/2005	61081 61082 61083/87	0.335	57.75-57.94
TOTAL		17.147	57.75-61.67

Table A.4: List of runs corresponding to GC ON data used on this analysis. Pedestal runs and Calibration runs used, as well as the observation time, and zenith angle window, are also indicated.

Date	Analyzed Runs	$T_{obs}$ (h)	ZA
31/05/2005	56774 56775 56776/80 56782/83	0.416	56.61-58.09
02/06/2005	57072 57073 57074/78 57080/84 57086/90 57092	1.005	55.67-58.29
05/06/2005	57438 57439 57440/44 57446/50 57452/56 57458/62 57464/68	1.559	55.61-60.49
07/06/2005	57720 57721 57722/25 57727/29 57754/64	1.353	56.53-60.97
09/06/2005	57872 57873 57875/84 57905/19	1.692	56.21-60.50
11/06/2005	58104 58105 58106/14 58140/47	1.100	56.40-60.57
13/06/2005	58349 58350 58351/58 58360 58383/91	1.503	56.33 - 60.42
15/06/2005	58593 58594 58595/96 58602/04	0.336	56.35-59.65
27/06/2005	59631 59632 59633/35 59648/50	0.426	55.92-61.58
29/06/2005	59724 59725 59726 59729/30 59749/55	0.593	56.04-57.48
01/07/2005	59852 59853 59854/58 59881/84	0.573	56.74-59.63
03/07/2005	60053 60054 60055/57 60082/86	0.586	56.09-59.37
05/07/2005	60301 60302 60303/06 60333/35	0.359	56.01-59.55
07/07/2005	60535 60536 60537/39 60558/64	0.791	55.81-59.04
09/07/2005	60763 60764 60765/67 60769/71 60785/88	0.609	55.91-56.64
11/07/2005	61076 61077 61078/80 61088/91 61094	0.312	55.69-56.05
TOTAL		13.213	55.61-61.58

Table A.5: List of runs corresponding to GC OFF data used on this analysis. Pedestal runs and Calibration runs used, as well as the observation time, and zenith angle window, are also indicated.

## Appendix B

# Analysis of the data: Differential Energy Spectrum $\alpha$ -plots

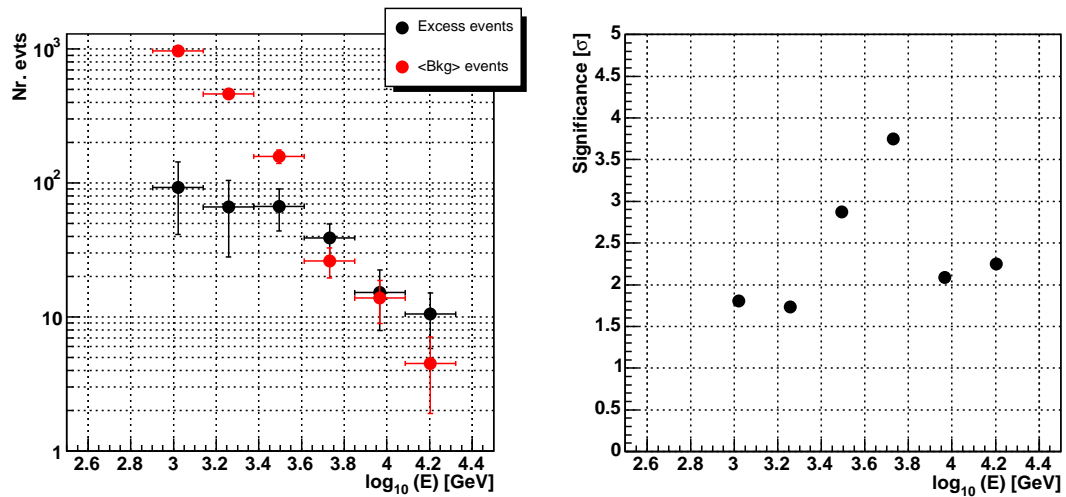


Figure B.1: (left) Excess and background events in the signal region for the different energy bins considered to evaluate the GC differential energy spectrum. (right) Significance per energy bin.

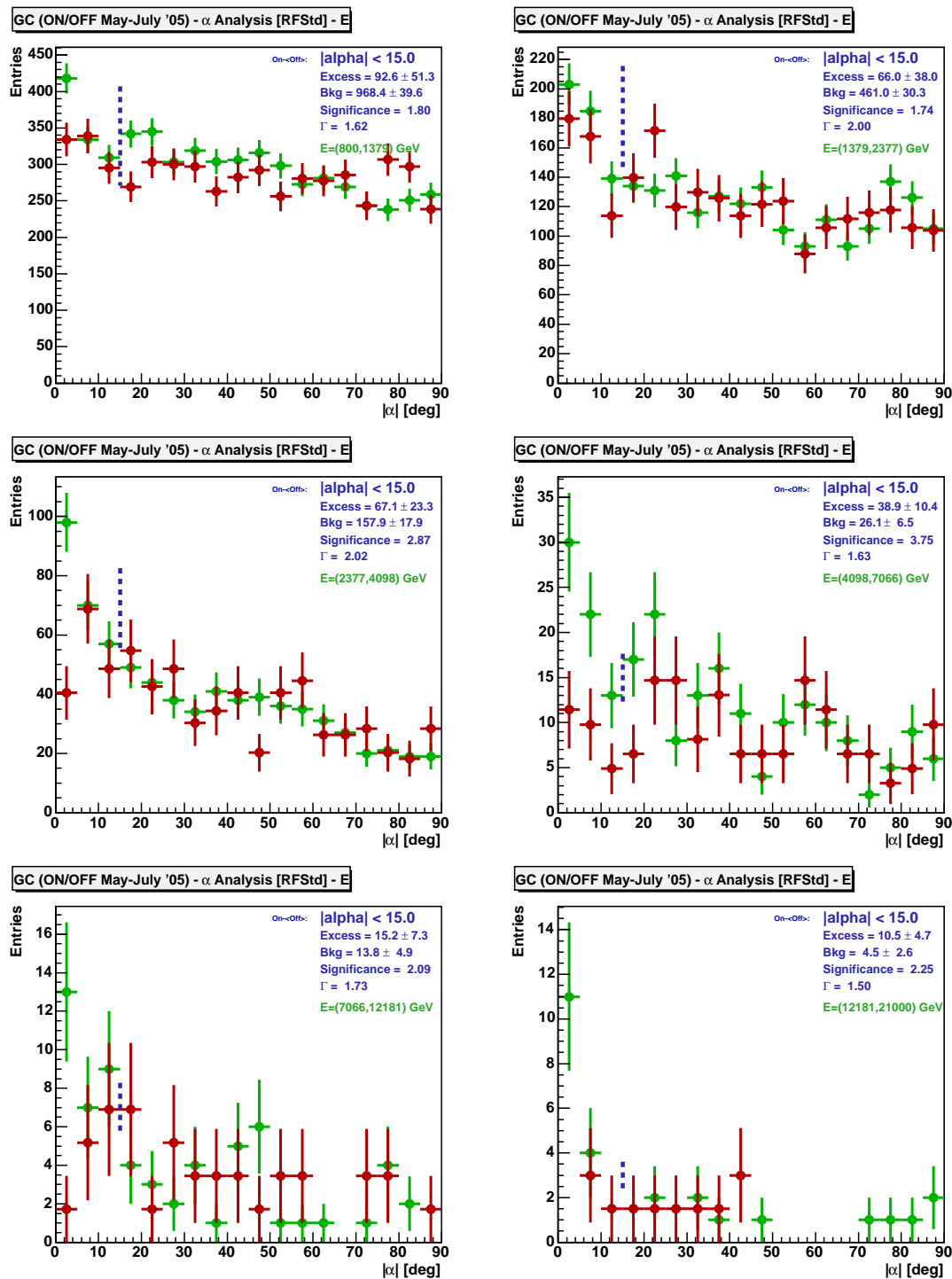


Figure B.2: ALPHA-plots for the different energy bins considered to evaluate the GC differential energy spectrum.

## Appendix C

# The Camera and Calibration Control: Technical details

Some technical details on the Camera and Calibration Control can be found in J. Cortina, J. Flix et al [210]. Some of the items showed here, complement the information that can be found there.

The most important *commands or actions* that the Camera and Calibration control (*La Guagua*) sends to each Subsystem Driver are listed in Tables C.2 and C.3. The available actions from the Central Control are listed in C.1.

The common fields for different *subsystem reports* are:

**DC-REPORT 5 2005 06 07 01 47 50 487 +00 +00 -Subsystem Contents-**

i.e, a subsystem identifier, status, date and time stamps and two control digits: one the report about transmission problems and the second to report about subsystem malfunction.

CeCo-Guagua command	Brief description
HV002:123,1200:124,1240:...	Set one HV channel (HV001) or various HV channels (i.e, HV024)
HVALL:0000:1203:...	Set all 577 HV channels
HVFIL:HVfile.txt	Set all 577 HV according to a file
STOPR	Stop HV ramping
LDCLS	Close Lid
LDOPN	Open Lid
LDSTP	Stop Lid movement
AMCON or AMCOFF	Switch ON/OFF AMC LEDs
LEDON or LEDOFF	Switch ON/OFF CaOs LEDs
DCSTA: RunNumber + ProjectName	Start a new anode DC currents run (save to file)
DCSTO	Stop a DC run
STACA:CalibrationScriptFile.txt	Start calibration sequence (of given type or pedestal)
STOCA	stop calibration sequence

Table C.1: Description of commands sent by the CeCo to “Guagua”.

Command	Brief Description
Camera Low Voltage	
LVOFF	Switch off low voltage
LVON!	Switch on low voltage
CPOFF	Switch off central pixel low voltage
CPON!	Switch on central pixel low voltage
Camera HV Settings (HV in V units)	
HV00N:123,1200:...	Send a HV value list of N elements: first number refers to each pixel and second refers to its HV value
HVALL:0000,1123,...	Send a HV value for all pixels in ascendent order
Camera HV Power Supply	
PSON!	Switch on power supply
SETHV	Set HV power supply to a given value (with ramping)
SETCL	Set HV limit current
STOPR	Stop HV ramping
PSOFF	Switch off power supply
Camera Cooling System (RH in % and T in degrees)	
STCAM	Set reference stabilization camera temperature with its variation
SETRH	Set humidity values to send and stop the flow of hot water to camera
STWAT	Set temperature values to switch on and off the water tank heater
STTFN	Set temperature values to switch on and off camera fans
STHFN	Set humidity values to switch on and off camera fans
COOFF	Force all cooling elements to be off (refrigerator, fans, resistor, pump and valve)
COLIB	Liberate all cooling system elements so that PLC control them
FNOFF	Force fans to switch off
FNON!	Force fans to switch on
FNLIB	Liberate fans so that PLC can control them
WTWLL	Set safety limits (maximum and minimum) for wall temperature
WTOPL	Set safety limits for optical transmitters temperature
WTCEN	Set safety limits for camera center temperature
WTWAT	Set safety limits for water tank temperature
WHWLL	Set safety limits for wall humidity
WHCEN	Set safety limits for camera center humidity
LIMTW	Set maximum water tank temperature for refrigerator malfunction alarm
Camera LIDs	
LDOPN	Open camera lids
LDCLS	Close camera lids
LDSTP	Stop lid movement

Table C.2: Description of commands sent by the “Guagua” to each subsystem (Part I).

Command	Brief Description
Calibration BOX	
SETPL	Set pulsed light pattern: 16 bits
SETCL	Set continuous light intensity to a given value
SETCO	Select color of the continuous light: 4-bits required (red, amber, green-blue and UV; 0000 for no-color)
HVON!	Switch on calibration HV
HVOFF	Switch off calibration HV
PDON!	Switch on pin diode
PDOFF	Switch off pin diode
Calibration I/O Card	
SETPF	Set pulse frequency
SETTF	Set train frequency
SETNP	Set number of pulses within a train
SETDL	Set delay in <i>ns</i>
SETVT	Set veto. 4-bits required: Pedestal, calibration, pin diode and laser
SETDM:1	Set values of digital module 1: 16-bits for module pattern
SETDM:2	Set values of digital module 2: 4-bits continuous light + 8-bits intensity + 4-bits veto
START	Start calibration run
STOPT	Stop calibration run
Auxiliary Systems	
CAOFF	Switch off the calibration LV power supply
CAON!	Switch on the calibration LV power supply
LEDOF	Switch CaOs LEDs off
LEDON	Switch CaOs LEDs on
AMCOF	Switch active mirror control LEDs off
AMCON	Switch active mirror control LEDs on
Common commands	
SETAR	Set periodic reports time (in <i>ms</i> )
SHUTD	Shutdown a subsystem

Table C.3: Description of commands sent by the “Guagua” to each subsystem (Part II).

GUAGUA Directories	
CaCo/cam_GUI.vi	La Guagua main Labview program to be executed
CaCo/calib/	Main calibration control Labview routines
CaCo/Calibration_Scripts/	All available calibration ASCII shell scripts
CaCo/comm/	TCP/IP daemons and all pipes
CaCo/config/	All configuration files. The most important is the main CaCo.conf configuration ASCII file
CaCo/data/	Temporal folder in which DC data is stored prior transfer to storage PC
CaCo/drivers/	All C/C++ subsystem drivers
CaCo/logbooks/	All camera and subsystem drivers logbooks
CaCo/macros/	ROOT macros to check performance of the system
CaCo/scripts/	Relevant scripts to launch cooling during daytime, data transfer, etc...
CaCo/subVis/	Main Camera control Labview routines

Table C.4: Main ‘Guagua’ directories and files.



## Appendix D

# The analysis techniques applied to the Crab Nebula

During and shortly after the telescope commissioning the MAGIC collaboration observed the Crab nebula. Its steady flux of gamma rays provides good means for studying the telescope performance. Moreover, the Crab nebula is a good source to test the analysis techniques which have been exposed in this chapter.

Here we present the results obtained from these Crab nebula observations, which were presented in the ICRC 2005 conference. We emphasize the success of the new analysis methods used to extract the Crab signals. In addition, by the time of this study, lot of discussion was going on in the collaboration trying to understand the limitations of the  $\gamma/h$  in the sub-100 GeV domain, and trying to find new ideas. The analysis that was presented avoided to focus on this region.

### D.1 The Crab Nebula

The Crab nebula is the remnant of a supernova explosion that occurred in 1054. In 1989, VHE emission was reported by the Whipple collaboration. It was the first source detected at TeV energies employing the IACT technique and it exhibits a stable and strong  $\gamma$ -emission. It therefore is frequently used as the standard candle in VHE  $\gamma$ -astronomy. The Crab nebula has been observed extensively in the past over a wide range of wavelengths, covering the radio, optical and X-ray bands, as well as high-energy regions up to nearly 100 TeV. Nevertheless, quite some new physics results are expected in the VHE domain, namely the spectrum showing an Inverse Compton (IC) peak close to 100 GeV, a cut-off of the pulsed  $\gamma$ -emission somewhere between 10 and 100 GeV, and the verification of true flux stability down to the percent level.

Currently the VHE-emission is very well described by electron acceleration followed by the IC scattering of photons generated by synchrotron radiation (SSC model). Probing the presence/absence of a small contribution of VHE  $\gamma$ s produced in hadronic interactions is a challenge for experimenters.

### D.2 Data Analysis

#### Data Sample

The data analyzed were taken during September and October 2004 and in January 2005. A total of 2.8M events in 2004 and 4.5M events from the 2005 observations were used. The analysis is

restricted to a sample of low zenith angle observations ( $ZA < 30$ ). Quality checks were performed in order to reject runs with unstable trigger rates due to variable atmospheric conditions. The overall observation time of the sample analyzed corresponds to 13 hours on-source.

## Data Analysis

The most relevant analysis steps were:

- **Calibration:** conversion factor from ADC counts to photoelectrons using the excess noise factor method.
- **Image cleaning:** *absolute cleaning* (10,5) algorithm was applied to the shower images to remove the contribution of the NSB.
- **$\gamma/h$  separation:** based on the Random Forest (RF) method, using MC  $\gamma$ s and real hadronic background data as training samples. The Hillas parameters SIZE, DIST, WIDTH, LENGTH, CONC and ASYM used in the training.
- **Energy estimation:** we trained RFs for each energy bin considered in the analysis using  $\log(\text{SIZE})$ , DIST, WIDTH, LENGTH,  $\log(\text{SIZE}/(\text{LENGTH} \times \text{WIDTH}))$ , CONC, LEAKAGE, and ZA.
- **Flux calculation:** application of the spill-over corrections.
- **Optimizing the DISP method:** optimization of the DISP method parameters with the train MC sample.

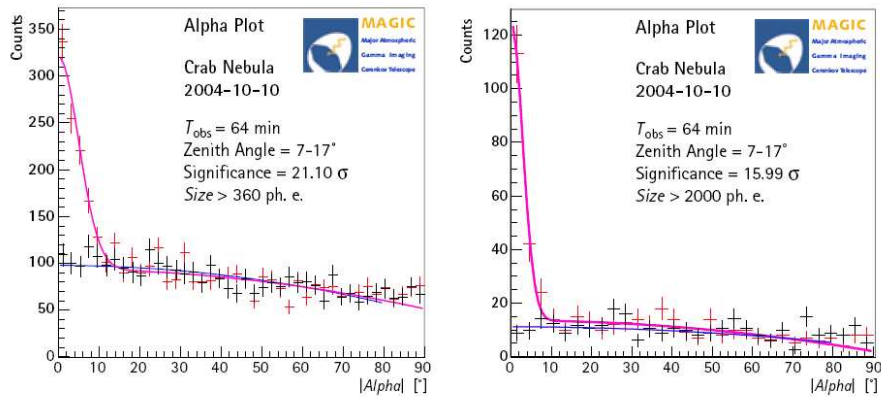


Figure D.1: ALPHA distribution for 64 minutes of Crab Nebula data.

## Results

The most relevant results obtained:

- **$\alpha$ -plots:** Figure D.2 shows two Alpha distributions for the data subsample of October 10, 2004, one above a SIZE of 360 photoelectrons (ph.e.), yielding a signal of  $20.4\sigma/\sqrt{h}$ , and a second distribution above a SIZE of 2000 ph.e. Note that the latter  $\gamma$ -sample is nearly background free.

- **DISP sky-map:** in Figure 7.7 we have already shown an excess sky map of the corresponding sky region obtained with the DISP method.
- **Energy resolution:**  $\sim 25\%$  at energies in the energy range from 100 GeV to 4 TeV.
- **Flux stability:** Figure D.2 shows the integral flux of the Crab nebula above 200 GeV for the individual days of this analysis. The result is compatible to a steady emission.
- **Flux spectra:** Figure D.3 shows the differential energy spectra of the Crab nebula. A power-law between 300 and 3000 GeV yielded a spectral index of  $2.58 \pm 0.16$ . In agreement with expectance, the measured data points below 300 GeV lie below the extrapolated power law.

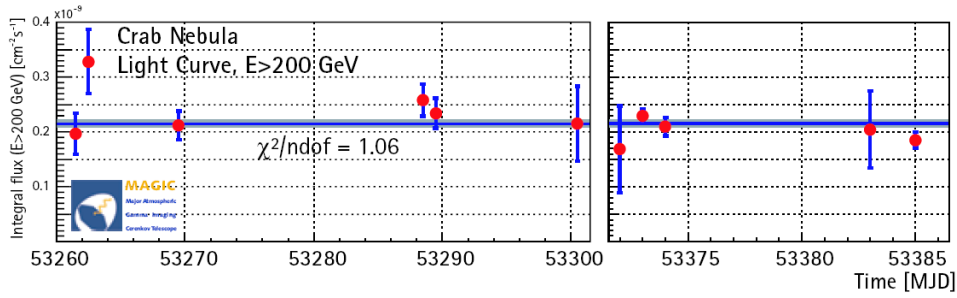


Figure D.2: Integral flux of the Crab Nebula for all days considered in the analysis. A fit assuming a constant flux gave a  $\chi^2/\text{ndof} = 1.06$ .

The Crab nebula was considered as the first target of observation since mid 2004, the period in which the MAGIC telescope started taking regular data. The source was observed to test the gross performance of the telescope and analysis techniques. The outcome of the analysis between 100 and 4000 GeV confirmed expectations and gave good agreement with observations made by other IACTs.

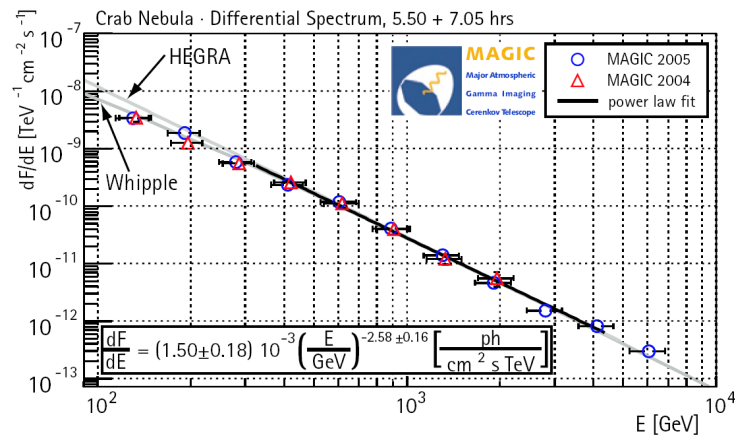


Figure D.3: Observed differential crab spectra for the 2004 and 2005 datasets. A power-law fit to the combined data is shown (from 300 GeV to 4 TeV), as well as the fit to the HEGRA data and the parameterization of WHIPPLE data.



# Appendix E

## The Hillas formalism

After calibration, pedestal subtraction and rejection of pixels only affected by the NSB, the resulting image of the EAS contain valuable information about the shower development, and hence can be used to estimate the energy, the direction and the type of primary particle responsible for the camera illumination. The characterization of an image is based on the use of the Hillas parameters [179].

Hillas image shower parameterization is based on the first, second and third moments of the two-dimensional distribution of the signal along the image. For the moment calculation, the position of each pixel included in the image is weighted with the fraction of the image signal content in it,

$$\omega_i = \frac{N_i}{\sum_k N_k}.$$

The Hillas parameters are calculated as:

- *Notation*

$(x_i, y_i)$ : coordinates of the pixel  $i$  in the original camera system.

$(x_0, y_0)$ : reference point in the camera (usually defined by the source position).

$N_i$ : number of photons measured in the pixel  $i$ .

$w_i$ : weight for the pixel  $i$ .

- *Definition of the moments of the signal distribution in the camera*

$$w_i = \frac{N_i}{\sum_k N_k} \tag{E.1}$$

$$\bar{x} = \sum_i w_i \cdot x_i \tag{E.2}$$

$$\bar{y} = \sum_i w_i \cdot y_i \tag{E.3}$$

$$\overline{x^2} = \sum_i w_i \cdot x_i^2 \tag{E.4}$$

$$\overline{y^2} = \sum_i w_i \cdot y_i^2 \tag{E.5}$$

$$\overline{xy} = \sum_i w_i \cdot x_i \cdot y_i \tag{E.6}$$

- *Definition of the correlations in the signal distribution in the camera*

$$c_{xx} = \overline{(x - \bar{x})^2} = \overline{x^2} - \bar{x}^2 \quad (\text{E.7})$$

$$c_{yy} = \overline{(y - \bar{y})^2} = \overline{y^2} - \bar{y}^2 \quad (\text{E.8})$$

$$c_{xy} = \overline{(x - \bar{x}) \cdot (y - \bar{y})} = \overline{x \cdot y} - \bar{x} \cdot \bar{y} \quad (\text{E.9})$$

- *Definition of basic hillas parameters*

$$SIZE = \sum_k N_k \quad (\text{E.10})$$

$$LENGTH = \sqrt{\frac{c_{xx} + 2a \cdot c_{xy} + a^2 \cdot c_{yy}}{1 + a^2}} \quad (\text{E.11})$$

$$WIDTH = \sqrt{\frac{a^2 \cdot c_{xx} - 2a \cdot c_{xy} + c_{yy}}{1 + a^2}} \quad (\text{E.12})$$

$$DIST = \sqrt{(\bar{x} - x_0)^2 + (\bar{y} - y_0)^2} \quad (\text{E.13})$$

$$ALPHA = \arcsin\left(\frac{|b|}{DIST \cdot \sqrt{1 + a^2}}\right) \quad 0^\circ \leq ALPHA \leq 90^\circ \quad (\text{E.14})$$

where  $a$  and  $b$  are evaluated as

$$a = \tan \delta = \frac{c_{yy} - c_{xx} + \sqrt{(c_{yy} - c_{xx})^2 + 4c_{xy}^2}}{2c_{xy}} \quad (\text{E.15})$$

$$b = \bar{y} - y_0 - a \cdot (\bar{x} - x_0) \quad (\text{E.16})$$

# Bibliography

- [1] E. Lorenz (MAGIC Collab.), *Status of the 17-m MAGIC telescope*, *New Astron. Rev.* **48** (2004) 339.
- [2] J. Einasto, *Dark matter: Early considerations*, (2004), astro-ph/0401341.
- [3] E. A. Baltz, *Dark matter candidates*, *ECONF C040802* (2004) L002, astro-ph/0412170.
- [4] C. Munoz, *Dark matter detection in the light of recent experimental results*, *Int. J. Mod. Phys.* **A19** (2004) 3093, hep-ph/0309346.
- [5] E. Opik, *Astrophys. J.* **55** (1922) 406.
- [6] F. Pease, *Proc. Natl. Acad. Sci.* **4** (1918) 21.
- [7] J. Oort, *Bull. Astr. Inst. Netherlands* **6** (1932) 249.
- [8] K. C. Zekser, *Dark Matter in the Local Galactic Disk*, (2004), astro-ph/0401185.
- [9] G. Gilmore et al., *Ann. Rev. Astron. Astrophys* **27** (1989) 555.
- [10] F. Zwicky, *Helv. Phys. Acta* **6** (1933) 110.
- [11] R. G. Carlberg et al., *The Dynamical Equilibrium of Galaxy Clusters*, (1996), astro-ph/9611204.
- [12] F. W. Rubin, V. and N. Thonnard, *Astrophys. J.* **225** (1978) L107.
- [13] G. R. Blumenthal et al., *Formation of galaxies and large-scale structure with cold dark matter*, *Nature* **311** (1984) 517.
- [14] T. Kuhn, Univ. of Chicago Press, 1970.
- [15] G. A. Mamon and E. L. Lokas, *Confronting LambdaCDM with the optical observations of elliptical galaxies: II. Weighing the dark matter component*, *Mon. Not. Roy. Astron. Soc.* **363** (2005) 705, astro-ph/0405491.
- [16] R. Bottema, *The maximum rotation of a galactic disc*, (1997), astro-ph/9706230.
- [17] W. J. G. de Blok et al., *Mass Density Profiles of LSB Galaxies*, (2001), astro-ph/0103102.
- [18] E. L. Lokas, G. A. Mamon, and F. Prada, *Dark matter distribution in the Draco dwarf from velocity moments*, *Mon. Not. Roy. Astron. Soc.* **363** (2005) 918, astro-ph/0411694.
- [19] L. V. E. Koopmans and T. Treu, *The Structure and Dynamics of Luminous and Dark Matter in the Early-Type Lens Galaxy of 0047-281 at  $z=0.485$* , *Astrophys. J.* **583** (2003) 606, astro-ph/0205281.

- [20] A. C. Fabian and S. W. Allen, *X-rays from Clusters of Galaxies*, (2003), astro-ph/0304020.
- [21] D. J. Sand, T. Treu, and R. S. Ellis, *The dark matter density profile of the lensing cluster MS2137-23: a test of the cold dark matter paradigm*, *Astrophys. J.* **574** (2002) L129, astro-ph/0207048.
- [22] A. D. Lewis, D. A. Buote, and J. T. Stocke, *Chandra Observations of Abell 2029: The Dark Matter Profile at  $<0.01 R_{\text{vir}}$  in an Unusually Relaxed Cluster*, *Astrophys. J.* **586** (2003) 135, astro-ph/0209205.
- [23] N. Dalal and C. R. Keeton, *(Lack of) lensing constraints on cluster dark matter profiles*, (2003), astro-ph/0312072.
- [24] A. Einstein, *The foundation of the general theory of relativity*, *Annalen Phys.* **49** (1916) 769.
- [25] A. Friedman, *Über die Krümmung des Raumes*, *Z. Phys.* **10** (1922) 377.
- [26] E. Hubble, *Distance and Radial Velocity Among Extragalactic Nebulae*, *Proc. Nat. Acad. Sci.* **15** (1929) 168.
- [27] G. Gamow, *Expanding Universe and the Origin of Elements*, *Phys. Rev. Lett.* **81** (1946) 1562.
- [28] A. Penzias and R. Wilson, *A Measurement of Excess Antenna Temperature at 4080 Mc/s*, *Astrophys. J.* **308** (1965) 5.
- [29] G. F. Smoot et al., *Statistics and Topology of the COBE DMR First Year Maps*, (1993), astro-ph/9312031.
- [30] S. M. Carroll, W. H. Press, and E. L. Turner, *The Cosmological constant*, *Ann. Rev. Astron. Astrophys.* **30** (1992) 499.
- [31] C. L. Bennett et al., *First Year Wilkinson Microwave Anisotropy Probe (WMAP) Observations: Preliminary Maps and Basic Results*, *Astrophys. J. Suppl.* **148** (2003) 1, astro-ph/0302207.
- [32] L. M. Krauss and M. S. Turner, *The cosmological constant is back*, *Gen. Rel. Grav.* **27** (1995) 1137, astro-ph/9504003.
- [33] J. Ostriker and P. Steinhardt, *Nature* **377** (1995) 600.
- [34] S. A. Shectman et al., *The Las Campanas Redshift Survey*, *Astrophys. J.* **470** (1996) 172, astro-ph/9604167.
- [35] S. Dodelson et al. (SDSS Collab.), *The three-dimensional power spectrum from angular clustering of galaxies in early SDSS data*, *Astrophys. J.* **572** (2001) 140, astro-ph/0107421.
- [36] G. Efstathiou et al. (2dFGRS Collab.), *Evidence for a non-zero Lambda and a low matter density from a combined analysis of the 2dF Galaxy Redshift Survey and Cosmic Microwave Background Anisotropies*, *Mon. Not. Roy. Astron. Soc.* **330** (2002) L29, astro-ph/0109152.
- [37] S. Weinberg, John Wiley & Sons, 1972.
- [38] A. H. Guth, *The Inflationary Universe: a possible solution to horizon and flatness problem*, *Phys. Rev.* **D23** (1981) 347.

- [39] A. D. Linde, *A new inflationary universe scenario: a possible solution to the horizon, flatness, homogeneity, isotropy and primordial monopole problems*, Phys. Lett. **B108** (1982) 389.
- [40] L. Guzzo, *Large-Scale Structure at the Turn of the Millennium*, (1999), astro-ph/9911115.
- [41] A. G. Sanchez et al., *Cosmological parameters from CMB measurements and the final 2dFGRS power spectrum*, Mon. Not. Roy. Astron. Soc. **366** (2006) 189, astro-ph/0507583.
- [42] Y.-T. Lin and B. D. Wandelt, *A Beginner's Guide to the Theory of CMB Temperature and Polarization Power Spectra in the Line-of-Sight Formalism*, Astropart. Phys. **25** (2006) 151, astro-ph/0409734.
- [43] <http://map.gsfc.nasa.gov>.
- [44] H. V. Peiris et al., *First year Wilkinson Microwave Anisotropy Probe (WMAP) observations: Implications for inflation*, Astrophys. J. Suppl. **148** (2003) 213, astro-ph/0302225.
- [45] K. A. Olive, *Dark matter*, (2003), astro-ph/0301505.
- [46] S. Perlmutter et al., *Measurements of the Cosmological Parameters Omega and Lambda from the First 7 Supernovae at  $z \leq 0.35$* , Astrophys. J. **483** (1997) 565, astro-ph/9608192.
- [47] A. G. Riess et al. (Supernova Search Team Collab.), *Observational Evidence from Supernovae for an Accelerating Universe and a Cosmological Constant*, Astron. J. **116** (1998) 1009, astro-ph/9805201.
- [48] S. Perlmutter, M. S. Turner, and M. J. White, *Constraining dark energy with SNe Ia and large-scale structure*, Phys. Rev. Lett. **83** (1999) 670, astro-ph/9901052.
- [49] U. Seljak et al., *SDSS galaxy bias from halo mass-bias relation and its cosmological implications*, Phys. Rev. **D71** (2005) 043511, astro-ph/0406594.
- [50] D. J. Eisenstein et al., *Detection of the Baryon Acoustic Peak in the Large-Scale Correlation Function of SDSS Luminous Red Galaxies*, Astrophys. J. **633** (2005) 560, astro-ph/0501171.
- [51] C. J. MacTavish et al., *Cosmological parameters from the 2003 flight of BOOMERANG*, (2005), astro-ph/0507503.
- [52] J. L. Sievers et al., *Implications of the Cosmic Background Imager Polarization Data*, (2005), astro-ph/0509203.
- [53] A. C. S. Readhead et al., *Extended Mosaic Observations with the Cosmic Background Imager*, Astrophys. J. **609** (2004) 498, astro-ph/0402359.
- [54] C. Dickinson et al., *High sensitivity measurements of the CMB power spectrum with the extended Very Small Array*, Mon. Not. Roy. Astron. Soc. **353** (2004) 732, astro-ph/0402498.
- [55] C.-I. Kuo et al. (ACBAR Collab.), *High Resolution Observations of the CMB Power Spectrum with ACBAR*, Astrophys. J. **600** (2004) 32, astro-ph/0212289.
- [56] N. W. Halverson et al., *DASI First Results: A Measurement of the Cosmic Microwave Background Angular Power Spectrum*, Astrophys. J. **568** (2002) 38, astro-ph/0104489.
- [57] S. Hanany et al., *MAXIMA-1: A Measurement of the Cosmic Microwave Background Anisotropy on angular scales of 10 arcminutes to 5 degrees*, Astrophys. J. **545** (2000) L5, astro-ph/0005123.

- [58] M. Tegmark et al. (SDSS Collab.), *The 3D power spectrum of galaxies from the SDSS*, *Astrophys. J.* **606** (2004) 702, astro-ph/0310725.
- [59] S. Cole et al. (The 2dFGRS Collab.), *The 2dF Galaxy Redshift Survey: Power-spectrum analysis of the final dataset and cosmological implications*, *Mon. Not. Roy. Astron. Soc.* **362** (2005) 505, astro-ph/0501174.
- [60] M. Roos, *Consensus values for cosmological parameters*, (2005), astro-ph/0509089.
- [61] W. Freedman, *Astrophys. J.* **533** (2001) 47.
- [62] A. G. Riess et al., *Cepheid Calibrations from the Hubble Space Telescope of the Luminosity of Two Recent Type Ia Supernovae and a Re-determination of the Hubble Constant*, *Astrophys. J.* **627** (2005) 579, astro-ph/0503159.
- [63] W. L. Freedman, *The Hubble Constant and the Expansion Age of the Universe*, *Phys. Rept.* **333** (2000) 13, astro-ph/9909076.
- [64] D. J. Fixsen et al., *The Cosmic Microwave Background Spectrum from the Full COBE/FIRAS Data Set*, *Astrophys. J.* **473** (1996) 576, astro-ph/9605054.
- [65] J. S. Bagla, *Cosmological N-Body simulation: Techniques, Scope and Status*, *Curr. Sci.* **88** (2005) 1088, astro-ph/0411043.
- [66] A. A. Klypin et al., *Where are the missing galactic satellites?*, *Astrophys. J.* **522** (1999) 82, astro-ph/9901240.
- [67] [http://krone.physik.unizh.ch/~sim\\$moore/pictures.html](http://krone.physik.unizh.ch/~sim$moore/pictures.html).
- [68] J. F. Navarro, C. S. Frenk, and S. D. M. White, *A Universal Density Profile from Hierarchical Clustering*, *Astrophys. J.* **490** (1997) 493, astro-ph/9611107.
- [69] B. Moore et al., *Resolving the Structure of Cold Dark Matter Halos*, *Astrophys. J.* **499** (1998) L5, astro-ph/9709051.
- [70] J. Diemand, B. Moore, and J. Stadel, *Convergence and scatter of cluster density profiles*, *Mon. Not. Roy. Astron. Soc.* **353** (2004) 624, astro-ph/0402267.
- [71] M. R. Merrifield, *Dark matter on Galactic scales (or the lack thereof)*, (2004), astro-ph/0412059.
- [72] J. F. Navarro et al., *The Inner Structure of LambdaCDM Halos III: Universality and Asymptotic Slopes*, *Mon. Not. Roy. Astron. Soc.* **349** (2004) 1039, astro-ph/0311231.
- [73] D. Reed et al., *Evolution of the Density Profiles of Dark Matter Haloes*, *Mon. Not. Roy. Astron. Soc.* **357** (2005) 82, astro-ph/0312544.
- [74] T. Fukushige, A. Kawai, and J. Makino, *Structure of Dark Matter Halos From Hierarchical Clustering. III. Shallowing of The Inner Cusp*, *Astrophys. J.* **606** (2004) 625, astro-ph/0306203.
- [75] F. Stoehr, *Circular velocity profiles of dark matter haloes*, *Mon. Not. Roy. Astron. Soc.* **365** (2006) 147, astro-ph/0403077.
- [76] P. Colin et al., *Dwarf Dark Matter Halos*, *Astrophys. J.* **612** (2004) 50, astro-ph/0308348.

- [77] F. Prada et al., *Dark Matter Annihilation in the Milky Way Galaxy: Effects of Baryonic Compression*, Phys. Rev. Lett. **93** (2004) 241301, astro-ph/0401512.
- [78] O. Y. Gnedin and J. R. Primack, *A universal dark matter profile in the galactic center*, Phys. Rev. Lett. **93** (2004) 061302, astro-ph/0308385.
- [79] J. Diemand et al., *Cusps in CDM halos: The density profile of a billion particle halo*, Mon. Not. Roy. Astron. Soc. **364** (2005) 665, astro-ph/0504215.
- [80] M. Mateo, *Dwarf Galaxies of the Local Group*, Ann. Rev. Astron. Astrophys. **36** (1998) 435, astro-ph/9810070.
- [81] J. Flix et al., *Do the Unidentified EGRET Sources Trace Annihilating Dark Matter in the Local Group?*, (2004), astro-ph/0412419.
- [82] J.-M. Lamarre et al., *The Planck High Frequency Instrument, a 3rd generation CMB experiment, and a full sky submillimeter survey*, (2003), astro-ph/0308075.
- [83] A. Kosowsky, *The Atacama Cosmology Telescope*, New Astron. Rev. **47** (2003) 939, astro-ph/0402234.
- [84] B. R. Johnson et al., *MAXIPOL: A Balloon-borne Experiment for Measuring the Polarization Anisotropy of the Cosmic Microwave Background Radiation*, (2003), astro-ph/0308259.
- [85] A. L. Coil et al. (The DEEP2 Survey Collab.), *The DEEP2 Galaxy Redshift Survey: Clustering of Galaxies in Early Data*, Astrophys. J. **609** (2004) 525, astro-ph/0305586.
- [86] O. Le Fevre et al., *The VIRMOS deep imaging survey: I. overview and survey strategy*, Astron. Astrophys. **417** (2004) 839, astro-ph/0306252.
- [87] D. H. Jones et al., *The 6dF Galaxy Survey: Samples, Observational Techniques and the First Data Release*, (2004), astro-ph/0403501.
- [88] P. Astier et al., *The Supernova Legacy Survey: Measurement of  $\Omega_M$ ,  $\Omega_\Lambda$  and  $w$  from the First Year Data Set*, (2005), astro-ph/0510447.
- [89] J. Sollerman et al., *Supernova Cosmology and the ESSENCE project*, (2005), astro-ph/0510026.
- [90] T. Abbott et al. (Dark Energy Survey Collab.), *The dark energy survey*, (2005), astro-ph/0510346.
- [91] J. Albert et al. (SNAP Collab.), *Supernova Acceleration Probe: Studying Dark Energy with Type Ia Supernovae*, (2005), astro-ph/0507459.
- [92] M. Bartelmann and P. Schneider, *Weak Gravitational Lensing*, Phys. Rept. **340** (2001) 291, astro-ph/9912508.
- [93] <http://pan-starrs.ifa.hawaii.edu/public/index.html>.
- [94] [http://www.lsst.org/lsst\\_home.shtml](http://www.lsst.org/lsst_home.shtml).
- [95] F. Gianotti and M. L. Mangano, *LHC physics: The first one-two year(s)*, (2005), hep-ph/0504221.

- [96] Y. Baryshev, *Conceptual problems of the standard cosmological model*, (2005), astro-ph/0509800.
- [97] M. Milgrom and J. Bekenstein, The modified newtonian dynamics as an alternative to hidden matter, in R. Donaldson and M. Gilchriese, editors, *Proceedings of the Dark Matter in the Universe Conference*, Princeton, 1985, IAU Symposium.
- [98] H. Hoekstra, H. K. C. Yee, and M. D. Gladders, *The Red-Sequence Cluster Survey: first lensing results*, (2001), astro-ph/0109514.
- [99] R. H. Sanders and S. S. McGaugh, *Modified Newtonian Dynamics as an Alternative to Dark Matter*, Ann. Rev. Astron. Astrophys. **40** (2002) 263, astro-ph/0204521.
- [100] N. W. Evans and V. Belokurov, *RIP: The MACHO era (1974-2004)*, (2004), astro-ph/0411222.
- [101] G. Bertone, D. Hooper, and J. Silk, *Particle dark matter: Evidence, candidates and constraints*, Phys. Rept. **405** (2005) 279, hep-ph/0404175.
- [102] J. Wess and B. Zumino, Nucl. Phys. B **70** (1974) 39.
- [103] M. Maltoni et al., *Status of three-neutrino oscillations after the SNO-salt data*, Phys. Rev. **D68** (2003) 113010, hep-ph/0309130.
- [104] C. Weinheimer, *The neutrino mass direct measurements*, (2003), hep-ex/0306057.
- [105] P. Peebles, Science **224** (1984) 1385.
- [106] P. Sikivie, *Axion searches*, Nucl. Phys. Proc. Suppl. **87** (2000) 41, hep-ph/0002154.
- [107] J. L. Feng, A. Rajaraman, and F. Takayama, *Superweakly-interacting massive particles*, Phys. Rev. Lett. **91** (2003) 011302, hep-ph/0302215.
- [108] T. Moroi, H. Murayama, and M. Yamaguchi, *Cosmological constraints on the light stable gravitino*, Phys. Lett. **B303** (1993) 289.
- [109] W. Buchmuller, K. Hamaguchi, and M. Ratz, *Gauge couplings at high temperature and the relic gravitino abundance*, Phys. Lett. **B574** (2003) 156, hep-ph/0307181.
- [110] L. Covi et al., *Axino dark matter and the CMSSM*, JHEP **06** (2004) 003, hep-ph/0402240.
- [111] C. Boehm and P. Fayet, *Scalar dark matter candidates*, Nucl. Phys. **B683** (2004) 219, hep-ph/0305261.
- [112] C. Boehm et al., *MeV dark matter: Has it been detected?*, Phys. Rev. Lett. **92** (2004) 101301, astro-ph/0309686.
- [113] N. Arkani-Hamed, A. G. Cohen, and H. Georgi, *Electroweak symmetry breaking from dimensional deconstruction*, Phys. Lett. **B513** (2001) 232, hep-ph/0105239.
- [114] A. Birkedal-Hansen and J. G. Wacker, *Scalar dark matter from theory space*, Phys. Rev. **D69** (2004) 065022, hep-ph/0306161.
- [115] T. Kaluza et al., Math. Phys. **1921** (1921) 966.
- [116] E. W. Kolb, D. J. H. Chung, and A. Riotto, *WIMPzillas!*, (1998), hep-ph/9810361.

- [117] G. Shiu and L.-T. Wang, *D-matter*, Phys. Rev. **D69** (2004) 126007, hep-ph/0311228.
- [118] J. R. Ellis et al., *Update on the direct detection of supersymmetric dark matter*, Phys. Rev. **D71** (2005) 095007, hep-ph/0502001.
- [119] D. Hooper et al., *Have atmospheric Cerenkov telescopes observed dark matter?*, JCAP **0409** (2004) 002, astro-ph/0404205.
- [120] J. Flix (The MAGIC Collab.), *Planned dark matter searches with the MAGIC telescope*, (2005), astro-ph/0505313.
- [121] J. Cortina et al. (MAGIC Collab.), *Technical performance of the MAGIC telescope*, Prepared for 29th International Cosmic Ray Conference (ICRC 2005), Pune, India, 3-11 Aug 2005.
- [122] J. D. Bjorken, *Cosmology and the standard model*, Phys. Rev. **D67** (2003) 043508, hep-th/0210202.
- [123] L. Bergstrom, P. Ullio, and J. H. Buckley, *Observability of gamma rays from dark matter neutralino annihilations in the Milky Way halo*, Astropart. Phys. **9** (1998) 137, astro-ph/9712318.
- [124] A. Tasitsiomi and A. V. Olinto, *The detectability of neutralino clumps via atmospheric Cherenkov telescopes*, Phys. Rev. **D66** (2002) 083006, astro-ph/0206040.
- [125] F. Stoehr et al., *Dark matter annihilation in the Milky Way's halo*, Mon. Not. Roy. Astron. Soc. **345** (2003) 1313, astro-ph/0307026.
- [126] G. Jungman, M. Kamionkowski, and K. Griest, *Supersymmetric dark matter*, Phys. Rept. **267** (1996) 195, hep-ph/9506380.
- [127] S. Weinberg, Phys. Rev. D **26** (1982) 287.
- [128] L. Hall and M. Suzuki, Nucl. Phys. B **231** (1984) 419.
- [129] B. C. Allanach, A. Dedes, and H. K. Dreiner, *Bounds on R-parity violating couplings at the weak scale and at the GUT scale*, Phys. Rev. **D60** (1999) 075014, hep-ph/9906209.
- [130] R. Bernabei et al., *Dark matter particles in the galactic halo: Results and implications from DAMA/NaI*, Int. J. Mod. Phys. **D13** (2004) 2127, astro-ph/0501412.
- [131] D. S. Akerib et al. (CDMS Collab.), *Limits on spin-dependent WIMP nucleon interactions from the Cryogenic Dark Matter Search*, (2005), astro-ph/0509269.
- [132] H. V. Klapdor-Kleingrothaus et al., *GENIUS-TF: A test facility for the GENIUS project*, Nucl. Instrum. Meth. **A481** (2002) 149, hep-ex/0012022.
- [133] Y. Ascasibar et al., *Constraints on dark matter and the shape of the Milky Way dark halo from the 511-keV line*, (2005), astro-ph/0507142.
- [134] F. E. Paige et al., *ISAJET 7.69: A Monte Carlo event generator for  $p p$ ,  $anti-p p$ , and  $e+e-$  reactions*, (2003), hep-ph/0312045.
- [135] P. Gondolo et al., *DarkSUSY: Computing supersymmetric dark matter properties numerically*, JCAP **0407** (2004) 008, astro-ph/0406204.
- [136] A. Djouadi, J.-L. Kneur, and G. Moultaka, *SuSpect: A Fortran code for the supersymmetric and Higgs particle spectrum in the MSSM*, (2002), hep-ph/0211331.

- [137] B. C. Allanach, *SOFTSUSY: A C++ program for calculating supersymmetric spectra*, Comput. Phys. Commun. **143** (2002) 305, hep-ph/0104145.
- [138] L. S. Stark et al., *New allowed mSUGRA parameter space from variations of the trilinear scalar coupling  $A_0$* , JHEP **08** (2005) 059, hep-ph/0502197.
- [139] J. Edsjo et al., *Accurate relic densities with neutralino, chargino and sfermion coannihilations in mSUGRA*, JCAP **0304** (2003) 001, hep-ph/0301106.
- [140] G. Zaharijas and D. Hooper, *Challenges in detecting gamma-rays from dark matter annihilations in the galactic center*, (2006), astro-ph/0603540.
- [141] M. Battaglia et al., *Updated post-WMAP benchmarks for supersymmetry*, Eur. Phys. J. **C33** (2004) 273, hep-ph/0306219.
- [142] J. L. Feng, K. T. Matchev, and T. Moroi, *Multi-TeV scalars are natural in minimal supergravity*, Phys. Rev. Lett. **84** (2000) 2322, hep-ph/9908309.
- [143] S. Profumo and C. E. Yaguna, *A statistical analysis of supersymmetric dark matter in the MSSM after WMAP*, Phys. Rev. **D70** (2004) 095004, hep-ph/0407036.
- [144] J. Binney, *Discreteness effects in cosmological N-body simulations*, Mon. Not. Roy. Astron. Soc. **350** (2004) 939, astro-ph/0311155.
- [145] S. H. Hansen and B. Moore, *A universal density slope - velocity anisotropy relation for relaxed structures*, (2004), astro-ph/0411473.
- [146] K.-J. Ahn and P. R. Shapiro, *Formation and Evolution of the Self-Interacting Dark Matter Halos*, Mon. Not. Roy. Astron. Soc. **363** (2005) 1092, astro-ph/0412169.
- [147] O. Y. Gnedin et al., *Response of dark matter halos to condensation of baryons: cosmological simulations and improved adiabatic contraction model*, Astrophys. J. **616** (2004) 16, astro-ph/0406247.
- [148] N. Fornengo, L. Pieri, and S. Scopel, *Neutralino annihilation into gamma-rays in the Milky Way and in external galaxies*, Phys. Rev. **D70** (2004) 103529, hep-ph/0407342.
- [149] O. J. Eggen, D. Lynden-Bell, and A. R. Sandage, *Evidence from the motions of old stars that the galaxy collapsed*, Astrophys. J. **136** (1962) 748.
- [150] K. A. K. M. Zeldovich, B. and C. Chechetkin, Soviet J. Nucl. Phys. **31** (1980) 664.
- [151] R. Jesseit, T. Naab, and A. Burkert, *The Validity of the Adiabatic Contraction Approximation for Dark Matter Halos*, (2002), astro-ph/0204164.
- [152] A. Klypin et al., Astrophys. J. **573** (2002) 597.
- [153] J. J. Binney and N. W. Evans, *Cuspy Dark-Matter Haloes and the Galaxy*, Mon. Not. Roy. Astron. Soc. **327** (2001) L27, astro-ph/0108505.
- [154] C. Afonso et al. (The EROS Collab.), *Bulge Microlensing Optical Depth from EROS 2 observations*, Astron. Astrophys. **404** (2003) 145, astro-ph/0303100.
- [155] P. Popowski et al., *Recent Microlensing Results from the MACHO Project*, (2003), astro-ph/0304464.

- [156] Y. Mambrini et al., *Adiabatic compression and indirect detection of supersymmetric dark matter*, JCAP **0601** (2006) 010, hep-ph/0506204.
- [157] E. Domingo-Santamaria et al. (MAGIC Collab.), *The DISP analysis method for point-like or extended gamma source searches / studies with the MAGIC telescope*, Prepared for 29th International Cosmic Ray Conference (ICRC 2005), Pune, India, 3-11 Aug 2005.
- [158] N. W. Evans, F. Ferrer, and S. Sarkar, *Dark matter annihilation and the dwarf spheroidals*, Phys. Rev. **D69** (2004) 123501, astro-ph/0311145.
- [159] M. I. Wilkinson et al., *Kinematically Cold Populations at Large Radii in the Draco and Ursa Minor Dwarf Spheroidal Galaxies*, ApJ **611** (2004) L21.
- [160] M. Odenkirchen et al. (SDSS Collab.), *New insights on the Draco dwarf spheroidal galaxy from SDSS: a larger radius and no tidal tails*, Astron. J. **122** (2001) 2538, astro-ph/0108100.
- [161] N. W. Evans, *The power-law galaxies*, MNRAS **267** (1994) 333.
- [162] H. C. Plummer, *On the problem of distribution in globular star clusters*, MNRAS **71** (1911) 460.
- [163] J. L. Sersic, *Atlas de galaxias australes*, Cordoba, Argentina: Observatorio Astronomico, 1968, 1968.
- [164] F. Stoehr et al., *The Milky Way's satellite population in a LambdaCDM universe*, Mon. Not. Roy. Astron. Soc. **335** (2002) L84, astro-ph/0203342.
- [165] S. Kazantzidis et al., *Density Profiles of Cold Dark Matter Substructure: Implications for the Missing Satellites Problem*, Astrophys. J. **608** (2004) 663, astro-ph/0312194.
- [166] J. Kleya et al., *Dark matter in dwarf spheroidals - II. Observations and modelling of Draco*, MNRAS **330** (2002) 792.
- [167] R. Braun, AstroP. Journal **372** (1991) 54.
- [168] A. Falvard et al., *Supersymmetric dark matter in M31: Can one see neutralino annihilation with CELESTE?*, Astropart. Phys. **20** (2004) 467, astro-ph/0210184.
- [169] J. Lavalle et al., *Indirect search for dark matter in M31 with the CELESTE experiment*, (2006), astro-ph/0601298.
- [170] V. Berezhinsky, V. Dokuchaev, and Y. Eroshenko, *Destruction of small-scale dark matter clumps in the hierarchical structures and galaxies*, Phys. Rev. **D73** (2006) 063504, astro-ph/0511494.
- [171] G. Bertone, A. R. Zentner, and J. Silk, *A new signature of dark matter annihilations: Gamma-rays from intermediate-mass black holes*, Phys. Rev. **D72** (2005) 103517, astro-ph/0509565.
- [172] P. Salati, *Quintessence and the relic density of neutralinos*, Phys. Lett. **B571** (2003) 121, astro-ph/0207396.
- [173] M. Fujii and M. Ibe, *Neutralino dark matter from MSSM flat directions in light of WMAP result*, Phys. Rev. **D69** (2004) 035006, hep-ph/0308118.

- [174] T. C. Weekes, *The atmospheric Cherenkov imaging technique for very high energy gamma-ray astronomy*, (2005), astro-ph/0508253.
- [175] G. F. Bignami and W. Hermsen, *GALACTIC GAMMA-RAY SOURCES*, Ann. Rev. Astron. Astrophys. **21** (1983) 67.
- [176] R. C. Hartman et al. (EGRET Collab.), *The Third EGRET catalog of high-energy gamma-ray sources*, Astrophys. J. Suppl. **123** (1999) 79.
- [177] D. S. Hanna et al., *The STACEE-32 ground based gamma-ray detector*, Nucl. Instrum. Meth. **A491** (2002) 126.
- [178] R. W. Atkins et al. (Milagro Collab.), *Milagrito, a TeV air-shower array*, Nucl. Instrum. Meth. **A449** (2000) 478, astro-ph/9912456.
- [179] A. Hillas, Proceedings 19th ICRC, La Jolla **3** (1985) 445.
- [180] J. A. Hinton (The HESS Collab.), *The status of the HESS project*, New Astron. Rev. **48** (2004) 331, astro-ph/0403052.
- [181] J. Albert i Fort et al. (MAGIC Collab.), *The MAGIC project: Contributions to ICRC 2005, Pune, India. Part 3: MAGIC detector and analysis details*, (2005), astro-ph/0508274.
- [182] J. Holder et al. (VERITAS Collab.), *Status and performance of the first VERITAS telescope*, (2005), astro-ph/0507451.
- [183] A. Kawachi et al., *The optical reflector system for the CANGAROO-II imaging atmospheric Cherenkov telescope*, Astropart. Phys. **14** (2001) 261, astro-ph/0007194.
- [184] F. Aharonian et al. (HESS Collab.), *The HESS survey of the inner galaxy in very high-energy gamma-rays*, Astrophys. J. **636** (2006) 777, astro-ph/0510397.
- [185] J. Albert et al. (MAGIC Collab.), *MAGIC observations of very high energy gamma-rays from HESS J1813-178*, Astrophys. J. **637** (2006) L41, astro-ph/0512283.
- [186] R. Ong, *Rapporteur Talk OG1 at the 29th ICRC, Pune, India*, (2005).
- [187] H. J. Volk, *New results from high energy gamma-ray astronomy*, (2006), astro-ph/0603501.
- [188] M. Longair, Cambridge University Press, 2nd ed. reprinted with corrections, 1997.
- [189] T. Gaisser, Cambridge University Press, 1990.
- [190] K. Greisen, Prog. Cosmic Ray Physics **3** (1956) 1.
- [191] J. Nishimura and K. Kamata, Progress in Theoretical Physics **7** (1952) 185.
- [192] M. Risse, *Properties of extensive air showers*, Acta Phys. Polon. **B35** (2004) 1787, astro-ph/0402300.
- [193] D. Paneque, PhD. Thesis, Technischen Universit .
- [194] A. Moralejo, PhD. Thesis, Universidad Complutense de Madrid (2000).
- [195] T. Weekes et al., ApJ **342** (1989) 379.
- [196] R. A. Ong, *Very high-energy gamma-ray astronomy*, Phys. Rept. **305** (1998) 93.

- [197] J. Albert i Fort et al. (MAGIC Collab.), *The MAGIC project: Contributions to ICRC 2005, Pune, India. Part 1: Observations*, (2005), astro-ph/0508244.
- [198] S. Bradbury et al., *A Project for a 17m Diameter Imaging Cherenkov Telescope*, Proceedings of the 24th ICRC, Rome **vol.1** (1995) 1051.
- [199] J. A. Barrio et al. (MAGIC Collab.), *The MAGIC telescope*, MPI-PhE/98-5 (1998).
- [200] A. Ostankov et al., *A study of the new hemispherical 6-dynodes PMT from electron tubes*, NIM A **442**, Issue **1-3** (2000) 117.
- [201] M. Gaug, PhD. Thesis, in preparation (2006).
- [202] F. Aharonian et al. (The H.E.S.S. Collab.), *A new population of very high energy gamma-ray sources in the Milky Way*, Science **307** (2005) 1938, astro-ph/0504380.
- [203] J. Albert et al. (MAGIC Collab.), *Observation of gamma rays from the galactic center with the MAGIC telescope*, Astrophys. J. **638** (2006) L101, astro-ph/0512469.
- [204] J. Albert et al. (MAGIC Collab.), Astrophys. J. submitted (2006).
- [205] E. Aliu et al. (MAGIC Collab.), *Observation of VHE gamma-ray emission from the active galactic nucleus 1ES1959+650 using the MAGIC telescope*, Astrophys. J. **639** (2006) 761, astro-ph/0508543.
- [206] J. Albert et al. (MAGIC Collab.), Astrophys. J. submitted (2006).
- [207] J. Albert et al., *Flux upper limit of gamma-ray emission by GRB050713a from MAGIC Telescope observations*, Astrophys. J. **641** (2006) L9, astro-ph/0602231.
- [208] D. Bastieri et al. (MAGIC Collab.), *An AGN observation catalogue for the MAGIC Cherenkov telescope*, Prepared for 28th International Cosmic Ray Conferences (ICRC 2003), Tsukuba, Japan, 31 Jul - 7 Aug 2003.
- [209] J. Rico et al. (MAGIC Collab.), *Status First Results, and Prospects for MAGIC*, (2005).
- [210] F. J. Cortina, J. et al., *The control system of the magic telescope*, in *Internal MAGIC document, MAGIC-TDAS 00-07, version 7.2*, 2006.
- [211] F. J. Cortina, J. et al. (MAGIC Collab.), *Camera control and central control of the MAGIC telescope*, Prepared for 28th International Cosmic Ray Conferences (ICRC 2003), Tsukuba, Japan, 31 Jul - 7 Aug 2003.
- [212] J. Bonache, Master Thesis (2004).
- [213] A. Armada, Master Thesis (2005).
- [214] J. Lopez, PhD. Thesis, in preparation (2006).
- [215] E. Domingo,  *$\gamma$ -ray emission from regions of star formation: Theory and observations with the MAGIC Telescope*, (2001), Phd. Thesis.
- [216] R. Mirzoyan and E. Lorenz, Max-Planck-Institut fur Physik report MPI-PhE/94-35 (1994).
- [217] D. Heck and J. Knapp, *EAS Simulation with CORSIKA: A User's Manual*, (2002).

- [218] H. Bartko et al. (MAGIC Collab.), *FADC pulse reconstruction using a digital filter for the MAGIC telescope*, (2005), astro-ph/0506459.
- [219] P. Liebing, Timing structure and inhomogeneities of the magic camera, in *Internal MAGIC document, MAGIC-TDAS 05-08*, 2005.
- [220] P. T. Reynolds et al., *Survey of candidate gamma-ray sources at TeV energies using a high resolution Cherenkov imaging system: 1988 - 1991*, *Astrophys. J.* **404** (1993) 206.
- [221] J. Zimmermann, *Statistical Learning in High Energy and Astrophysics*, PhD. Thesis, Ludwig-Maximilians-Universit .
- [222] V. P. Fomin et al., *New methods of atmospheric Cherenkov imaging for gamma-ray astronomy. 1: The False source method*, *Astropart. Phys.* **2** (1994) 137.
- [223] D. Kranich and L. S. Stark (HEGRA Collab.), *A new method to determine the arrival direction of individual air showers with a single air Cherenkov telescope*, Prepared for 28th International Cosmic Ray Conferences (ICRC 2003), Tsukuba, Japan, 31 Jul - 7 Aug 2003.
- [224] R. W. Lessard et al., *A new analysis method for reconstructing the arrival direction of TeV gamma-rays using a single imaging atmospheric Cherenkov telescope*, *Astropart. Phys.* **15** (2001) 1, astro-ph/0005468.
- [225] J. Albert et al. (MAGIC Collab.), *Discovery of VHE gamma-ray emission from 1ES 1218+30.4*, (2006), astro-ph/0603529.
- [226] J. Albert et al. (MAGIC Collab.), *Observations of Mkn 421 with the MAGIC Telescope*, (2006), astro-ph/0603478.
- [227] T. P. Li and Y. Q. Ma, *Analysis methods for results in gamma-ray astronomy*, *Astrophys. J.* **272** (1983) 317.
- [228] W. Wittek, Determination of the effective observation time, in *Internal MAGIC document, MAGIC-TDAS 02-02*, 2002.
- [229] G. D. Lafferty and T. R. Wyatt, *Where to stick your data points: The treatment of measurements within wide bins*, *Nucl. Instrum. Meth.* **A355** (1995) 541.
- [230] W. Wittek, Unfolding, in *Internal MAGIC document, MAGIC-TDAS 05-05*, 2005.
- [231] A. Goldwurm, *The Galactic Center at High Energies*, (2005), astro-ph/0511221.
- [232] F. Melia and H. Falcke, *The Supermassive Black Hole at the Galactic Center s*, *Ann. Rev. Astron. Astrophys.* **39** (2001) 309, astro-ph/0106162.
- [233] G. Belanger et al., *Repeated X-ray Flaring Activity in Sagittarius A\**, *Astrophys. J.* **635** (2005) 1095, astro-ph/0508412.
- [234] C. L. Fryer et al., *The Sgr B2 X-ray Echo of the Galactic Center Supernova Explosion that Produced Sgr A East*, *Astrophys. J.* **638** (2006) 786, astro-ph/0506242.
- [235] K. Koyama et al., *ASCA View of Our Galactic Center: Remains of Past Activities in X-Rays?*, *Publ. Astron. Soc. Jap.* **48** (1996) 249.
- [236] D. Hooper and B. Dingus, *Improving the angular resolution of EGRET and new limits on supersymmetric dark matter near the galactic center*, (2002), astro-ph/0212509.

- [237] M. Pohl, *A variability and localization study of 3EG J1746-2851*, (2004), astro-ph/0412603.
- [238] F. Aharonian et al. (HESS Collab.), *H.E.S.S. observations of the Galactic Center region and their possible dark matter interpretation*, Phys. Rev. Lett. submitted (2006).
- [239] F. Aharonian et al. (The HESS Collab.), *Very high energy gamma rays from the direction of Sagittarius A\**, Astron. Astrophys. **425** (2004) L13, astro-ph/0408145.
- [240] W. Wittek, *Transformations between the sky, the local and the camera reference systems*, in *Internal MAGIC document, MAGIC-TDAS 05-07*, 2005.
- [241] N. Tonello, *Study of the VHE  $\gamma$ -ray emission from the Active Galactic Nucleus 1ES 1959+650*, (2006), Phd. Thesis.
- [242] K. Tsuchiya et al. (CANGAROO-II Collab.), *Detection of sub-TeV gamma-rays from the galactic center direction by CANGAROO-II*, Astrophys. J. **606** (2004) L115, astro-ph/0403592.
- [243] K. Kosack et al. (The VERITAS Collab.), *TeV gamma-ray observations of the galactic center*, Astrophys. J. **608** (2004) L97, astro-ph/0403422.
- [244] F. Aharonian et al. (H.E.S.S. Collab.), *Discovery of very-high-energy gamma-rays from the galactic centre ridge*, (2006), astro-ph/0603021.
- [245] D. Horns, *TeV gamma-radiation from dark matter annihilation in the galactic center*, Phys. Lett. **B607** (2005) 225, astro-ph/0408192.
- [246] R. Firpo, *Study of MAGIC telescope sensitivity for Large Zenith Angle observations*, Master Thesis (2006).
- [247] S. Profumo, *TeV gamma-rays and the largest masses and annihilation cross sections of neutralino dark matter*, Phys. Rev. **D72** (2005) 103521, astro-ph/0508628.
- [248] A. Neronov and F. Aharonian, *TeV gamma rays from Sgr A\**, AIP Conf. Proc. **745** (2005) 409.
- [249] E. Quataert and A. Loeb, *Nonthermal THz to TeV Emission from Stellar Wind Shocks in the Galactic Center*, Astrophys. J. **635** (2005) L45, astro-ph/0509265.
- [250] K. S. Cheng, D. O. Chernyshov, and V. A. Dogiel, *Annihilation Emission from the Galactic Black Hole*, (2006), astro-ph/0603659.
- [251] S.-M. Liu et al., *Stochastic acceleration in the galactic center HESS source*, (2006), astro-ph/0603137.
- [252] F. Aharonian et al. (The H.E.S.S. Collab.), *Detection of TeV gamma-ray emission from the shell-type supernova remnant RX J0852.0-4622 with HESS*, (2005), astro-ph/0505380.
- [253] D. Grasso and L. Maccione, *Sgr A East as a possible high energy neutron factory in the galactic centre*, Astropart. Phys. **24** (2005) 273, astro-ph/0504323.
- [254] S. Profumo and M. Kamionkowski, *Dark matter and the CACTUS gamma-ray excess from Draco*, JCAP **0603** (2006) 003, astro-ph/0601249.
- [255] J. Albert i Fort et al., *Physics and astrophysics with a ground-based gamma-ray telescope of low energy threshold*, Astropart. Phys. **23** (2005) 493.

- 
- [256] R. M. Crocker, F. Melia, and R. R. Volkas, *Neutrinos from the galactic center in the light of HESS*, *Astrophys. J.* **622** (2005) L37, astro-ph/0411471.
- [257] W. de Boer et al., *The supersymmetric interpretation of the EGRET excess of diffuse galactic gamma rays*, (2005), hep-ph/0511154.
- [258] L. Bergstrom et al., *Is the dark matter interpretation of the EGRET gamma excess compatible with antiproton measurements?*, (2006), astro-ph/0602632.